NITROXIDES AT THE INTERFACE: BIOINSPIRED POLYMER ADHESIVES FOR CONTROLLING BIOFILM-RELATED INFECTIONS

Zur Erlangung des akademischen Grades eines

DOKTORS DER NATURWISSENSCHAFTEN

(Dr. rer. nat.)

von der KIT-Fakultät für Chemie und Biowissenschaften

des Karlsruher Instituts für Technologie (KIT)

genehmigte

DISSERTATION

von

M.Sc. Hendrik Wöhlk

geboren in Kiel, Deutschland

KIT-Dekan:	Prof. Dr. Reinhard Fischer
Referenten:	Prof. Dr. Christopher Barner-Kowollik, Dr. James P. Blinco
Korreferent:	Prof. Dr. Patrick Théato

Tag der mündlichen Prüfung: 13.12.2018

Die vorliegende Arbeit wurde vom Juli 2015 bis Oktober 2018 unter Anleitung von Prof. Dr Christopher Barner-Kowollik, A/Prof. Dr Kathryn E. Fairfull-Smith und Dr. James P. Blinco am Karlsruher Institut für Technologie (KIT) und der Queensland University of Technology (QUT) im Rahmen einer gemeinschaftlichen Betreuung angefertigt.

dedicated to my family

Abstract

This thesis reports a sophisticated avenue for the generation of nitroxide-containing bioadhesive polymers. The versatile polymer coating platform was applied to the precision design of various material interfaces, equipping them with nitroxide-stemming multi-radical, electroactive and antibiofilm properties.

First, the synthesis of a polymerisable catecholamine equipped with a nitroxide functional group is introduced. L-3,4-Dihydroxyphenylalanine (L-DOPA) was amide linked to a 2,2,6,6-tetramethylpiperidine-1-oxyl (TEMPO) derivative, implemented by standard protecting group chemistries. The tailor-made monomer, denoted as DOPA-TEMPO, was employed as the corresponding hydroxylamine dihydrochloride species for subsequent aerobic polymerisation under slightly alkaline, aqueous conditions. The oxidation of the catechol moiety toward *o*-quinoic species was ascribed a critical role during the initial build-up of reactive oligomeric intermediates as investigated by UV–visible spectroscopy. An accelerated nitroxide radical formation (overall 85%) derived from aerobic hydroxylamine oxidation was observed in the second stage of DOPA-TEMPO polymerisation. Furthermore, the covalent nature of poly(DOPA-TEMPO) scaffolds was confirmed by high-resolution electrospray ionisation mass spectrometry (HR-ESI-MS). Oligomers with up to six repeating units were identified and indole-like building blocks have been proposed as important structural motifs constituting the polymer backbone.

The HR-ESI-MS characterisation platform was further expanded for the structural elucidation of an analogous polymer system using the methoxyamine derivative of DOPA-TEMPO as the corresponding monomer. Broad oligomer profiles with up to eight repeating units were detected by HR-ESI-MS indicating a heterogeneous polymer composition with multiple coexisting and structurally diverse building blocks. Dihydroxyindole was designated as the key structural element along the polymer backbone. However, a clear trend toward higher content of incorporated uncyclised catecholic building blocks was observed with increasing polymer chain length.

Subsequently, the DOPA-TEMPO polymerisation protocol was applied as a versatile coating strategy for substrate-independent nitroxide surface functionalisations. The adhesive performances of poly(DOPA-TEMPO) coatings were examined using various types of substrates including silicon, ceramic alumina, metallic titanium and chemically inert poly(tetrafluoroethylene) (PTFE). X-ray photoelectron spectroscopy (XPS), atomic force microscopy (AFM) and contact angle measurements were employed to critically assess the formation of thin nitroxide-containing polymer films deposited on all employed surfaces after 24 h of polymerisation. The inherent surface roughness of uncoated PTFE most likely compensated for the predominant weak (noncovalent) binding interactions between the interfacial modifier and the underlying substrate during the initial stage of polymerisation (12 h). In contrast, a decelerated polymer film formation was overserved when smooth silicon was employed as a substrate. A continuously growing polymer film formation on silicon with an average growth rate close to 1.1 $nm \cdot h^{-1}$ was monitored by spectroscopic ellipsometry. AFM height profile measurements confirmed the polymer film thicknesses and further depicted the inherent surface roughness of poly(DOPA-TEMPO) coatings. The reversible redox properties of nitroxide polymer films adherent on glassy carbon or platinum working electrodes were assessed electrochemically by cyclic voltammetry (CV). In addition, an advanced photopolymerisation protocol for poly(DOPA-TEMPO) coatings was established for light-controlled (UV-B) polymer film formations onto surfaces.

Dynamic covalent alkoxyamine switches were introduced at the interface of poly(glycidyl methacrylate) (PGMA) microspheres. PGMA microspheres were coated beforehand by a thin nitroxide-containing polymer film obtained through oxidative copolymerisation of dopamine and DOPA-TEMPO (molar ratio 9:1). Coding and decoding of nitroxide functional microspheres were performed in consecutive nitroxide radical coupling (NRC) and thermal alkoxyamine fission reaction steps. As a proof of concept, the rewritable surface properties were illustrated using chloroalkyl- and fluoroalkyl-functionalised 2-bromoisobutyrate derivatives as NRC agents with good XPS contrast. Moreover, the versatile nitroxide coating platform was expanded for spatially resolved surface photopatterning with synthetic polymer strands. Photoactive poly(methyl methacrylate) (PMMA) and poly(2,2,2-trifluoroethyl methacrylate) (PTFEMA) polymer strands, terminated with an Irgacure 2959 photoinitiator system, were rapidly conjugated to nitroxide-decorated poly(dopamine) surfaces using NRC photo-click reactions. Dual polymer surface patterning was evidenced by time-of-flight secondary ion mass spectrometry (ToF-SIMS) and XPS imaging.

In the final part of the thesis, an evolving strategy for the prevention of biofilm formation on surfaces is presented. Nitroxide-coated hydroxyapatite surfaces were exposed to *Pseudomonas aeruginosa* biofilm cultivation (for 72 h under flow conditions) using a green fluorescent protein (GFP)-labelled PA14 strain. The antibiofilm coating properties were unambiguously assigned to the polymer-embedded nitroxide functional moieties with no side effects stemming from the surrounding polymer matrix. Synergistic effects of nitroxide functional coatings and antibiotic ciprofloxacin were demonstrated in biofilm eradication assays. The versatile and adaptable nitroxide coating system was further exploited in nitroxide surface immobilisations onto titanium implants with spatial resolution. The photopatterned antibiofilm domains showed substantial resistance toward *P. aeruginosa* biofilm formation, which further demonstrates the wide-ranging potential of this versatile antibiofilm coating strategy in biomedical applications.

In conclusion, the macromolecular design of nitroxide functional materials was explored. The mild polymerisation and straightforward surface coating strategies ensured a widespread practical use for the precision surface engineering of various material interfaces. The herein presented results promoted the design of smart functional materials including dynamic covalent polymer materials and sustainable electroactive composite materials. Most importantly, the fusion of nitroxide-stemming antibiofilm properties with a bioinspired and substrate-independent coating technique has emerged as a novel prophylactic strategy to reduce biofilm-related infections.

Zusammenfassung

In der vorliegenden Arbeit wird eine biologisch inspirierte Syntheseroute zur Darstellung von nitroxidfunktionalisierten, adhäsiven Makromolekülen präsentiert. Ein vielseitiges Polymerbeschichtungsverfahren wurde angewendet, um verschiedene Materialoberflächen gezielt mit nitroxidcharakteristischen multi-radikalen, elektroaktiven und Antibiofilm-Eigenschaften zu versehen.

Zu Beginn ist die Synthese eines polymerisierbaren Katecholamins beschrieben, das mit einer Nitroxid-funktionellen Gruppe verknüpft worden ist. L-3,4-Dihydroxyphenylalanin (L-DOPA) wurde mittels einer Amid-Kupplungsreaktion und unter Anwendung von konventioneller Schutzgruppenchemie an ein Derivat von 2,2,6,6-Tetramethylpiperidin-1-oxyl (TEMPO) gebunden. Das maßgeschneiderte Monomer, gekennzeichnet als DOPA-TEMPO, wurde als entsprechendes Hydroxylamin Dihydrochlorid-Salz in der darauffolgenden aeroben Polymerisation unter leicht alkalischen wässrigen Bedingungen eingesetzt. Anhand von UV/VIS-spektroskopischen Messungen wurde der Oxidation der Katecholeinheit, einhergehend mit der Enstehung von *ortho*-Chinon abgeleiteten Struktureinheiten, eine entscheidene Rolle im anfänglichen Aufbau von reaktiven Oligomerzwischenstufen zugewiesen. Eine vermehrte Nitroxidradikalentstehung (ingesamt 85%) ausgehend von der aeroben Oxidation des Hydroxylamins wurde im zweiten Abschnitt der DOPA-TEMPO Polymerisation beobachtet. Des Weiteren wurde der kovalente Charakter von Poly(DOPA-TEMPO) anhand der hochauflösenden Massenspektrometrie mit Elektrospray-Ionisation (HR-ESI-MS) bewiesen. Oligomere mit bis zu sechs Wiederholeinheiten wurden identifiziert und Indol-ähnliche Bausteine wurden als wichtige Strukturmotive, geltend für das Polymerrückgrat, vorgeschlagen.

Die Charakterisierung mittels hochauflösender Massenspektrometrie wurde weiterhin für die Strukturanalyse eines vergleichbaren Polymersystems vollzogen, bei dem das entsprechende Methoxyderivat von DOPA-TEMPO als Monomer diente. Breite Oligomerprofile mit bis zu acht Wiederholeinheiten wurden mittels HR-ESI-MS detektiert, das auf eine äußerst heterogene Polymerzusammensetzung mit einer Vielzahl an koexistenten und strukturell vielseitigen Struktureinheiten schließen lässt. Dihydroxyindol wurde als elementarer Grundbaustein im

Polymerrückgrat nachgewiesen. Dennoch wurde eine klare Tendenz hinzu des vermehrten Einbaus an nichtzyklischen Katecholeinheiten mit steigender Polymerkettenlänge beobachtet.

Anschließend wurde das DOPA-TEMPO Polymerisationsverfahren in eine vielseitige Beschichtungsstrategie umgewandelt, welches eine substratunabhängige Nitroxid-Oberflächenfunktionalisierung ermöglichte. Die Haftungseigenschaften von Poly(DOPA-TEMPO)-Oberflächenbeschichtungen wurden in Abhängigkeit verschiedener Substrattypen getestet. Hierbei kamen Silicium, keramisches Aluminiumoxid, Titan und chemisch-inertes Poly(tetrafluoroethylen) (PTFE) als Materialien zum Einsatz. Anhand von Röntgenphotoelektronenspektroskopie (XPS), Rasterkraftmikroskopie (AFM) und Kontaktwinkelmessungen wurde die Bildung von nitroxidhaltigen Polymerfilmen auf den oben genannten Oberflächen kritisch nach einer Reaktionsdauer von 24 Stunden untersucht. Die inhärente Oberflächenrauigkeit von unbeschichtetem PTFE kompensierte hierbei womöglich die vorherrschenden schwachen (nichtkovalenten) Bindungswechselwirkungen zwischen dem Grenzflächenmodifizierer und dem Substrat, wie es XPS Messungen in der Anfangsphase der Polymerisation nach 12 Stunden gezeigt haben. Im Gegensatz dazu wurde eine verlangsamte Polymerablagerung auf glatten Siliciumoberflächen beobachtet. Ein kontinuierlich wachsender Polymerfilm mit einer gemittelten Wachstumsrate von ca. 1,1 nm pro Stunde wurde anhand von Ellipsometriemessungen ermittelt und die Polymerschichtdicken anschließend mittels AFM Höhenprofilmessungen bestätigt. Des Weiteren wurde die Oberflächenrauigkeit der Beschichtungen mittels AFM genauestens bestimmt. Die reversiblen Redoxeigenschaften von Nitroxidpolymeren, die zuvor auf Glasskohlenstoff- und Platinarbeitselektroden immobilisiert worden sind, wurden mittels Cyclovoltammetrie elektrochemisch analysiert. Weiterhin wurde ein lichtabhängiges (UV-B) Photopolymerisationsverfahren für die Darstellung von Poly(DOPA-TEMPO) Oberflächenbeschichtungen etabliert.

Dynamisch-kovalente Alkoxyamin-funktionelle Gruppen wurden auf Oberflächen von Poly(glycidylmethylacrylat) (PGMA) Mikropartikeln aufgebracht. Dabei wurden die PGMA Mikropartikel zuerst mit einer dünnen nitroxidhaltigen Polymerschicht umhüllt, die mittels einer oxidativen Copolymerisation von Dopamin und DOPA-TEMPO (molares Verhältnis 9:1) generiert wurde. Die nitroxidhaltigen

Mikropartikel wurden in aufeinanderfolgenden Nitroxidradikalkupplungsreaktionen (NRC) und thermischen Alkoxyaminbindungsbrüchen reversibel funktionalisiert. Als Machbarkeitsnachweis der wiederbeschreibaren Oberflächeneigenschaften wurden chloroalkyl- und fluoroalkylfunktionalisierte 2-Bromoisobutyratderivate als NRC Reagenzien eingesetzt, da diese Moleküle einen guten XPS Kontrast aufwiesen. Zudem wurde das vielseitige Nitroxidbeschichtungsverfahren erweitert, indem eine ortsaufgelöste Oberflächenfunktionalisierung mit synthetischen Polymersträngen präsentiert wurde. Photochemisch aktives Poly(methymethacrylat) (PMMA) und Poly(2,2,2-trifluoroethylmethacrylat) (PTFEMA), die jeweils mit einem Irgacure 2959 Photoinitiatorsystem terminiert worden sind, wurden an nitroxid-dekorierten Polydopaminoberflächen mittels NRC-Photoklick-Reaktionen gebunden. Die zweifache Oberflächenmusterung mit den entsprechenden Polymeren wurde anhand von Flugzeit-Sekundärionen-Massenspektrometrie (ToF-SIMS) and XPS Bildgebungsmethoden nachgewiesen.

Im letzten Teil der Dissertation wurde eine neue Strategie zur Prävention von Biofilmen auf Oberflächen präsentiert. Nitroxidbeschichtete Hydroxylapatit-oberflächen wurden einer *Pseudomonas aeruginosa* Biofilmkultivierung ausgesetzt (für 72 Stunden unter einem kontinuerlichen Fluss des Nährmediums). Hierbei wurde ein mit grünfluoreszierendem Protein (GFP) gekennzeichneter PA14 Stamm verwendet. Die Antibiofilm-Eigenschaften wurden eindeutig den im Polymer eingebauten Nitroxiden zugeordnet. Etwaige Nebenwirkungen von der umgebenen Polymermatrix konnten ausgeschlossen werden. Des Weiteren wurden Synergieeffekte zwischen nitroxidfunktionalisierten Oberflächen und antibiotisch wirkendem Ciprofloxacin in der Eradikation von Biofilmen verdeutlicht. Das vielseitige und anpassungsfähige Nitroxidbeschichtungssytem wurde weiterhin für die ortsaufgelöste Oberflächenimmobilisierung von Nitroxiden auf Titanimplantaten angewendet. Die von Licht gesteuerte Entstehung von Antibiofilm-Domänen wiesen eine beachtliche Resistenz gegenüber *P. aeruginosa* Biofilmen auf. Das weitreichende Potential dieses vielseitigen Beschichtungsverfahren in biomedizinischen Anwendungen wurde hiermit aufgezeigt.

Zusammenfassend wurde die makromolekulare Gestaltung von nitroxidfunktionellen Oberflächen präsentiert. Unter Anwendung eines milden Polymerisationsverfahren und einer weitreichenden Oberflächenbeschichtungsstrategie wurden ver-

schiedene Materialgrenzflächen präzise modifiziert. Die in der vorliegenden Arbeit präsentieren Ergebnisse tragen zur Entwicklung von hochfunktionellen Materialien bei, einschließlich der Weiterentwicklung von dynamisch-kovalenten Polymermaterialien und nachhaltigen elektroaktiven Verbundsmaterialien. Besonders vielversprechend erwies sich die Verschmelzung von nitroxidbasierenden Antibiofilm-Eigenschaften mit einer biologisch inspirierten und substratunabhängigen Beschichtungsverfahrenweise, aus der eine neuartige prophylaktische Strategie zur Reduzierung von biofilmassoziierten Infektionen hervorgetreten ist.

Table of Contents

Abstract i

Zusammenfassung iv

Table of Contents viii

Publications Arising from the Thesis x

Erklärung xi

Chapter 1: Introduction and Motivation 1

Chapter 2: Literature Review 7

2.1 Nitroxides as Functional Materials 7

2.2 Bioinspired Polymer Coatings 26

2.3 Bacterial Biofilms and Biofouling 42

Chapter 3: Incorporating Nitroxides within Poly(catecholamine) Scaffolds 53

3.1 Preface 53

3.2 Design and Synthesis of a Nitroxide Functional Catecholamine 54

3.3 Oxidative Polymerisation of DOPA-TEMPO 59

3.4 Mass Spectrometric Identification of Poly(DOPA-TEMPO) Structures 67

3.5 Conclusion 72

Chapter 4: Structural Elucidation of Poly(catecholamine)s by HR-MS 73

4.1 Preface 73

4.2 Synthesis and Polymerisation of DOPA-TEMPO-CH_3 74

4.3 In-Depth Characterisation of Poly(DOPA-TEMPO-CH_3) Key Structural Elements 78

4.4 Conclusion 88

Chapter 5: Nitroxide Surface Decoration Using Bioadhesion 91

5.1 Preface 91

5.2 Exploiting the Versatile Character of Poly(DOPA-TEMPO) Coatings 92

5.3 Characterisation of Nitroxide-Containing Thin Polymer Films 96

5.4 Light-Controlled Polymerisation and Nitroxide Surface Immobilisation 100

5.5 Conclusion 103

Chapter 6: Dynamic Nitroxide Functional Materials 105

6.1 Preface 105

6.2 Engineering Nitroxide Functional Microspheres with Rewritable Properties 106

6.3 Polymer Photo-Click Surface Ligations with Spatial Resolution 113

6.4 Conclusion 118

Chapter 7: Versatile Antibiofilm Coatings 119

7.1 Preface 119

7.2 Synthesis of DOPA-Cy as a Reference Coating Agent 120

7.3 Manufacturing of TEMPO- and Cy-containing Polymer Coatings 122

7.4 *P. aeruginosa* Biofilm Cultivation and Eradication Assays 126

7.5 Photolithographic Nitroxide Polymer Immobilisation onto Titanium Implants 131

7.6 Spatially Controlled Antibiofilm Surfaces 136

7.7 Conclusion 137

Chapter 8: Concluding Remarks 139

Chapter 9: Experimental Section 147

9.1 Materials 147

9.2 Characterisation Methods and Instrumentations 149

9.3 Experimental Procedures 154

Bibliography 169

Appendices 185

Appendix A Supporting Information for Chapter 3 185

Appendix B Supporting Information for Chapter 4 187

Appendix C Supporting Information for Chapter 5 194

Appendix D Supporting Information for Chapter 6 197

Appendix E Supporting Information for Chapter 7 200

List of Figures 204

List of Schemes 215

List of Tables 218

List of Abbreviations 220

List of Publications and Conference Contributions 223

Acknowledgements 225

Publications Arising from the Thesis

1. **Dynamic Nitroxide Functional Materials**

   H. Woehlk, A. Lauer, V. Trouillet, A. Welle, L. Barner, J. P. Blinco, K. E. Fairfull-Smith and C. Barner-Kowollik, *Chem. Eur. J.*, **2018**, *24*, 18873-18879.

2. **Engineering Nitroxide Functional Surfaces Using Bioinspired Adhesion**

   H. Woehlk, J. Steinkoenig, C. Lang, L. Michalek, V. Trouillet, P. Krolla, A. S. Goldmann, L. Barner, J. P. Blinco, C. Barner-Kowollik and K. E. Fairfull-Smith, *Langmuir*, **2018**, *34*, 3264-3274.

3. **Oxidative Polymerization of Catecholamines: Structural Access by High-Resolution Mass Spectrometry**

   H. Woehlk, J. Steinkoenig, C. Lang, A. S. Goldmann, L. Barner, J. P. Blinco, K. E. Fairfull-Smith and C. Barner-Kowollik, *Polym. Chem.*, **2017**, *8*, 3050-3055.

Erklärung

Hiermit erkläre ich, dass die vorliegende Arbeit im Rahmen der Betreuung durch Prof. Dr. Christopher Barner-Kowollik, Associate Prof. Dr. Kathryn E. Fairfull-Smith (QUT) und Dr. James P. Blinco (QUT) selbstständig von mir verfasst wurde und keine anderen als die angegebenen Quellen und Hilfsmittel verwendet wurden. Die wörtlich oder inhaltlich übernommenen Stellen wurden als solche kenntlich gemacht. Die Regeln zur Sicherung guter wissenschaftlicher Praxis des Karlsruher Instituts für Technologie (KIT) wurden beachtet und die Abgabe und Archivierung der Primärdaten gemäß Abs. A (6) der Regeln zur Sicherung guter wissenschaftlicher Praxis des KIT beim Institut ist gesichert. Die elektronische Version der Arbeit stimmt mit der schriftlichen überein. Die Arbeit wurde im Rahmen der bestehenden Cotutelle-Vereinbarung zwischen dem KIT und der QUT gemeinschaftlich durchgeführt und ist ebenfalls an der ausländischen Universität als Bestandteil einer Prüfungs- oder Qualifikationsleistung zur Erlangung des dortigen Doktorgrades (Doctor of Philosophy) vorgelegt. Des Weiteren erkläre ich, dass ich keine vorausgegangenen Promotionsversuche unternommen habe und mich derzeit nur in dem oben genannten laufenden Cotutelle-Promotionsverfahren befinde.

Ort, Datum

Unterschrift

Chapter 1: Introduction and Motivation

Nitroxides are stable organic free radicals that exhibit unique and truly remarkable properties owing to the unpaired electron delocalised over the nitrogen and oxygen atoms. Nitroxides catalyse organic reactions, assist in the construction of well-defined and complex macromolecular architectures, operate as electrochemically active composites in the emerging field organic radical batteries, and control a plethora of functions in biological systems.[1-2] The wide-ranging potential of nitroxides has been recently expanded owing to their nitric oxide (NO) mimetic character — a key signalling molecule in the lifecycle of bacterial biofilms.[3] Initial biofilm studies have revealed that low doses of nitroxides, employed as NO substitutes, effectively inhibit biofilm formation of Gram-negative bacteria. Furthermore, biofilm dispersal of preformed biofilms was observed in the presence of nitroxides with potentiation of subsequent antimicrobial treatment for complete eradication of the perforated biofilm.[4-5] Most strikingly, nitroxides are capable of overcoming the inherent drawbacks of NO with advantages in safe handling, long-term stability, and negligible toxicity. In addition, various straightforward chemical design strategies are available with nitroxides, including the construction of various nitroxide molecular scaffolds, the fusion with other bioactive functional moieties, as well as the facile implementation of nitroxides within polymer drug delivery systems.[1-2, 6] Clearly, nitroxides are promising candidates as potential antibiofilm agents to reduce biofilm-related nosocomial infections — an inherent risk in hospitalisation and a substantial economic burden for global healthcare systems.

Biofilms, the predominant lifestyle of bacteria, are surface-attached multicellular communities embedded in a self-produced matrix composed of extracellular polymeric substances.[7-9] The formation of a biofilm has evolved as an elaborate strategy of bacteria to survive in hostile environments. Biofilms, which are often illustrated as ‘microbial cities’ when fully matured to three-dimensional conglomerates, are present everywhere.[10] The downside of these sessile bacterial communities is their detrimental impact to global public health. It is estimated that more than 80% of all infections in the human body are caused by bacteria existent in a biofilm and not induced by individual planktonic pathogens.[11] Chronic lung infections of patients with cystic fibrosis (CF), for instance, are highly vulnerable to *Pseudomonas aeruginosa* biofilm colonisation of their respiratory system, which is the main determinant of morbidity and mortality to CF patients.[12] The problem is that bacteria within a biofilm are highly adaptive toward external environmental cues and are encased in a polymer matrix that provides substantial protective shielding. Thus, biofilms are very difficult to eradicate with standard antimicrobial countermeasures (which might have been proven powerful against planktonic bacteria). Several studies suggest that bacteria within a biofilm are up to 10,000-fold more resistant to antibiotics.[13] Novel strategies such as antibiofilm agents and antimicrobial peptides have emerged over the last decade specifically targeting the biofilm mode of growth, however these chemical approaches are in the initial stages of development.[14-16]

Once a biofilm has formed on a surface, it becomes an immense threat for the patient and in hospitalisation acting as a nidus for acute and persistent infections with few effective countermeasures. Thus, prophylactic strategies, *i.e.* the inhibition of biofilm formation on surfaces, are urgently needed to reduce nosocomial infections resulting from biofilm contaminations of medical devices and implants. Polymer coatings have emerged as powerful and versatile tools to tailor the properties of material interfaces in a precise manner. Various antimicrobial and antifouling polymer coatings have been introduced without directly approaching the predominant bacterial mode of growth: the biofilm.[17-18] Antibiofilm coatings specifically designed to inhibit sessile planktonic bacteria agglomeration and the formation of biofilm structures have remained elusive as a nonbactericidal strategy, based on the manipulation of the biofilm's intercellular communication system. Biofilm-preventing coatings offer a new prophylactic strategy to combat bacterial surface colonisation with potential synergistic effects of existing (but limiting) antimicrobial and antifouling surface modification techniques.

The current doctoral thesis is driven by the acute and urgent need to develop new chemical advances to combat pathogenic biofilm formation on surfaces. Herein, a pioneering and mild antibiofilm coating strategy is presented based on the generation of nitroxide functional surfaces with inherent biofilm-preventing properties. A versatile coating strategy for substrate-independent nitroxide surface immobilisations is introduced using bioinspired adhesive polymer scaffolds obtained through oxidative polymerisation of a functional catecholamine.

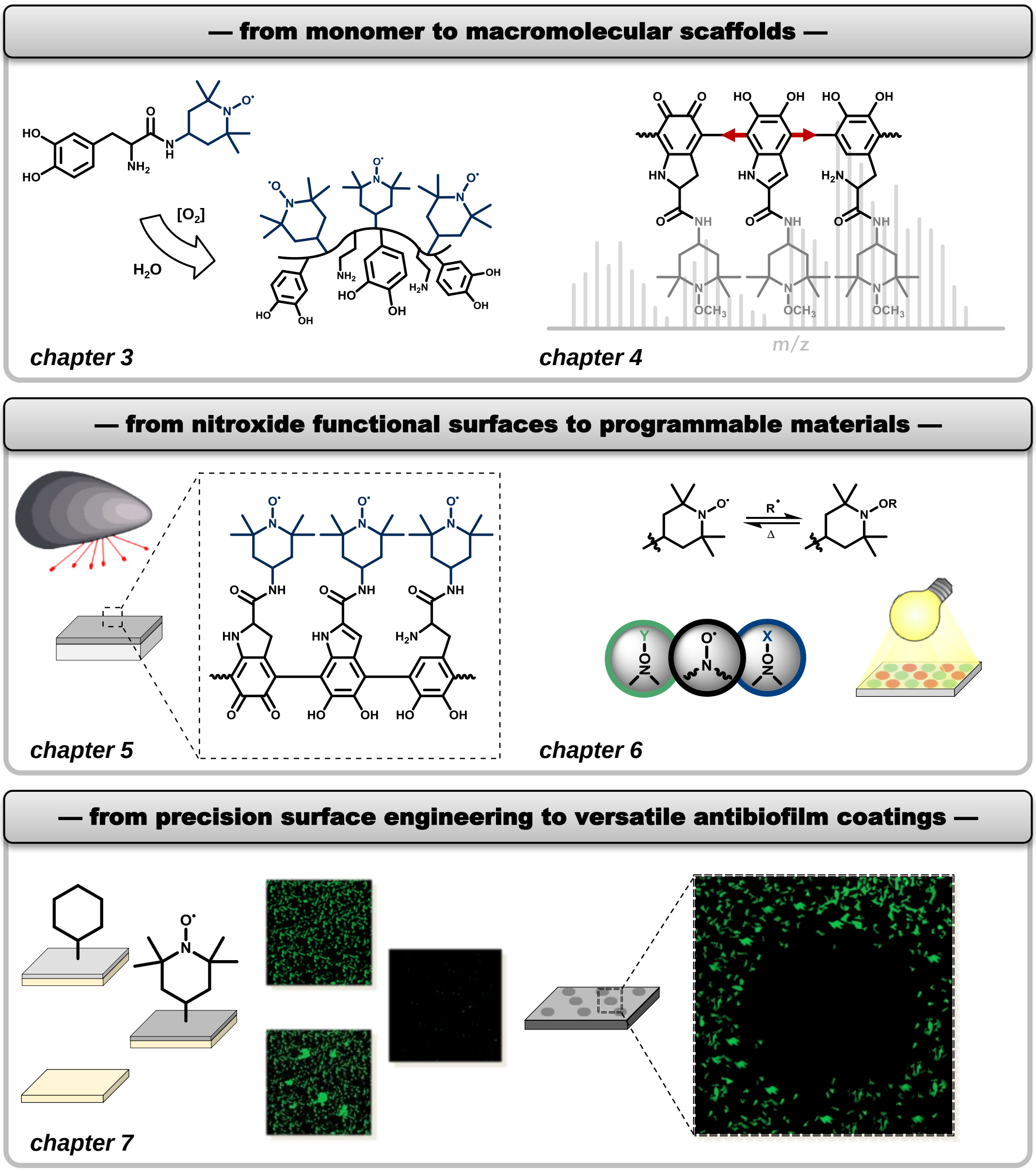
— from monomer to macromolecular scaffolds —
HO
HO
O
N
H
NH2
N
O•
[O2]
H2O
HO
OH
HO
HN
NH
OCH3
H2N
m/z
chapter 3
chapter 4
— from nitroxide functional surfaces to programmable materials —
R•
Δ
OR
Y
X
chapter 5
chapter 6
— from precision surface engineering to versatile antibiofilm coatings —
chapter 7

Figure 1.1. Schematic illustration of the projects presented in the current thesis.

The doctoral thesis encompasses the molecular design of tailor-made (*e.g.,* nitroxide functional) monomers for the construction of bioadhesive macromolecular scaffolds. The elaborate construction of nitroxide-decorated surfaces is exploited yielding functional material interfaces with customised (*e.g.*, antibiofilm) properties, irrespective of the underlying substrate (**Figure 1.1**). Fundamental investigations are presented throughout each stage of the macromolecular design of tailor-made material interfaces. The main part of the current thesis is subdivided as follows:

- **Chapter 3:** A sophisticated methodology for the generation of nitroxide-containing polymer scaffolds with inherent bioadhesive properties is presented. The synthesis and polymerisation of a catecholamine-based monomer equipped with a nitroxide functional group is thoroughly investigated in terms of the compatibility of the nitroxide's persistent radical character and the employed oxidative polymerisation strategy. Detailed mechanistic and structural insights of the nitroxide functional polymer system are described.

- **Chapter 4:** A high-resolution electrospray ionisation mass spectrometric characterisation platform for the structural elucidation of bioderived polycatecholic systems is introduced. The complex polymer backbone composition of a functional and nitroxide-derived poly(catecholamine) system is structurally deconvoluted into various coexisting building blocks with distinct structural motifs.

- **Chapter 5:** The previously obtained mechanistic and structural insights of the tailor-made nitroxide functional polymer system are translated into a versatile coating strategy for substrate-independent nitroxide surface functionalisations. Various types of materials are coated with thin nitroxide-containing polymer films following an easy-to-operate coating procedure. The nitroxide-decorated surfaces are carefully analysed using advanced surface characterisation techniques. In addition, precise control over the oxidative polymerisation and surface coating is gained using light as an external trigger.

- **Chapter 6:** The wide spectrum of nitroxides employed as versatile synthetic tools and functional units is exploited for the generation of dynamic nitroxide functional materials with programmable properties. Nitroxide-decorated polymeric microspheres are reversibly coded and decoded with small functional units based on efficient nitroxide radical coupling reactions and the formation of thermo-labile alkoxyamine adducts. In addition, nitroxide functional surfaces are rapidly conjugated with synthetic polymer strands with spatial resolution following a photolithographic experimental setup.

- **Chapter 7:** The biofilm preventing qualities of tailor-made nitroxide functional surfaces are carefully examined against *Pseudomonas aeruginosa* biofilm cultivation. The antibiofilm performance is hereby critically assigned to the nitroxide moieties and potential side effects arising from the surrounding polymer matrix are discussed. Light-controlled nitroxide surface immobilisation on titanium implants is presented generating antibiofilm coatings with spatial resolution.

Chapter 2: Literature Review

The following literature review outlines the chemistry of nitroxides in a broader context. The use of nitroxides as versatile synthetic tools and functional moieties in modern material design is introduced. Subsequently, a truly fascinating bioadhesive system originating from marine mussels is carefully elucidated. Various biomimetic chemical approaches are presented and the versatile adhesive performances of these polymer coatings are discussed. The literature review concludes with the properties of bacterial biofilms and gives a critical update on current strategies to combat and to prevent bacterial surface colonisation targeting to reduce biofilm-related infections.

2.1 NITROXIDES AS FUNCTIONAL MATERIALS

2.1.1 Chemistry of Nitroxide Free Radicals

Nitroxides are a unique class of stable organic free radicals with ever-growing interest in organic synthesis, polymer chemistry, biomedicine and materials sciences.[1] The persistent character of the nitroxyl radical arises from the delocalisation of the unpaired electron over the *N*,*N*-disubstituted nitrogen and the oxygen atoms with a delocalisation energy of around 120 kJ·mol^{-1} (**Scheme 2.1**).[19-20]

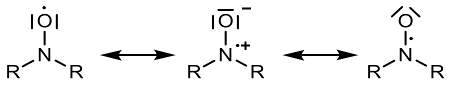

Scheme 2.1. The nitroxyl key structural element of nitroxides with an unpaired electron delocalised over the *N*,*N*-disubstituted nitrogen atom and the oxygen atom.

The existence of a persistent nitroxyl radical was first reported in 1845 with the discovery of the inorganic nitrosodisulfonate salt (Fremy's salt),[21] followed by first organic analogues in the early twentieth century,[22-23] and the synthesis of 2,2,6,6-tetramethylpiperidine 1-oxyl (TEMPO) based nitroxides in 1959, which have evolved as an important class of nitroxides in chemistry and materials sciences since then.[1] Numerous different types and classes of nitroxides are known in the literature, however, nitroxides with tertiary alkyl groups adjacent to the nitroxyl moiety (and often fused with cyclic core structures) exhibit enhanced stabilities. Contrary to that, nitroxides with primary or secondary alkyl groups at the α-position are prone to undergo disproportionation reactions forming the corresponding nitrone and the hydroxylamine species.[24] In addition, steric shielding effects derived from the tertiary alkyl groups adjacent to the radical moiety prevent the nitroxide from dimerisation. Other radical coupling reactions, *e.g.* with carbon-centred radicals are not suppressed by the bulky groups adjacent to the nitroxyl moiety.

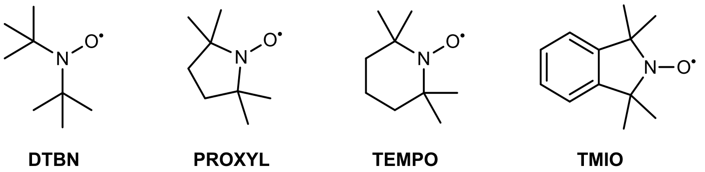

Figure 2.1. Commonly employed classes of nitroxides with different core structures.

Di-*tert*-butyl nitroxide (DTBN) was exemplarily chosen as a representative non-cyclic nitroxide structure (**Figure 2.1**) with a huge variety of potential nitroxyl-adjacent functional groups ranging from complex alkyl groups to aromatic systems or incorporated heteroatoms in close proximity to the radical moiety. Many of these nitroxides have been employed as the corresponding alkoxyamines in modern polymerisation avenues as initiators and regulators.[1, 25-27] Cyclic nitroxides, such as 2,2,5,5-tetramethylpyrrolidine 1-oxyl (PROXYL), the aforementioned piperidine-derived analogous TEMPO, and nitroxides fused to an aromatic skeleton, such as 1,1,3,3-tetramethylisoindoline 2-oxyl (TMIO), possess remarkably robust structures[28] with enhanced photostability for the latter example.[29] Isoindoline-based nitroxides have further become important core structures and precursors in the preparation of profluorescent nitroxides,[30] which find their applications as sensors and probes monitoring various redox and radical processes (refer to Chapter 2.1.3).

Preparation of Nitroxides

Nitroxides are commonly prepared by oxidation of the corresponding secondary amines using organic peroxides (*e.g.*, *meta*-chloroperoxybenzoic acid, *m*CPBA),[31] or hydrogen peroxide with catalytic amounts of tungstate reagent or other transition metal analogues (**Scheme 2.2a**).[32] A milder oxidation route benefits from using hydroxylamines as nitroxide precursors and oxidising reagents such as lead(IV) oxide.[33] Hydroxylamines are also prone to oxidise under aerobic alkaline conditions forming the corresponding nitroxides, which is a convenient access route for the generation of persistent nitroxide radicals in aqueous solutions.[34-36] Other synthetic pathways for the preparation of nitroxides encompass the reaction of nitrones with organometallic compounds (*e.g.*, Grignard or organolithium reagents, with subsequent oxidation of the deprotonated hydroxylamine), or *via* nitrone radical trapping reactions ultimately yielding the corresponding alkoxyamines (owing to second radical trapping event of the *in situ* generated nitroxide species; refer to **Scheme 2.2b**).[1, 37] This type of reaction, also known as the nitrone-mediated radical coupling (NMRC) reaction, has been exploited, for instance, for the generation of complex polymer systems in solution and on the surface.[38-41]

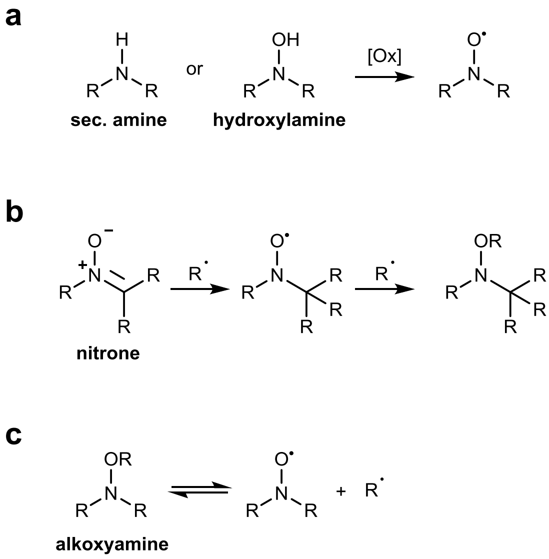

Scheme 2.2. Overview of synthetic pathways for the preparation of nitroxides.

Alkoxyamines are often employed as ideal sources for the *in situ* generation of stable free nitroxide radicals (**Scheme 2.2c**).[42] The persistent radical effect (PRE) of alkoxyamines (with labile NO–C bonds) is a general principle that explains the high selectivity during recombination of nitroxide persistent and alkyl transient radicals.[43-45] This principle is widely employed in polymer chemistry and materials sciences including the nitroxide-mediated radical polymerisation (NMP) technique,[46] nitroxide radical coupling (NRC) reactions[47] and in dynamic covalent polymer materials (refer to Chapter 2.1.2).[48] Alkoxyamine fission can be triggered, for instance, *via* thermolysis, photolysis or chemically. The latter example often proceeds in the presence of oxidising agents such as *m*CPBA.[49-50] In this context, the methoxyamine functional group has become a readily available protecting group strategy to temporarily mask the nitroxide moiety in synthetic organic chemistry. The deprotection of methoxyamines yielding the corresponding nitroxide free radicals is typically conducted in the presence of *m*CPBA following a Cope-type elimination process.[50] Protection of the nitroxide moiety, on the other hand, forming the corresponding methoxyamine derivate is carried out using Fenton chemistry in dimethyl sulfoxide (DMSO).[50-51] Thermo-induced alkoxyamine fission with PRE commonly proceeds at elevated temperatures. The type of alkyl substituent and the nitroxide derivative are hereby crucial as they influence the labile character of the NO–C bond upon thermal stimulus.[42, 52-54] Photosensitive alkoxyamines have been successfully introduced with PRE upon light exposure. The photochemical systems were hereby either linked to the nitroxide core structure[55-57] and/or conjugated to the nitroxyl group *via* an alkoxyamine linkage.[57-60] The covalently attached chromophores operate hereby as antenna for light absorption with subsequent energy transfer inducing dissociation of the alkoxyamine NO–C bond.[55] The principle of light-induced alkoxyamine dissociation has been employed, for instance, in organic and polymer synthetic protocols,[61-62] in photopolymerisations,[56] and in spatially resolved surface photopatterning.[58, 60, 63-64] In addition to the above mentioned external stimuli, electrochemical and electrostatic cues have been recently introduced as alternative triggers for alkoxyamine fission in the emerging field of synthetic organic electrochemistry.[65]

Structural Characterisation of Nitroxides Functional Scaffolds

Molecular events, such as nitroxide radical trapping reactions or nitroxide-mediated redox processes, result in the loss of the nitroxide's unpaired electron spin and thus the paramagnetic properties. Changes of the electron spin, *e.g.* from paramagnetic to diamagnetic electron configuration, can be monitored and quantified using electron paramagnetic resonance (EPR) spectroscopy with applied microwave radiation.[66-67] EPR spectroscopy allows the determination of the spin density at the nitrogen atom expressed as the nitrogen coupling constant, also known as the hyperfine splitting constant (α^N).[68] Allocation of the spin density is hereby influenced by nitroxyl-adjacent atoms and functional groups. Hence, structural information obtained from EPR spectroscopy is narrowed to the direct chemical environment of the nitroxyl spin centre. Monomeric nitroxides are typically identified as three-line EPR signals derived from coupling of the free electron with the ^{14}N nucleus. Persistent multi-radical systems such as nitroxide-containing polymers show EPR signal broadening induced by comprehensive intramolecular spin–spin exchange and dipole–dipole interactions which reduces the transition time from the excited to the ground state of the electron spins. This phenomenon is influenced by various factors including the free radical regional density along the polymer scaffold. [69-70]

Precise structural analysis of nitroxides by nuclear magnetic resonance (NMR) spectroscopy, a standard characterisation method in organic and polymer chemistry, is limited due to the presence of the unpaired electron spin inducing NMR signal broadening. In fact, nitroxide-adjacent chemical structures, such as the tetramethylpiperidine skeleton of TEMPO, commonly remain unresolved in the corresponding NMR spectrum. Only silencing of the unpaired electron spin provides detailed structural access by NMR spectroscopy. This is typically achieved by addition of suitable reducing agents to the NMR analyte (*e.g.*, pentafluorophenylhydrazine,[69] or ammonium formate and palladium on carbon (Pd/C))[71] masking the nitroxide as a corresponding hydroxylamine. Also acidic reductive conditions yielding protonated hydroxylamine species result in well-resolved NMR spectra.[72] Careful consideration of unwanted side reactions when masking the nitroxyl radical is advised in regard to other redox and/or acid-labile functional groups which are linked to the nitroxide.[71] Alternative

NMR characterisation approaches focus on the structural elucidation of nitroxide precursors (*e.g.*, secondary amines)[73] or post-modified nitroxides trapped as diamagnetic derivatives (*e.g.*, as the corresponding methoxyamines).[50]

The identification and structural characterisation of nitroxides is also accessible by other standard characterisation techniques including elemental analysis, infrared (IR) and UV–vis spectroscopy, as well as X-ray crystallography. IR absorption of the nitroxyl moiety has been reported to appear between 1360–1460 cm^{-1}.[61, 68, 74-75] The UV–vis absorption of stable nitroxyl radicals is described to appear at 230 nm (π–π*) and between 410–550 nm (n–π*).[68] X-ray crystallography offers the three-dimensional molecular structural resolution of crystalline nitroxides and nitroxide conjugates.[76-77] The electroactive properties of nitroxides, *e.g.* the reversible oxidation to the *N*-oxoammonium cation followed by the reduction to the nitroxide free radical, are typically investigated by cyclic voltammetry (CV),[78-79] which is of particular interest for nitroxide polymer systems and their use as composite materials in electronic devices and as energy storage materials.[80]

Mass spectrometry (MS) provides rapid and detailed structural access to nitroxide containing systems. Small molecule nitroxides are typically identified as molecular ions which have been ionised through one-electron oxidation employing electrospray ionisation (ESI). Also singly and doubly protonated appearances of nitroxides are observed as ionised species using (+)ESI. The abundance of the detected ionised species and their individual fragmentation patterns are strongly dependent on the type of nitroxide and the additional structural elements conjugated to the persistent radical. [81-82] The methyl groups adjacent to the nitroxyl moiety have been reported to be ESI-labile. In negative ion mode, the formation of the nitrone species through methyl radical liberation has been suggested as a typical fragmentation pattern.[83] Nitroxide containing polymers have been investigated in high-resolution (HR) using ESI as a soft ionisation method.[84-86] Employing the negative ion mode combined with the chloride attachment method confirmed fully intact nitroxide functional groups, and no redox defects of nitroxide side chain groups of a poly(styrene) (PS)-based copolymer were observed. Precise characterisation of the polymer structures with various persistent radical content (up to 30 mol%) was accessible using advanced MS techniques such as collision-induced dissociation (CID) for sensitivity enhancement as well as comparison of isotopic pattern simulated spectra with experimentally obtained HR-MS spectra.[86]

2.1.2 Nitroxides in Polymer and Materials Sciences

Nitroxides master a plethora of functions in modern polymer chemistry and materials sciences owing to the persistent radical character, which opens the broad field of radical reactions and their use as redox-active functional groups. The principle of nitroxide radical reactions yielding alkoxyamine adducts with dynamic covalent character has been discussed before. This chapter highlights important nitroxide-involved synthetic strategies for the generation of well-defined and advanced polymer systems. The nitroxide-mediated polymerisation technique is presented, followed by nitroxide exchange and nitroxide radical coupling reactions applicable for polymer functionalisations, the design of complex polymer architectures, and polymer ligations to surfaces. The labile character of the alkoxyamine-characteristic NO–C bond is briefly discussed under the topic of dynamic covalent polymer networks with self-healing properties. Following on, the focus is shifted toward the synthesis of nitroxide-containing polymers with persistent multi-radical character, which are of emerging interest in materials sciences with widespread applications ranging from organic electronic devices to biomedicine.

Nitroxides as Synthetic Tools for the Design of Well-defined Polymers

Nitroxide-mediated Polymerisation

Nitroxides, as small molecules, are commonly employed as synthetic tools in polymer science mediating radical polymerisations, also known as the nitroxide-mediated polymerisation (NMP) technique.[1, 46, 87] Among other reversible-deactivation radical polymerisation (RDRP) methodologies (*e.g.*, the reversible addition-fragmentation chain transfer (RAFT)[88-89] polymerisation, or atom transfer radical polymerisation (ATRP))[90-91] NMP has become a widely employed and state-of-the-art access route for the preparation of precise macromolecular structures with adjustable molecular weights and narrow dispersities. The principle of NMP is based on the PRE of alkoxyamines and the formation of highly reactive propagating polymer radical chains, and persistent nitroxide radical counter species upon external stimulus such as heat or light (refer to Chapter 2.1.1). Rapid and highly specific radical recombinations between transient and persistent radicals transform the reactive polymer chains into dormant alkoxyamine polymer adducts (**Scheme 2.3**). The overall concentration of carbon-centred radicals is therefore maintained at a low level due to the presence of nitroxides resulting in a reduction of unwanted polymer termination reactions, such as disproportionation or recombination reactions, and greater chain length control for the preparation of well-defined functional polymers. The NMP technique is a sulphur- and copper-free polymerisation method, which is of particular interest for the manufacturing of redox-sensitive electronic devices or in biomedical applications. Limitations are given according to the scope of suitable monomers which is often narrowed to styrene and its derivatives. In addition, elevated temperatures above 100 °C are typically necessary in NMP.[46]

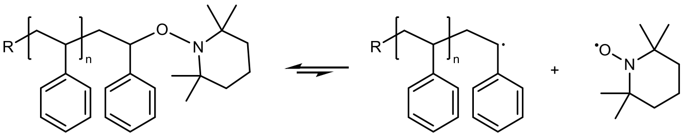

Scheme 2.3. The principle of the nitroxide-mediated polymerisation technique.

Polymer chains obtained through NMP are inherently equipped with a nitroxide-derived alkoxyamine functional group at the polymer terminus offering a variety of synthetic routes for post-polymerisation modifications. For instance, alkoxyamine end group capped polymers have been employed as macroinitiators in polymer chain extension reactions generating linear blockcopolymers.[92-93] Functional groups have been introduced or substituted following the concept of nitroxide exchange reactions at elevated temperatures, which was employed for the post-polymerisation conjugation with chromophores[94-95] as well as for grafting and de-grafting of polymer brushes on surfaces.[96] Polymer surface functionalisations, generally speaking, are accessible by application of the above-mentioned RDRP techniques directly onto premodified surfaces (conjugated with suitable initiators) yielding *grafting from* polymer brushes covalently bound to the solid phase.[97-98] The surface-initiated nitroxide-mediated polymerisation (SI-NMP) often proceeds from TEMPO-derived alkoxyamine functional surfaces, *e.g.* obtained through silanisation and formation of self-assembled monolayers on silicon substrates. SI-NMP, in analogy to in-solution polymerisation procedures, is typically utilised for styrenic monomers.[98-99]

Nitroxide Radical Coupling Reactions

Polymer functionalisations as well as the preparation of various copolymers *via* alkoxyamine linkages are further accessible following various nitroxide radical coupling (NRC) reaction protocols. NRCs refer to the class of click-type reactions[100-101] as highly efficient coupling strategies in organic and polymer chemistry between persistent nitroxide radicals and transient (*i.e.*, *in situ* generated) carbon-centred radicals. NRC reactions proceed rapidly with near quantitative yield, and little or no side reactions. NRCs are highly tolerant toward a wide range of functional groups, and the ligation strategy is often conducted in a one-step reaction procedure.[47]

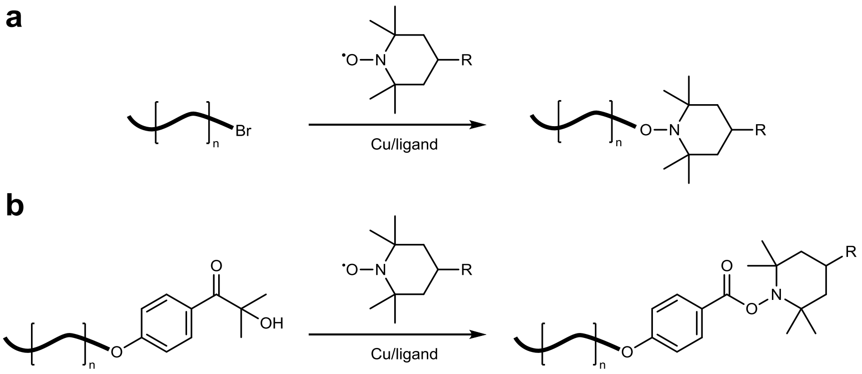

Scheme 2.4. Schematic presentation of (**a**) copper-mediated or (**b**) photo-induced nitroxide radical coupling reactions for polymer end group functionalisations.

Suitable coupling agents for NRCs are readily available in organic and polymer chemistry using halogenated compounds as radical sources which are typically activated in a copper-mediated catalytic cycle. Matyjaszewski *et al.* introduced the Cu(I)-mediated synthesis of small molecule alkoxyamines *via* NRC using brominated species activated through an atom transfer radical addition mechanism.[102] Brominated small molecules are widely and commercially available, *e.g.* α-bromoisobutyrate derivates which are typically employed as

ATRP initiators.[103] In addition, terminal polymer functionalisations *via* NRC can be carried out using principally any polymer prepared by ATRP or single electron transfer-living radical polymerisation (SET-LRP). These polymers can be exploited as macroradical precursors as they are inherently equipped with halide (*e.g.*, bromide) chain ends (**Scheme 2.4a**). The group of Huang has established an atom transfer nitroxide radical coupling (ATNRC) protocol for polymer end group conjugations, with a reported coupling reaction rate close to diffusion controlled.[104] That means the total reaction rate is generally limited by the *in situ* generation of the carbon-centred radicals.[105] Optimisation of copper-mediated NRC processes was accomplished in analogy to the development of SET-LRP using Cu(0) as catalytic active species resulting in a significantly accelerated radical formation rate.[106-107] Single electron transfer nitroxide radical coupling (SETNRC) reactions are typically performed at lower temperatures and with reactions times of several minutes.[108] Copper-mediated radical generation processes, either by AT or SET, are determined and influenced by the employed copper/ligand system as well as the solvent. ATNRC reactions, for instance, have been conducted using CuBr/*N*,*N*,*N'*,*N''*,*N''*-pentamethyldiethylenetriamine (PMDETA) in toluene/DMSO or *N*,*N*-dimethylformamide (DMF) at elevated temperatures.[104] SETNRC reactions catalysed by Cu(0), on the other hand, were conducted at ambient temperatures using, for instance, CuBr/tris(2-(dimethylamino)ethyl)amine (Me_6TREN). The employed ligand facilitated the disproportionation of the Cu(I) species to active Cu(0) in toluene/DMSO as a solvent mixture.[71, 109] NRCs have been exploited for terminal polymer functionalisations, linear block copolymer syntheses, and for the design of complex polymer architectures. Polymer end group polymer modifications *via* NRC were readily accessible using a library of nitroxide-based functional molecules (*e.g.*, 4-substituted TEMPO derivatives) conjugated with orthogonal and/or click-type moieties,[109] monomers, or biomolecules.[71] Linear block copolymers,[108] brush copolymers,[110] multi-arm stars polymers[109] have been synthesised as well. ABC triblock copolymers were obtained combining NRC with copper-catalysed azide-alkyne cycloaddition (CuAAC) click chemistry or other highly efficient polymer ligation strategies.[104] Furthermore, a nitroxide radical coupling step growth polymerisation (NRC-SGP) technique has been established generating thermally degradable poly(alkoxyamine) scaffolds.[111]

Transient carbon-centred radicals for rapid and *in situ* nitroxide radical trapping reactions are also readily available using radical generating photoinitiator (PI) systems combined with light irradiation as a powerful tool to trigger the photodissociation. Nitroxide photo-click coupling reactions have been performed with polymer-terminated photoreactive moieties, such as α-hydroxyalkyl carbonyl groups, for polymer functionalisations (**Scheme 2.4b**)[112] and polymer conjugations onto surfaces including biomaterial interfaces.[99, 113-114] Photoinitiators such as Irgacure 2959 (2-hydroxy-4′-(2-hydroxyethoxy)-2-methylpropiophenone) undergo clean Norrish-type I photochemistry upon UV irradiation yielding the corresponding acyl radicals which are highly reactive toward the nitroxide radical counter species yielding acylated alkoxyamines. Side reactions with likewise generated tertiary radical fragments (*e.g.*, 2-hydroxyl-2-propyl) also occur, however, the resulting alkoxyamine adduct rapidly decomposes to the hydroxylamine species under elimination of acetone.[99, 113] Recently, photo-click NRC reactions have been applied for reversible single-chain folding of polymeric nanoparticles in a light-triggered folding reaction pathway. Unfolding, thus alkoxyamine fission, was performed chemically using *m*CPBA as an oxidising agent.[49]

Dynamic Covalent Polymer Materials

Nitroxides covalently incorporated into polymer structures as the corresponding alkoxyamine functional groups are of particular interest in materials sciences and the development of self-healing polymer networks.[115] The dynamic covalent character of poly(alkoxyamine) scaffolds arises from incorporated thermo-labile NO–C linkages, either located along the polymer backbone[116-117] or functioning as cross-linking moieties in polymer networks.[115, 118] Upon heating, fission of the NO–C alkoxyamine bond occurs inducing radical crossover reactions and reassembly of the scissored polymer strands. Upon cooling, ‘scrambled’ polymer scaffolds[119] have been reorganised with altered materials properties.[116-118] Recent advances were achieved in reducing the homolysis temperature for self-healing polymer properties to ambient temperatures,[120] or by introduction of photo-labile alkoxyamine junctions within polymer networks.[121]

Nitroxide-containing Polymers with Persistent Multi-radical Character

Nitroxide functional macromolecular scaffolds are of particular interest as advanced materials owing to the persistent multi-radical character and the redox-active properties derived from the multiple expressed nitroxide moieties present in the polymer side chains.[2, 6] Recent applications of nitroxide polymer materials, including their use as recyclable oxidation catalysts, profluorescent imaging agents, or composite materials in organic radical batteries, are discussed in Chapter 2.1.3.

Synthesis of Nitroxide-containing Polymers

The routes to prepare nitroxide-containing polymers with persistent radical character are limited in standard and industrial relevant free radical polymerisations due to the radical scavenging properties of the nitroxide. Direct access to nitroxide polymers, however, is given by other common polymerisation methods that rely on non-radical chain growth mechanisms including ionic polymerisations, ring-opening metathesis polymerisations (ROMPs), or other transition metal-catalysed polymerisations (**Scheme 2.5**).

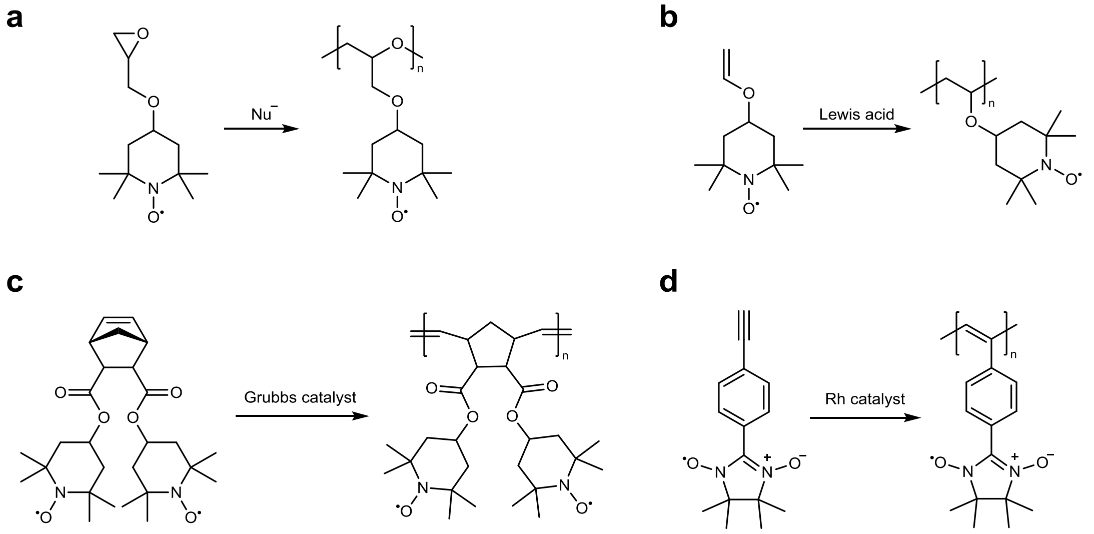

Scheme 2.5. Synthetic pathways with direct access to nitroxide-containing polymers. Common examples include (**a**) the anionic ring-opening polymerisation of TEMPO-glycidyl ether, (**b**) cationic polymerisation of TEMPO-vinyl ether, (**c**) ROMP of a norbornene derivative, and (**d**) the generation of nitroxide substituted poly(phenylacetylene)s.

The anionic polymerisation technique has often been applied for the polymerisation of TEMPO methacrylate (TMA) monomers initiated by nucleophilic organometallic reagents such as butyllithium or 1,1-diphenylhexyllithium.[122-125] The ring-opening polymerisation of nitroxide functional glycidyl ether also proceeds *via* anionic chain propagation mechanisms (**Scheme 2.5a**).[70, 74, 126-127] Access to biocompatible nitroxide polymer scaffolds targeting biomedical applications was achieved in a ring-opening polymerisation of a nitroxide-containing carbonate monomer.[69] Cationic polymerisations are typically conducted using nitroxide functional vinyl ethers (**Scheme 2.5b**).[128-131] Norbornene-type monomers equipped with nitroxide functional groups undergo ROMP using ruthenium-based Grubbs-type catalytic systems yielding poly[2,3-bis(2',2',6',6'-tetramethylpiperidin-1'oxyl-4'-oxocarbonyl)-5-norbornene] (PTNB) and its derivatives as common examples (**Scheme 2.5c**).[132-135] Other transition metal (*e.g.*, Rh-based) catalysed polymerisation techniques have been further exploited, *e.g.* for the preparation of nitroxide substituted poly(phenylacetylene)s (**Scheme 2.5d**).[136-137] All of the above mentioned polymerisation techniques were mostly applied for the generation of electroactive nitroxide-containing polymer materials.

Alternative routes for the preparation of nitroxide radical polymers encompass post-polymerisation transformations and modification reactions. The polymerisation of monomers equipped with secondary amines as functional groups is a common and widely employed method for the generation of polymer precursor scaffolds, which can then be transformed into the nitroxide-containing analogues upon post-polymerisation amine oxidation. In particular, 2,2,6,6-tetramethlpiperidyl-4-methacrylate (TMPM) has been exploited as a secondary amine-containing monomer in free radical polymerisations yielding PTMPM as polymeric intermediate, and ultimately poly(TMA) (PTMA) upon oxidation (*e.g.*, using *m*CPBA) (**Scheme 2.6**).[68, 138-139] RDRP-based protocols yielding PTMPM have also been established with no or only minor reported issues in terms of potential side reactions (*e.g.* aminolysis of the employed RAFT agent[140] or interferences with copper/amino-ligand catalysts during ATRP).[140-141] Surface-initiated ATRP (SI-ATRP) has been employed for *grafting from* surface conjugation with PTMPM polymer brushes, followed by oxidation toward TEMPO functional groups present in the polymer side chains of PTMA.[142-146] Characterisation of nitroxide functional surfaces and nitroxide polymer coatings by X-ray photoelectron spectroscopy (XPS) is presented shortly.

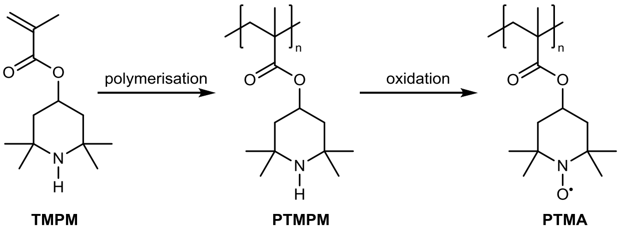

Scheme 2.6. General procedure for the preparation of PTMA using TMPM as a monomer, followed by the post-polymerisation oxidation to the corresponding nitroxide-containing polymer.

Other post-polymerisation techniques for the generation of nitroxide functional polymer scaffolds encompass the use of 'pronitroxide'[36] polymers bearing for example TEMPO-derived hydroxylamine hydrochloride functional groups with subsequent oxidation.[147] Common nitroxide protecting group chemistries have also been applied for the generation of nitroxide multi-radical polymer scaffolds.[148-149] In addition, standard polymer ligation protocols have been employed for the introduction of nitroxides to polymer strands *via* CuAAC click reactions,[100, 150-152] nucleophilic substitutions,[49, 86, 153] or using activated esters.[154-156]

Characterisation of Surface-immobilised Nitroxide Functional Scaffolds

X-ray photoelectron spectroscopy (XPS) offers an access route for the structural characterisation of nitroxide-containing polymer brushes covalently tethered to surfaces. The acquisition of high-resolution N 1s XP spectra provides detailed information about the chemical state of the nitroxide species. Hung *et al.* monitored the *in situ* generation of surface-tethered nitroxide polymer brushes obtained through oxidation of PTMPM brushes (equipped with secondary amines as functional side chains) yielding nitroxide-containing PTMA brushes.[142] A clear shift of the amine-assigned peak toward higher binding energies (BEs) has been reported indicating successful conversion to the corresponding nitroxide functional group. However, prolonged exposure to *m*CPBA (employed as an oxidising agent) resulted in the formation of overoxidised by-products, which have been referred to as *N*-oxoammonium cations, appearing at higher BEs. Precise allocation of the nitroxide functional groups in N 1s XP spectra is challenging due to various redox states of the nitroxyl moiety appearing at different binding energies.[157] In addition, literature reported BEs characteristic for the nitroxyl moiety vary under the aspect of the employed calibration system, the type of nitroxide as well as potential interaction with the underlying material.[158-160]

2.1.3 Modern Applications of Nitroxide Functional Scaffolds

Nitroxides, present either as molecular constructs or within polymeric scaffolds, exhibit various applications in chemistry, biomedicine and materials sciences. Some of them have already been presented in previous chapters. Due to the unique properties as paramagnetic and redox-active persistent organic radicals, nitroxides are often considered as green, non-toxic alternatives to transition metals with similar properties, which are commonly used in electronic devices or as MRI contrast agents.[1-2] In the following section, three common examples are discussed in more detail. The use of nitroxides as antibiofilm agents is presented in Chapter 2.3.3.

Recyclable oxidation catalysts

Nitroxides and the corresponding *N*-oxoammonium salts (readily generated by acidic treatment of the nitroxide precursor) are commonly employed as catalysts for the oxidation of primary and secondary alcohols yielding the corresponding aldehydes and ketones as well as carboxylic acid functional groups.[161-163] The *N*-oxoammonium analogous species is hereby often used in catalytic amount and in the presence of a secondary co-oxidant (*e.g.* sodium hypochlorite)[164] for the reoxidation of the forming hydroxylamine species (upon alcohol oxidation) back to the catalytic active *N*-oxoammonium salt (**Scheme 2.7**).

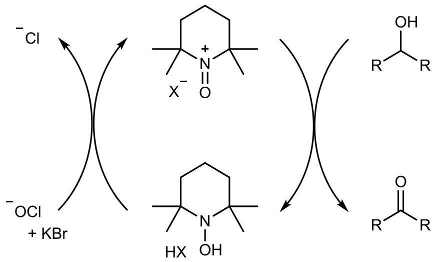

Scheme 2.7. Nitroxide-mediated oxidation of an alcohol in the presence of cooxidant NaOCl and KBr.

The immobilisation of active nitroxide functional groups onto solid supports or their embedment into polymeric materials have led to the development of recyclable and reusable oxidation catalysts[165] complying with the green chemistry agenda.[166] Nitroxide functional materials, such as silica[157] or Fe_3O_4-based superparamagnetic (nano)particles,[145, 167] as well as conventional polymer scaffolds,[168-169] have been successfully synthesised and were subsequently employed as reusable catalysts without significant losses of the activity or selectivity. After usage, nitroxide catalysts can be isolated and recovered in a simplified work-up, *e.g.* by filtration, centrifugation,[157] or application of a magnetic field.[145, 167]

Profluorescent Nitroxides

Nitroxides possess the extraordinary ability to quench excited electronic states of fluorophores, which can be visualised by fluorescence suppression and monitored by EPR spectroscopy. The quenching effect caused by the paramagnetic nature of the nitroxide can occur both intra- and intermolecularly, and fluorescence can be restored upon trapping or masking of the nitroxyl radical.[170-173] Covalently linked nitroxide–fluorophore conjugates, which have been termed profluorescent nitroxides (PFNs), have been successfully introduced as sensitive probes monitoring radical and redox events (**Scheme 2.8**).[30, 174] PFNs have been exploited, for instance, for the detection and imaging of oxidative stress induced by reactive oxygen species (ROS) in biological systems[175] or as sensors in polymer degradation studies.[176-177] A broad spectrum of small molecule nitroxide–fluorophore conjugates exists in the literature varying in the properties of the fluorophore, the type of linkage, and the employed nitroxide.[30] Isoindoline-based PFNs and carbon–carbon linkages are commonly favoured as they exhibit an enhanced stability toward hydrolysis or photo-induced degradation processes.[176, 178-179] The use of boron dipyrromethene (BODIPY) as a chromophore in PFNs has become attractive shifting the fluorescence into the red- and near-infrared (NIR) emission region for better biological imaging applications.[77]

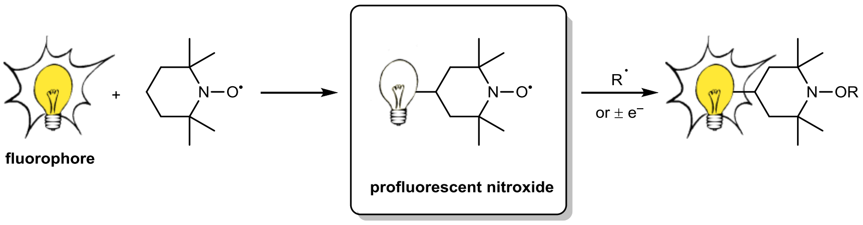

Scheme 2.8. Schematic illustration of the preparation of profluorescent nitroxides and the regeneration of the fluorescence upon radical trapping reaction or redox processes. Adapted with permission from reference [30]. Copyright (2011) CSIRO Publishing.

Profluorescent polymer systems with nitroxides in close spatial proximity to the fluorophore have become a promising and tuneable platform for constructing advanced redox and radical imaging agents and complex self-reporting systems.[152, 180] Different stimuli response systems have been introduced such as visible light activation of spin-silenced fluorescence,[181] or *via* thermo-reversible hetero-Diels–Alder ligation of the fluorophore to a nitroxide-functional polymer scaffold.[75] A pH-sensitive drug release system has been presented with doxorubicin as fluorescent cancer therapeutic agent.[182] Upon pH increase of the surrounding medium the fluorescence is turned on indicating the hydrolysis of the pH-sensitive hydrazone bond linking the fluorescent drug to the nitroxide-containing polymer scaffold. Recently, the principle of profluorescent self-reporting systems has been successfully applied to refoldable single-chain polymer nanoparticles *via* UV-induced photo-click NRC reactions (folding) and *m*CPBA-mediated alkoxyamine fission (unfolding).[49]

Organic Radical Batteries

Nitroxides are intriguing candidates as redox-active organic molecules for the incorporation into electrochemical active materials such as organic radical batteries (ORBs). The electroactive principle is based on the reversible nitroxide oxidation to the corresponding *N*-oxoammonium cation, followed by the reduction back to the free radical species. ORBs are considered as promising alternatives to standard lithium ion batteries with benefits in their environmental impact, safe handling, as well as their flexible and light-weight material properties.[183-185] The immobilisation of nitroxides on solid supports is hereby necessary to prevent dissolution of the active radical species, which ensures a long life-time of the battery. Nitroxide radical polymers with precise control over the solubilities in the battery electrolyte have emerged as promising electroactive polymer composites. A variety of different classes of nitroxide polymers have been introduced in the literature (refer to Chapter 2.1.2), however, PTMA is by far the most commonly applied nitroxide radical polymer in present ORB research.[138, 186]

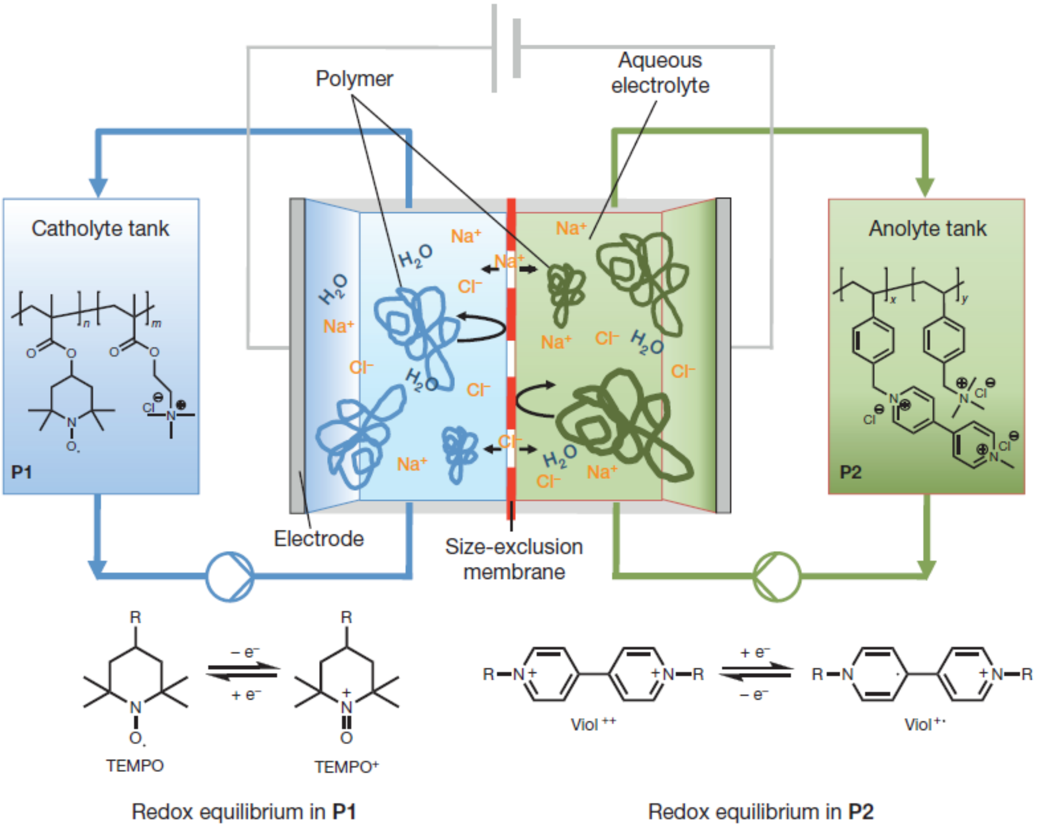
Polymer
Aqueous electrolyte
Catholyte tank
P1
Anolyte tank
P2
H_2O
Na^+
Cl^-
Electrode
Size-exclusion membrane
R
– e⁻
+ e⁻
TEMPO
TEMPO+
Viol ++
Viol +•
Redox equilibrium in P1
Redox equilibrium in P2

Figure 2.2. Schematic representation of a redox flow battery based on a nitroxide polymer catholyte and a viologen polymer anolyte. Adapted and reproduced with permission from reference [187]. Copyright (2015) Springer Nature.

Schubert and co-workers have promoted the field of redox flow batteries[80] with their recent development of an aqueous organic battery design based on watersoluble nitroxide-containing polymers as catholyte material and a polymer-based on viologen, a 4,4’-bipyridine derivate, employed as an anolyte (**Figure 2.2**).[187] The overall costs of this type of battery were reduced due to the application of a low-cost dialysis membrane,[188] which is important for potential large-scale applications. Furthermore, the use of environmentally friendly materials including organic polymer scaffolds and aqueous battery electrolytes drives research technologies toward the development of sustainable and simple energy storage solutions.

2.2 BIOINSPIRED POLYMER COATINGS

The precision surface engineering of solid materials is of pivotal interest across all research fields including chemistry, materials sciences, and biomedicine. A broad range of surface modification techniques is provided in the literature such as chemical vapour deposition (CVD),[189] lithography,[190] or self-assembled monolayers (SAM).[191-193] However, many of these surface functionalisation techniques typically involve elaborate and time-consuming synthetic protocols and the need of special instrumentation, which overall limit their practical use in various applications. In addition, high control over the chemical interactions between the interfacial modifier and the substrate is crucial for the formation of stable coatings. Common examples of coating technologies encompass the chemistry of silanes or thiols which applicability is restricted to hydroxylated surfaces or noble metals, respectively.[192-193] In the need of a convenient surface modification strategy, functional polymer coatings have emerged as versatile tools for controlling the material properties.[194-195] The immobilisation of macromolecules onto surfaces can be achieved following well-established *grafting to* or *grafting from* protocols.[196] In addition, the versatile toolbox of post-polymerisation modification techniques enables the precision design of functional polymer materials and coatings.[197]

Nature has often served as a great source of inspiration for the development of novel smart materials.[198] The remarkable climbing abilities of the gecko, for instance, has given rise to functional advanced materials, such as re-attachable dry adhesives and microfabrics.[199-200] In analogy to that, the permanent adhesion system of marine mussels have gained widespread attention for the development of wet adhesives and substrate-independent coatings.[201]

2.2.1 Mussel Foot Proteins as Bioadhesives

Marine mussels exhibit an extraordinary adhesion system, which allows them to survive under rough environmental living conditions (*e.g.,* in tidal zones). They adhere to virtually all types of materials including rocks, wood piers, metallic ship propellers, and polymer composites. This remarkable wet adhesion system, mostly studied on the genus *Mytilus*, has become a great source of inspiration for the development of bioadhesive composite materials and versatile coatings.[202-203]

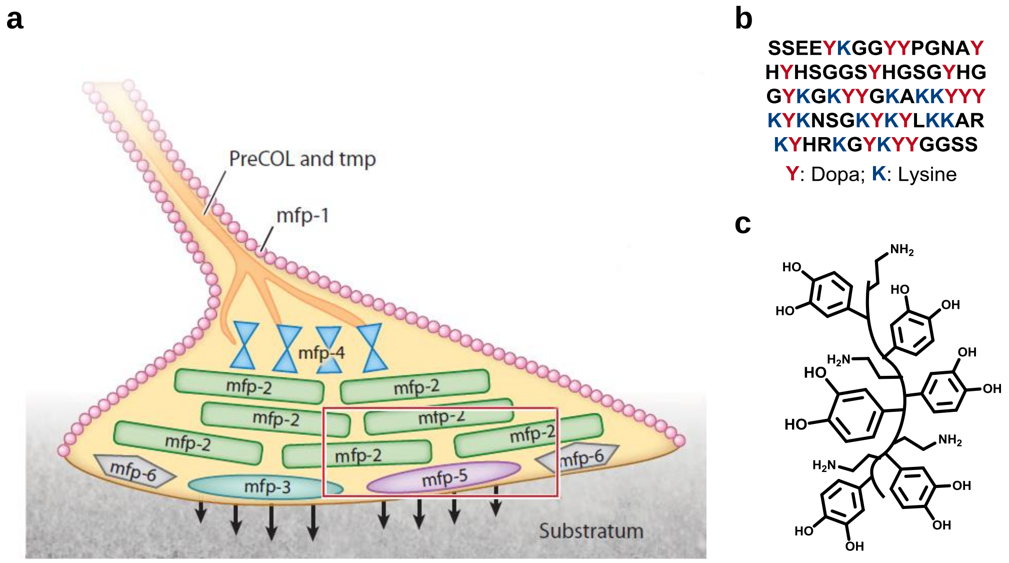
a
PreCOL and tmp
mfp-1
mfp-4
mfp-2
mfp-2
mfp-2
mfp-2
mfp-2
mfp-2
mfp-2
mfp-6
mfp-3
mfp-5
mfp-6
Substratum
b
SSEEYKGGYYPGNAY
HYHSGGSYHGSGYHG
GYKGKYYGKAKKYYY
KYKNSGKYKYLKKAR
KYHRKGYKYYGGSS
Y: Dopa; K: Lysine
c
NH2
HO
HO
HO
OH
H2N
OH
HO
OH
HO
NH2
H2N
OH
HO
OH
OH

Figure 2.3. The adhesion system of the mussel byssus based on mfps. (**a**) Schematic illustration of the adhesive plaque composed of various types of mfps, which are found at the end of the mussel's byssal thread. (**b**) Peptide sequence of mfp-5. (**c**) Simplified molecular structure of a mfp with DOPA-derived catechol surface anchors and lysine-derived amino side chains. Adapted and reproduced with permission from references [204] and [203]. Copyright (2011) Annual Reviews and (2007) American Association for the Advancement of Science.

The sophisticated adhesion system of marine mussels derives from the mussel byssus, which is composed of a bundle of filaments secreted by the bivalve with adhesive plaques located at the distal ends. Several proteins have been identified to be present in the byssal thread including mussel foot proteins (mfps) and collagen-like proteins (**Figure 2.3a**).[204] Five mfps (mfp-2–6) are unique to the plaque with important contributions to the overall adhesive properties. Briefly, mfp-2 is the most abundant plaque protein (25 wt%), which possesses low levels of the amino acid L-3,4-dihydroxyphenylalanine (L-DOPA) stemming from posttranslational modification of tyrosine.[202, 205] Similar observations hold for the mfp-4, which is significantly larger than the mfp-2 analogue. Mfp-3 and mfp-5 possess high concentrations of L-DOPA and other amino acids such as lysine. The peptide sequence of mfp-5 (the least polymorphic mfp) is depicted in **Figure 2.3b**.[206] Both DOPA-enriched proteins are predominantly located at the plaque–substrate interface, and the presence of multiple catechol groups along the peptide chains have been proposed to serve as versatile surface anchors with synergistic effects stemming from other amino acids, mostly lysine residues (**Figure 2.3c**).[207-208] Lastly, mfp-6 contains high levels of lysine, tyrosine and glycine but only low concentrations of DOPA (typically less than 2%).

2.2.2 Biomimetic Approaches to Multifunctional Coatings

The bioadhesive properties of mfps have been translated into various synthetic strategies generating catechol-containing polymer materials and versatile surface coatings. A general overview of existing coating strategies is given in **Figure 2.4**.

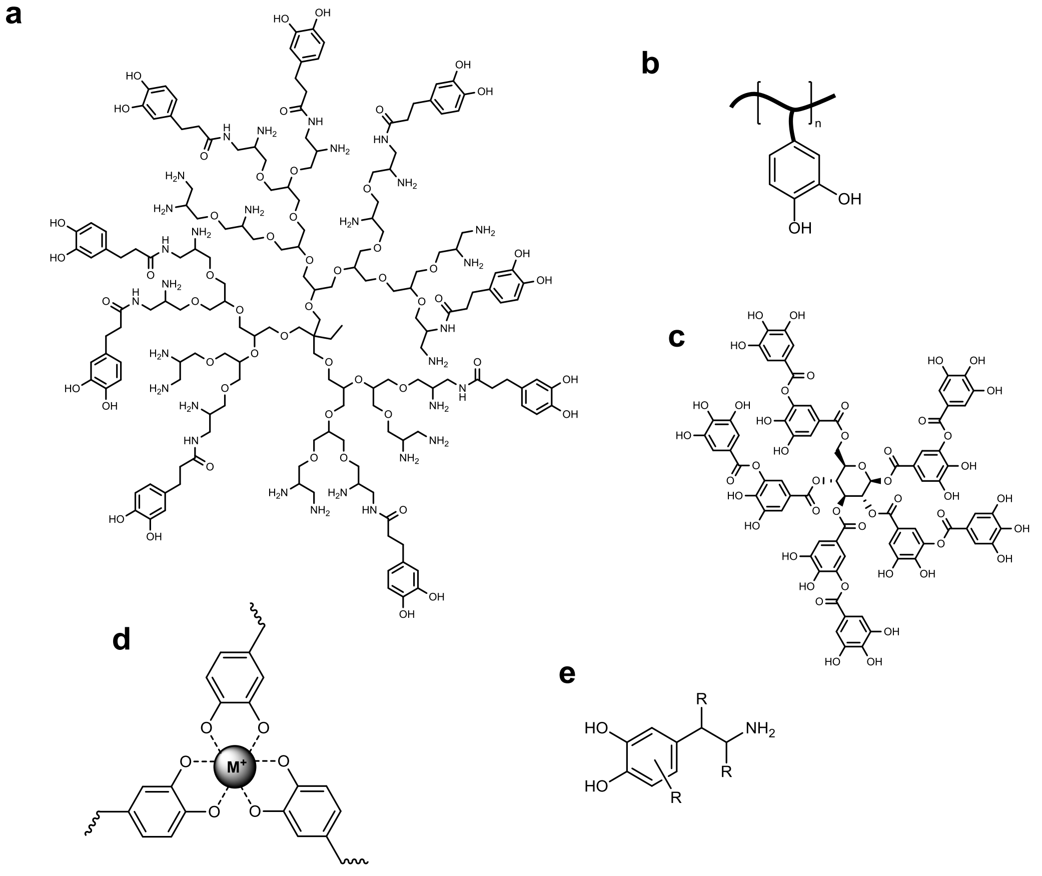

Figure 2.4. Overview of bioinspired approaches for the generation of functional polymer coatings: (**a**) mfp-like dendritic polymers, (**b**) catechol-containing (linear) polymers, (**c**) tannic acid and other plant polyphenolic coating agents, (**d**) metal-phenolic hybrid networks, and (**e**) catecholamines as polymerisable coating agents.

Mussel-inspired Dendritic Polymers

Dendritic catechol- and amine-functionalised polymers composed of a polyglycerol core structure have been introduced as bioadhesives mimicking the properties of specific mfps, including their globular shapes, molecular weights, and important structural features (**Figure 2.4a**).[209] The preparation of mfp-mimicking coatings was readily carried out following a simple dip-coating procedure. Subsequent post-modification reactions with perfluoroalkyl functional groups, aliphatic fatty acids, or metal nanoparticles have resulted in the formation of tailor-made surface coatings with various features ranging from superhydrophilic to superhydrophobic (or superamphiphobic) properties.[209-212] Furthermore, rapid access to antibacterial coatings was gained after surface attachment of silver nanoparticles.[210]

Catechol-containing Linear Polymers and Hydrogels

Many chemical approaches have been presented in the literature for the design of catechol-containing polymers. Polymer chains equipped with a catechol functional group located at the polymer terminus were prepared, for instance, using poly(ethylene glycol) (PEG) or small peptide conjugates (mimicking important peptide sequences of mfps) for the generation of nonfouling surfaces (refer to Chapter 2.2.4).[213-214] Bioadhesive macromolecular structures with multiple expressed catechol surface anchors were synthesised using suitable vinyl monomers equipped with catechol side chains (**Figure 2.4b**).[215-216] The preparation of bioadhesive hydrogels, for instance, has been presented utilising catechol-functionalised methacrylamide and cross-linking PEG diacrylate.[217] However, dihydroxy-substituted aromatic compounds (*e.g.*, catechols), typically inhibit radical-driven polymerisations.[218] Therefore, catechol-protected monomers are commonly employed in radical polymerisations present either as silyl ether[219] or methoxy derivatives,[220-221] or as cyclic bidentate structures.[222] Protected or unprotected catechol monomers have been extensively employed in copolymerisations for the design of hydrophobic[223] or antifouling surfaces[224-225] and as underwater adhesives.[226-227]

Plant Phenols and Polyphenols

Phenolic biomolecules are readily available as low-cost materials for the generation of multifunctional coatings with pyrogallol (benzene-1,2,3-triol) and tannic acid as the most prominent examples.[228-232] The latter species is a dendritic polyphenol composed of five digalloyl ester groups attached to a central glucose core structure (**Figure 2.4c**). Deposited onto a substrate, polyphenol coatings appear as colourless thin films equipped with intrinsic antibacterial properties against Gram-negative and Gram-positive bacteria.[232] The group of Messersmith further investigated various other natural (poly)phenolic compounds as potential surface modifying agents. Based on their studies, it is assumed that molecules bearing aromatic vicinal diols (*e.g.*, the catechol or the pyrogallol functional group) are the most promising and effective coating agents.[233]

Metal-phenolic Hybrid Coatings

Metal-phenolic networks (MNP), a term introduced by the group of *Caruso* in 2013, are a rapidly growing class of organic–inorganic hybrid materials.[234-235] MNPs are typically employed as versatile and multifunctional tools for the precise surface engineering of inorganic, organic and biological objects. The macromolecular network formation is based on the noncovalent self-assembly of organic phenolic ligands coordinated to metal ions (**Figure 2.4d**). A common example of MNPs is the stable octahedral self-assembly originating from the complexation of Fe(III) ions by tannic acid.[234, 236] In recent studies, a library of different organic and inorganic ligands has been introduced after screening of various metal ions and polyphenolic compounds.[237-238] The use of MNPs as functional coatings possesses many advantages such as low-cost starting materials combined with straightforward and rapid synthetic procedures. MNPs have been exploited for diverse fields of applications including drug delivery, bioimaging and catalysis.[237]

Catecholamines as Versatile Coating Agents

Catecholamines, which are small organic molecules equipped with a catechol and an amino functional group, are widely employed coating agents in modern material design (**Figure 2.4e**).[239] Naturally occurring catecholamines, including dopamine (DA), L-DOPA and norepinephrine, have been extensively utilised for the preparation of multifunctional coatings.[240-241] The use of dopamine and tailor-functionalised catecholamines is discussed in Chapter 2.2.3 and Chapter 2.2.4, respectively. Moreover, L-DOPA and its structural derivatives have been identified to play a key role in the formation of melanins, which are a class of naturally occurring pigments found in animals, plants, and lower organisms.[242-243]

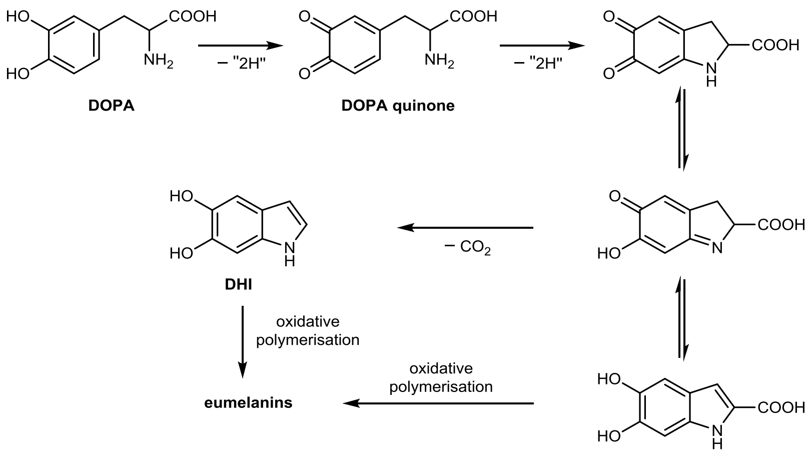
HO
HO
COOH
NH2
DOPA
– "2H"
O
O
COOH
NH2
DOPA quinone
– "2H"
O
O
COOH
N
H
HO
HO
N
H
DHI
– CO2
O
HO
COOH
N
oxidative
polymerisation
eumelanins
oxidative
polymerisation
HO
HO
COOH
N
H

Scheme 2.9. Biosynthesis of eumelanins explained by the Raper–Manson mechanism. Adapted and reproduced with permission from reference [239]. Copyright (2016) John Wiley and Sons.

The biosynthesis of eumelanins, a subclass of melanins, can be described by the Raper–Manson mechanism depicted in **Scheme 2.9**.[244-245] The oxidation of the catechol group of L-DOPA to the corresponding DOPA quinone structure constitutes the initial step of the biopolymer synthesis. Further oxidative reactions cascades lead to the formation of cyclised intermediates such as aminochrome- and indole-like structures. Remarkably, the carboxylic acid group of DOPA exhibits a low stability during polymerisation resulting in the formation of 5,6-dihydroxyindole (DHI) building blocks, which have been identified as important structural features present in eumelanins.[246-247] The formation of covalently linked oligomer clusters proceeds *via* intermolecular cross-coupling reactions through positions 2, 4 and 7 of DHI as the building block.[247] HR-ESI-MS has been carried out for the structural elucidation of eumelanins following a bottom-up synthetic approach.[248] The mass spectrometric characterisation of polymerised L-DOPA, however, has revealed that the formation of poly(DOPA) oligomers was exclusively driven by noncovalent supramolecular forces, including π–π stacking, ionic interactions and hydrogen bonding.[248]

2.2.3 Poly(dopamine) Coatings

The ability of dopamine to polymerise in aqueous aerobic solutions has been translated into a convenient and universal coating strategy by the group of Messersmith in 2007.[203] Dopamine comprises the two main structural features identified in mfps, which are responsible for the versatile bioadhesive properties: the catechol and the amino functional groups. Dissolved in slightly alkaline aqueous solutions (mimicking the natural environment of marine mussels) and in the presence of atmospheric oxygen, DA rapidly forms cross-linked polymer networks, which deposit as thin polymer films on virtually all types of surfaces. The obtained poly(dopamine) (PDA) adhesive system appears to be insoluble in common organic and aqueous solvents, which strongly hampers its structural elucidation by standard solution state characterisation techniques (*e.g.*, NMR spectroscopy, MS, high-performance liquid chromatography (HPLC) or size-exclusion chromatography (SEC)).[249] Thus, the complex polymer composition of PDA and its natural and synthetic polymer analogous systems is extremely challenging to characterise. Various polymerisation mechanisms, the structural elucidation of DA-originating incorporated building blocks, and the resulting covalent and noncovalent cohesive and adhesive forces are still under scientific discussion.[208, 250-256]

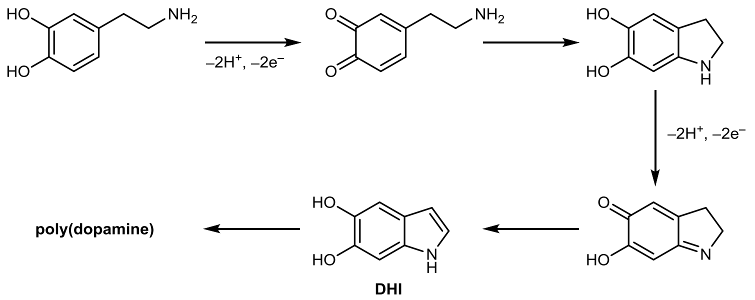

Scheme 2.10. Proposed intramolecular reaction pathway of DA (under oxidative conditions) prior to its polymerisation.

The DA polymerisation proceeds in close analogy to the Raper–Manson mechanism.[203] DA rapidly oxidises to dopamine-*o*-quinone under slightly alkaline conditions induced by atmospheric oxygen or other oxidising agents.[257] The resulting *o*-quinoic intermediate further reacts to cyclic structures such as leukodopaminechrome (also known as 5,6-dihydroxyindoline) and DHI. The latter species was assigned a key role during the construction of PDA (**Scheme 2.10**) and similar observations have been made for the natural analogous system — the eumelanin biopolymers (refer to **Scheme 2.9**). Subsequent copolymerisation of DHI with other reactive DA-derived intermediates have been proposed to occur *via* oxidative intermolecular cross-coupling reactions concomitant with supramolecular self-assembly.[203]

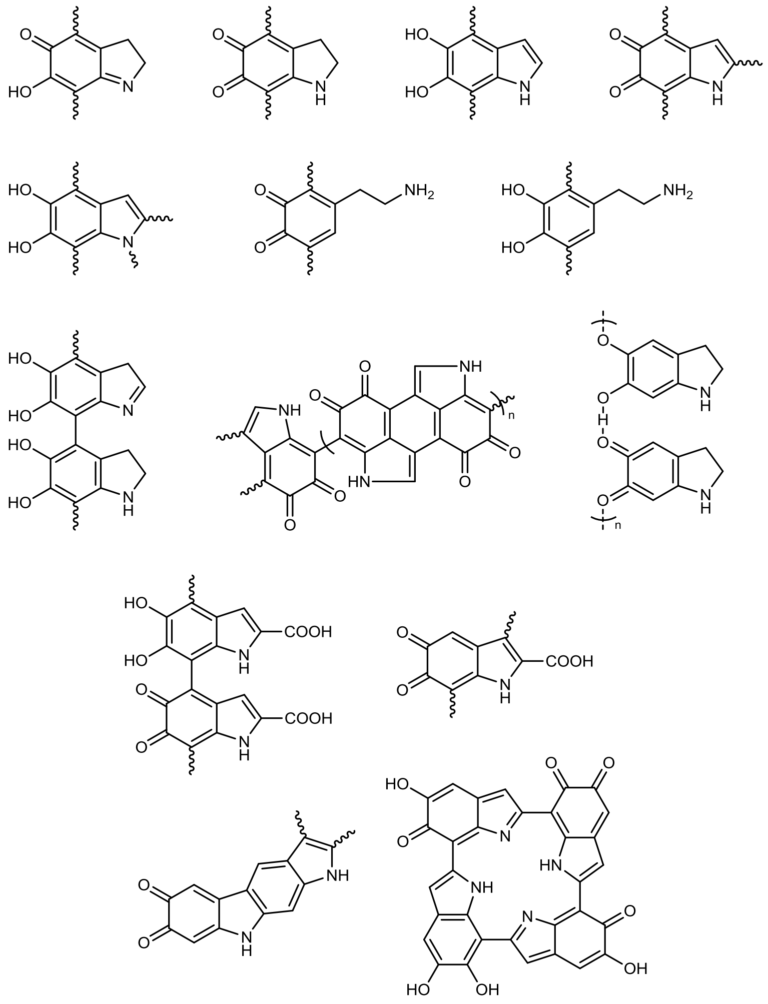

Figure 2.5. Proposed structural key elements for PDA and its derivatives (*e.g.*, eumelanins). Adapted and reproduced with permission from reference [252]. Copyright (2013) The American Chemical Society.

Numerous structural key elements and various types of covalent and noncovalent polymer self-assembly mechanisms of PDA have been proposed in the literature (**Figure 2.5**).[247, 251-252] The DA derivatives incorporated within PDA structures, for instance, have been reported to possess various oxidation states, including catechol, semiquinone or *o*-quinone functional groups. In addition, covalent cross-coupling reactions concomitant with C–C bond formations have been suggested to occur not only *via* the benzo moiety (*e.g.*, through positions 2 and 4 of DHI) but also *via* the adjacent pyrrole group (*e.g.*, through position 7). These observations were supported, for instance, by computational calculations, which have investigated the most reactive positions of DHI for subsequent oligomer formation.[258] A clear tendency toward planar oligomer assembly (up to the tetramer level) was described with enhanced intermolecular π–π interactions for the formation of graphite-like oligomer layers. Other proposed structures, which are displayed in **Figure 2.5**, refer also to natural eumelanins with L-DOPA as a key building block.[252]

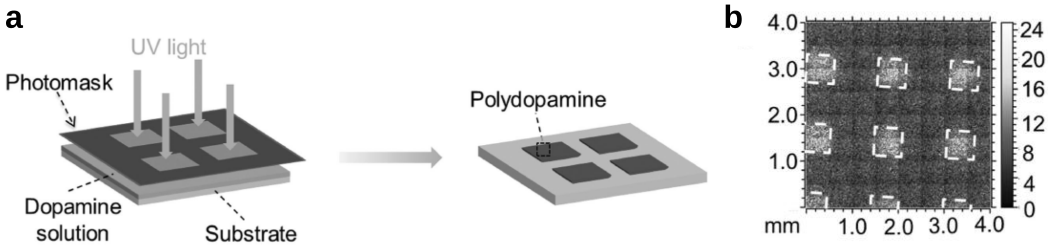

Figure 2.6. Polymer surface patterning of PDA. (**a**) Schematic representation of the UV-assisted DA photopolymerisation concomitant with PDA surface deposition in spatially confined areas. (**b**) ToF-SIMS characterisation of polymer patterned surface *via* imaging of PDA-characteristic $[CN]^-$ fragments. Adapted and reproduced with permission from reference [263]. Copyright (2014) John Wiley and Sons.

The polymerisation of DA is typically conducted in aqueous aerobic systems. Recent advances, however, have expanded the applicable scope of synthetic protocols for the generation of PDA coatings.[257, 259-262] The group of Levkin, for instance, introduced UV-light as an external stimulus to temporally and spatially control the polymerisation of DA (**Figure 2.6**).[263] The synthetic procedure is based on the light-dependent generation of reactive oxygen species (ROS) derived from dissolved molecular oxygen. The increased formation of ROS, when the coating solution is exposed to UV light, leads to an accelerated oxidation of the catechol moiety and a rapid build-up of reactive *o*-quinone derivatives for the subsequent formation of PDA oligomers. The DA photopolymerisation protocol was further exploited for the PDA surface immobilisation with spatial resolution, which concept has also been applied to other plant polyphenols.[230-231, 263]

Poly(dopamine) Post-polymerisation Modifications

Surface adherent PDA films often serve as a versatile platform for substrate-independent post-modification reactions such as metallisation[203, 264] or the surface immobilisation of small (bio)molecules[265] and grafted polymers.[266] Covalent surface attachment of organic and polymeric scaffolds can be achieved in multiple ways based on the broad range of functional groups present in the PDA films (**Scheme 2.11**).

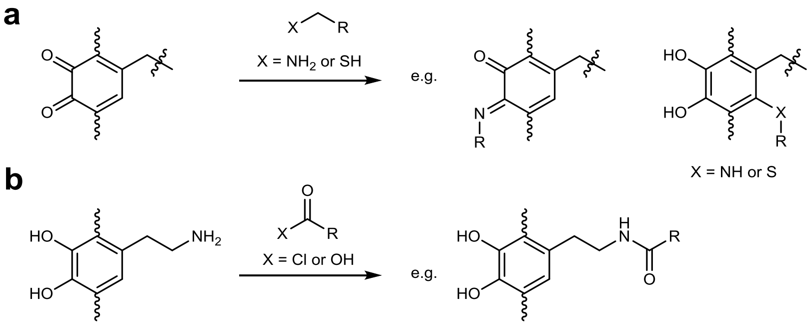

Scheme 2.11. Schematic depiction of PDA post- modification pathways: (**a**) nucleophilic conjugation with primary amino or mercapto groups (*e.g.*, *via* Schiff base or Michael-type addition reactions) and (**b**) acylation reactions.

Amino or mercapto functional molecules are commonly employed for the nucleophilic conjugation with PDA-incorporated *o*-quinone or catechol species following Schiff base or Michael-type reactions (**Scheme 2.11a**).[203, 265, 267-268] The acylation of the free primary amino groups (stemming from PDA-incorporated dopamine moieties) has been reported as an alternative synthetic pathway for the PDA post-modification (**Scheme 2.11b**).[266, 269-270] Various synthetic polymer strands as well as biopolymers have been immobilised onto PDA-coated surfaces following either *grafting to* or *grafting from* synthetic protocols. Ligation *via grafting to* was predominantly performed with amino or thiol end group functionalised polymer strands.[265, 271] In a similar approach, conductive polymers were grafted onto maleimide-functionalised PDA surfaces using Diels–Alder ligation chemistry.[269]

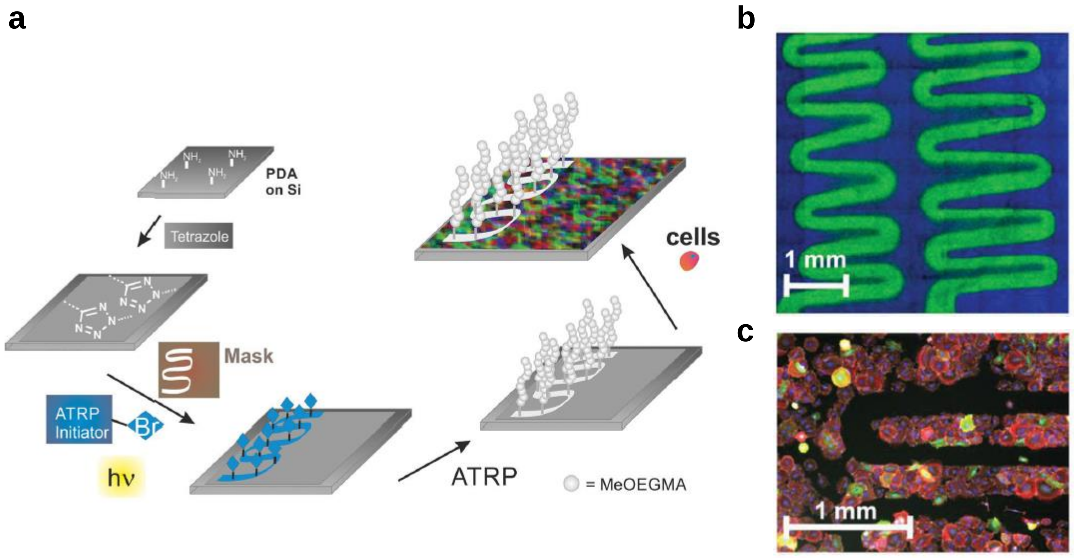

Figure 2.7. Surface photopatterning of poly(MeOEGMA) polymer brushes onto PDA precoated surfaces. (**a**) Schematic representation for the generation of photo-active PDA surfaces, followed by the SI-ATRP of MeOEGMA in spatially defined areas. (**b**) ToF-SIMS overlay image of poly(MeOEGMA)-characteristic fragments (green) exclusively detected in areas which have been exposed to UV irradiation. Fragments derived from the underlying PDA layer are illustrated in blue. (**c**) Corresponding cell pattern with meander shaped antifouling domains. Adapted and reproduced with permission from reference [266]. Copyright (2013) John Wiley and Sons.

SI-ATRP *grafting from* protocols have been applied, for instance, for the formation of PEG-functionalised surfaces with non-fouling properties by our team. The spatial control over cell adhesion (exemplified using rat embryonic fibroblasts) was achieved following an advanced photoligation protocol for the *grafting from* poly(oligo(ethylene glycol) methyl ether methacrylate) (poly(MeOEGMA) polymer brushes in confined areas with anti-fouling properties (**Figure 2.7**).[266]

2.2.4 Tailor-Made Catecholamines as Versatile Coating Agents

A one-step synthetic strategy for the design of tailor-made material interfaces uses prefunctionalised catecholamines as versatile coating agents (**Scheme 2.12**). Direct access to functional surfaces with superhydrophobic and self-cleaning properties, for instance, was achieved using a DOPA derivative which was modified with a perfluorinated alkyl side chain (**Scheme 2.12a**).[272] Following a similar surface modification strategy, protein resistant and antifouling surfaces were prepared by fusing the adhesive properties of DOPA with PEG polymer strands (**Scheme 2.12b**).[213] Degradable poly(catecholamine) networks with incorporated disulphide bridges as cleavable functional moieties have been recently presented in the literature.[273] Two DOPA molecules were covalently linked *via* a disulphide bond and subsequently employed as a polymerisable coating agent. The controlled degradation of surface adherent polymer films was carried out using glutathione (GSH) as a reducing agent (**Scheme 2.12c**).

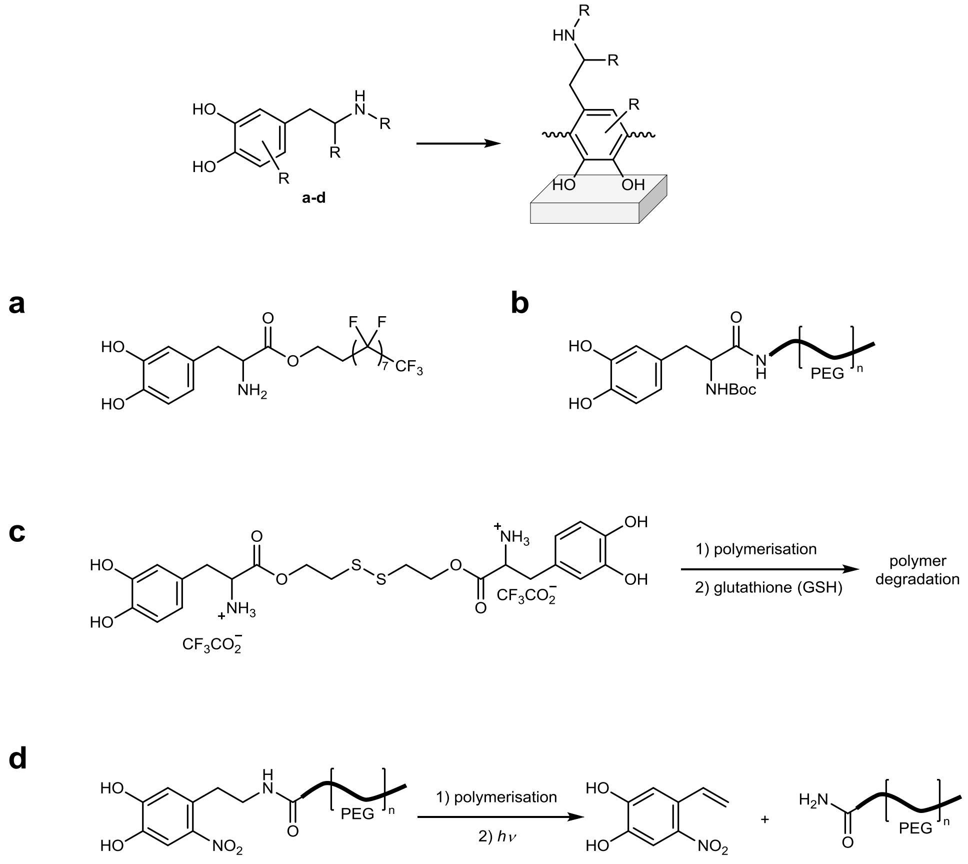

Scheme 2.12. Direct access to highly defined surfaces using prefunctionalised catecholamines as coating agents.[213, 272-274]

The group of del Campo introduced an avenue of photodegradable polycatecholic hydrogels and polymer coatings with debonding on demand properties and potential use as biocompatible surgical glues.[274] A nitrodopamine derivative attached to a four-arm PEG moiety was synthesised and subsequently polymerised using $NaIO_4$ as a strong oxidising agent (**Scheme 2.12d**). In addition, polymer networks based on metal-phenolic complexation utilising Fe(III)-ions have been presented, which were subsequently photo-depolymerised under UV irradiation.

The fusion of biomimetic catechol surface chemistry and efficient post-polymerisation orthogonal ligation techniques has been successfully exploited in multiple ways for the generation of tailor-made surfaces (**Scheme 2.13**). CuAAC click chemistry has been applied for the precise surface engineering of TiO_2 and magnetic Fe_3O_4 nanoparticles, which were readily functionalised with fluorophores,[275] water-solubilising polymers,[276] or biomolecules (**Scheme 2.13a**).[277] Thermo-reversible Diels–Alder switches[278] as well as rapid hetero-Diels–Alder reactions[279] were employed for *grafting to* polymer surface conjugations of various substrates with synthetic and biopolymers (**Scheme 2.13b**). Furthermore, an advanced photoligation protocol was fused with bioinspired surface chemistry providing spatial control over the polymer surface immobilisation (**Scheme 2.13c**).[280] *o*-Methyl benzaldehyde (photoenol) derivatives were attached to gold surfaces *via* catechol anchoring and subsequently activated by UV irradiation. Efficient Diels–Alder photo-click reactions between surface-attached (*in situ* generated) dienes and maleimide-end group functionalised polymer strands were carried out with spatial precision using a shadow mask. The successful polymer surface patterning was evidenced by time-of-flight secondary ion mass spectrometry (ToF-SIMS) and the imaging of polymer-characteristic fragments exclusively present in areas which have been exposed to UV irradiation.[280] *Grafting from* polymer brushes have been successfully prepared *via* SI-ATRP for the design of hollow poly(2-hydroxyethyl methacrylate) (PHEMA) capsules (**Scheme 2.13d**).[281] Dopamine was attached to a 2-bromoisobutyryl derivative *via* amidation, and the newly-synthesised DA derivative (equipped with an ATRP initiator) was thereafter copolymerised with DA. After the formation of thin polymer films deposited onto the immersed poly(styrene) core particles, the *grafting from* polymerisation of

2-hydroxyethyl methacrylate (HEMA) was carried out, followed by the elimination of the PS template.

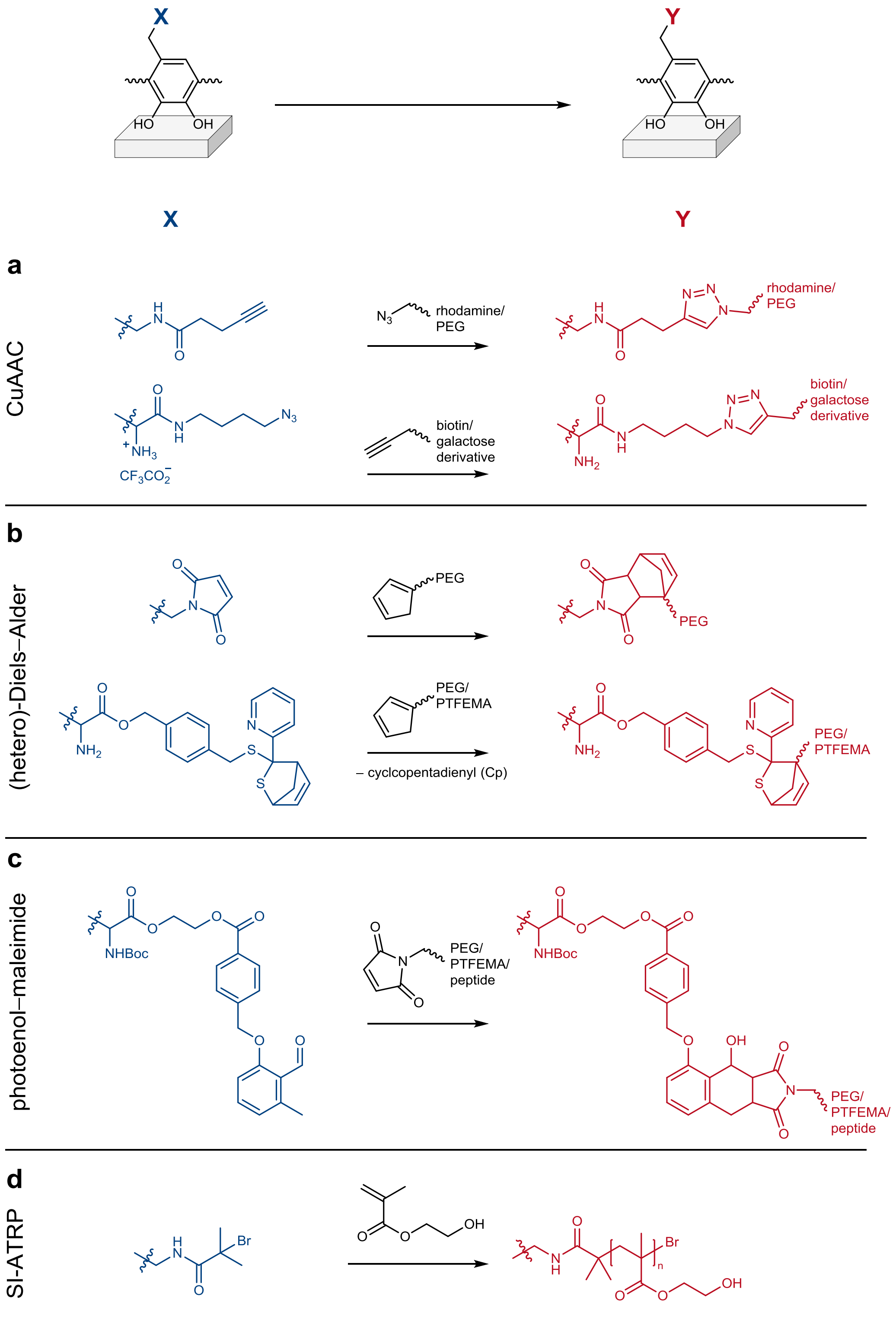
X
Y
HO
OH
a
CuAAC
rhodamine/ PEG
biotin/ galactose derivative
$CF_3CO_2^-$
b
(hetero)-Diels–Alder
PEG
PEG/ PTFEMA
– cyclcopentadienyl (Cp)
c
photoenol–maleimide
NHBoc
PEG/ PTFEMA/ peptide
d
SI-ATRP
Br
OH

Scheme 2.13. Examples of bioinspired surface immobilisations of various functional groups for subsequent (orthogonal) post-coating modification reactions.[276-281]

It is important to consider that the position and the type of the functional moiety attached to DA or L-DOPA strongly influences the ability of the catecholamine derivative to polymerise in aqueous solutions. Therefore, the overall design of the coating agent needs to be carefully assessed in terms of its (covalent and noncovalent) self-assembly behaviour and its adhesive performances. In comparison to the DA polymerisation mechanism (refer to Chapter 2.2.3), the functionalisation of the DA core structure significantly changes its reactivity toward subsequent intramolecular and intermolecular reaction cascades. All the previously discussed key structural features and intermolecular interactions decide over both, the cohesive and adhesive forces of the catechol-based coating system and thus strongly influence the overall coating stability.[194] For the prefunctionalised coatings agents presented in the current subchapter (refer to **Scheme 2.12** and **2.13**), the predominant driving forces for the formation of stable coatings were often not clearly elucidated in the literature. It is important to differentiate between monomer-like catechol–substrate interactions (resulting in monolayer type coatings) and polymer film formation (*via* oxidative polymerisation in aqueous solutions) resulting in multivalent polycatechol–substrate interactions. The introduction of functional groups *via* the free amino group of DA or L-DOPA yielding the corresponding catecholamide structures (refer to **Scheme 2.12d** and **Scheme 2.13**) has to be critically assessed in terms of significant changes in their polymerisation reactivity. For example, important cyclisation reactions generating indole-like structures might be strongly hampered due to the absence of the free primary amine, which, as a consequence, strongly influences the polymer composition and the resulting adhesive properties. In case of additional substituents, which have been introduced to the aromatic core structure of the catecholamine, the subsequent oligomer formation is most likely strongly hampered as covalent intermolecular cross-coupling reactions have been proposed to occur *via* the 1,4-connection of the benzo moiety.[252] DOPA-containing coating agents, however, are promising precursor molecules for the design of advanced surface coating technologies with PDA-like adhesive properties. A convenient synthetic approach is the introduction of the targeted functional group *via* the carboxylic acid group of DOPA without changing the polymerisable DA-like core structure. However, additional bulky side groups attached to DOPA, such as perfluorinated alkyl groups (refer to **Scheme 2.12a**), clearly affect subsequent catecholamine polymerisation and coating formation. Therefore, $NaIO_4$ has often been employed as a harsh oxidising agent (substituting atmospheric oxygen as a mild analogue) to accelerate the polymerisation of functionalised DOPA and DA derivatives. Precise structural and mechanistic insights into the polymerisation of modified catecholamines have remained widely elusive. The group of Liebscher suggested close structural similarities of a polymerised DOPA amide system carrying *N*-hydroxyethyl groups in the polymer side chains compared to polymerised DA networks.[277] They identified various PDA-like building blocks constituting the poly(DOPA amide) polymer backbone by solid-state ^{13}C NMR spectroscopy. In addition, UV–vis spectroscopy has been proven beneficial for the monitoring of the polymerisation of functional catecholamine derivatives based on changes in the UV–vis absorption during catechol oxidation toward *o*-quinone derivatives.[272]

2.3 BACTERIAL BIOFILMS AND BIOFOULING

2.3.1 Bacterial Biofilms and Biofilm-Related Infections

Biofilms are surface-attached bacterial communities enclosed in a self-produced polymeric matrix.[8] The biofilm formation is initialised by the reversible surface attachment of planktonic (free-floating) bacteria and further proceeds over several distinct stages (**Figure 2.8**). The bacterial surface adhesion becomes irreversible once cell division has taken place and first microcolonies have formed. This process is accompanied by the production of a surrounding polymer matrix, which is composed of hydrated extracellular polymeric substances (EPSs), mainly polysaccharides, proteins, extracellular DNA, and lipids.[9] These biopolymers are pivotal for the construction of the biofilm's physical appearance and its mechanical stability. Furthermore, the matrix determines the cohesive forces within a biofilm and strengthens the adhesive properties to the underlying surface. Enclosed in this matrix, bacterial cells are kept in close proximity facilitating the intercellular cell communication and further, they are effectively shielded from the hostile environment. A fully matured biofilm exhibits a complex and heterogeneous three-dimensional structure with transport channels connecting the microcolonies for nutrient and oxygen circulation as well as for the removal of metabolic waste products.[9, 282]

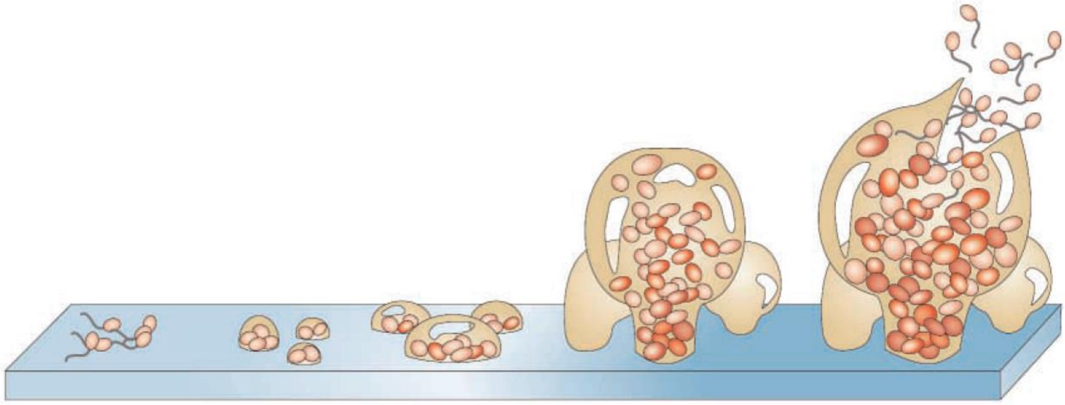

Figure 2.8. The lifecycle of a bacterial biofilm including the reversible bacterial surface attachment and microcolonisation, followed by biofilm maturation and biofilm dispersal. Reproduced with permission from reference [11]. Copyright (2003) Springer Nature.

The complex biofilm development with spatial cell differentiation is regulated by various intercellular signalling mechanisms (*e.g.*, quorum sensing).[283] Quorum sensing has been extensively studied in *Pseudomonas aeruginosa* — a Gram-negative opportunistic pathogen with clinical burden in worldwide healthcare systems. Moreover, it has become a model microorganism in biofilm research.[284-285] Quorum sensing is considered to regulate the biofilm development of *P. aeruginosa* based on small diffusible messenger molecules. Several classes of autoinducers exist including *N*-acylated homoserine lactones (AHLs), which are released by the microorganism into their local environment. The accumulation of those signalling molecules within a biofilm induces transcription of specific genes throughout the biofilm population and triggers specific molecular events in biofilm maturation.[286]

In the last stage of biofilm maturation, planktonic cells are released from the biofilm able to colonise new areas. Contrary to passive bacteria detachment, such as sloughing or erosion, the biofilm dispersal event is considered as a programmed release of planktonic cells from the biofilm.[287] Biofilm dispersal can be triggered by specific environmental cues, *e.g.* the lack of nutrients and oxygen supply, changes in the pH, or different levels of small messenger molecules, such as nitric oxide.[3, 288] The latter species, for instance, is directly linked to the intracellular messenger cyclic-di-GMP (c-di-GMP), which has received attention as an important regulatory system in the lifecycle of a biofilm.[287] The active role of nitric oxide and its derivatives in biofilm regulation is further discussed in Chapter 2.3.3.

Biofilm Contamination — a Major Risk in Worldwide Public Health

The formation of a biofilm is often the root cause in industrial biofouling and responsible for many bacterial infections in the clinics.[289] It is estimated that over 80% of all microbial infections in the human body are caused by biofilms — the predominant bacterial mode of growth.[11] Most impressively, biofilms can withstand host immune responses and are highly adaptive toward external environmental cues. Furthermore, they exhibit an inherent resistance to antimicrobial agents as conventional antibiotic therapy simply fails to penetrate the full depth of a biofilm. In combination with different phenotypes of a biofilm and spatial heterogeneity within those multicellular conglomerates, biofilms are up to 10–10,000-fold more resistant to antimicrobial agents compared to planktonic bacteria resulting in hard-to-treat and chronic infections.[290]

Bacterial biofilms, for instance, are the major cause of chronic lung infections in Cystic Fibrosis (CF) patients. CF is a genetic defect leading to a higher susceptibility of bacterial colonisation in lungs. Standard antibiotic treatment typically fails to cure the ongoing infection leading to lung damage and thus a short median life expectancy of CF patients.[8, 11] Furthermore, hospital acquired (nosocomial) infections induced by bacterial surface colonisation and biofilm formation on medical devices display a significant challenge in worldwide healthcare systems.[17, 291] Once a biofilm has evolved on a medical implant, it becomes an immense threat for the patient with only a few effective countermeasures, including the surgical removal of the afflicted areas. Other current strategies to control biofilm formation on surfaces (*e.g.*, preventive strategies) are discussed in the next Chapter.

2.3.2 Current Strategies to Control Biofilm-Related Infections

Several approaches have emerged over the last decade to combat biofilms. Promising examples include the use of specific antibiofilm agents (*e.g.*, antimicrobial peptides with enhanced activity against biofilms), the use of advanced drug delivery systems, or electrochemical methods as alternative approaches to standard antibiotic therapies.[15]

The prevention of biofilm formation on surfaces is commonly achieved by modifying the surface properties of the exposed material. Two chemical strategies are commonly employed: antimicrobial and antifouling coatings (**Figure 2.9**).[17] Antimicrobial surfaces are typically equipped with inhibitory or lethal concentrations of biocides (*e.g.*, antibiotics), which are released over the course of time.[18, 292] Alternatively, contact-killing agents have been immobilised on the surface, such as quaternary ammonium compounds or (cationic) antimicrobial peptides disrupting the microbial cell wall or cell membrane.[293-295] Both strategies, however, have demonstrated limited success (when applied to the surface) due to the loss of activity when the antibiotic has been released or as a result of the accumulation of dead biomass masking the underlying contact-active surface properties. In addition, the use of antibiotics in sublethal doses (after initial burst release) has shown to accelerate antimicrobial resistance and to promote biofilm formation.[17]

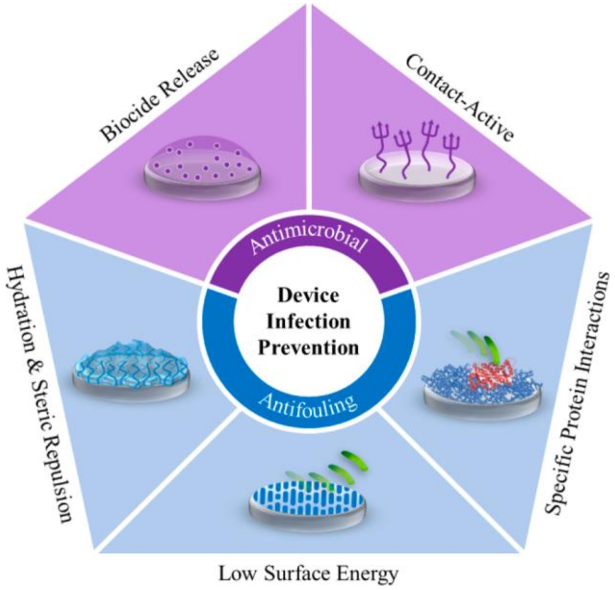
Biocide Release
Contact-Active
Antimicrobial
Device Infection Prevention
Antifouling
Hydration & Steric Repulsion
Specific Protein Interactions
Low Surface Energy

Figure 2.9. Common antibacterial and antifouling coating strategies for the reduction of device-associated infections. Reproduced with permission from reference [17]. Copyright American Chemical Society.

Several antifouling strategies have been developed against bacterial surface attachment and protein adsorption. PEG-functionalised surfaces are frequently applied for the generation of nonfouling material interfaces owing to hydration forces and steric hindrance effects, which molecular mechanisms, however, are not completely understood until now.[296-298] The passivation of surfaces with albumin has been presented as a preventive strategy against bacterial adhesion and nonspecific surface attachment of other proteins.[299-300] Furthermore, low energy surfaces have been employed increasing the interfacial tension between the liquid and the substrate, which, on the other hand, impedes bacterial surface attachment.[301] Fluoropolymers (*e.g.*, PTFE) and silicones are widely employed materials with chemically-inert and bioinert character.[17, 302-303] In addition to the herein presented chemical design strategies, the surface topography, including the surface roughness, also significantly impact the overall nonfouling properties of the modified surface.[304]

2.3.3 Nitroxides as Potential Antibiofilm Agents

The persistent radical character of nitroxides has been exploited in multiple ways, and various applications have emerged in the literature (refer to Chapter 2.1). Recently, nitroxides have been employed as promising antibiofilm agents owing to their nitric oxide mimetic character.

Nitric oxide is a colourless diatomic molecule and existent as a gaseous free radical species with a short half-life of only a few seconds. At low nanomolar concentrations, NO plays an important role as a signalling molecule in many biological processes, including the bacterial mode of growth.[305] NO is endogenously produced by the microorganism itself. For instance, it occurs as an intermediate in the metabolic pathway of the denitrification, where nitrate is reduced *via* nitric oxide to N_2 by specific enzymes, such as nitrite reductase in *P. aeruginosa* (encoded by the gene *nirS*).[4, 305]

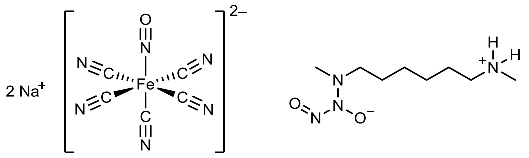

Sodium nitroprusside (SNP)

MAHMA NONOate

Figure 2.10. Common examples of small NO donor molecules.

In biofilm research, several chemical agents have emerged as external sources to deliver highly reactive NO at the interface of surface-attached bacteria. Common approaches encompass the use of inorganic sodium nitroprusside (SNP) and small organic NO donor molecules, such as 6-(2-hydroxy-1-methyl-2-nitrosohydrazino)-*N*-methyl-1-hexanamine (MAHMA NONOate) (**Figure 2.10**).[3, 305] Furthermore, functional polymers capable of releasing NO have been developed as advanced drug delivery systems.[306] For instance, polymer-coated gold nanoparticles were equipped with NO donor molecules leading to a significant reduction of bacterial proliferation on the surface.[307] The exogenous delivery of NO as a therapeutic agent, however, still remains challenging due to its high reactivity, the inherent toxicity at higher concentrations as well as limited release mechanisms of NO donor molecules.

Nitroxides, which have been referred to as sterically hindered NO analogues,[4] are capable of overcoming the above-mentioned inherent drawbacks of NO as they possess a negligible toxicity and are easy to handle. Furthermore, they exhibit an excellent long-term stability in the solid state, and wide-ranging chemical design strategies exist in the literature for the precise preparation of various types of nitroxides and nitroxide functional materials. The NO-mimicking properties of nitroxides were first examined in *P. aeruginosa* swarming motility assays in order to study their effect on multicellular bacterial behaviours (**Figure 2.11**).[4]

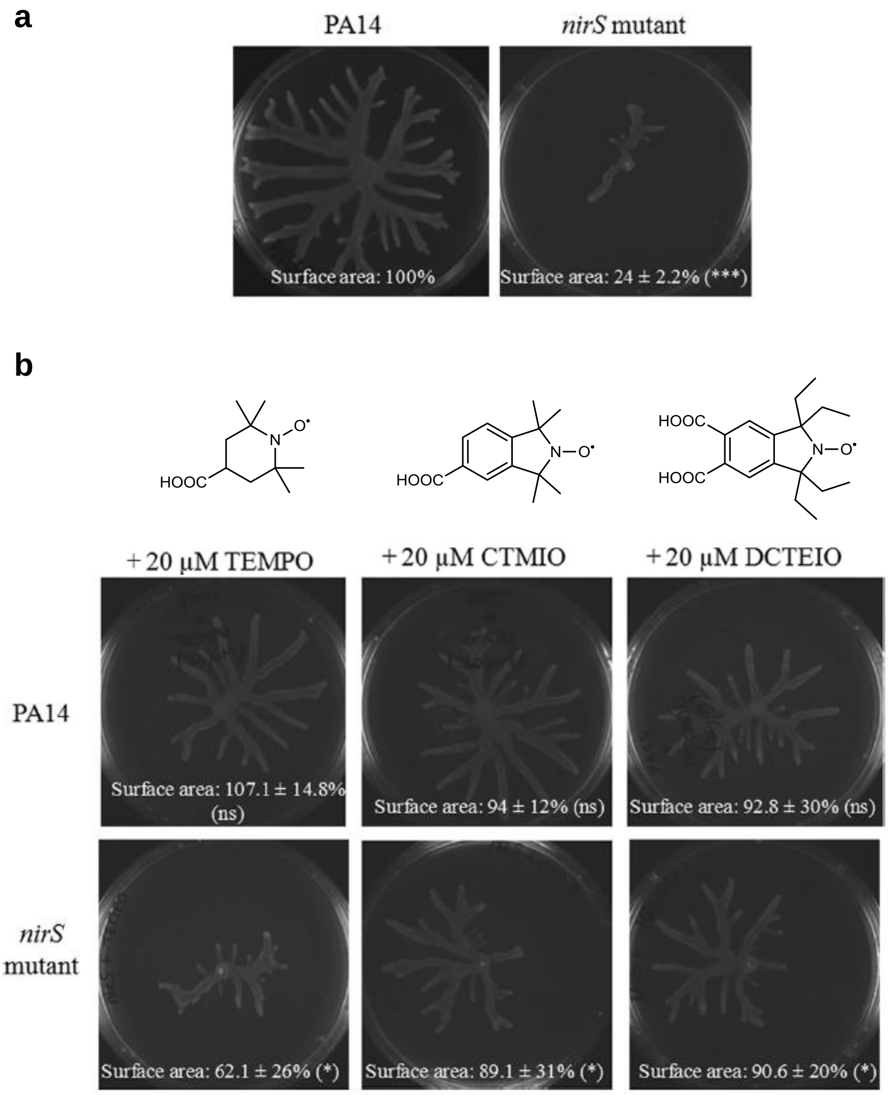

a
PA14
nirS mutant
Surface area: 100%
Surface area: 24 ± 2.2% (***)
b
HOOC
N
O•
HOOC
N—O•
HOOC
HOOC
N—O•
+20 µM TEMPO
+20 µM CTMIO
+20 µM DCTEIO
PA14
Surface area: 107.1 ± 14.8% (ns)
Surface area: 94 ± 12% (ns)
Surface area: 92.8 ± 30% (ns)
nirS mutant
Surface area: 62.1 ± 26% (*)
Surface area: 89.1 ± 31% (*)
Surface area: 90.6 ± 20% (*)

Figure 2.11. Images of swarming motility experiments with PA14 wild-type and a *nirS* mutant in the presence of nitroxides. Adapted and redrawn with permission from reference [4]. Copyright (2013) American Society for Microbiology.

A *nirS* mutant unable to produce NO endogenously was employed in this study showing a limited swarming motility (24%) compared to the PA14 wild-type (100%) (**Figure 2.11a**). In the presence of selected nitroxides, however, the swarming ability of the *nirS* mutant was substantially restored (**Figure 2.11b**). The use of isoindoline-based nitroxides (abbreviated as CTMIO and DCTEIO in **Figure 2.11b**) resulted in a recovery of the swarming motility of the *nirS* mutant to nearly wild-type levels (> 89%). The more hydrophilic 4-carboxy-TEMPO species showed a lower surface coverage (62%) compared to the aromatic analogous structures.

In subsequent experiments, the influence of nitroxides on the sessile mode of bacterial growth was investigated. Similar to the swarming motility assays, the *nirS* mutant was deficient in forming mature biofilm structures due to the absence of endogenously produced NO as an intercellular signalling molecule. In the presence of low doses (20 μM) of 4-carboxy-TEMPO or DTCEIO, however, the ability of the *nirS* mutant to form a biofilm was substantially restored compared to the PA14 wild-type (**Figure 2.12**). The potential of nitroxides to inhibit initial biofilm formation and to disperse existing biofilms was assessed thereafter (**Figure 2.13**). PA14 biofilm formation was completely suppressed within the first 72 h of biofilm cultivation when 4-carboxy-TEMPO (20 μM) was present. In addition, the treatment of preformed biofilms (48 h) with 4-carboxy-TEMPO (20 μM for 24 h) successfully triggered biofilm dispersal as shown in **Figure 2.13** (right image).[4]

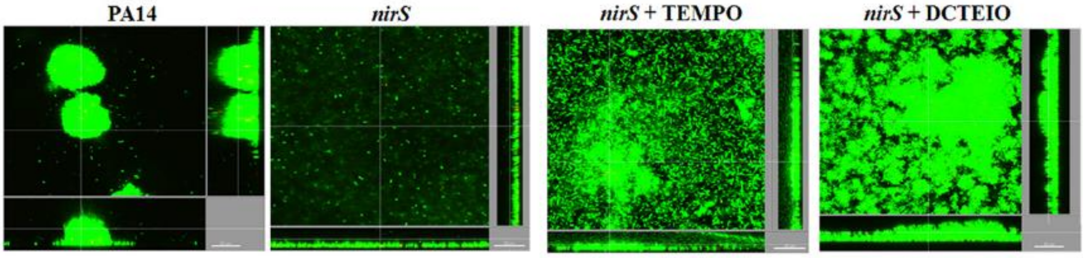

Figure 2.12. *P. aeruginosa* biofilm experiments with the PA14 wild-type and a *nirS* mutant in the presence of nitroxides (20 μM). Adapted and redrawn with permission from reference [4]. Copyright (2013) American Society for Microbiology

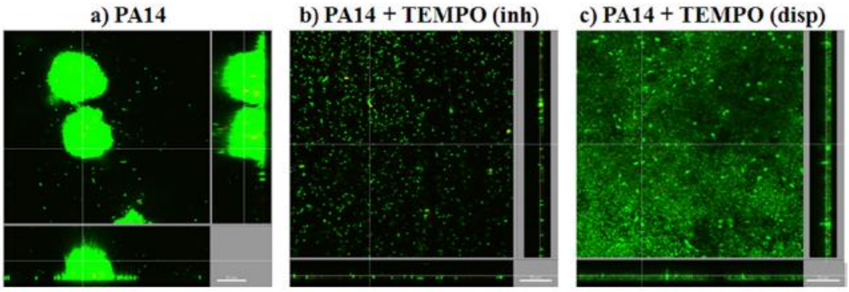

Figure 2.13. *P. aeruginosa* biofilm inhibition and biofilm dispersal assays using 4-carboxy-TEMPO (20 μM). Adapted and redrawn with permission from reference [4]. Copyright (2013) American Society for Microbiology

In a follow-up study, the increased susceptibility of dispersed biofilms toward antimicrobial treatment was demonstrated using the standard antibiotic ciprofloxacin at its minimum inhibitory concentration (MIC) (**Figure 2.14**).[5] The synergistic effects of antibiofilm-active nitroxides (20 μM) and antibiotic ciprofloxacin were shown against Gram-negative PA14 (320 ng·mL^{-1}) and *E. coli* O157 (20 ng·mL^{-1}) preformed biofilms. The MIC is the lowest concentration of an antimicrobial agent necessary to prevent planktonic cell growth, however, this does not hold true for bacteria within a biofilm. As clearly shown in **Figure 2.14**, treatment with ciprofloxacin at its MIC completely failed to eradicate the preformed biofilm, which were grown in the absence of 4-carboxy-TEMPO. When biofilm cultivation was performed with nitroxides added to the media, only minor biofilm constructs have evolved on the surface and, subsequent treatment with ciprofloxacin resulted in a complete biofilm eradication due to the increased vulnerability of the perforated biofilm toward antibiotics. Importantly, no antibiofilm effect of 4-carboxy-TEMPO on Gram-positive *Staphylococcus aureus* MRSA biofilms was observed.[5]

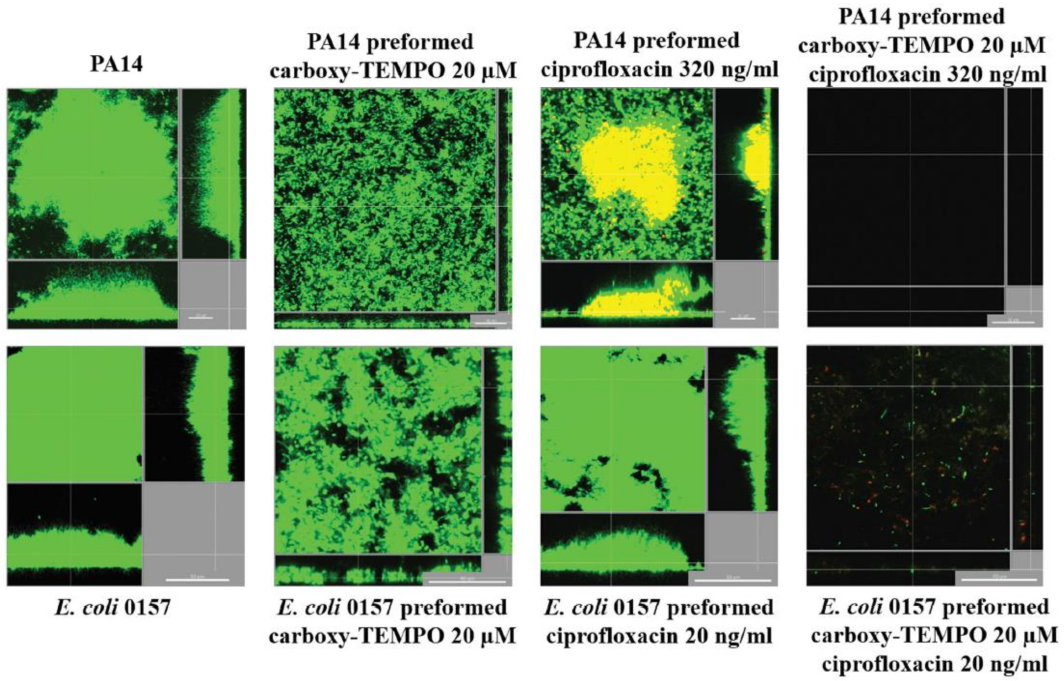
PA14
PA14 preformed carboxy-TEMPO 20 µM
PA14 preformed ciprofloxacin 320 ng/ml
PA14 preformed carboxy-TEMPO 20 µM ciprofloxacin 320 ng/ml
E. coli 0157
E. coli 0157 preformed carboxy-TEMPO 20 µM
E. coli 0157 preformed ciprofloxacin 20 ng/ml
E. coli 0157 preformed carboxy-TEMPO 20 µM ciprofloxacin 20 ng/ml

Figure 2.14. Biofilm eradication experiments with 4-carboxy-TEMPO and antibiotic ciprofloxacin using Gram-negative *P. aeruginosa* and *E. coli*. Reproduced with permission from reference [5]. Copyright (2015) Oxford University Press.

Recent advances have been made in examining the antibiofilm properties of various types of nitroxides and nitroxide conjugates. The group of Schiesser screened more than 20 different nitroxide species as potent antibiofilm agents using crystal violet staining as a quantification method.[308-309] A dodecanethiyl-substituted pyrrolinoxyl nitroxide was identified as a promising antibiofilm agent based on close structural similarities to an important signalling molecule in *P. aeruginosa* quorum sensing. In order to promote the synergistic effects stemming from dispersed biofilm structures and conventional bacterial eradication therapies, novel chemical strategies have been developed by our team, including the introduction of various nitroxide–ciprofloxacin hybrid molecules.[310-311] The use of an isoindoline-based nitroxide, which was linked to the secondary amine of the piperazine ring of ciprofloxacin, has resulted in a substantial biofilm removal (94%) owing to the dual-acting antibiofilm and antimicrobial properties of the nitroxide and the ciprofloxacin core structure.[310] In order to combat biofilm-related biofouling on surfaces, spin-coated PTMA-PMMA polymer films (> 300 nm in thickness) have been recently introduced with certain antibiofilm properties.[312] The biofilm cultivation on nitroxide-coated silicon wafers was performed for 24 h with subsequent evaluation using the colony forming unit (CFU) method. A reduction of biofilm-derived bacteria up to 99.96% was observed when 100 wt% PTMA was employed as a polymer coating compared to the PMMA homologous polymer system. Similar strong effects (greater than 99.6%) were described even on surfaces with lower wt% of the nitroxide monomer. However, precise evaluation of other potential side effects stemming from the employed copolymer matrix (*e.g.*, different surface topographies)[313] and complementary confocal microscopy images of the biofilm constructs grown on PTMA were not presented.[312]

Chapter 3: Incorporating Nitroxides within Poly(catecholamine) Scaffolds

3.1 PREFACE

Nitroxide-containing polymers are of emerging interest as multifunctional synthetic tools and high-tech materials, ranging from the design of complex polymer systems to electroactive composites in electronic devices and in biomedical applications. The current chapter introduces a new methodology for the generation of nitroxide functional polymers with inherent adhesive properties for targeted nitroxide surface immobilisation onto various materials. The adhesive polymer matrix for nitroxide embedment was carefully selected regarding a substrate-independent and versatile coating strategy for a widespread practical use, *e.g.* to deliver nitroxides at materials interfaces of medical devices to prevent biofilm formation. Bioinspired poly(catecholamine) scaffolds fulfil the above-mentioned criteria with multiple expressed catechol surface anchoring units along the polymer backbone generating highly adhesive multifunctional coatings. First, the fusion of a catecholamine monomer with a nitroxide functional group is presented. The newly-synthesised and tailor-made molecule, denoted as DOPA-TEMPO, was thoroughly characterised and examined in regard to the structural verification of the polymerisable catecholamine moiety as well as the appearance of the (temporary masked) nitroxide radical moiety. Subsequent oxidative polymerisation toward poly(DOPA-TEMPO) was performed under mild conditions employing an easy-to-operate experimental setup. The complex and various oxidative polymerisation pathways of the nitroxide-functionalised catecholamine were carefully investigated by UV–vis spectroscopic identification of various redox intermediate states during polymer assembly. These findings were then critically correlated to EPR spectroscopic quantification of the nitroxide-assigned unpaired electron spin throughout the aerobic polymerisation. Intermolecular oxidative cross-coupling reactions yielding covalently linked

---

Parts of the current chapter are adapted or reproduced from reference [314]: H. Woehlk, J. Steinkoenig, C. Lang, L. Michalek, V. Trouillet, P. Krolla, A. S. Goldmann, L. Barner, J. P. Blinco, C. Barner-Kowollik and K. E. Fairfull-Smith, *Langmuir*, **2018**, 34, 3264-3274, with permission from the American Chemical Society. Mass spectrometric data acquisition presented in chapter 3.3 was conducted by J. Steinkoenig (KIT/QUT).

oligomeric structures were confirmed by HR-ESI mass spectrometry and key structural units along the polymer backbone were identified.[314]

3.2 DESIGN AND SYNTHESIS OF A NITROXIDE FUNCTIONAL CATECHOLAMINE

The introduction of functional groups (*e.g.*, nitroxides) to polymer strands is typically accessible *via* two synthetic strategies: the polymerisation of functional monomers toward targeted macromolecular structures or *via* post-polymerisation modification pathways using various well-established polymer ligation protocols.[197, 315] The first chemical approach of using prefunctionalised catecholamines as monomers for the generation of nitroxide-containing polymers has been conceptually favoured as it ensures a widespread practical use for targeted nitroxide surface decoration of various materials following a simple and one-step dip-coating procedure (refer to Chapter 5). The properties of the comprising polymer strands with persistent multi-radical character can readily be controlled following the proposed nitroxide-containing monomer approach, *e.g. via* copolymerisation with other suitable catecholamine-based monomers for incorporation of additional functional groups or to adjust the overall nitroxide density within the adhesive polymer film (refer to Chapter 6). Furthermore, the versatile toolbox of post-polymerisation modification techniques is available for precise tailoring of nitroxide functional polymer materials and coatings, *e.g. via* nitroxide radical coupling reactions (conducted in Chapter 6).

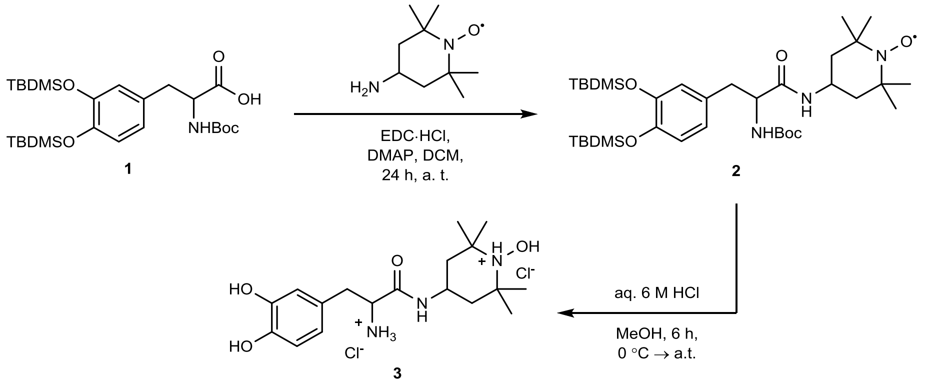

Scheme 3.1. Synthetic pathway for the preparation of DOPA-TEMPO (**3**), isolated as the corresponding hydroxylamine dihydrochloride salt. Adapted with permission from reference [314]. Copyright (2018) American Chemical Society.

The design of a nitroxide-containing adhesive monomer was carried out by fusing the chemistry of polymerisable catecholamines containing dopamine (3,4-dihydroxyphenethylamine) as a core structural unit with a selected nitroxide, namely TEMPO, as a key functional group. L-DOPA was employed as a catecholamine precursor composed of a dopamine structural element constituting the adhesive macromolecular matrix upon polymerisation and equipped with a carboxylic acid functional group. The additional functional group offers a convenient docking site for nitroxide attachment, *e.g. via* esterification or amidation with the corresponding nitroxide primary alcohol or the nitroxide primary amine, respectively. Several synthetic protocols have been reported in the literature for the preparation of tailor-made DOPA-based monomers employing a catechol- and amino-protected DOPA derivative (**1**) as a suitable precursor.[217, 272-273, 279-280] Compound **1** was synthesised according to a literature procedure[217] by implementation of standard *tert*-butyldimethylsilyl (TBDMS) ether and *tert*-butyloxycarbonyl (Boc) protecting group protocols (**Scheme 3.1**). The additional free carboxylic acid moiety of $(TBDMS)_2$-*N*-Boc-DOPA (**1**) was employed for the introduction of TEMPO *via* an amide linkage, which exhibits a favourable stability throughout the synthetic pathway compared to the corresponding acid-labile ester bond. The 1-ethyl-3-(3-dimethylaminopropyl)carbodiimide (EDC)-mediated amide coupling reaction of **1** with commercially available 4-amino-TEMPO was performed in high yield (72%) including a column chromatographic purification step.

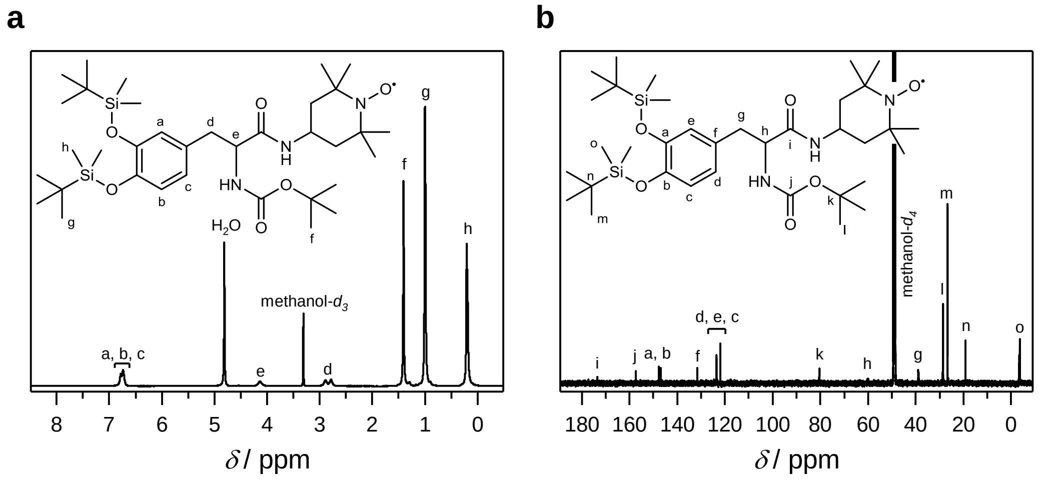

Figure 3.1. NMR spectroscopic characterisation of **2**. (**a**) ^1H NMR (600 MHz) and (**b**) ^{13}C NMR spectra (151 MHz) of $(TBDMS)_2$-*N*-Boc-DOPA-TEMPO (**2**) were recorded in methanol-d_4 at 298 K. Adapted with permission from reference [314]. Copyright (2018) American Chemical Society.

The introduction of a nitroxide-derived unpaired electron spin to intermediate **2**, denoted as $(TBDMS)_2$-*N*-Boc-DOPA-TEMPO (**2**), was unambiguously confirmed by EPR spectroscopy with the appearance of a typical three line signal in the EPR spectrum (refer to **Figure A.1** in the Appendix). Consequently, ^1H and ^{13}C NMR spectroscopic characterisation of **2** was hampered owing to its paramagnetic properties (**Figure 3.1**). Radical-induced NMR peak broadening resulted in unresolved signals of the TEMPO functional group. The molecular structure of the protected DOPA motif, however, could be identified by NMR spectroscopy. The presence of the newly-established amide linkage between both structural key elements was indicated by the appearance of a carbon signal at 170.0 ppm in the ^{13}C NMR spectrum. In addition, successful conjugation of protected DOPA with TEMPO was clearly evidenced by HR-ESI-MS with *m/z*(exp) 701.4231 $[M+Na]^+$ (*m/z*(theo) 701.4226).

The subsequent reaction step (refer to **Scheme 3.1**) targeted the removal of the TBDMS and Boc protecting groups. A simple synthetic protocol was established for the one-step cleavage of both protecting groups using acidic (HCl) conditions yielding the polymerisable catecholamine structural motif with the amino functional group as the corresponding hydrochloride salt. The reaction was performed in an aqueous and methanolic solution of hydrogen chloride, and monomer **3** was isolated in quantitative yields without the need of further purification. The usage of the above mentioned acidic and reductive (*i.e.*, methanolic) conditions transformed the nitroxyl moiety into the corresponding protonated hydroxylamine species. This acid-induced reaction pathway proceeds *via* nitroxyl radical disproportionation reactions forming the protonated hydroxylamine species as well as the *N*-oxoammonium cation.[72, 316] The latter species is known to rapidly undergo a reduction in the presence of an alcohol, forming the corresponding hydroxylamine species in its protonated form (refer to Chapter 2.1.3). Therefore, DOPA-TEMPO (**3**) was exclusively isolated as the corresponding hydroxylamine dihydrochloride salt with excellent water solubility for subsequent aqueous polymerisation.

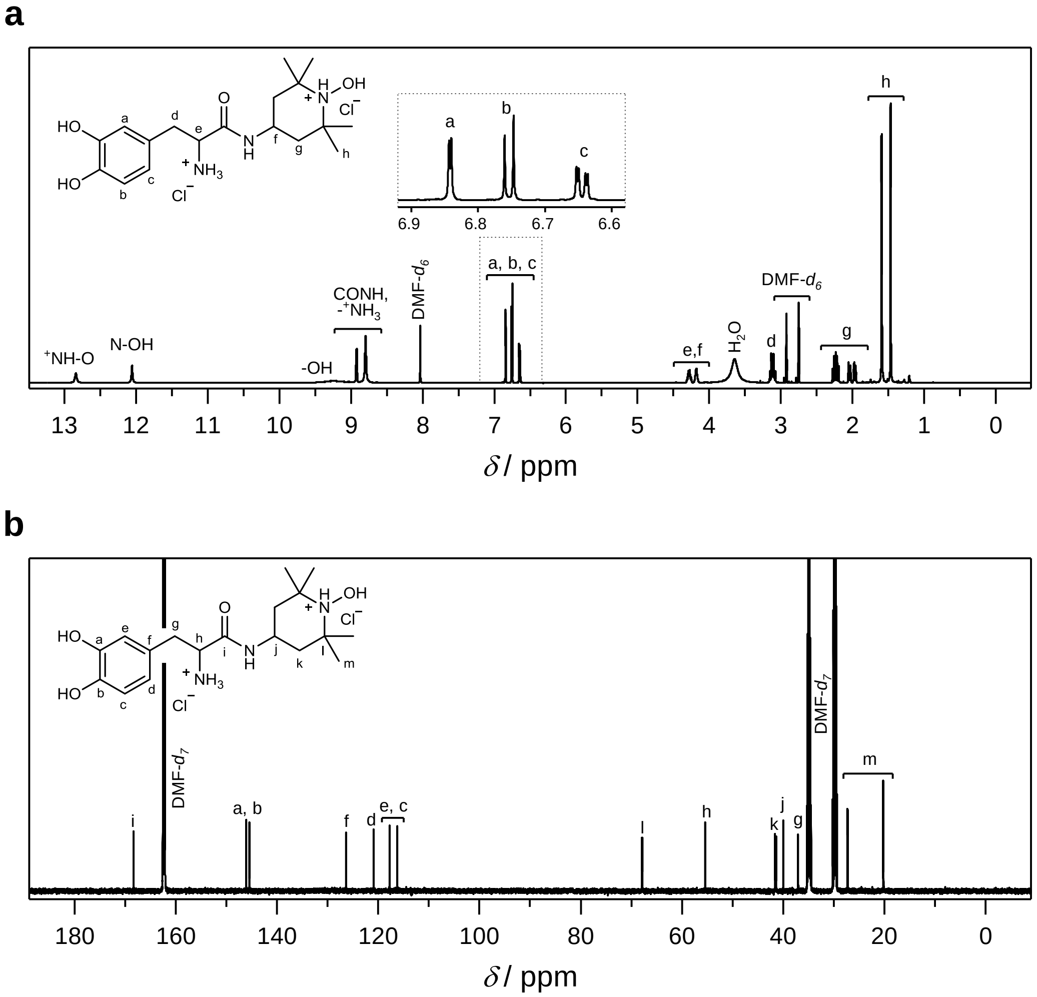

Figure 3.2. NMR spectroscopic characterisation of **3**. (**a**) ^{1}H NMR (600 MHz) and (**b**) ^{13}C NMR spectra (151 MHz) of DOPA-TEMPO (**3**), present as the hydroxylamine dihydrochloride salt, were recorded in DMF-d_7 at 298 K. Adapted with permission from reference [314]. Copyright (2018) American Chemical Society.

The silencing of the nitroxyl radical, temporarily masked as the diamagnetic hydroxylamine species, allowed precise structural characterisation by NMR spectroscopy. The corresponding ^{1}H and ^{13}C NMR spectra of compound **3** were recorded in deuterated DMF (DMF-d_7) for full resolution and clear assignment of all labile proton signals, which typically undergo hydrogen-deuterium solvent exchange reactions during NMR spectroscopic characterisation (**Figure 3.2**). The nitroxide-derived hydroxyammonium functional group of **3** was unambiguously shown by the appearance of highly–deshielded ^{1}H NMR signals at 12.05 and 12.85 ppm, respectively. Furthermore, the ^{1}H NMR signals corresponding to the free catechol and the protonated amino group indicated the successful and complete removal of the protecting groups toward the displayed molecule DOPA-TEMPO (**3**), which is in agreement with the absence of Boc and TBDMS derived NMR signals. The six-membered *N*-heterocyclic core structure of TEMPO was assigned to NMR signals in the lower aliphatic region at 4.28 ppm and between 2.30–1.46 ppm. The DOPA amide structure was evidenced, for instance, by the appearance of ^{1}H NMR signals in the aromatic region with matching proton-proton coupling constants for a trisubstituted aromatic system (see inset in the ^{1}H NMR spectrum in **Figure 3.2a**) and by the carbonyl signal of the amide linkage in the corresponding ^{13}C NMR spectrum at 168.3 ppm. Additional evidence was given by HR-ESI-MS analysis with *m/z*(exp) 352.2232 $[M{-}HCl{-}Cl]^+$ (*m/z*(theo) 352.2231) assigned to the hydrogen chloride uncoordinated protonated species of **3**.

It has been well-reported that nitroxide-derived protonated hydroxylamine species are prone to oxidise under aerobic aqueous conditions forming the corresponding nitroxide species with persistent radical character.[34-36] This oxidation process is accelerated in alkaline environments, which in turn are the employed conditions for the catecholamine polymerisation of **3** (refer to Chapter 3.3). Thus, no synthetic effort was undertaken to unmask the nitroxide radical *via* hydroxylamine oxidation with respect to the adjacent oxidation-sensitive catechol moiety. Instead, the corresponding protonated hydroxylamine species of DOPA-TEMPO (**3**) was employed as a monomer and the oxygen-induced nitroxide radical formation, concurrent with the catecholamine polymerisation, was carefully examined in the following section.

3.3 OXIDATIVE POLYMERISATION OF DOPA-TEMPO

The polymerisation of DOPA-TEMPO (**3**) was performed in an aqueous alkaline buffer system mimicking the natural environment of marine mussels and their evolved DOPA-enriched adhesion system based on mussel foot proteins (refer to Chapter 2.2).[203-204] This well-established polymerisation and coating procedure complies with the increasing awareness of sustainable 'green' chemistry[166, 317] using water as an environmentally friendly, non-hazardous solvent and atmospheric oxygen as a mild, natural oxidising agent. No harmful chemical additives were needed and the polymerisation of **3** was conducted without an elaborate experimental setup. DOPA-TEMPO (**3**) polymerisations were conducted in Tris–HCl buffer (pH 8.5) at ambient temperatures. The reaction conditions were carefully adjusted according to the purpose of the polymerisation. These included variations in the concentration of monomer **3**, the polymerisation reaction times, the pH value of the employed buffer system, as well as the supply of oxygen as a catalyst regulated through the air-liquid interface. **Scheme 3.2** summarises the polymerisation pathway of DOPA-TEMPO (**3**) with proposed key reactive intermediates **3a**–**c** ultimately yielding poly(DOPA-TEMPO) (**4**), which is depicted as a simplified but representative molecule structure. In the following section, the catecholamine polymerisation of **3** involving the above-mentioned intermediate states **3a**–**c** was carefully investigated and correlated to the concurrent nitroxide radical formation derived from oxidation of the protonated hydroxylamine functional group.

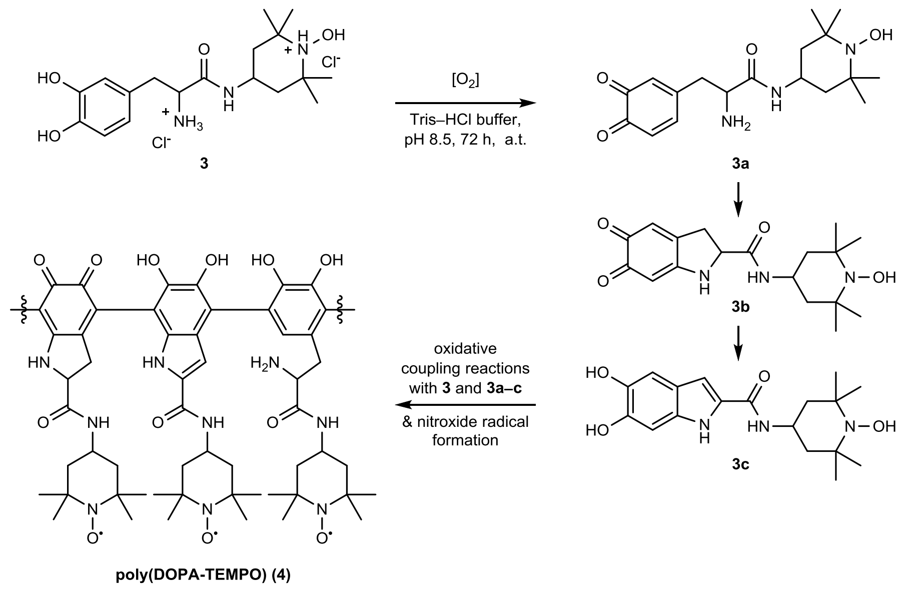
3
[O_2]
Tris–HCl buffer, pH 8.5, 72 h, a.t.
3a
3b
3c
oxidative coupling reactions with 3 and 3a–c
& nitroxide radical formation
poly(DOPA-TEMPO) (4)

Scheme 3.2. Oxidative polymerisation of DOPA-TEMPO (**3**). The reaction was performed under aerobic alkaline conditions using Tris–HCl buffer (pH 8.5) at ambient temperature. Several catecholamine-derived structures (**3a–c**) have been proposed as key intermediate states throughout polymerisation. Adapted with permission from references [314] and [327]. Copyright (2018) American Chemical Society and (2017) The Royal Chemical Society.

Gaining insights into oxidative cross-coupling reactions of catecholamines and other catecholic or polyphenolic systems is challenging due to the complex heterogeneous polymer compositions and restricted structural access routes.[247, 252] Poly(catecholamine)s exhibit inherent limited solubilities in common organic solvents and aqueous systems, with larger cross-linked oligomer aggregates becoming completely insoluble, which dramatically impedes their structural elucidation using solution state characterisation techniques. The main issue, however, is the complex structural composition and the dynamic character of this bioinspired class of polymers including PDA and poly(DOPA) derivatives. For PDA, various incorporated building blocks, different types of intermolecular covalent cross-linkages at different reactive sites, and various supramolecular interactions have been suggested in the literature to contribute to the formation of complex oligomer assembled and macromolecular structures.[247, 251-252, 318] Proposed polymerisation mechanisms and key structural elements of poly(catecholamine) systems have been discussed in detail (refer to Chapter 2.2.3). The presence of persistent unpaired electron spins embedded in the polymer matrix of **4** further impeded structural analysis, *e.g.* by standard NMR spectroscopy. The frequent use of an NMR compatible reducing agent, such as pentafluorophenylhydrazine,[69] in order to silence the paramagnetic property of the nitroxide (converting it into a diamagnetic state) was not advisable for polymer **4** due to the redox-sensitive catechol and *o*-quinoic functional groups along the polymer backbone. EPR spectroscopy was applied to monitor the presence of nitroxide radicals throughout the polymerisation of **4**, however, no precise structural information of the polymer construct could be obtained employing this characterisation technique.

The oxidative polymerisation pathway of DOPA-TEMPO (**3**) was mechanistically studied using a tandem UV–vis and EPR spectroscopic technique. Various key redox states and reactive intermediates during catecholamine polymerisation of **3** were identified and monitored by UV–vis spectroscopy. These findings were then correlated to the nitroxide radical formation (derived from aerobic hydroxylamine oxidation), and the stability of the radical persistent character, when embedded in redox-active macromolecular structures of **4**, was carefully investigated. The polymerisation was performed under dilute conditions in order to suppress polymer precipitation for adequate UV–vis spectrophotometric characterisation and quantification of reactive intermediate states induced by the catecholamine oxidation. In addition, the determination of the nitroxide-derived unpaired electron spins was accessed by solution state EPR spectroscopy. The reaction mixture was vigorously stirred for a homogenous supply of atmospheric oxygen through the air-liquid interface, although the overall access to fresh air was restricted as the reaction was performed in a sealed system in order to suppress unwanted solvent evaporation. The carefully adjusted polymerisation parameters (as described above) significantly decelerated the catecholamine polymerisation, which in turn allowed accurate monitoring and deconvolution of the concurrent oxidation processes: the catechol and the hydroxylamine oxidation. Importantly, the results obtained from each characterisation method (UV–vis and EPR spectroscopy) could be exclusively assigned to one of the two predominant and concurrent oxidation processes. Time-dependent changes of the UV–vis absorption were directly linked to the oxidative catecholamine polymerisation, which allowed tracking of reactive intermediate states (**Figure 3.3a**, solid lines and **Figure 3.3b**). UV–vis spectroscopic control measurements studying the absorption behaviour of 4-hydroxy-TEMPO (TEMPOL) obtained by aerobic oxidation of the corresponding hydroxylamine hydrochloride (employing the same reaction conditions as for **3**) showed a negligible absorption behaviour in the high-energy UV range (**Figure 3.3a**, red and purple dashed lines). EPR spectroscopy, on the other hand, was employed to quantify the TEMPO radical formation resulting from hydroxylamine oxidation, and to investigate the radical stability throughout oxidative polymerisation of **3**. The analogous TEMPOL system served once again as a reference. The inherent radical character of polycatecholic structures (*e.g.*, as reported for PDA)[319] was considered negligible compared to the predominant persistent radical character of the nitroxide moiety.

A gradual change of colour from colourless *via* yellow and orange to brown was observed without any visible polymer aggregation during aqueous aerobic polymerisation of DOPA-TEMPO (**3**). **Figure 3.3a** depicts selected UV–vis absorption spectra during the time-dependent polymerisation study of **3** highlighting important stages of the oxidative catecholamine polymerisation (complementary UV–vis spectra are displayed in **Figure A.2** in the Appendix). The UV–vis absorption of monomer **3** showed a characteristic peak at $\lambda_{max} = 282$ nm (**Figure 3.3a**, red solid line, shortly recorded after dissolving **3** in Tris–HCl buffer), which is unambiguously assigned to the catechol moiety.[272, 320-323] With proceeding polymerisation time, a second peak at longer wavelengths emerged, progressively rising in intensity and reaching a maximum at $\lambda_{max} = 333$ nm after 9 days (yellow line). Simultaneously, the formation of a broad shoulder at $\lambda = 450$ nm was observed. Both distinct absorption patterns indicate the catechol oxidation toward *o*-quinoic structures, which have been identified as reactive key intermediates during catecholamine polymerisation absorbing at longer wavelengths. In dopamine polymerisation, for instance, a similar UV–vis absorption behaviour was observed which has been assigned to dopamine-*o*-quinone and cyclised aminochrome structures. [272, 322-323] Therefore, it is assumed that DOPA-TEMPO (**3**) exhibits similar reactive intermediates when polymerised in aqueous solutions. The corresponding uncyclised (**3a**) and cyclised (**3b**) *o*-quinoic structures are depicted in **Scheme 3.2** as intermediates. Furthermore, and within the same time period, the previously catechol-assigned peak slowly broadened and shifted to shorter wavelengths.

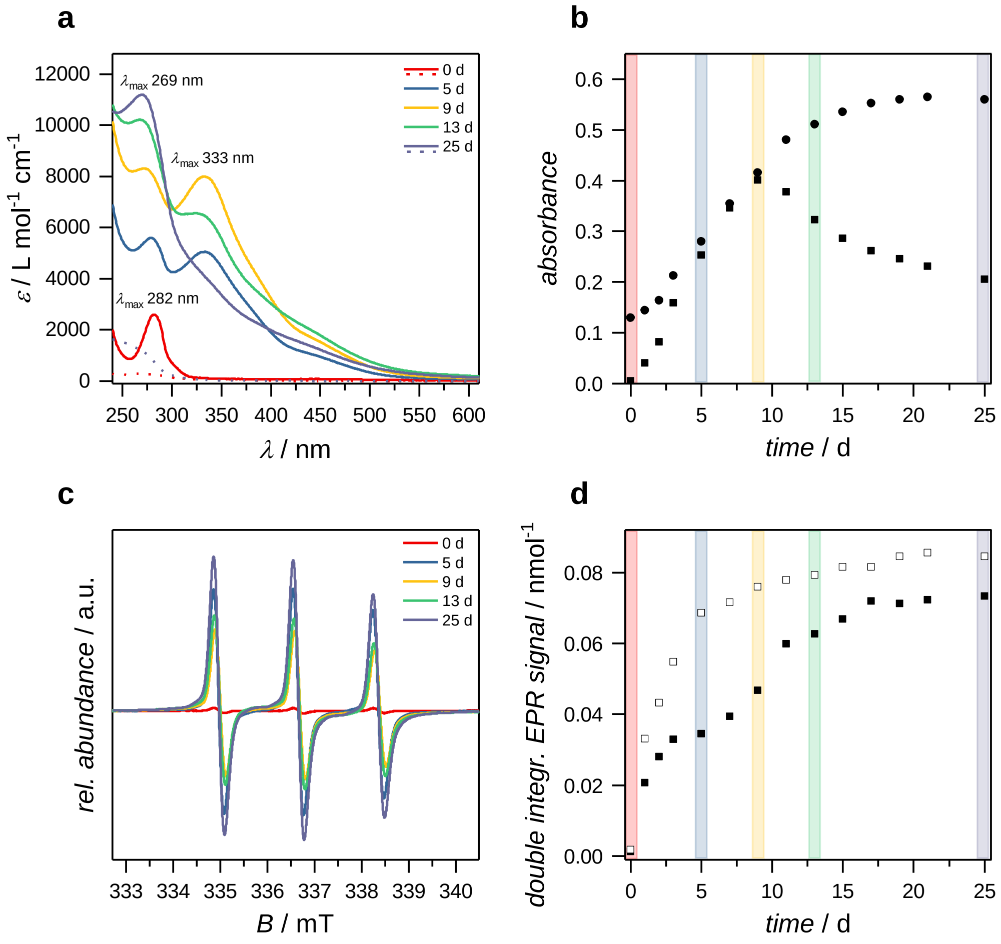

Figure 3.3. UV–vis and EPR spectroscopic monitoring of the oxidative polymerisation of DOPA-TEMPO (**3**) in Tris–HCl buffer (1mM, pH 8.5). (**a**) Selected UV–vis spectra showing the aerobic polymerisation of **3** (solid lines), complemented by reference measurements (dashed lines) with TEMPOL (initially present as the hydroxylamine hydrochloride salt). Aliquots were diluted by factor 20 prior to spectrophotometric analysis. (**b**) Time-dependent absorbances of **3** at $\lambda_{max} = 282 \rightarrow 269$ nm (●) indicating the polymerisation progress and at $\lambda = 333$ nm (■) implying *o*-quinoic reactive intermediates. (**c**) Selected first-derivative EPR spectra monitoring the nitroxide radical formation during aerobic polymerisation of **3**, initially present as a hydroxylamine dihydrochloride species. (**d**) Corresponding time-resolved radical quantification of **3** (■) in comparison to the nitroxide radical formation of the hydroxylamine hydrochloride salt of TEMPOL serving as a reference (☐). EPR quantification was performed by double integration of the EPR signals depicted in (**c**). Adapted with permission from reference [314]. Copyright (2018) American Chemical Society.

The maximum absorption at λ_{max} = 333nm after 9 days appeared to be a critical turning point during polymerisation of **3** as a steady decrease was observed from 9 days onward (green and purple solid lines), ultimately resulting in a broad shoulder after 25 days, which is also reflected in the brown colourisation of the solution. The relatively short lifespan of the distinct but temporary signal at λ_{max} = 333 nm supports the hypothesis that *o*-quinoic structures are exclusively formed as reactive intermediates inducing subsequent intramolecular reaction cascades and intermolecular oxidative cross-coupling reactions toward oligomeric structures. The formation of DHI-like structures (*e.g.*, **3c**), a key element constituting the polymer scaffold of PDA and its derivatives,[203, 247] was not clearly evident during UV–vis spectrophotometric analysis. This is most likely attributed to the broad overlapping absorptions of various incorporated building blocks (please note, the UV–vis absorption of DHI in aqueous solutions has been reported to appear at $\lambda_{max} = 296$ nm).[324] Also, the steady shift of the catechol-assigned peak toward shorter wavelengths ($\lambda_{max} = 269$ nm after 25 days) could not be assigned to another specific structure (*e.g.*, DHI-related motifs) as poly(catecholamine)s are heterogeneously composed dynamic polymer systems with complex and diverse supramolecular interactions constituting the adhesive polymeric matrix.

Figure 3.3b summarises the UV–vis spectroscopic polymerisation study of **3** with additional depicted data points (obtained from **Figure A.2** depicted in the Appendix) for better a time-dependent evaluation and visualisation of the oxidation processes. The overall polymerisation progress is reflected in the steadily increasing absorption maximum in the high-energy UV range, initially at $\lambda_{max} = 282$ nm, reaching a plateau after 17 days accompanied by a continuous shift to $\lambda_{max} = 269$ nm within 25 days ($\lambda_{max} = 282 \text{ nm} \rightarrow 269$ nm, ●). The formation of reactive *o*-quinoic intermediates was monitored at $\lambda = 333$ nm (■) with an absorption maximum after 9 days), which subsequently underwent further reaction cascades, *e.g.* the formation of DHI-like structures and oxidative cross-couplings, resulting in a steady decline of *o*-quinoic species present in the reaction mixture.

Simultaneously, the oxidation of the hydroxylamine hydrochloride functional group of monomer **3**, yielding the corresponding TEMPO free radical, was monitored by EPR spectroscopy. Selected EPR spectra are depicted in **Figure 3.3c** (the same time points have been selected in correspondence to the displayed UV–vis spectra in **Figure 3.3a**) showing the typical hyperfine triplet-like EPR signals derived from the persistent nitroxide radical. Radical quantification during DOPA-TEMPO (**3**) polymerisation (**Figure 3.3d**, ■) was assessed by double integration of the obtained EPR first-derivative signals. The previously introduced reference system monitoring the nitroxide radical formation obtained through oxidation of a TEMPOL derived hydroxylamine hydrochloride species was added to **Figure 3.3d** (labelled as ☐) for comparison. A retarded radical formation of **3** was observed reaching a plateau after 5 days, whereas the catecholamine-lacking reference system was rapidly oxidised to the nitroxide free radical species in the same time period and slowly approached a plateau thereafter. For DOPA-TEMPO (**3**) however, reaching a temporary plateau in the first couple of days of the polymerisation study suggested that the oxidation processes of the catecholamine moiety were predominant at this stage and consequently, the nitroxide radical formation was hampered during polymerisation of **3** (indicated by the rising concentration of *o*-quinoic structures as evident in **Figure 3.3b, ■**). After 5 days, however, the nitroxide radical formation continued, which was expressed in EPR signal broadening (**Figure 3.3c**, blue and yellow line). EPR signal broadening is typically induced by close spatial proximity of nitroxide radicals, a phenomenon typically observed for nitroxide-containing polymers.[325] This implies that DOPA-TEMPO oligomer formation (*e.g.*, dimerisation) was more pronounced at that stage caused by highly reactive *o*-quinoic structures inducing the (rather slow) construction of the polymer scaffold.

After 9 days and at the maximum of oxidised reactive intermediates (*e.g.*, *o*-quinoic species) detected by UV–vis spectroscopy (refer to **Figure 3.3b**), a continuous formation of radicals was observed by EPR spectroscopy reaching a plateau after 17 days, which complies with the plateauing of the catecholamine polymerisation (**Figure 3.3b**, ●). Overall, more than 85% of poly(DOPA-TEMPO) (**4**) radicals were generated from hydroxylamine oxidation, as determined by EPR spectroscopy. The dynamic redox character of the nitroxide moiety and the steady interactions with the surrounding catecholic polymer matrix most likely impeded quantitative conversion toward persistent radicals within polymer **4**. Importantly, the oxidative polymerisation of **3** involving various redox-active intermediates only temporary (and non-destructively) hampered the persistent radical formation toward polymer **4**. It should be noted that the experimental data shown in **Figure 3.3** are representative results and may vary in time and intensity due to the initial concentration of dissolved oxygen, which is a critical parameter initialising the various and simultaneously occurring oxidation processes during polymerisation of **3** (refer to Chapter 9 for detailed information about data acquisition and evaluation). Other influencing factors such as light exposure (*e.g.*, daylight) also contribute in the formation of reactive oxygen species (ROS), which rapidly induce catechol polymerisations (refer to Chapter 5).[263]

The oxidative polymerisation mechanism employing DOPA-TEMPO (**3**) as a monomer has been discussed in detail above, however precise structural assignments obtained from the UV–vis and EPR spectroscopic study were difficult and the conclusions which have been made as a consequence were predominantly correlated to observations made in the literature for analogous polymer systems. Detailed structural insights of polymer **4** still remain elusive, including the confirmation of DHI-like appearances, such as **3c**, as key structural units as well as the overall composition of the isolated polymer scaffold of **4**. In addition, the covalent nature and the overall degree of monomer cross-coupling reactions could not be carefully examined by the above mentioned characterisation techniques. The covalent linkages within poly(DOPA-TEMPO) (**4**) constructs are particularly important to confirm, as the nitroxide radical unambiguously affects the catecholamine polymerisation. For PDA (the referred model system), for istance, it is has been suggested that supramolecular interactions are exclusively the driving forces for the formation of monomer aggregates without any contribution of covalent intermolecular monomer conjugations.[251] In the following section, a mass spectrometric approach is presented for the structural elucidation of poly(DOPA-TEMPO) (**4**) with the main focus on investigating the covalent nature of this tailor-functionalised adhesive polymer system.

3.4 MASS SPECTROMETRIC IDENTIFICATION OF POLY(DOPA-TEMPO) STRUCTURES

HR-ESI-MS has become a powerful tool in polymer science providing structural access of complex macromolecular systems,[84] including the recently detailed HR-MS characterisation of nitroxide-containing polymers,[69, 86] which are known to have limited structural access by standard NMR spectroscopy owing to the unpaired electron spins present in the polymer side chains. A detailed introduction into HR-MS supported polymer characterisations is given in Chapter 4, where a general protocol for the structural elucidation of tailor-made poly(catecholamine)s by HR-ESI-MS has been established analysing a poly(DOPA-TEMPO) analogous system. The main objective of this chapter is to investigate the covalent nature of polymerised DOPA-TEMPO structures and to further elucidate the polymerisation pathways toward poly(DOPA-TEMPO) (**4**) as previously discussed in Chapter 3.3.

The polymerisation of monomer **3** for subsequent ESI-MS polymer characterisation was performed under accelerated reaction conditions employing a 10 mM reaction mixture of **3**, vigorously stirred in an open glass vial for continuous supply of oxygen through the air-liquid interface. A rapid colourisation from yellow to dark brown was observed within the first hours of polymerisation, followed by the formation of brown precipitate when left stirring overnight. The reaction time was prolonged to 72 h for higher yields. The precipitated polymer particles were thoroughly washed with deionised water to remove small monomeric building blocks as well as Tris–HCl salts for enhanced polymer ionisation during ESI. The structural examination of poly(DOPA-TEMPO) (**4**) was carried out using an Orbitrap spectrometer equipped with an electrospray ion source. The in-source collision-induced dissociation (CID) fragmentation technique was applied using a collision energy of 70 eV.

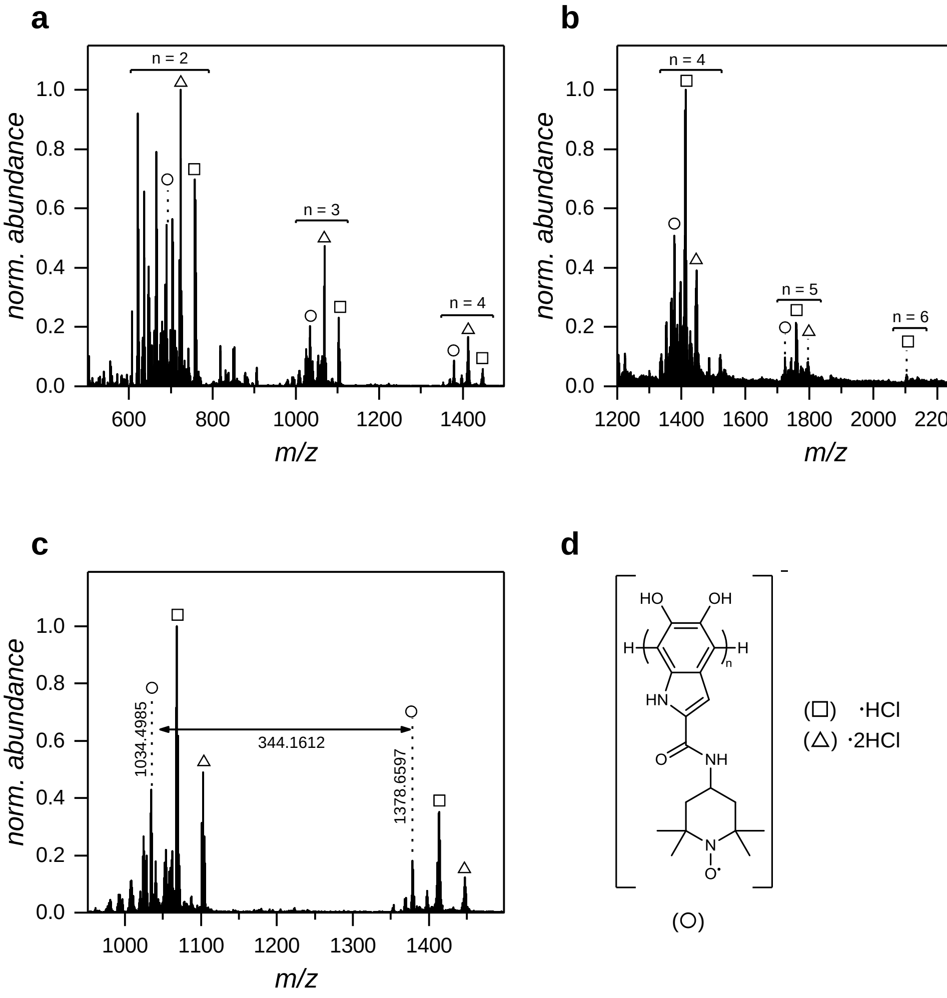

Figure 3.4. (−)ESI-CID (70 eV) mass spectra of poly(DOPA-TEMPO) (**4**). (**a**–**b**) Overview spectra recorded in THF/MeOH 3:2 (*v*/*v*) doped with 100 µM NaI. Single-charged oligomer structures composed of n = 2–6 repeating units were detected as molecular ions or deprotonated hydroxylamine species (labelled as ○), monohydrochloride adducts (□), or dihydrochloride adducts (△). (**c**) Expanded region exemplarily showing the trimer and tetramer profiles of **4**. (**d**) Proposed structure of homotrimer (*m/z*(theo) 1034.4982) and homotetramer (*m/z*(theo) 1378.6592) with n = 3–4 composed of covalently linked DHI units along the polymer backbone and free radical TEMPO moieties in the polymer side chains. Adapted with permission from reference [314]. Copyright (2018) American Chemical Society.

Oligomers with up to six repeating units were identified as single-charged species employing the negative ion mode (**Figure 3.4a**–**b**). The most abundant peaks within each oligomer profile correspond to either uncoordinated ionised species (○), monohydrochloride (△), or dihydrochloride adducts (□). An expanded MS region depicted in **Figure 3.4c** shows the trimer and tetramer profiles of polymer **4**. Structural elucidation revealed that the oligomer structures were predominantly composed of cyclised, indole-like units along the polymer backbone. This observation is supported by structural assignments of the most abundant molecular ions (○) within the trimer and tetramer regions. A homotrimer and homotetramer composed of covalently linked dihydroxyindole units along the polymer backbone and free radical TEMPO moieties in the side chains (**Figure 3.4d**) are proposed poly(DOPA-TEMPO) (**4**) oligomers, which are in perfect agreement with the corresponding high-resolution △*m/z*(exp−theo) values with *m/z*(exp) 1034.4985 for the homotrimer (*m/z*(theo) 1034.4982) and *m/z*(exp) 1378.6597 for the homotetramer (m/z(theo) 1378.6592), respectively. These findings support the identification of DHI structural motifs as key elements constituting the polymer backbone of **4,** which has already been proposed for other poly(catecholamine) systems such as PDA as well as naturally occurring melanins.[203, 247] Structural examination of the hydrochloride coordinated ions (☐ and △) further indicated the presence of *o*-quinoic structural appearances of cyclised DOPA-derived building blocks with predominant peaks at lower *m/z* values within the profile patterns. The incorporation of higher molecular weight building blocks, such as the open-chain DOPA units, could not be clearly identified within the oligomer patterns. The assignment of the most abundant peaks of the tetramer profile is listed in **Table A.1** in the Appendix.

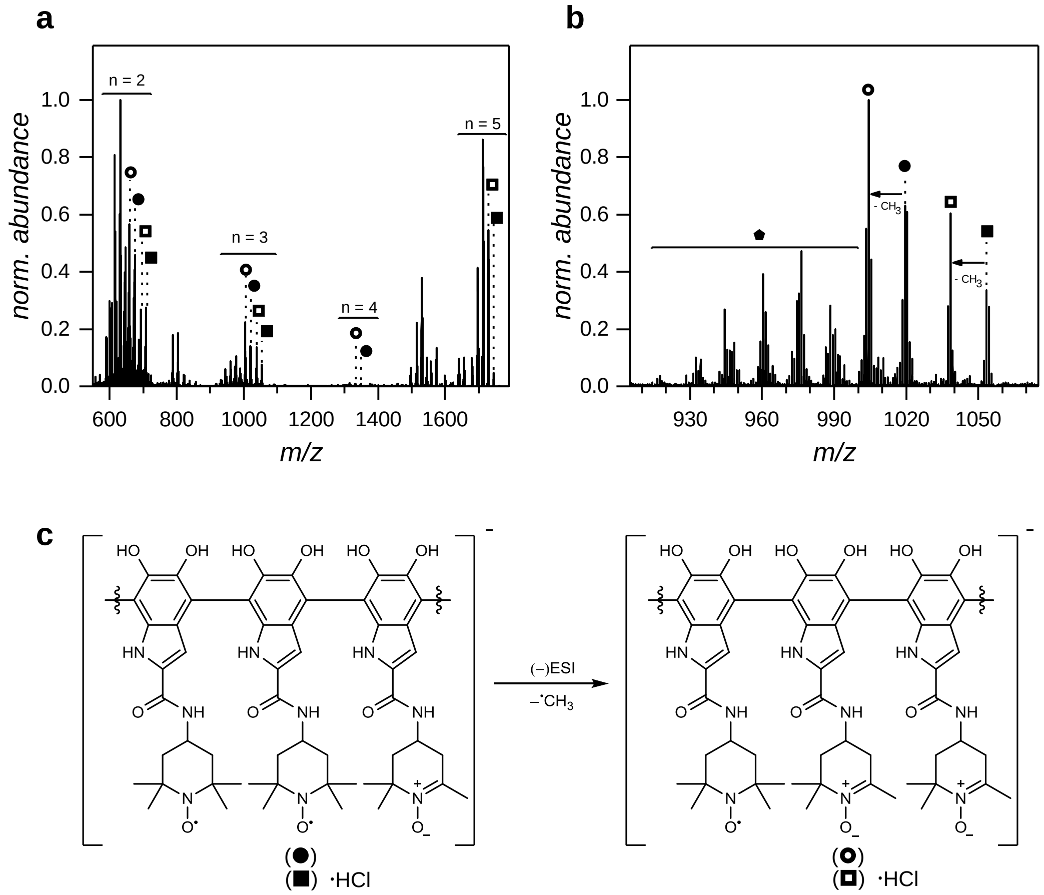

Figure 3.5. (−)ESI-CID (70 eV) HCD (35 eV) MS/MS characterisation of a pentamer hydrochloride adduct of **4** apparent at *m/z* 1757. (**a**) Overview spectrum recorded in THF/MeOH 3:2 (*v*/*v*) doped with 100 µM NaI and (**b**) expanded trimer fragmentation region. Uncoordinated fragments are labelled as ● and ○, hydrochloride adducts are labelled as ■ and □. Filled and unfilled symbols present typical (−)ESI-induced fragmentation pattern with multiple ejections of TEMPO-derived methyl radicals. Further fragmentations are summarised as ⬢ and correspond to repetitive losses of CH_x and/or OH fragments. (**c**) Proposed DHI-timer of **4** with suggested nitrone formation during (−)ESI. Adapted with permission from reference [314]. Copyright (2018) American Chemical Society.

ESI tandem mass spectrometry (MS/MS) supported the identification of poly(DOPA-TEMPO) (**4**) oligomeric scaffolds (**Figure 3.5**). A distinct fragmentation pattern of a pentameric hydrochloride adduct appearing at *m/z* 1757 (the most abundant of the pentamer profile, refer to **Figure 3.4b**) into mainly dimer and trimer daughter ions was observed. Within these fragmentation profiles, multiple losses of methyl radicals assigned to the nitroxyl-adjacent methyl groups most likely resulted in the formation of nitrone species during (−)ESI.[83] A proposed fragmentation pathway considering the most abundant peaks of the trimer profile is displayed in **Figure 3.5c**. The structural assignment is in agreement with the existence of a homotrimer composed of covalently linked DHI-like units along the polymer backbone, which further underpins the importance of DHI derivatives as key structural elements in catecholamine polymerisations. Corresponding MS peak assignments are exemplary reported for the most abundant trimer fragments in **Table A.2** in the Appendix.

To conclude Chapter 3.4, structural access for the precise characterisation of poly(DOPA-TEMPO) (**4**) was inherently restricted by common characterisation techniques owing to the complex polymer composition, the limited polymer solubilities in common organic and aqueous solvents, and the presence of unpaired (redox-sensitive) electrons located in the polymer side chains. High-resolution mass spectrometry, however, offered structural insights into the overall appearance of polymer **4** composed of covalently linked various DOPA-TEMPO building blocks. The broad structural variety of incorporated DOPA-derived building blocks combined the various detected HCl adducts and different appearances of the nitroxide moiety strongly hampered precise structural assignment of the overlapping peaks within each oligomer profile. The nitroxide functional group, for instance, can be existent as the hydroxylamine species (refer to monomer **3**) paired with various redox states, which can also be attributed to MS artefacts during (−)ESI. Thus, structural variations of the incorporated building blocks could not clearly be assigned and deconvoluted into individual DOPA appearances in the polymer backbone and different TEMPO species located in the polymer side chain. The covalent nature, however, was clearly evidenced by HR-ESI-MS with detected oligomer species up to hexamers.

3.5 CONCLUSION

In summary, a new and sophisticated methodology for the generation of nitroxide-containing polymeric scaffolds has been introduced using a polymerisable catecholamine, which has been equipped with an additional nitroxide functional group. Monomer **3**, denoted as DOPA-TEMPO was carefully characterised and subsequently polymerised in an aqueous aerobic buffer system yielding poly(DOPA-TEMPO) (**4**). Various key reactive intermediates during oxidative polymerisation of **3** were confirmed by UV–vis spectroscopy, and the persistent radical character of the evolving macromolecular scaffolds of **4** was analysed by EPR spectroscopy. Structural access given by HR-ESI-MS confirmed the formation of oligomer fragments composed of covalently linked, structurally diverse building blocks. The herein presented synthetic pathway — from the preparation of a suitable monomer to the generation of polymeric nitroxide functional scaffolds — combined with fundamental mechanistic and structural insights are important milestones for the following chapters. In Chapter 4, a HR-ESI-MS platform for the structural analysis of polymerised catecholamines is introduced employing a poly(DOPA-TEMPO) (**4**) analogous system. Furthermore, the newly introduced monomer **3** is exploited as a versatile coating agent for nitroxide surface functionalisations, which is presented in Chapter 5.

Chapter 4: Structural Elucidation of Poly(catecholamine)s by HR-MS

4.1 PREFACE

Bioinspired poly(catecholamine)s have become a widely-employed and versatile coating platform for precise polymer surface functionalisations. Among other catechol-containing and polyphenolic substances, catecholamines often serve as coating agents for polymer coatings across all fields in science, technology and engineering. The resulting polycatecholic matrices with structural similarities to eumelanins, an important class of natural pigments, are extremely challenging to characterise, and only limited structural access routes are available. Mechanistic insights into the oxidative polymerisation mechanisms, the structural elucidation of the generated polymer system, and structural correlations to the inherent and unique adhesive properties have been under continuous scientific discussion since the pioneering introduction of dopamine as a universal coating agent in 2007.[203] Mass spectrometric analyses of polycatecholic systems and related polymerised scaffolds have significantly contributed to structural insights into this class of (bioinspired) adhesive polymers.[248, 252, 318, 326] However, only limited knowledge has been gained regarding tailor-made functional catecholamines and their ability to polymerise under aerobic aqueous conditions yielding adhesive covalent polymer networks.[277]

In the current chapter, an avenue for the structural elucidation of functional poly(catecholamine) scaffolds by HR-ESI-MS is presented. A DOPA-based catecholamine monomer equipped with a TEMPO derived methoxyamine group, denoted as DOPA-TEMPO-CH_3, was synthesised and subsequently polymerised under aerobic aqueous conditions in analogy to previously established synthetic protocols presented in Chapter 3. The polymer composition of poly(DOPA-TEMPO-CH_3) was carefully investigated using HR-ESI-MS as a powerful characterisation platform combined with advanced MS techniques such as CID,

---

Parts of the current chapter are adapted or reproduced from reference [327]: H. Woehlk, J. Steinkoenig, C. Lang, A. S. Goldmann, L. Barner, J. P. Blinco, K. E. Fairfull-Smith and C. Barner-Kowollik, *Polym. Chem.*, **2017**, 8, 3050-3055 with permission from The Royal Chemical Society. Mass spectrometric data acquisition presented in chapter 4.2 was conducted by J. Steinkoenig (KIT).

MS/MS, and isotopic pattern simulations. A general protocol for the MS characterisation of poly(catecholamine)s has been established where structural access is typically limited using standard characterisation techniques (*e.g.*, NMR spectroscopy or SEC). The formation of covalent oligomeric structures was readily confirmed by MS. More importantly, the polymer composition was precisely examined with detailed peak assignments within the broad oligomer profile patterns to distinct structural motifs. Multiple diverse building blocks were identified as key structural units constituting the polymer backbone, yet strongly varying in their relative abundance of the isolated polymer scaffolds.[327]

4.2 SYNTHESIS AND POLYMERISATION OF DOPA-TEMPO-CH$_3$

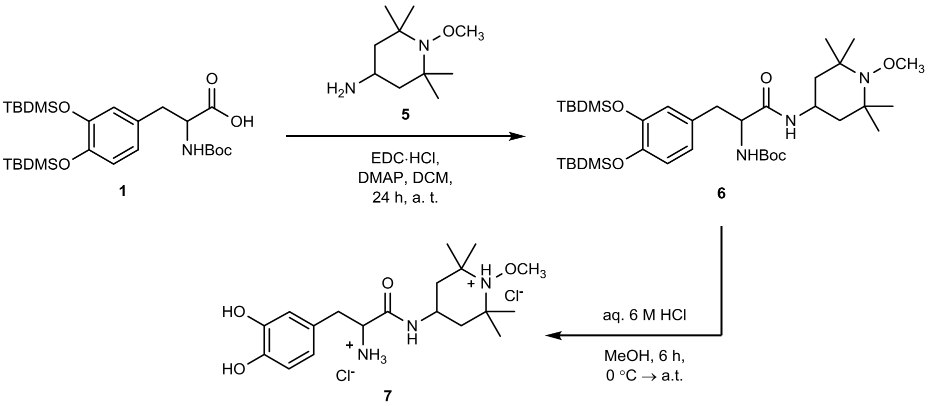

Scheme 4.1. Synthetic pathway for the generation of DOPA-TEMPO-CH$_3$ (**7**), isolated as the corresponding dihydrochloride salt. Adapted with permission from reference [327]. Copyright (2017) The Royal Chemical Society.

The preparation of DOPA-TEMPO-CH$_3$ (**7**) was conducted following the same synthetic pathway as described earlier for preparation of DOPA-TEMPO (**3**) using catechol- and amino-protected DOPA (**1**) as a catecholamine precursor and 1-methoxy-2,2,6,6-tetramethylpiperidin-4-amine (**5**) for conjugation with **1** (**Scheme 4.1**). Compound **5** was prepared following a well-established synthetic protocol using Fenton chemistry for the conversion of 4-amino-TEMPO to the corresponding methoxyamine.[50] The corresponding ^{1}H and ^{13}C NMR spectra for structural elucidation of **5** are depicted in **Figures B.1** and **B.2** in the Appendix. Successful preparation of **5** was further supported by HR-ESI-MS with *m/z*(exp) 187.1808

$[M+H]^+$ (*m/z*(theo) 187.1805). The covalent conjugation of **1** and **5** was achieved in an EDC-mediated amide coupling reaction. Intermediate **6**, denoted as (TBDMS)$_2$-*N*-Boc-DOPA-TEMPO-CH_3, was isolated in high yield (83%) after a column chromatographic purification step. Subsequent cleavage of the protecting groups under methanolic acidic conditions was achieved in quantitative yield and DOPA-TEMPO-CH_3 (**7**) was isolated as the corresponding dihydrochloride salt.

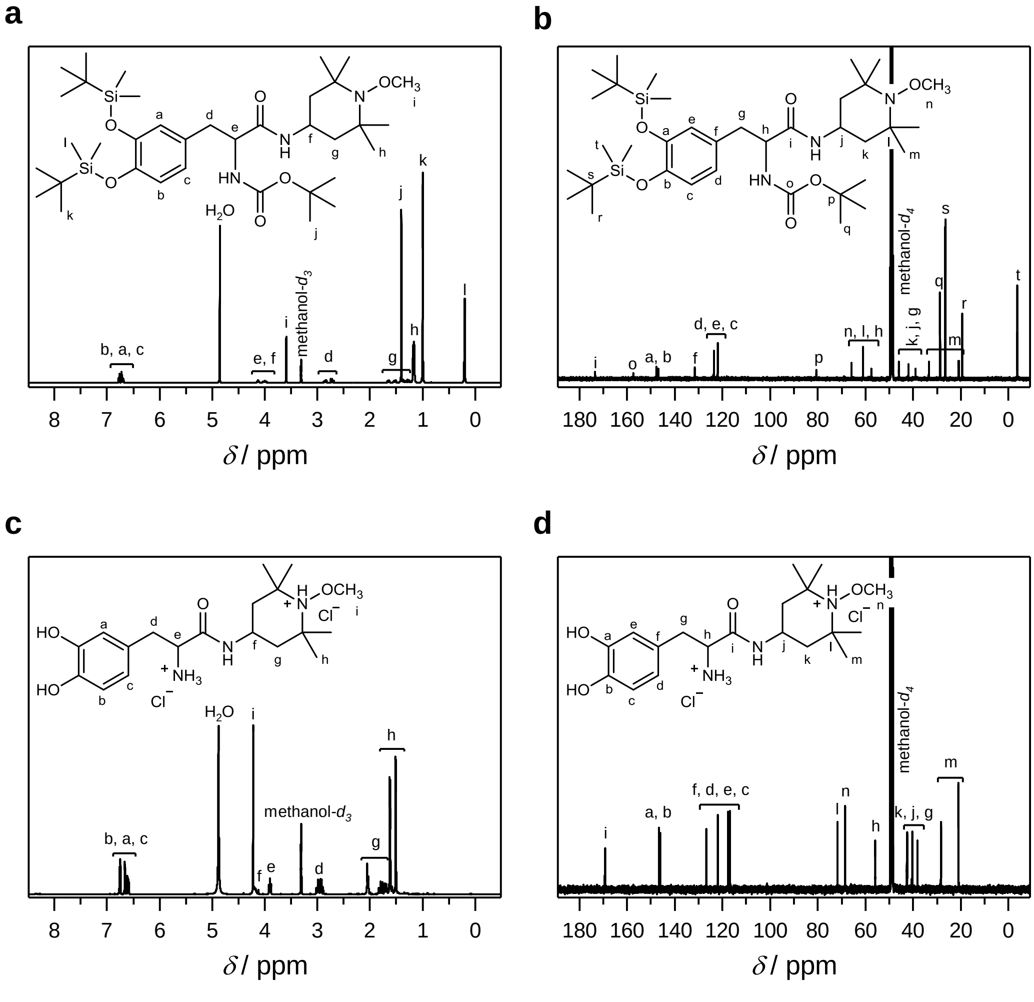

Figure 4.1. NMR spectroscopic characterisation of **6** and **7**. (**a**) ^1H NMR (400 MHz) and (**b**) ^{13}C NMR spectra (101 MHz) of (TBDMS)$_2$-*N*-Boc-DOPA-TEMPO-CH_3 (**6**). (**c**) ^1H NMR (400 MHz) and (**d**) ^{13}C NMR spectra (101 MHz) of DOPA-TEMPO-CH_3 (7), present as the dihydrochloride salt. All spectra were recorded in methanol-*d*$_4$ at 298 K. Adapted with permission from reference [327]. Copyright (2017) The Royal Chemical Society.

The corresponding NMR spectra of intermediate **6** and final monomer **7** are depicted in **Figure 4.1**. As the nitroxide radical moiety has been converted to the corresponding methoxyamine functional group, all NMR spectra of **6** and **7** show well-resolved NMR signals. The introduction of the methoxyamine group to the DOPA scaffold of **6** was evidenced by the appearance of a ^{1}H NMR singlet resonance appearing at 3.59 ppm (**Figure 4.1a**). A clear shift of the $-OCH_3$-assigned resonance toward 4.22 ppm was observed for compound **7** indicating the conversion to the protonated methoxyamine species due to the acidic (HCl) treatment. The presence of the protonated methoxyamine group is further evidenced in the corresponding ^{13}C NMR spectra (**Figure 4.1b** and **d**). A slight chemical shift of the $-OCH_3$ group of compound **6** toward **7** from 65.88 to 68.52 ppm was observed, which was further supported by a clear shift of the adjacent quaternary carbon atoms from 60.99 to 71.74 ppm and 71.85 ppm, respectively. In summary, NMR characterisation confirmed the fully intact molecule structures of **6** and **7**. HR-ESI-MS completed the small molecule structural analyses with *m/z*(exp) 694.4648 $[M+H]^+$ (*m/z*(theo) 694.4641) for compound **6** and *m/z*(exp) 366.2389 $[M-HCl-Cl]^+$ (*m/z*(theo) 366.2387) for compound **7**, respectively.

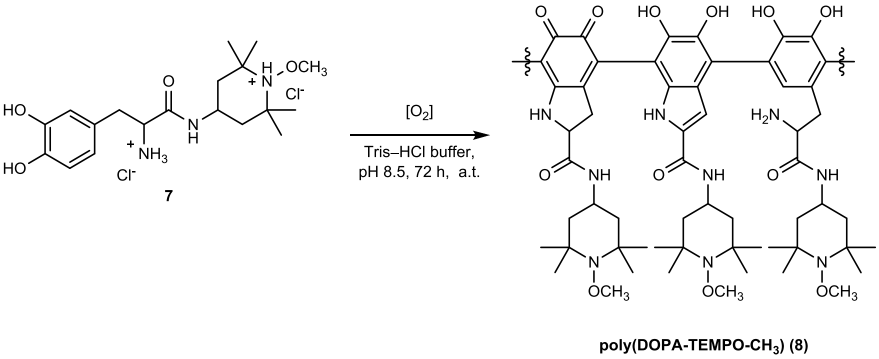

Scheme 4.2. Oxidative polymerisation of DOPA-TEMPO-CH_3 (**7**). The reaction was performed under aerobic alkaline conditions using Tris–HCl buffer (pH 8.5) at ambient temperature. Adapted with permission from reference [327]. Copyright (2017) The Royal Chemical Society.

The oxidative polymerisation of DOPA-TEMPO-CH_3 (**7**) was performed under aqueous aerobic conditions using an alkaline Tris–HCl buffer system initially adjusted to pH 8.5. In contrast to DOPA-TEMPO (**3**) polymerisation presented in Chapter 3, the buffer solution was readjusted and maintained at pH 8.25 within the first 30 minutes of polymerisation. Rapid dark discolourisation and polymer aggregation was observed in the initial phase of polymerisation, and the precipitated polymer particles were isolated after 72 h, followed by a thorough washing procedure to remove the Tris buffer agent, which can cause strong ion suppression during ESI-MS characterisation,[328] and to remove loosely conjugated small oligomers. Polymer **7** exhibited good solubilities in aqueous and organic solvent mixtures, which allowed structural characterisation by NMR spectroscopy and MS. The corresponding ^{1}H and ^{13}C NMR spectra of poly(DOPA-TEMPO-CH_3) (**8**) showed polymer-characteristic broad aromatic and aliphatic resonances, which could be assigned to the polymer scaffold of **8** (refer to **Figures B.3** and **B.4** in the Appendix). Precise structural elucidation, however, was strongly limited using NMR spectroscopy as a characterisation technique. The identification of key structural elements constituting the polymer backbone with various incorporated DOPA-derived building blocks was not feasible due to the broad and overlapping NMR resonances. The tested good solubilities of polymer **8**, however, implies a different polymer composition compared to unfunctionalised PDA structures and their inherent insolubilities in common organic and aqueous solvents. This observation made for polymer **8** is also valid for the nitroxide analogous polymer system **4** and might be attributed to the additional bulky piperidine-based side chain, which is amide-linked to the polymerisable DOPA functional group. It is assumed that this impedes not only monomer cross-linking reactions as one reactive site is already occupied by the additional amide-linked functional group, yet also influences intermolecular interactions and oligomer aggregation based on various supramolecular forces.[251] For structural analysis, however, this issue has been proven to be beneficial for the targeted in-depth HR-ESI-MS characterisation of polymer **8**.

4.3 IN-DEPTH CHARACTERISATION OF POLY(DOPA-TEMPO-CH_3) KEY STRUCTURAL ELEMENTS

The polymer composition of poly(DOPA-TEMPO-CH_3) (**8**) was analysed using a high-resolution ESI-Orbitrap mass spectrometer. A variety of single charged oligomers with overlapping isotopic patterns was detected employing the in-source CID fragmentation technique for sensitivity enhancement and a CID energy of 80 eV. Oligomers with up to seven repeating units were identified, which have been ionised by deprotonation events employing the negative ion mode (**Figure 4.2a** and **b**). Fragmentations within these oligomer patterns were less pronounced compared to previously characterised poly(DOPA-TEMPO) (**4**), and structural assignments suggest the liberation of –OH, –CH_3, –OCH_3 as well as portions of the DOPA phenyl ring.[203] This typical fragmentation pattern is depicted in **Figure 4.2c** for the tetramer region. The focus of the shortly presented in-depth MS structural elucidation of **8** has been set to the deprotonated species denoted as $[M_n-H]^-$, which display the most abundant peaks within each oligomer profile. In positive ion mode, oligomers with up to eight repeating units were identified, predominantly ionised by H^+ with minor species ionised by Na^+ or present as HCl or NaCl adducts (refer to **Figure 4.3**). HCl and NaCl adduct formation was more pronounced for oligomer structures with higher molecular weights, *e.g.* as displayed in **Figure 4.3c** and the appearance of $[M_8+H+NaCl]^+$ species as the most abundant peaks. Detailed structural evaluation of (+)-ionised heptamers and octamers (depicted in **Figure 4.3b** and **c**) is discussed at the end of this subchapter as the MS characterisation is performed with increasing molecular weights starting with poly(DOPA-TEMPO-CH_3) (**8**) dimers. Noteworthy, the covalent incorporation of Tris, initially employed as a buffer agent, was not observed in this MS study, which has been reported for Tris buffered dopamine polymerisations.[319, 329] All corresponding peak assignments are listed in **Tables B.1.–B.3** in the Appendix.

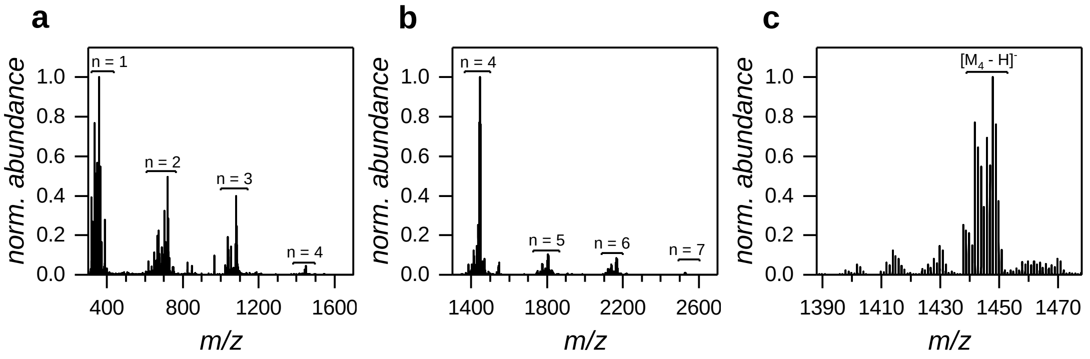

Figure 4.2. (−)ESI-CID (80 eV) mass spectra of poly(DOPA-TEMPO-CH_3) (**8**). Overview spectra depicted in (**a**) and (**b**) were recorded in H_2O/acetonitrile 1:1 (*v*/*v*) doped with 0.1% (*v*/*v*) acetic acid. A selected expanded oligomer region is depicted in (**c**) showing the single-charged tetramer profile. Characteristic patterns at lower *m/z* derived from $[M_4{-}H]^-$ tetramer fragmentations suggesting liberations of –OH, –CH_3, –OCH_3 and portions of the phenyl ring. Adapted with permission from reference [327]. Copyright (2017) The Royal Chemical Society.

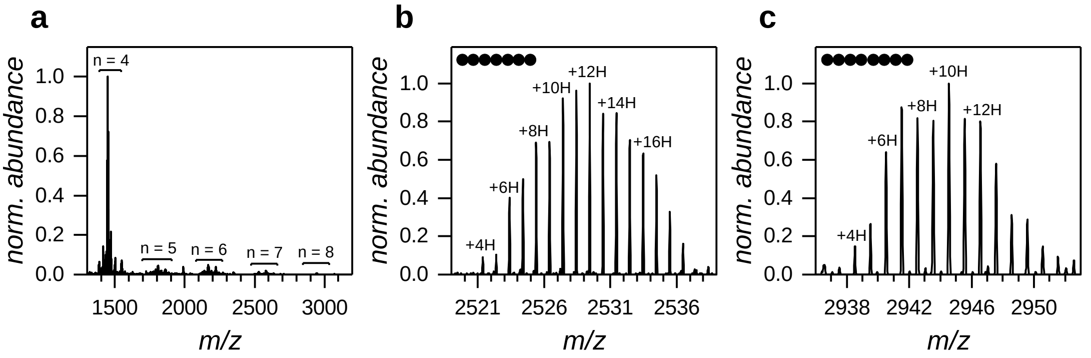

Figure 4.3. (+)ESI-CID (80 eV) mass spectra of poly(DOPA-TEMPO-CH_3) (**8**). Overview spectrum depicted in (**a**) was recorded in H_2O/acetonitrile 1:1 (*v*/*v*) doped with 0.1% (*v*/*v*) acetic acid. (**b**–**c**) Zoomed spectra showing the $[M_7{+}H]^+$ heptamer profile and the $[M_8{+}H{+}NaCl]^+$ octamer profile. Peak assignments in (**b**) and (**c**) labelled with (± *x*H) refer to the corresponding DHI homooligomers. Adapted with permission from reference [327]. Copyright (2017) The Royal Chemical Society.

The presence of TEMPO-derived methoxyamine groups in the polymer side chain of poly(DOPA-TEMPO-CH_3) (**8**), in exchange for nitroxide free radicals existing in the poly(DOPA-TEMPO) (**4**) analogous system, yielded unprecedented insights into the polymer backbone structures of tailor-functionalised poly(DOPA) derivatives. In a nutshell, in-depth HR-ESI-MS characterisation of the previously characterised polymer **4** was hampered, for instance, due to various appearances of the nitroxide functional group (*e.g.*, the free nitroxyl radical species and the hydroxylamine derivative), nitroxide-related one-electron redox processes during ESI, and various interfering, often overlapping ionised species and adducts (*e.g.*, predominant mono- and dihydrochloride adducts). In MS/MS, an inherent lability of nitroxyl adjacent methyl groups of polymer **4** was observed resulting in multiple liberations of methyl radicals. These events could be significantly reduced or excluded using the methoxyamine derivative of TEMPO (amide-linked to the poly(DOPA) backbone of (**8**) during HR-ESI-MS. The methoxyamine functional groups in the polymer side chains remained stable during ESI, and the most abundant regions within the oligomer profiles were unambiguously assigned to (−)ESI deprotonated, or (+)ESI protonated species with only minor overlapping peaks of other ionised species. However, broad profiles of the similarly ionised species suggested overlapping isotopic patterns of various polymeric structures composed of differently incorporated building blocks, which are further investigated in detail.

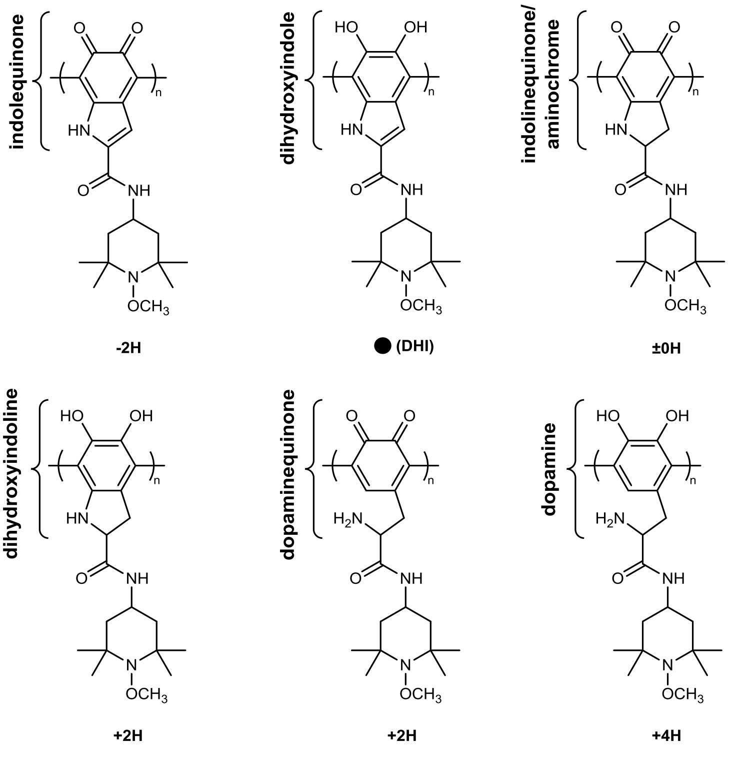

Figure 4.4. Proposed structures of poly(DOPA-TEMPO-CH_3) (**8**) incorporated building blocks. The building block composed of a DHI element constituting the polymer backbone was designated as a key structural unit (labelled with ●). Other structures refer to the DHI building block and are labelled with ± *x*H (*x* = even number of additional hydrogen atoms). Adapted with permission from reference [327]. Copyright (2017) The Royal Chemical Society.

The in-depth structural elucidation of polymer **8** composed of various oligomer species with broad isotopic patterns was conducted under several assumptions due to the complexity of this polymer system. First, each single MS oligomer peak represents numerous isomeric (and thus isobaric) species consisting of randomly linked diverse building blocks, unknown in its sequence. The building block composed of a DHI moiety constituting the polymer backbone was designated as a key structural unit (labelled with ●) and served as a reference for other identified incorporated species (labelled with $\pm x$H; x representing an even number of additional hydrogen atoms). DHI has been known as a key structural unit in PDA systems as well as in eumelanin analogous structures.[203, 247, 252] Other potential structures may differ in their redox state (*e.g.*, catecholic or *o*-quinoic structures), the constitution of the cyclic skeleton (*e.g.*, non- or partially conjugated indoline systems) as wells as the covalent incorporation of open-chain dopamine structures. Proposed structures with the above mentioned key structural deviations are depicted in **Figure 4.4**. All structural variations refer to DHI and are indicated by their deviation in the (even) number of hydrogen atoms. The illustrated structures of poly(DOPA-TEMPO-CH_3) (**8**) are only displayed connected through 4,7'-positions although other constitutional isomers (isobars) of DHI oligomers and their derivatives may be favoured.[258, 330-331] Other intermolecular cross-linking points (*e.g.*, position 3 of DHI) or other types of covalent linkages,[252] which result in the formation of oligomeric structures and networks, are not considered in the present study. Ultimately, poly(catecholamine)s are highly dynamic polymer systems and sensitive to atmospheric oxygen, which can result in various reaction cascades along the polymer scaffold including redox reaction, rearrangement reactions, tautomerisms and other appearances. The displayed polymer structure of poly(DOPA-TEMPO-CH_3) (**8**) (*e.g.*, depicted in **Scheme 4.2**) serves as a representative illustration of the polymer composition, which structural evidence was strongly supported by the results obtained in the currently presented ESI-MS study, and further complies with the previously identified key intermediate structures during DOPA-TEMPO (**3**) polymerisation presented in Chapter 3. This concept and the above mentioned assumptions were applied to all displayed poly(catecholamine) scaffolds in the current thesis. The structural appearances can be summarised as cyclic DHI structures, incorporated open-chain DOPA building blocks as well as *o*-quinoic appearances, such as aminochrome (also denoted as indolinequinone) building blocks, all equipped with TEMPO-CH_3 side chains for polymer **8** or TEMPO functional groups for polymer **4**, respectively.

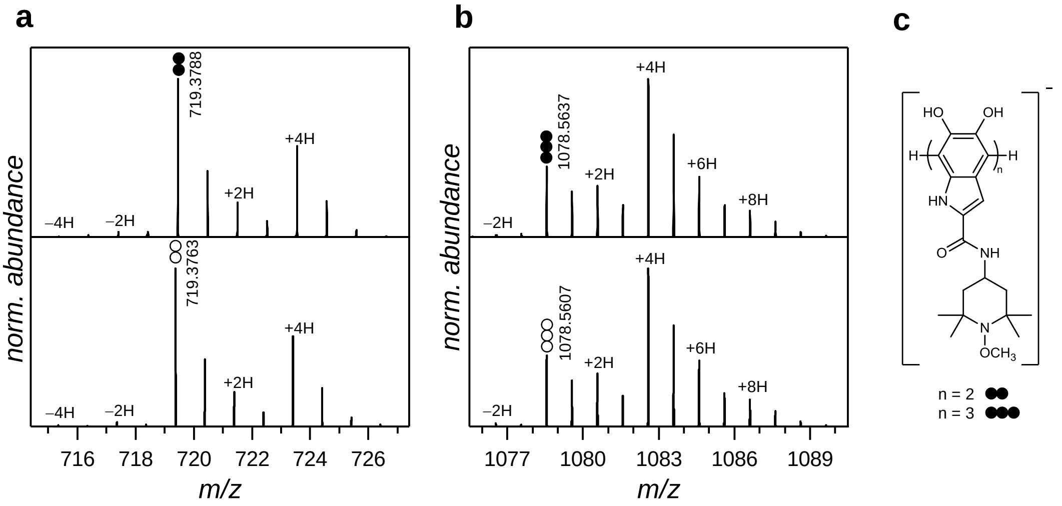

Figure 4.5. (−)ESI-CID expanded mass spectra of poly(DOPA-TEMPO-CH_3) (**8**) dimers and trimers. Comparison of experimentally obtained spectra (top) with simulated isotopic patterns (bottom) of (**a**) $[M_2{-}H]^-$ dimer region and (**b**) $[M_3{-}H]^-$ trimer region. (**c**) Proposed structures with DHI as the polymer backbone repeating unit (labelled as ●) identified as the corresponding homodimer in (**a**) and homotrimer in (**b**). Unfilled circles (○) represent simulated molecular ion peaks of the DHI homooligomers. Other peak assignments labelled with ± *x*H refer to the DHI homooligomers. Adapted with permission from reference [327]. Copyright (2017) The Royal Chemical Society.

Multiple dimers with different molecular compositions were identified as deprotonated species $[M_2{-}H]^-$ in the range of *m/z* 715–727 (**Figure 4.5a**, top panel, and **Table 4.1**), and the existence of five distinct dimer combinations (at different *m/z* values) was supported by isotopic pattern simulations (bottom panel). Following the above mentioned analytical concept, the most abundant peak of this region at *m/z*(exp) 719.3788 (*m/z*(theo) 719.3763) was assigned to a homodimer composed of two covalently linked DHI building blocks forming the polymer backbone of **8**. The corresponding structure is displayed in **Figure 4.5c**. At lower *m/z* values, dimers with −2H and −4H were detected, however as less abundant species. These signals confirm the existence of incorporated oxidised species such as indolequinones in polymer **8**. Similar observations were made for poly(DOPA-TEMPO) (**4**), where *o*-quinoic structures appeared to be more pronounced during ESI-MS analysis. At higher *m/z* values, dimers with +2H and +4H were identified, which can be associated with species consisting of isoindoline units as well as open-chain dopamine units, either present as catechols or *o*-quinones (refer to **Figure 4.4**) The +2H species only played a minor role within the overall appearance of the dimer profile featuring significant overlap with the isotopic pattern of the previously designated homodimer present as the most abundant peak. However, isotopic pattern simulations unambiguously confirmed the presence of a dimer species with +2H (refer to **Figure B.5** in the Appendix).

Table 4.1. (−)ESI-CID MS peak assignments of $[M_2{-}H]^-$ dimers of poly(DOPA-TEMPO-CH_3) (**8**). The *m/z*(theo) values were obtained from isotopic pattern simulations of each individual profile pattern. The displayed relative ratios were employed for constructing the simulated spectra. Adapted with permission from reference [327]. Copyright (2017) The Royal Chemical Society.

$[M_2{-}H]^-$ DIMERS ●● ± 2*x*H

label	formula of M_2	*m/z*(exp)	*m/z*(theo)	Δ*m/z*	Δ*m/z* [ppm]	relative ratio
-4H	$C_{38}H_{48}N_6O_8$	715.3471	715.3450	0.0021	2.94	0.01
-2H	$C_{38}H_{50}N_6O_8$	717.3631	717.3603	0.0028	3.90	0.03
●●	$C_{38}H_{52}N_6O_8$	719.3788	719.3763	0.0025	3.48	1.00
+2H	$C_{38}H_{54}N_6O_8$	721.3959	721.3885	0.0074	10.26	0.21
+4H	$C_{38}H_{56}N_6O_8$	723.4102	723.4071	0.0031	4.29	0.57

Table 4.2. (−)ESI-CID MS peak assignments of $[M_3{-}H]^-$ trimers of poly(DOPA-TEMPO-CH_3) (**8**). Adapted with permission from reference [327]. Copyright (2017) The Royal Chemical Society.

$[M_3{-}H]^-$ TRIMERS ●●● ± 2*x*H

label	formula of M_3	*m/z*(exp)	*m/z*(theo)	Δ*m/z*	Δ*m/z* [ppm]	relative ratio
-2H	$C_{57}H_{75}N_9O_{12}$	1076.5486	1076.5451	0.0034	3.16	0.02
●●●	$C_{57}H_{77}N_9O_{12}$	1078.5637	1078.5607	0.0030	2.78	0.46
+2H	$C_{57}H_{79}N_9O_{12}$	1080.5788	1080.5738	0.0050	4.63	0.29
+4H	$C_{57}H_{81}N_9O_{12}$	1082.5949	1082.5914	0.0035	3.23	1.00
+6H	$C_{57}H_{83}N_9O_{12}$	1084.6078	1084.6032	0.0046	4.24	0.29
+8H	$C_{57}H_{85}N_9O_{12}$	1086.6257	1086.6192	0.0065	5.98	0.14

Similar observations were made for the trimer region with six identified species appearing at different *m/z* values (with $\Delta m/z = 2$) in the range of *m/z* 1076–1090 (**Figure 4.5b**). The DHI-homotrimer $[M_3{-}H]^-$ of poly(DOPA-TEMPO-CH$_3$) (**8**) appeared at *m/z*(exp) 1078.5637 (*m/z*(theo) 1078.5607), and the presence of corresponding (oxidised) indolequinones structures were confirmed at −2H (**Table 4.2**). However, the most abundant peak of the trimer region appeared at higher *m/z* suggesting a tendency toward the formation of oligomers composed of higher molecular weight building blocks such as open-chain dopamine structures. Indeed, the incorporation of uncyclised catecholic dopamine moieties was verified by the appearance of the +8H trimer species at *m/z*(exp) 1086.6257 (*m/z*(theo) 1086.6192), confirmed by detailed isotopic pattern simulations (refer to **Figure B.6** in the Appendix). Structural deconvolution of this peak employing the proposed structures in **Figure 4.4** leads to numerous statistically linked isomers with eight additional hydrogen atoms (referred to the DHI homotrimer). Possible structures, however, only exist with incorporated open-chain units, and structural modelling suggested the incorporation of one uncyclised unit (2 × dihydroxyindoline and 1 × dopamine), two uncyclised units (*e.g.*, 1 × DHI and 2 × dopamine) or even three incorporated units (2 × dopaminochrome and 1 × dopamine). Proposed structures corresponding to the +8H peak are displayed in **Figure 4.6**.

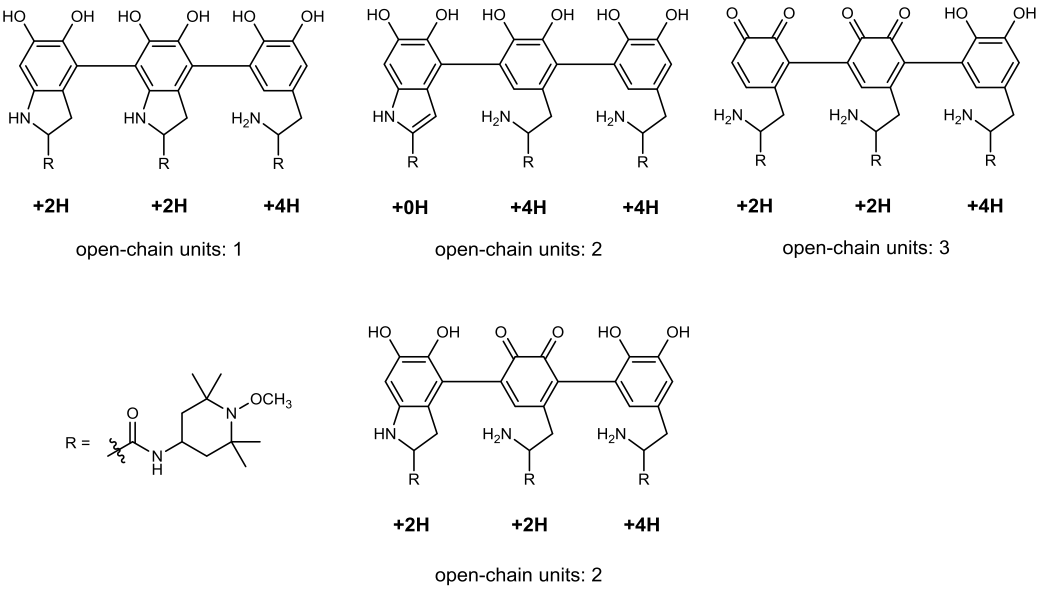

Figure 4.6. Proposed structures of +8H trimeric isomers with *m/z*(theo) 1086.6192 (*m/z*(exp) 1086.6257) and different numbers of incorporated open-chain units. Adapted with permission from reference [327]. Copyright (2017) The Royal Chemical Society.

As an interim conclusion, the structural elucidation of the dimer and trimer profiles of poly(DOPA-TEMPO-CH_3) (**8**) revealed the presence of covalently linked various cyclised and open-chain building blocks, present in different oxidation states such as the catechol and the *o*-quinone form. In addition, further support was provided that DHI plays a key role in the formation of covalently linked poly(catecholamine)s. Moreover, previously identified reactive intermediates (*e.g.*, **3a**–**c** for the nitroxide analogous polymer system **4** depicted in **Scheme 3.2**) were also present in the isolated polymer scaffolds of **8**, most likely with a tendency to undergo further reactions to more stable structures.

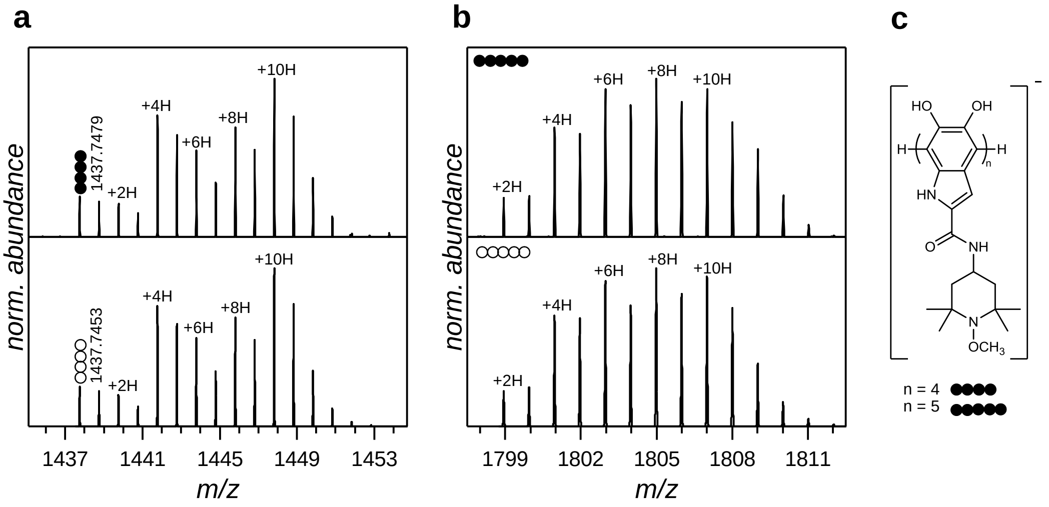

Figure 4.7. (−)ESI-CID expanded mass spectra of poly(DOPA-TEMPO-CH_3) (**8**) tetramers and pentamers. Comparison of experimentally obtained spectra (top) with simulated isotopic patterns (bottom) of (**a**) $[M_4{-}H]^-$ tetramer region and (**b**) $[M_5{-}H]^-$ pentamer region. (**c**) Proposed structure of DHI homooligomers with n = 4–5. Adapted with permission from reference [327]. Copyright (2017) The Royal Chemical Society.

Six tetramer and five pentamer structures were detected as deprotonated $[M_4{-}H]^-$ and $[M_5{-}H]^-$ species, respectively (**Figure 4.7**). A homotetramer consisting of four DHI repeating units can be assigned at *m/z*(exp) 1437.7479 (*m/z*(theo) 1437.7453), a homopentamer analogous structure, however, was not detected. Instead, both profiles followed the previously described trend toward oligomers composed of higher molecular weight building blocks, most likely open-chain dopamine moieties.[329, 332] This is an important observation, as free primary amine groups have been reported to contribute to the inherent adhesive properties of poly(catecholamine)s along with synergistic effects of catechol neighbouring groups.[207, 209] The isotopic pattern simulations for the deprotonated tetramer and pentamer profiles (the same holds for the dimer and trimer profiles) are in perfect agreement with the experimentally obtained mass spectra with various overlapping species, each with an individual isotopic pattern. This observation is valid along the *m/z* axis (with Δ*m/z*(exp−theo) values within < 4 ppm range for the tetramer and pentamer profiles) but also in their peak height profiles, which highlights HR-ESI-MS as a suitable and precise characterisation platform for functional poly(catecholamine)s (**Table 4.3** and **Table 4.4**).

Table 4.3. (−)ESI-CID MS peak assignments of $[M_4{-}H]^-$ tetramers of poly(DOPA-TEMPO-CH_3) (**8**). Adapted with permission from reference [327]. Copyright (2017) The Royal Chemical Society.

$[M_4{-}H]^-$ TETRAMERS ●●●● ± 2*x*H						
label	**formula of M_4**	***m/z*(exp)**	***m/z*(theo)**	**Δ*m/z***	**Δ*m/z* [ppm]**	**relative ratio**
●●●●	$C_{76}H_{102}N_{12}O_{16}$	1437.7479	1437.7453	0.0026	1.81	0.31
+2H	$C_{76}H_{104}N_{12}O_{16}$	1439.7605	1439.7563	0.0042	2.92	0.14
+4H	$C_{76}H_{106}N_{12}O_{16}$	1441.7791	1441.7758	0.0034	2.36	0.89
+6H	$C_{76}H_{108}N_{12}O_{16}$	1443.7913	1443.7874	0.0039	2.70	0.38
+8H	$C_{76}H_{110}N_{12}O_{16}$	1445.8102	1445.8055	0.0047	3.25	0.72
+10H	$C_{76}H_{112}N_{12}O_{16}$	1447.8255	1447.8211	0.0044	3.04	1.00

Table 4.4. (−)ESI-CID MS peak assignments of $[M_5{-}H]^-$ pentamers of poly(DOPA-TEMPO-CH_3) (**8**). Adapted with permission from reference [327]. Copyright (2017) The Royal Chemical Society.

$[M_5{-}H]^-$ PENTAMERS ●●●●● ± 2*x*H						
label	**formula of M_5**	***m/z*(exp)**	***m/z*(theo)**	**Δ*m/z***	**Δ*m/z* [ppm]**	**relative ratio**
+2H	$C_{95}H_{129}N_{15}O_{20}$	1798.9469	1798.9455	0.0014	0.78	0.35
+4H	$C_{95}H_{131}N_{15}O_{20}$	1800.9596	1800.9592	0.0004	0.22	0.90
+6H	$C_{95}H_{133}N_{15}O_{20}$	1802.9748	1802.9727	0.0021	1.16	0.90
+8H	$C_{95}H_{135}N_{15}O_{20}$	1804.9910	1804.9881	0.0029	1.61	1.00
+10H	$C_{95}H_{137}N_{15}O_{20}$	1807.0075	1807.0031	0.0044	2.43	0.85

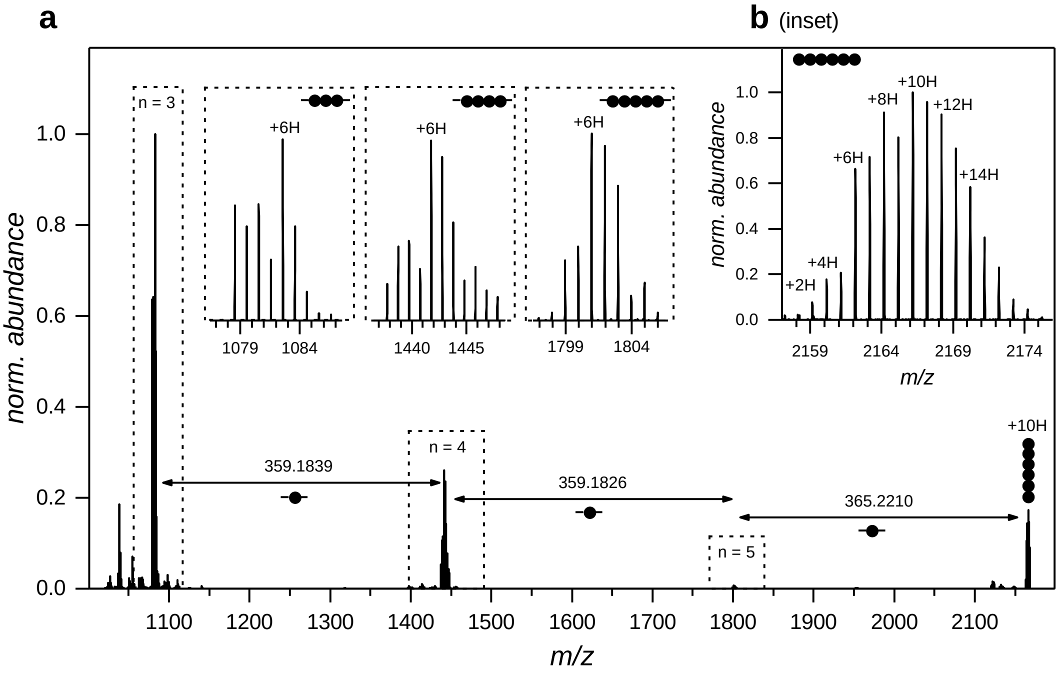

Figure 4.8. (−)ESI-CID MS and (−)ESI-HCD (15 eV) MS/MS characterisation of poly(DOPA-TEMPO-CH_3) (**8**) hexamers. (**a**) MS/MS analysis of most abundant hexamer species of **8** apparent at *m/z* 2166 ± 5. The spectrum was recorded in THF/MeOH 3:2 (*v*/*v*). Insets show complementary zoomed spectra of fragmentation regions with n = 3–5. The fragmentation pattern can be assigned to multiple losses of monomer units and filled circles (●) refer to DHI fragments ($C_{19}H_{25}N_3O_4$) with Δ*m/z*(theo) 358.1840. (**b**) Expanded mass spectrum of **8** showing the $[M_6{-}H]^-$ hexamer profile. The spectrum was recorded in H_2O/acetonitrile 1:1 (*v*/*v*) doped with 0.1% (*v*/*v*) acetic acid. Other peak assignments labelled with (± *x*H) refer to the DHI homooligomers. Adapted with permission from reference [327]. Copyright (2017) The Royal Chemical Society.

ESI-tandem MS (MS/MS) was employed for further evidence of the proposed structural appearances of poly(DOPA-TEMPO-CH_3) (**8**) *via* higher-energy collision dissociation (HCD). The most abundant peak of the hexamer profile with ten additional hydrogen atoms referenced to the DHI homohexamer (refer to **Figure 4.8b**, labelled with +10H) was subjected to MS/MS analysis with *m/z* 2166 ± 5. The distinct fragmentation pattern depicted in **Figure 4.8a** underpinned the presence of a polymer scaffold composed of diverse but consistent monomer units. Consecutive C–C bond cleavages between the monomer units is suggested for the subjected +10H hexamer resulting in discrete fragments composed of predominantly three and four repeating units. Pentamer fragments were detected less abundant (the zoomed spectra are depicted as insets in **Figure 4.8a**). The interval of Δ*m/z*(exp) 359.1826 of the most abundant peaks of the pentamer and tetramer fragments correlates to a loss of one DHI-TEMPO-CH_3 fragment (Δ*m/z*(theo) 359.1840). The same observation is valid for the tetramer and trimer fragmentation profiles with Δ*m/z*(exp) 359.1839.

MS/MS peak assignments of the most abundant peaks are listed in **Table B.3** in the Appendix. No further extensive fragmentations within the pentamer to trimer profiles were observed as it was the case for the poly(DOPA-TEMPO) (**3**) pentamer subjected to MS/MS (refer to Chapter 3.4).

In positive ion mode, poly(DOPA-TEMPO-CH_3) (**8**) heptamers and octamers were detected. The heptamer profile exhibited species in the range of +4H to +16H identified as protonated $[M_7+H]^+$ species with the most abundant peak at *m/z*(exp) 2527.4202 (*m/z*(theo) 2527.3869) corresponding to the +10H heptamer (**Figure 4.3b**). Protonated octamer species $[M_8+H]^+$ were less abundant, however, the corresponding sodium chloride adducts $[M_8+H+NaCl]^+$ were assigned to the region with the most abundant peak at *m/z*(exp) 2946.5641 (*m/z*(theo) 2946.5371) (**Figure 4.3c**).

4.4 CONCLUSION

In conclusion, the synthesis and polymerisation of a functional catecholamine monomer carrying an amide-linked, TEMPO-derived methoxyamine group in the side chain was presented. The structural composition of poly(DOPA-TEMPO-CH_3) (**8**) was critically examined by HR-ESI-MS in terms of the presence of covalent assemblies during DOPA-TEMPO-CH_3 (**7**) polymerisation, followed by an in-depth characterisation of the polymer backbone composition. Oligomers with up to eight repeating units were identified apparent as broad overlapping oligomer profiles. The polymer composition demonstrated close structural similarities to PDA with diverse cyclised building blocks, incorporated open-chain units as well as the coexistence of catechol and *o*-quinone groups leading to a heterogeneous, multifunctional polymer system. Intramolecular cyclisation to DHI-like core structures, initiated by aerobic catechol oxidation, occurred irrespective of the additional side chain functionality. However, the additional TEMPO-CH_3 group had strong influences on the polymerisation and cross-linking behaviour as the number of reactive sites for oxidative couplings was reduced, and steric effects most likely influenced the reactivity of intra- and intermolecular reactions, oxidative building block cross-couplings, and supramolecular self-assembly. Other reactive intermediate states, such as the aminochrome structure identified during poly(DOPA-

TEMPO) (**3**) assembly, were also covalently incorporated within poly(DOPA-TEMPO-CH_3) (**8**) scaffolds. Their existence, however, appeared to be less abundant in this MS study. Also the presence of oxidised DHI units (the indolequinones structures) appeared to be more pronounced during ESI-MS characterisation of polymer **3**, which might be attributed to the predominant presence of hydrochloride polymer adducts. Overall, the evidenced structural diversity in the polymer backbone and the fact that covalent cross-linking occurred are important structural characteristics in terms of the strong and substrate-independent adhesion properties of poly(catecholamine)s. The dynamic system composed of multiple expressed catechol anchoring units, the corresponding *o*-quinone structures, fully conjugated DHI-like systems and free primary amino groups — they all contribute to multi- and heterovalent polymer–substrate binding interactions and are most likely differently pronounced in respect to the type of underlying material interface. The precise structural elucidation of the employed poly(catecholamine) functional system (conducted under several assumptions) was exclusively accessible by the powerful HR-ESI-MS platform offering a general access route for the characterisation of complex systems such as poly(catecholamine)s and their derivatives.

Chapter 5: Nitroxide Surface Decoration Using Bioadhesion

5.1 PREFACE

Precise tuning of material interfaces is of pivotal interest in modern material design, and polymer coatings have become widely-applicable auxiliary tools for the generation of tailor-made surfaces. The use of polycatecholic scaffolds with bioderived inherent adhesive properties has been particularly in the spotlight since 2007 as a facile access route for versatile surface functionalisations.[203] Nitroxide-containing functional materials, on the other hand, are of demanding scope in applied chemistry, materials sciences and biosciences, *e.g.* as recyclable oxidation catalysts, energy storage materials, or as redox and radical sensors in biological systems. The delivery of nitroxides to the interface of materials is also of rising interest in biofilm research as nitroxides are known to actively disperse sessile bacterial communities, making them more susceptible to biofilm eradication countermeasures.[4-5] This implies that nitroxide-decorated surfaces have the great potential to prevent biofilm formation on surfaces, which can lead to a reduction of biofouling in industrial processes and biofilm contaminations on medical devices in the hospital. Fusing the emerging chemistry of nitroxides with the state-of-the-art universal coating strategy based on poly(catecholamine)s represents an attractive access route for the generation of persistent multi-radical surfaces with widespread practical use.

The current chapter presents a convenient coating strategy for the preparation of nitroxide functional surfaces using bioinspired adhesion. The previously introduced catecholamine monomer equipped with a nitroxide moiety, denoted at DOPA-TEMPO, was herein employed as a versatile coating agent for substrate-independent nitroxide surface functionalisations. The facile dip-coating experimental setup and the use of non-hazardous reagents (such as water as a solvent and

---

Parts of the current chapter are adapted or reproduced from reference [314]: H. Woehlk, J. Steinkoenig, C. Lang, L. Michalek, V. Trouillet, P. Krolla, A. S. Goldmann, L. Barner, J. P. Blinco, C. Barner-Kowollik and K. E. Fairfull-Smith, *Langmuir*, **2018**, 34, 3264-3274 with permission from the American Chemical Society. XPS characterisation was conducted by V. Trouillet (KIT), AFM measurements were performed by P. Krolla (KIT) and L. Michalek (QUT).

atmospheric oxygen as a mild oxidant) ensure a widespread practical use and follow the concept of green chemistry. A detailed characterisation of the resulting polymer coatings was undertaken by a multitude of advanced surface characterisation techniques. First, the adhesive performance of the *in situ* generated poly(DOPA-TEMPO) scaffolds deposited on various material interfaces was assessed by XPS, AFM, and static water contact angle measurements. The overall polymer surface coverage was critically correlated to the underlying substrate properties, such as the chemical composition and inherent surface roughness of the employed materials. In-depth XPS analysis investigated the structural composition of the adhesive polymer matrix and examined different chemical states of the covalently incorporated nitroxide moieties. The continuously growing polymer film was monitored by spectroscopic ellipsometry (SE), and accurate determination of the film thicknesses was complemented by AFM height profile measurements. The electroactive character of the multi-radical polymer system was shown by CV measurements. Finally, precise control over the polymerisation of the nitroxide functional monomer was achieved using light as an external stimulus. An advanced polymerisation protocol based on the UV-light accelerated generation of ROS inducing the polymerisation of DOPA-TEMPO was established and carefully investigated by UV–vis and EPR spectroscopy, and SE.

5.2 EXPLOITING THE VERSATILE CHARACTER OF POLY(DOPA-TEMPO) COATINGS

The immobilisation of nitroxides onto various surfaces was achieved using DOPA-TEMPO (**3**) as a versatile coating agent dissolved in Tris–HCl buffer (10 mM, pH 8.5). Selected substrates were immersed into a 10 mM coating solution of **3**, and the polymerisation — concomitant with *in situ* polymer surface deposition — was performed under aerobic conditions and under vigorous stirring for continuous supply of oxygen through the air-liquid interface. Poly(DOPA-TEMPO) (**4**) coatings were conducted at ambient temperature without any additional (harmful) chemicals (**Scheme 5.1**). In addition, no elaborate experimental setup was required. The substrates, namely silicon, titanium, alumina and PTFE, were placed vertically into the coating solution in order to suppress polymer particle sedimentation, and coatings were typically performed for 12 h or 24 h, respectively. Silicon wafers were selected as model substrates for subsequent in-depth surface characterisation of the nitroxide polymer coatings and with rapid access to the polymer film thickness by SE. The other selected materials were chosen as representative examples for metallic (titanium), ceramic (alumina) or inert polymer (PTFE) uncoated objects in order to investigate the versatile and substrate-independent character of this coating approach. Furthermore, the employed materials cover a broad range of important composites found in medical devices (*e.g.*, titanium screws, artificial joints and hip replacements, and catheters), which are, by all means, prone to surface-related biofilm contaminations in the hospital.

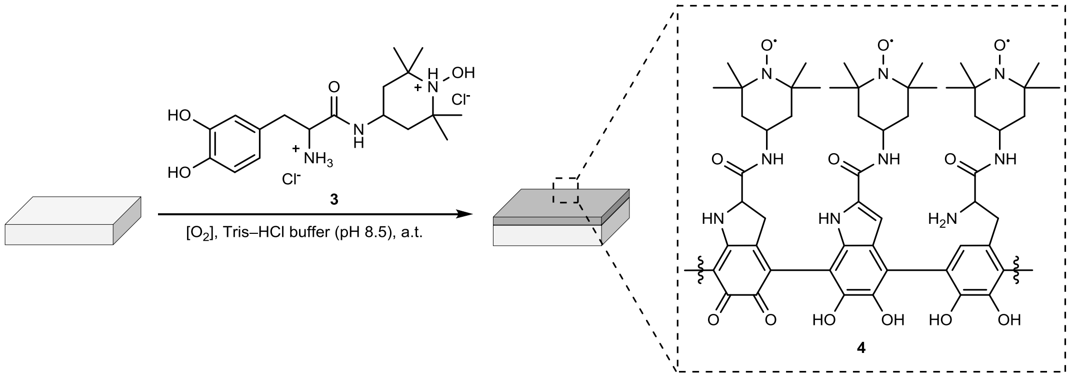

Scheme 5.1. Synthetic route for the oxidative polymerisation of **3** (10 mM) with *in situ* polymer surface deposition onto various immersed substrates. The dip-coating procedure was performed in Tris–HCl buffer (10 mM, pH 8.5) under aerobic conditions. Substrates were typically coated for 12 or 24 h, respectively. Uncoated objects encompass silicon, titanium, alumina and PTFE flat substrates. Adapted with permission from reference [314]. Copyright (2018) American Chemical Society.

A first indication of the proceeding polymerisation of **3** was evidenced by a rapid yellow-brown colourisation of the coating solution. In addition, polymer film formation on the immersed substrates was clearly visible to the naked eye. This observation was supported by intrinsic changes of the water wettability properties and the comparison of the static water contact angles of uncoated and polymer **4** coated materials (**Table 5.1**). Harmonised water contact angles in the range of 53 and 63° were determined on all polymer-coated objects (24 h), which implies that polymer film formation has occurred irrespective of the underlying material properties. Noteworthy, water contact angles in a similar range have been reported for PDA-coated substrates.[254, 333] Most strikingly, uncoated superhydrophobic PTFE (118.6°) showed significantly decreased water repellent forces when coated with polymer **4** (56.9°) (refer to **Figure C.1** in the Appendix for the corresponding images). Changes of the water wettability of the other employed uncoated and coated materials were less pronounced, however, a clear trend toward harmonised values when coated with polymer **4** was observed.

Table 5.1. Surface characterisation of uncoated and poly(DOPA-TEMPO) (**4**) coated substrates by XPS, AFM and static water contact angle measurements. Adapted with permission from reference [314]. Copyright (2018) American Chemical Society.

	XPS residual substrate-characteristic peaks [atom %][a]		**AFM RMS surface roughness [nm]**[b]		**Static water contact angles [°]**	
	coated (12 h)	*coated (24 h)*	*uncoated*	*coated (12 h)*	*uncoated*	*coated (24 h)*
Silicon	16.2	3.2	0.5 ± 0.1	28.9 ± 3.3	55.5 ± 1.2	62.3 ± 2.1
Titanium	0.8	0.1	31.9 ± 8.3	41.4 ± 9.3	77.5 ± 1.4	53.7 ± 0.7
Alumina	2.6	0.8	179.5 ± 13.9	208.5 ± 12.0	70.0 ± 1.6	61.7 ± 4.0
PTFE	3.5	0.2	N/A[c]	N/A[c]	118.6 ± 1.0	56.9 ± 2.0

[a] substrate-characteristic peaks of selected substrates refer to silicon (Si 2p), titanium (Ti 2p), aluminium (Al 2p), and fluorine (F 1s), respectively; [b] determined over a 20 × 20 μm^2 area; [c] determination of uncoated and coated PTFE surface roughness was strongly distorted by electrostatic interactions between cantilever tip and the substrate. A shielding effect was observed for PTFE when covered with polymer **4**.

Further evidence of successful polymer film coverage irrespective of the underlying substrate properties was given by XPS and the quantification of the residual substrate-specific peaks after coating with polymer **4** for 12 and 24 h, respectively (**Table 5.1**). All employed materials (silicon, titanium, alumina, and PTFE) showed decreased intensities of the substrate-characteristic peaks (Si 2p, Ti 2p, Al 2p, and F 1s, respectively) with proceeding coating time (12 and 24 h). Simultaneously, increasing C 1s, N 1s and O 1s peaks were observed attributed to poly(DOPA-TEMPO) (**4**) film formation.

XPS quantification of the residual substrate-characteristic peaks with concentrations of 0.8 atom % titanium, 2.6 atom % aluminium, and 3.5 atom % fluorine after 12 h of polymerisation suggested an evenly growing polymer film on titanium, alumina and PTFE, respectively, which appeared to be irrespective of the underlying materials properties. A reduction of the substrate-specific peaks to less than 1 atom % for the above-mentioned materials was observed when coated for 24 h, indicating polymer film thicknesses close to 10 nm. The employed silicon wafers showed a slower polymer film formation with 16.2 atom % silicon (12 h) and 3.2 atom % after 24 h of coating time. This observation is most likely attributed to the smooth surface topography of the employed material with a root mean square (RMS) surface roughness of 0.5 nm over a 20 × 20 μm^2 area determined by AFM (**Table 5.1**). A comparison of the smooth surface of silicon with the surface properties of the other employed uncoated objects suggests that the initial polymer–surface binding interactions and the overall 'grip' of polymer **4** are critically dependent on the topographical properties of the underlying substrate. Expressed in absolute numbers, the surface roughness of uncoated titanium (31.9 nm) and alumina (179.5 nm) is multiple times higher compared to silicon (0.5 nm). For PTFE, the good polymer surface coverage can be explained by the inherent surface roughness of the employed material, which seems to overcome the general weak binding interactions between polymer **4** and the underlying chemically inert polymer composite material.[194] The precise determination of the surface roughness of bare PTFE, however, was strongly distorted by electrostatic interactions between the AFM cantilever tip and the substrate. A comparison of uncoated and coated PTFE objects only showed a strong shielding effect after coating with polymer **4**. In general, an increasing RMS surface roughness (determined after 12 h of coating time) was observed for all other employed materials indicating a successful ad-layer polymer formation. Further AFM measurements are presented shortly.

5.3 CHARACTERISATION OF NITROXIDE-CONTAINING THIN POLYMER FILMS

First, the chemical and structural composition of surface-deposited polymer **4** was investigated by XPS. Later on, the polymer film formation and the topographical properties were assessed by SE and AFM. The electrochemical properties of nitroxide-decorated electrode materials were characterised by CV.

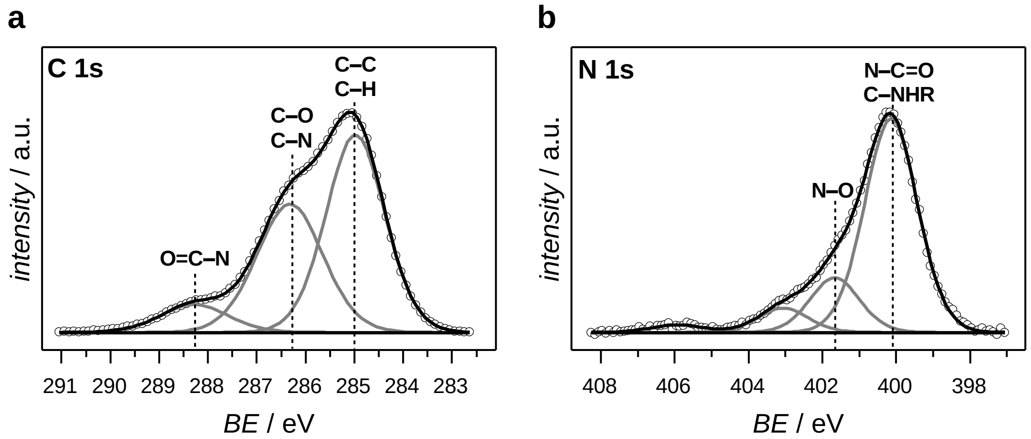

Figure 5.1. XPS characterisation poly(DOPA-TEMPO) (**4**) thin films. (**a**) C 1s and (**b**) N 1s high-resolution XP spectra of **4** deposited on Si for 24 h. Adapted with permission from reference [314]. Copyright (2018) American Chemical Society.

In-depth C 1s and N 1s XPS characterisation revealed identical polymer surface compositions irrespective of the underlying material properties. **Figure 5.1** shows the high-resolution C 1s and N 1s XP spectra of coated silicon substrates (24 h). The C 1s XPS peak was deconvoluted into three main components corresponding to C–C and C–H (at 285.0 eV, 35.6 atom %), C–O and C–N (at 286.3 eV, 26.1 atom %) and O=C–N (at 288.3 eV, 5.8 atom %).[334] Other functional groups such as *o*-quinones, which have been identified in previous studies, were not evidenced in the C 1s XP spectrum.[266, 335] This observation complies with the general assumption that *o*-quinoic species are less abundant in the final polymer backbone composition although they have been identified as important key intermediate states during catecholamine polymerisation. Also, the presence of pyrrole carboxylic acid moieties, which have been proposed as structural motifs to appear in PDA coatings, was not pronounced in the C 1s XP spectrum.[329, 336]

The corresponding high-resolution N 1s XP spectrum (**Figure 5.1b**) was deconvoluted into four nitrogen components with a dominant peak at 400.1 eV (6.8 atom %), and three minor nitrogen species at higher binding energies. The main peak structurally corresponds to the polymer backbone with various appearances of N-containing structures including uncyclised amino groups as well as cyclised indole- and indoline-like structures. The amide functional group of polymer **4** also contributes to the dominant peak in the N 1s XP spectrum. The nitroxyl moiety was identified to appear at 401.6 eV (1.6 atom %), which was supported by XPS reference measurements of a TEMPO-containing polymer analogous system, namely PTMA, with a characteristic main peak at 401.5 eV assigned to the N–O functional group (refer to **Figure C.2** in the Appendix). Two other identified N-containing components appearing at higher binding energies (403.1 eV, 0.7 atom % and 405.9 eV, 0.2 atom %) are presumably protonated or higher oxidised nitrogen species. The latter peak, for instance, has been referred to the presence of overoxidised *N*-oxoammonium cations.[142] Noteworthy, the relative abundances of the peaks at higher BEs assigned to various nitroxyl species fluctuated during XPS analysis (*e.g.*, when measuring different batches of polymer-coated materials), which indicates the dynamic and oxygen-sensitive character of the incorporated nitroxide persistent radicals.

The preparation of polycatecholic coatings is known to be dependent on various parameters, for instance, the pH value and the employed buffer system, the type of oxidant, as well as the monomer concentration.[257, 319, 337] Recently, the use of light as a powerful tool to control the oxidative polymerisation of catecholic monomers has been introduced.[230, 263] This concept has been adapted for compound **3** employed as a monomer and coating agent and is further discussed in Chapter 5.3. In the present study, the surface deposition of poly(DOPA-TEMPO) (**4**) onto silicon substrates was monitored during the initial stage of the polymerisation of **3**. Monomer **3** (10 mM) was dissolved in Tris–HCl buffer (10 mM, pH 8.5), and the coating solution was exposed to atmospheric oxygen as an oxidant. A continuously growing polymer film was observed within the first 12 h of polymerisation, and an estimated growth rate close to 1.1 $\mathrm{nm \cdot h^{-1}}$ was determined by SE (calculated as an average after 12 h of coating time, refer to **Figure 5.2a**). The growth rate was significantly slower compared to literature-reported values for dopamine polymerisations (~3.6 nm·h^{-1})[254] and other phenolic and polyphenolic systems, such as tannic acid or pyrogallol, respectively.[229] This observation is most likely attributed to steric and electronic effects of the additional TEMPO functional group impeding both, intramolecular cyclisation reactions to DHI-like appearances as well as intermolecular cross-linking reactions of reactive intermediates of **3**. Also the number of active sites for multilateral monomer coupling reactions is reduced as one cross-linking point is already occupied by the amide-linked TEMPO moiety (in comparison to unmodified dopamine). Furthermore, it was previously shown in Chapter 3.3 that persistent nitroxide radicals strongly interfere with the oxidative catecholamine polymerisation of **3**, which might impact the overall coating formation.[258]

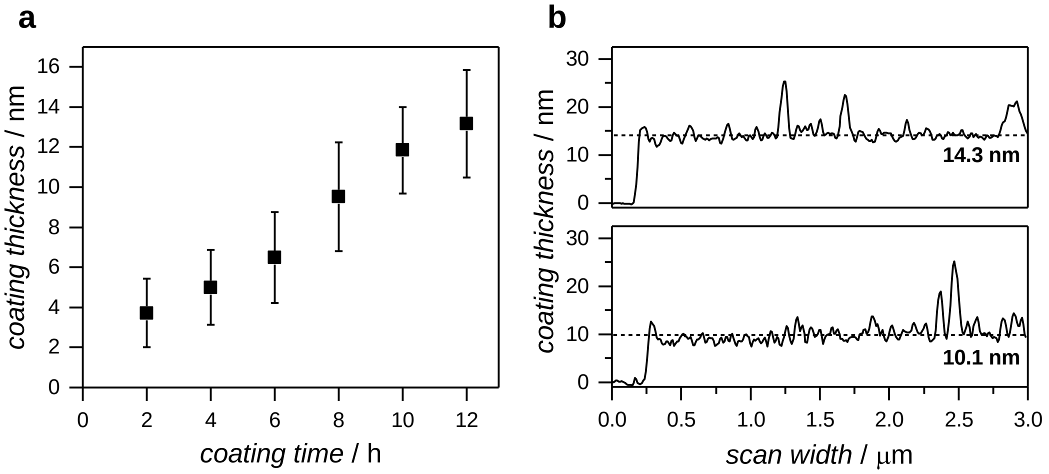

Figure 5.2. Time-resolved determination of coating thicknesses of polymer **4** deposited on silicon substrates. (**a**) Monitoring of growing polymer film formation during the initial stage of polymerisation (between 1 and 12 h) accessed through SE. (**b**) Selected AFM height profiles of polymer-coated silicon substrates after 12 h of polymerisation. Dashed lines indicate averaged polymer film thickness with 14.3 nm (top panel, excluding peaks ≥ 18 nm derived from polymer particle sedimentation) and 10.1 nm (bottom panel, excluding peaks ≥ 15 nm). Adapted with permission from reference [314]. Copyright (2018) American Chemical Society.

AFM measurements were performed as a complementary access route to characterise the overall surface coverage of poly(DOPA-TEMPO) (**4**) and to critically evaluate the coating thicknesses obtained by SE. AFM height profiles of selected polymer-coated silicon substrates after 12 h of coating time were recorded and are displayed in **Figure 5.2b**. An average polymer film thickness of 14.3 nm (top panel) was calculated under exclusion of peaks ≥ 18 nm (to lower the impact of sedimented polymer particles). The obtained AFM coating thickness is hereby in excellent agreement with the film thickness obtained by SE (14.7 nm, determined prior to AFM measurements). Similar observations were made when analysing a replicate surface coated with polymer **4** (12 h). A slightly thinner polymer film was apparent by AFM measurements (10.1 nm, peaks ≥ 15 nm were excluded) and SE characterisation (11.6 nm as an average of multiple measured spots on the surface). As evident from **Figure 5.2b** and the raw AFM images depicted in **Figures C.3** and **C.4** in the Appendix, high surface roughness and adherent polymer particles were typical side effects of surface-immobilised nitroxide polymer scaffolds, which is a critical but inherent issue for this class of bioadhesive polymer coatings.[194, 229]

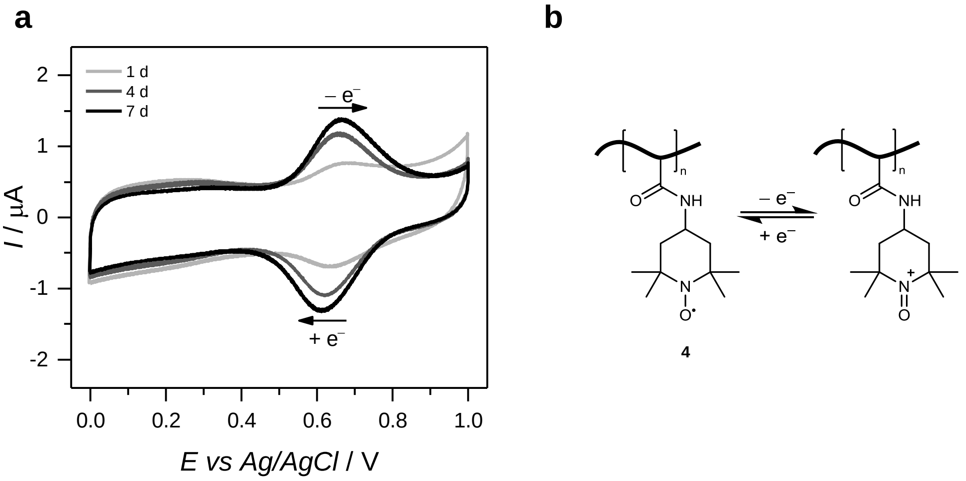

Figure 5.3. Electrochemical characterisation of poly(DOPA-TEMPO) (**4**) thin films deposited on a glassy carbon working electrode for 1, 4 and 7 days, respectively. (**a**) Cyclic voltammograms (five cycles) recorded with a scan rate of 100 mV·s^{-1} in 0.1 M aqueous NaCl solution. (**b**) Schematic illustration of polymer **4** showing the reversible nitroxide oxidation to corresponding *N*-oxoammonium cationic species and subsequent reduction back to the nitroxide free radicals. Adapted with permission from reference [314]. Copyright (2018) American Chemical Society.

Furthermore, the electrochemical properties of the nitroxide-containing polymer system were investigated by CV to reveal the potential use of polymer **4** as an electroactive material composite, *e.g.* in organic radical batteries. Thin polymer films of **4** were deposited on a glassy carbon and on a platinum working electrode, respectively. In addition, CV experiments were performed with different nitroxide densities localised at the electrode's interface. An increasing polymer film thickness was obtained by extending the coating time (1, 4 and 7 days) and further addition of monomer **3** to the coating solution. The recorded cyclic voltammograms depicted in **Figure 5.3** for the coated glassy carbon electrode (employed as a working electrode) show the reversible oxidation and reduction cycles owing to surface-deposited nitroxide polymer scaffolds. Increased current values were observed as a function of the nitroxide polymer film thickness. The one-electron oxidation is hereby referred to the formation of the *N*-oxoammonium cations with subsequent reduction and reformation of the free radical species.[78] Furthermore, repetitive CV measurements (five redox cycles) confirmed a good cycling stability of the nitroxide-containing polymer (**4**). Similar observations as described above were made for the coated platinum working electrode (refer to **Figure C.5** in the Appendix).

5.4 LIGHT-CONTROLLED POLYMERISATION AND NITROXIDE SURFACE IMMOBILISATION

The versatile and adaptable nitroxide coating system was further expanded using UV-light as an external stimulus to trigger the polymerisation of DOPA-TEMPO (**3**). Light has been become a widely-employed and powerful tool in modern polymer chemistry and materials sciences.[195, 338] In catecholamine polymerisations (and other related catecholic compounds), UV irradiation has been exploited for the generation of ROS, originating from dissolved molecular oxygen, as a simple control mechanism to initiate the complex oxidative cascade reactions of the catechol functional group.[230-231, 263] In the present study, careful optimisation of the coating parameters employing monomer **3** (5 mM) dissolved in Tris–HCl buffer (10 mM, initially adjusted to pH 8.5) resulted in a suppression of the polymerisation when the reaction was performed in the dark, and contrary to this, an accelerated polymer formation was observed under UV irradiation (λ_{max} = 313 nm) (**Scheme 5.2**).

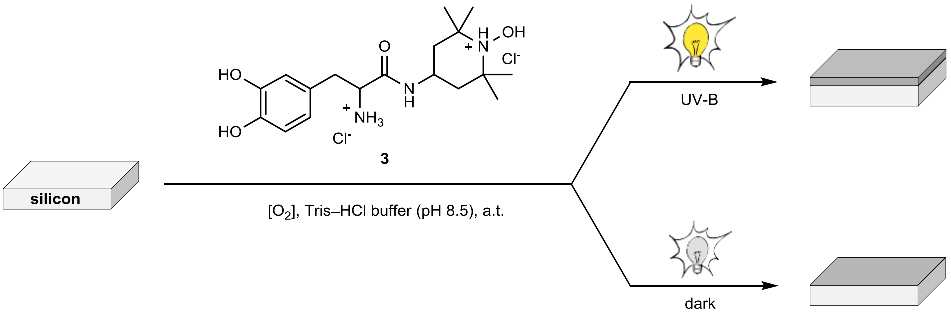

Scheme 5.2. Light-dependent oxidative polymerisation of DOPA-TEMPO (**3**) (5 mM) with *in situ* polymer surface deposition onto immersed silicon substrates. The reaction was performed in Tris–HCl buffer (10 mM, pH 8.5) for 0–12 h under UV-B irradiation (λ_{max} = 313 nm) and in the dark, respectively.

The light-dependent polymerisation of **3** concomitant with polymer deposition onto immersed silicon substrates was carefully investigated by various characterisation techniques (**Figure 5.4**). The ROS-induced rapid build-up of reactive *o*-quinoic intermediates upon UV exposure was evidenced by UV–vis spectroscopy (**Figure 5.4b**, left panel) and the appearance of a band (λ = 333 nm) adjacent to the catechol-assigned absorption at higher energies (λ = 280 nm) (refer to Chapter 3.3 for precise UV–vis spectroscopic structural assignments). This observation was less pronounced when the reaction was performed in the dark with only minor changes of the UV–vis absorbances as depicted in **Figure 5.4b** (right panel). After 12 h of polymerisation, an increasing turbidity of the reaction solution was observed, which hampered UV–vis and EPR spectroscopic analyses thereafter.

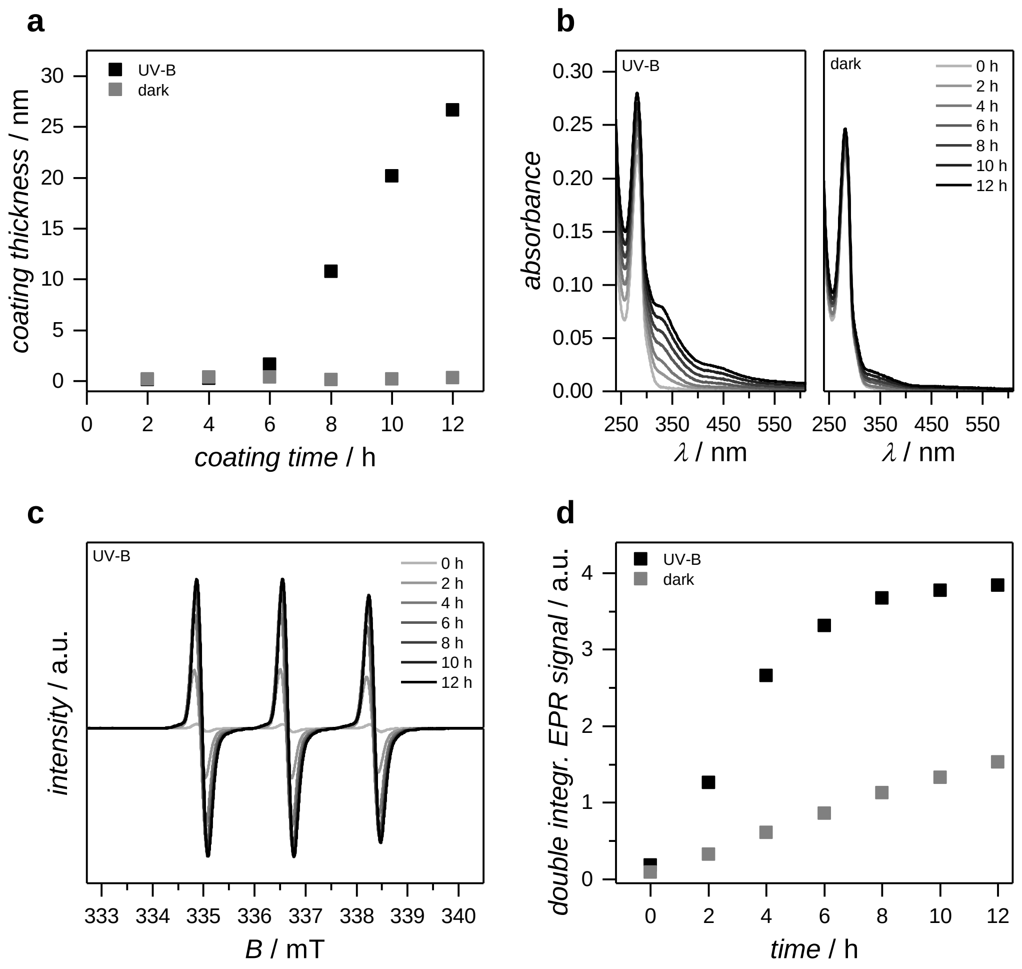

Figure 5.4. In-depth and time-resolved characterisation of light-dependent polymerisation of **3** with *in situ* polymer surface deposition onto immersed silicon substrates. (**a**) Determination of coating thickness of polymer **4** by SE. (**b**) UV–vis spectroscopic monitoring of oxidative polymerisation of **3** under UV-B irradiation (left panel) and in the dark (right panel). (**c**) First derivative EPR spectra during polymerisation of **3** concomitant with nitroxide radical formation. (**d**) EPR quantification of nitroxide-derived unpaired electron spins *via* double integration of the recorded EPR signals.

The impact of the UV-B irradiation on the hydroxylamine oxidation of monomer **3** yielding the free nitroxide radical species was investigated by EPR spectroscopy. The recorded EPR spectra depicted in **Figure 5.4c** for the UV-triggered reaction pathway showed rapidly increasing EPR responses within the first 12 h of DOPA-TEMPO (**3**) polymerisation. The corresponding first-derivative EPR spectra for the polymerisation performed in the dark are depicted in **Figure C.6** in the Appendix. EPR quantification of the simultaneously conducted experiments — the UV-assisted polymerisation and the polymerisation performed in the dark — showed a significantly accelerated nitroxide radical formation when the reaction was performed under continuous generation of ROS induced by UV irradiation (**Figure**

5.4d). At the same time, the light-controlled polymer film formation on silicon substrates was investigated by SE (**Figure 5.4a**). A rapid increase of the coating thickness was observed after reactive oligomeric structures have formed in the initial stage of polymerisation (between 0 and 6 h). In the dark, polymer film formation on silicon substrates was suppressed within the first 12 h of polymerisation as the concentration of reactive intermediates of **3** was maintained low (**Figure 5.4b**, right panel). Thus, no activated building blocks were present accelerating the construction of the adhesive polymer scaffold. Single-molecule surface adhesion, however, most likely occurred regardless of the employed reaction conditions owing to the wide-ranging catechol surface anchoring properties of monomer **3** (indicated as a deposited monolayer in **Scheme 5.2**, bottom reaction pathway). Noteworthy, the herein presented light-dependent polymerisation and coating investigative study employing **3** as a monomer and coating agent are based on representative experimental results, which may vary in time and intensity due to the initial concentration of dissolved oxygen (similar observations have been made before in Chapter 3.3).

5.5 CONCLUSION

In summary, a versatile and sophisticated avenue for the generation of nitroxide functional surfaces was presented. The inherent bioadhesive properties of polymerised catecholamines were exploited for substrate-independent nitroxide surface decorations, even to inert surfaces such as PTFE. Adhesive performance tests of poly(DOPA-TEMPO) (**4**) coatings revealed that the substrate-specific surface roughness and chemical composition crucially determine the initial polymer surface interactions and subsequent polymer film formation. Good control over the polymer film deposition on selected materials was achieved, and the polymer composition was carefully analysed by advanced surface characterisation techniques. In addition, UV-light as an auxiliary tool was introduced for light-dependent polymerisation of DOPA-TEMPO employed as a monomer and coating agent. This concept is further expanded for spatially resolved micropatterning of nitroxide polymer scaffolds on surfaces presented in Chapter 7. In the following chapter, the use of nitroxide functional surfaces is exploited as a programmable and widely-applicable ligation platform for precise and substrate-independent ad-layer surface functionalisations.

Chapter 6: Dynamic Nitroxide Functional Materials

6.1 PREFACE

Nitroxides and their corresponding alkoxyamine adducts have been extensively exploited as synthetic tools and functional units in polymer chemistry and materials science. The high coupling selectivity between persistent nitroxide radicals and transient carbon-centred radicals, explained by the persistent radical effect, typically yields alkoxyamine functional moieties with covalent yet labile character of the emerging NO–C bond. Deriving from that, nitroxides have been utilised as mediators in radical-driven polymerisations generating well-defined macromolecular scaffolds with precise control over their molecular weights. In addition, nitroxide radical coupling reactions have been proven efficient in post-polymerisation modifications, surface functionalisations, and for the design of complex polymer architectures and dynamic covalent polymer materials.[6, 47, 119]

The current chapter introduces a versatile nitroxide-based coating platform for temporally and spatially controlled coding of various material interfaces. First, poly(glycidyl methacrylate) (PGMA) microspheres were encased with a robust nitroxide-containing polymer film obtained through oxidative copolymerisation of dopamine (DA) and the previously introduced DOPA-TEMPO (**3**) monomer resulting in polymer film formation onto the suspended microparticles. Subsequently, the concept of using nitroxides as dynamic covalent switches was exploited for reversible surface modification and programming of the nitroxide-decorated microspheres, which was exemplified in a small molecule conjugation study. Bonding (*via* NRC) and debonding (*via* thermal alkoxyamine dissociation) on demand was hereby monitored by EPR spectroscopy and quantified by XPS. The versatile nitroxide functional coating platform was further employed for spatially

---

Parts of the current chapter are adapted or reproduced from reference [339]: H. Woehlk, A. Lauer, V. Trouillet, A. Welle, L. Barner, J. P. Blinco, K. E. Fairfull-Smith and C. Barner-Kowollik, *Chem. Eur. J.*, **2018**, *24*, 18873-18879 with permission from John Wiley and Sons. XPS characterisation was conducted by V. Trouillet (KIT) and ToF-SIMS measurements were performed by A. Welle (KIT). Compound **11**, polymer **12** and polymer **13** were prepared, characterised and kindly provided by A. Lauer (KIT) and D. Fast (TU Graz, Austria).

defined polymer surface conjugations driven by rapid photoligation chemistry. Specifically, the nitroxide surface functionalisation of silicon substrates was achieved in a simple PDA post-coating modification step. *Grafting to* polymer surface photopatterning with submillimeter resolution was conducted using photoinitiator (PI) terminated poly(methyl methacrylate) (PMMA) and poly(2,2,2-trifluoroethyl methacrylate) (PTFEMA) polymer strands, obtained through chain transfer polymerisations with a thiol-functionalised Irgacure 2959 derivative. Sequenced photo-click polymer surface ligation onto nitroxide-immobilised PDA surfaces upon UV irradiation was successfully visualised by ToF-SIMS and XPS imaging techniques.[339]

6.2 ENGINEERING NITROXIDE FUNCTIONAL MICROSPHERES WITH REWRITABLE PROPERTIES

The diverse applicability and adaptability of the previously presented bioderived polycatecholic coating strategy fused with nitroxides as key functional groups was herein exploited for the nitroxide surface decoration of PGMA microspheres, which are commonly used as solid support materials in chromatographic applications, *e.g.* for protein separation and purification.[340-342]

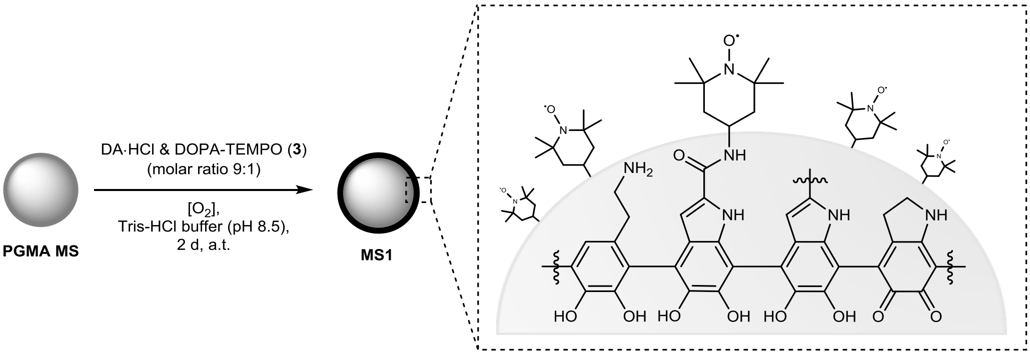

Scheme 6.1. Synthetic pathway for the preparation of nitroxide-coated PGMA microspheres. The oxidative copolymerisation of DA hydrochloride and DOPA-TEMPO (**3**) (molar ratio 9:1) concomitant with copolymer film deposition onto suspended PGMA microspheres was performed under aerobic conditions in Tris–HCl buffer (10 mM, pH 8.5) for 2 d. Adapted with permission from reference [339]. Copyright (2018) John Wiley and Sons.

The nitroxide immobilisation onto the polymeric support was performed in an oxidative copolymerisation[281] of DA and DOPA-TEMPO (**3**) concomitant with *in* *situ* polymer surface deposition onto the suspended microspheres (**Scheme 6.1**). The use of DA as a co-agent provided control over the free radical density throughout the adherent polymer film, and thus it determined the level of nitroxide radical docking sites present at the microsphere’s interface for targeted reversible conjugation of small functional units. Furthermore, copolymerisation of DA and **3** facilitated the formation of a robust adherent polymer film, which is most likely attributed to multilateral cross-linking effects of DA compared to monomer **3**, where one reactive site is already occupied by the additional amide-linked TEMPO moiety. The effect was clearly observed in initial experiments when the molar ratio of DA and **3** was varied. An increased coating stability (*e.g.*, towards organic solvents) was observed with higher mole fractions of DA. Ultimately, a molar ratio of 9:1 was employed for copolymerisation of DA and **3** concomitant with *in situ* copolymer film formation onto the suspended microspheres. The coatings were performed in aqueous Tris–HCl buffer (10 mᴍ, pH 8.5) in the presence of atmospheric oxygen. The PGMA microparticles were coated for 2 d, followed by a thorough washing procedure with various organic solvents and water to remove loosely deposited oligomeric particles and unconjugated building blocks.

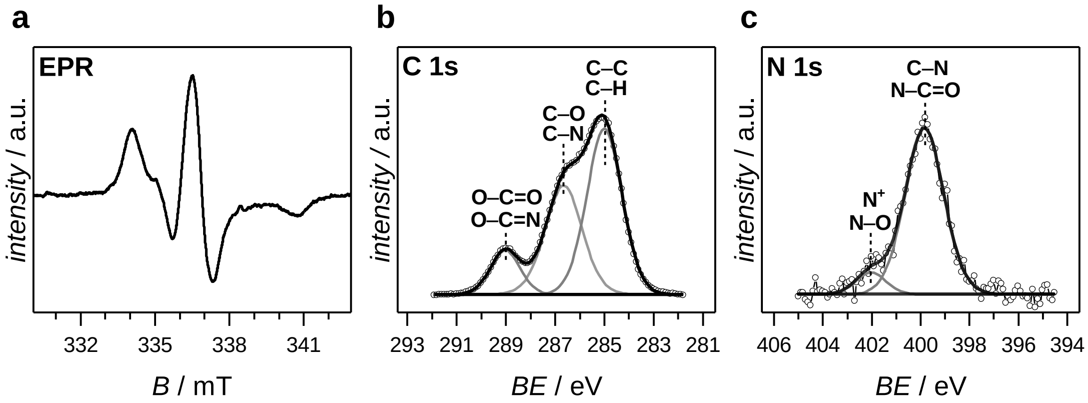

Figure 6.1. EPR and XPS characterisation of **MS1**. (**a**) EPR spectrum showing the persistent radical character of the nitroxide encased PGMA microspheres (suspended in aqueous solutions for solution state EPR analysis). (**b**) C 1s XP spectrum deconvoluted into three components: C−C and C−H (at 285.0 eV), C−O and C−N (286.6 eV), and O−C=O and N−C=O (288.9 eV) assigned to PGMA core structures and thin nitroxide functional polymer film. (**c**) N 1s XP spectrum with dominant peak at 399.8 eV assigned to poly(catecholamine) backbone structures. Minor peak at 402.0 eV corresponds to the nitroxide functional group and most likely other oxidised N-containing species. Adapted with permission from reference [339]. Copyright (2018) John Wiley and Sons.

Successful nitroxide immobilisation onto PGMA microspheres was readily evidenced by EPR spectroscopy and further supported by XPS (**Figure 6.1**). The recorded broad EPR signal depicted in **Figure 6.1a** unambiguously confirmed the presence of surface-immobilised nitroxide units onto **MS1**. However, radical quantification was not feasible employing solution state EPR spectroscopy as a rapid sedimentation of the suspended microspheres (in aqueous solution) was observed during EPR measurements. XPS analysis and deconvolution of the obtained C 1s XP spectrum (depicted in **Figure 6.1b**) only showed minor changes with respect to unmodified microspheres attributed to dominant signals derived from the underlying PGMA solid support and similar chemical composition of the encasing poly(catecholamine) thin film with nitroxide functional groups.[340] In-depth analysis of the corresponding N 1s XP spectrum, however, clearly revealed successful thin nitroxide-containing polymer film formation onto **MS1** with two deconvoluted main components (**Figure 6.1c**). The dominant peak at 399.8 eV is assigned to various PDA and poly(DOPA-TEMPO) polymer backbone structures with different environments of the nitrogen atoms (*e.g.*, cyclised indole-like, or open-chain dopamine-like structures) and the amide functional group of incorporated DOPA-TEMPO (**3**) building blocks. The nitroxyl species was identified at higher binding energies (402.0 eV), yet with only a minor contribution to the overall N 1s signal.

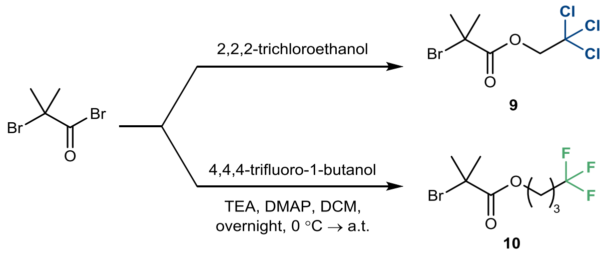

Scheme 6.2. Synthesis of 2,2,2-trichloroethyl 2-bromoisobutyrate (**9**) and 4,4,4-trifluorobutyl 2-bromoisobutyrate (**10**) for targeted NRC reactions.

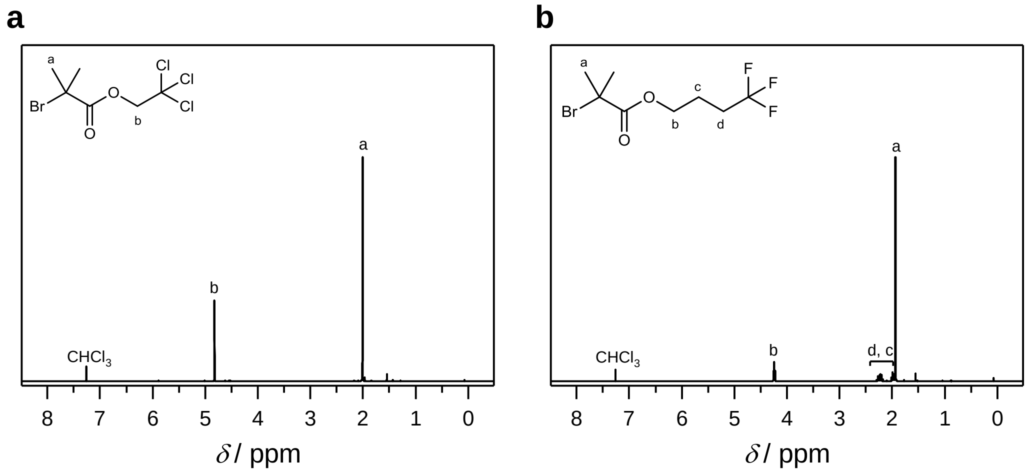

Figure 6.2. ^{1}H NMR spectra (400 MHz, $CDCl_3$, 298 K) of (**a**) chlorine-tagged NRC agent **9** and (**b**) fluorine-tagged NRC agent **10**. Adapted with permission from reference [339]. Copyright (2018) John Wiley and Sons.

Alkyl halides were chosen as suitable NRC agents to exemplify the reversible NRC coding strategy. These molecules are known to generate transient C-centered alkyl radicals in the presence of a copper/ligand catalytic system. A wide range of alkyl halides, *e.g.* 2-bromoisobutyrate derivatives are commercially available and commonly employed for the generation of reactive alkyl radical intermediates (*e.g.*, in ATRP). In the present study, however, tailor-made NRC agents were synthesised equipped with distinct alkyl halide functional side groups for good XPS contrast and consequently, facile characterisation after surface conjugation to the nitroxide functional microspheres. Specifically, 2,2,2-trichloroethyl 2-bromoisobutyrate (**9**) as well as 4,4,4-trifluorobutyl 2-bromoisobutyrate (**10**) were readily synthesised in high yields (~90%) using the corresponding chlorinated and fluorinated alcohol precursors and α-bromoisobutyryl bromide as starting materials (**Scheme 6.2**). ^{1}H NMR spectroscopy verified the successful esterification reaction evidenced by a clear shift of the methylene group adjacent to the newly formed ester linkage from 4.15 (doublet) to 4.82 ppm (singlet) for compound **9**, and from 3.71 (multiplet) to 4.24 ppm (triplet) for compound **10**, respectively (**Figure 6.2**). Further structural evidence of the successful synthesis of compound **9** and **10** was given by ^{13}C and ^{19}F NMR spectroscopy (refer to **Figures D.1–D.3** in the Appendix) as well as HR-ESI-MS.

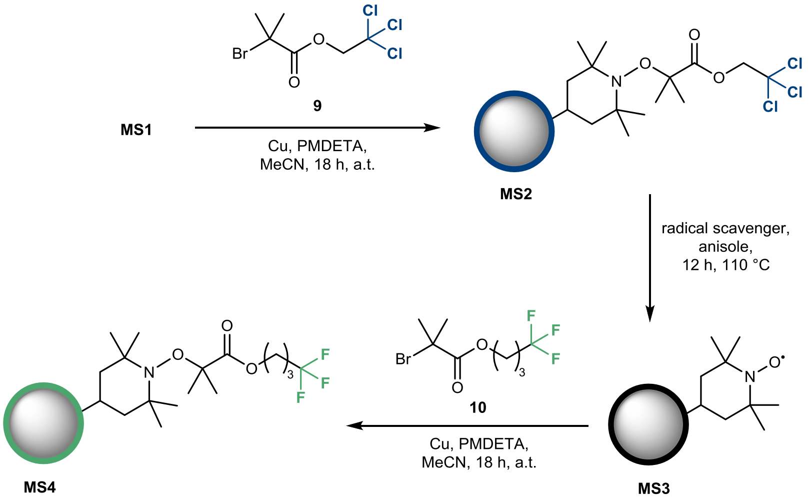

Scheme 6.3. Thermo-reversible small molecule conjugations onto nitroxide-decorated microspheres. Coding of **MS1** was performed in a copper-mediated NRC reaction with compound **9**. Subsequent thermal alkoxyamine dissociation of **MS2** was conducted in the presence of a radical scavenger (*e.g.*, TMIO or atmospheric oxygen). Re-coding of **MS3** was carried out using compound **10** as a NRC agent. Adapted with permission from reference [339]. Copyright (2018) John Wiley and Sons.

The nitroxide radical trapping reaction was performed in deoxygenated acetonitrile at ambient temperature using elemental copper and PMDETA as catalysts.[103] Coupling agent **9** was first employed for the NRC-mediated surface conjugation onto the suspended microspheres, and the reaction was performed for 18 h followed by thorough washing. Complete nitroxide radical trapping was confirmed by the loss of the nitroxide-characteristic EPR signal (**Figure 6.3a**, bottom panel). Simultaneously, a distinct Cl 2p peak (0.6 atom %) was observed during XPS analysis, which confirms the successful formation of chlorine-tagged alkoxyamine functional groups (**Figure 6.3b,** bottom panel). Beside the major peak at 200.4 eV assigned to covalently bound chlorine, a minor peak at 197.5 eV was observed, which corresponds to anionic chloride species.

Subsequently, the alkoxyamine linkages were thermally cleaved regenerating the persistent nitroxide radical character at the microsphere's interface (refer to **Scheme 6.3**). The reaction was performed at 110 °C for 12 h in deoxygenated anisole. TMIO was added to the suspension as a radical scavenger for efficient trapping of cleaved alkyl radicals. The reaction solvent was replaced after 6 h by a new TMIO-containing solution. An EPR control experiment was conducted under aerobic conditions (in the absence of TMIO radical scavenging molecules) for the unambiguous assignment of the recorded EPR signal to surface-attached nitroxide free radicals of **MS3** (**Figure 6.3a**, middle panel). Quantitative XPS analysis showed a significant decrease of the Cl 2p peak (0.2 atom %) after thermally-triggered alkoxyamine fission (**Figure 6.3b,** middle panel). A complete elimination of the chlorine peak, however, was not possible, most likely due to various radical side reactions with the surrounding polycatecholic adhesive matrix, either during initial NRC-mediated conjugation of **9** or during thermal alkoxyamine cleavage.[228]

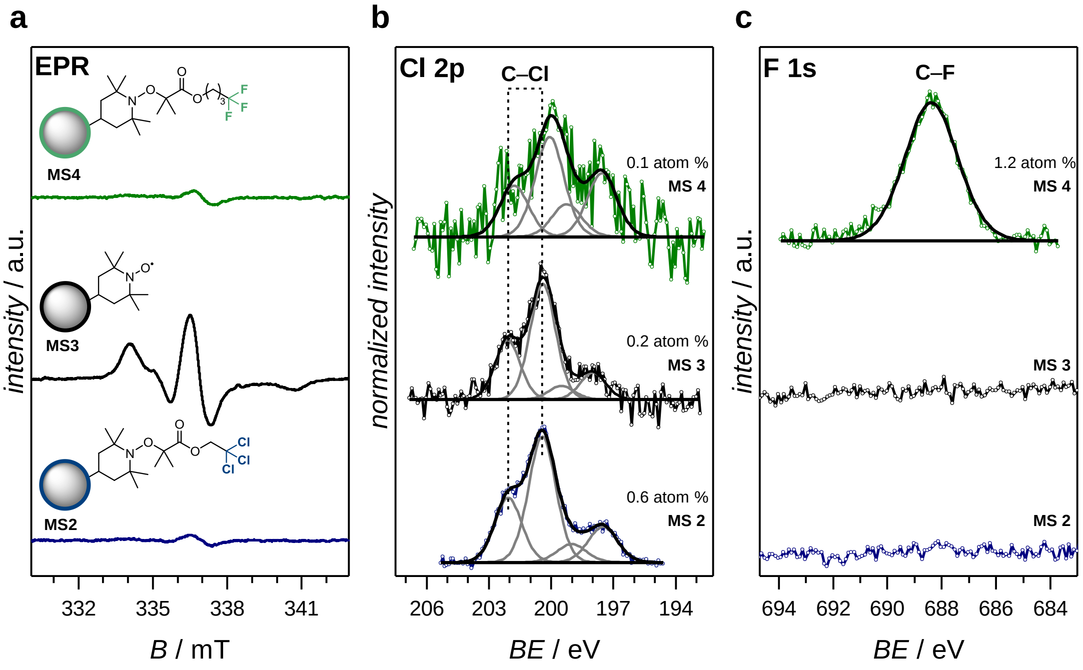

Figure 6.3. EPR and XPS characterisation of **MS2**–**MS4**. (**a**) Qualitative EPR analysis with EPR silent alkoxyamine derivatives **MS2** and **MS4** as well as EPR active **MS3**. (**b**) and (**c**) Cl 2p and F 1s XP spectra quantifying the rewritable properties of nitroxide functional microspheres based on NRC reactions and alkoxyamine fission exemplified in a small molecule conjugation study with chlorine- and fluorine-tagged NRC agents **9** and **10**. Adapted with permission from reference [339]. Copyright (2018) John Wiley and Sons.

The rewritable properties of the nitroxide functional coating system were demonstrated in a second NRC reaction employing **10** as a coupling agent. The same synthetic procedure was applied as mentioned above. A nitroxide-characteristic EPR signal was not evident during EPR analysis (**Figure 6.3a**, top panel), and the appearance of a distinct F 1s XPS signal at 688.5 eV (1.2 atom %) unambiguously confirmed successful conjugation of **10** onto the nitroxide functional microspheres (**Figure 6.3c**). Noteworthy, the selectivity of performed radical coupling reactions between *in situ* generated C-centred radical species and surface-conjugated nitroxide moieties has not been investigated with respect to other potential radical side reactions with the surrounding polycatecholic matrix. For example, the use of copper for the generation of carbon radicals must be seen critical in terms of unwanted radical side reactions with catechol functional groups.[228]

6.3 POLYMER PHOTO-CLICK SURFACE LIGATIONS WITH SPATIAL RESOLUTION

The versatile and broad applicability of nitroxide functional surfaces was further expanded for advanced *grafting to* polymer surface ligation of photoactive PMMA and PTFEMA polymer strands in spatially confined areas (**Scheme 6.4**).

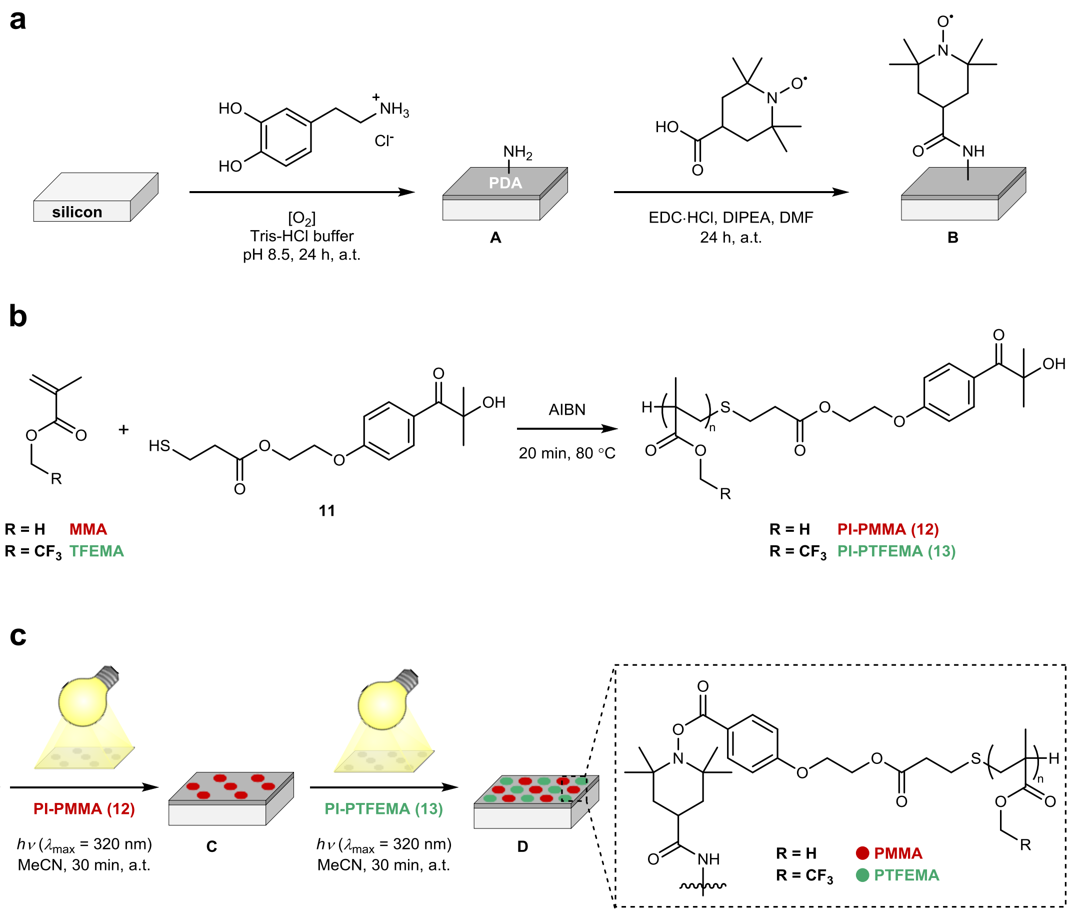
a
HO
HO
$\overset{+}{N}H_3$
Cl^-
silicon
$[O_2]$
Tris-HCl buffer
pH 8.5, 24 h, a.t.
NH_2
PDA
A
HO
O
N
O•
EDC·HCl, DIPEA, DMF
24 h, a.t.
NH
B
b
O
R
+
HS
O
OH
11
AIBN
20 min, 80 °C
H
S
n
R = H MMA
R = CF_3 TFEMA
R = H PI-PMMA (12)
R = CF_3 PI-PTFEMA (13)
c
B
PI-PMMA (12)
hν (λ_{max} = 320 nm)
MeCN, 30 min, a.t.
C
PI-PTFEMA (13)
hν (λ_{max} = 320 nm)
MeCN, 30 min, a.t.
D
R = H ● PMMA
R = CF_3 ● PTFEMA

Scheme 6.4. Synthetic overview for the preparation of nitroxide-decorated PDA surfaces employed for photopatterning with PI-terminated polymer strands. (**a**) Oxidative DA polymerisation concomitant with PDA surface deposition onto silicon substrates and subsequent nitroxide ad-layer surface functionalisation in an EDC-mediated amide coupling reaction of PDA incorporated free amino side chains and 4-carboxy-TEMPO. (**b**) Chain transfer polymerisations of MMA and TFEMA in the presence of thiol-functionalised Irgacure 2959 (**11**) yielding end group photoreactive PI-PMMA (**12**, M_n = 7000 g·mol^{-1}) and PI-PTFEMA (**13**, M_n = 12000 g·mol^{-1}) polymer strands. (**c**) Consecutive surface photopatterning with **12** and **13** onto nitroxide-functionalised PDA surface **B**. Adapted with permission from reference [339]. Copyright (2018) John Wiley and Sons.

The herein presented nitroxide surface decoration was achieved in a simple PDA post-modification route, a commonly applied synthetic strategy for substrate-independent functionalisations of material interfaces (refer to Chapter 2.2.3).[203] PDA-coated surfaces were readily prepared in an aerobic DA polymerisation and PDA surface deposition onto the immersed silicon wafers, which were employed as model substrates (**Scheme 6.4a**). The coating was performed according to a previously reported literature procedure using a Tris–HCl buffered (10 mM, pH 8.5) coating solution of DA ($2\ \mathrm{mg \cdot ml^{-1}}$). The obtained PDA-coated surfaces served thereafter as a platform for the immobilisation of nitroxide functional groups onto the surface. Several synthetic strategies have been proposed in the literature for the post-modification of PDA including amidation reactions with PDA incorporated free amino functional groups.[266, 270] Commercially available 4-carboxy-TEMPO was covalently linked to PDA in an EDC-mediated amide coupling reaction. Successful nitroxide surface immobilisation was evidenced by ToF-SIMS and the appearance of the nitroxide-characteristic $[\mathrm{NO}]^-$ fragment at *m/z* 30.00 (**Figure 6.4a**). In agreement, ToF-SIMS analysis of precursor surface **A** did not show the nitroxyl-assigned peak at *m/z* 30.00. Other TEMPO-characteristic peaks (including the newly formed amide linkage between the nitroxide and PDA) could not be identified by ToF-SIMS due to overlapping peaks associated with the underlying PDA layer. In analogy, the deconvolution of the C 1s XP spectrum of surface **B** (**Figure 6.4b**) was dominated by strong and overlapping peaks derived from the underlying PDA matrix, and thus clear assignment of nitroxide functional groups conjugated to PDA was not feasible by XPS. Similar observations have been made before for an analogous PDA system.[266]

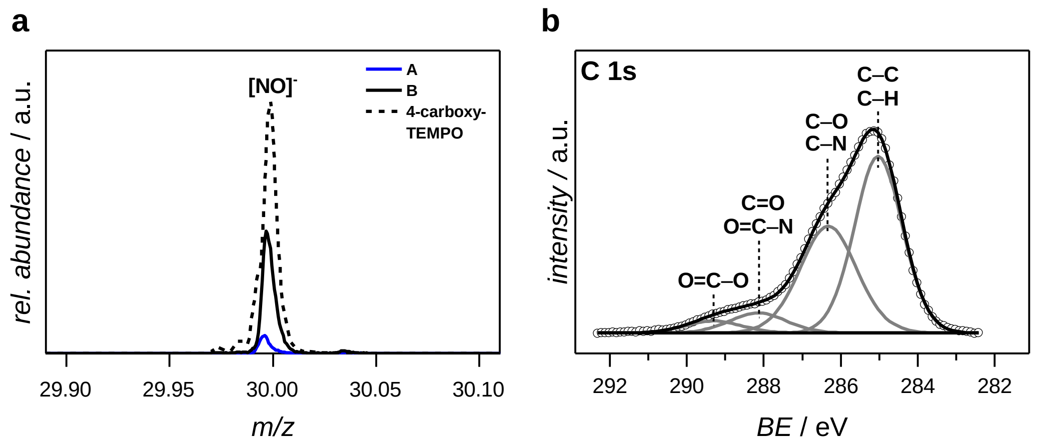

Figure 6.4. ToF-SIMS and XPS characterisation of precursor surfaces **A** and **B**. (**a**) (−)ToF-SIMS spectra of non-functionalised (**A**) and nitroxide conjugated (**B**) surfaces. The nitroxide immobilisation (**B**, black solid line) onto PDA precoated Si substrates (**A**, blue solid line) was evidenced by the appearance of the $[NO]^-$ fragment at *m/z* 30.00. 4-carboxy-TEMPO (black dashed line) served as a reference. (**b**) C 1s XP spectrum of surface **B** deconvoluted into four components: C−C and C−H (at 285.0 eV), C−O and C−N (286.3 eV), C=O and N−C=O (288.1 eV), and O−C=O (289.3 eV) assigned to PDA with only minor contribution of the surface-immobilised nitroxide functional groups. Adapted with permission from reference [339]. Copyright (2018) John Wiley and Sons.

Photo-induced *grafting to* dual polymer ligations in spatially confined areas was achieved using a well-established photo-coupling system based on α-hydroxyalkylphenylketone PIs, which undergo clean Norrish-type I cleavage upon UV irradiation. PI end group terminated polymers were readily prepared *via* chain transfer polymerisations of MMA and TFEMA, respectively, in the presence of a thiol-functionalised Irgacure 2959 derivative (**11**) employed as a transfer agent (refer to **Scheme 6.4b)**. Compound **11** was obtained through esterification of commercially available Irgacure 2959 with 3-mercaptopropionic acid (corresponding ^1H and ^{13}C NMR spectra of **11** are depicted in **Figures D.4** and **D.5** in the Appendix).

PI end group capped synthetic polymers, denoted as PI-PMMA (**12**) and PI-PTFEMA (**13**), were obtained with molecular weights (M_n) of 7000 g·mol^{-1} for polymer **12**, and 12000 g·mol^{-1} for polymer **13**, respectively, as determined by SEC (refer to **Figure D.6** in the Appendix). Polymer surface photoligations with **12** and **13** were carried out in deoxygenated acetonitrile at ambient temperature and surface **B** was covered by a shadow mask prior to UV irradiation (λ_{max} = 320 nm) (refer to **Scheme 6.4c**). The photo-click NRC reaction using polymer **12** was performed for 30 min, and subsequent polymer ligation with polymer **13** was conducted likewise using the PMMA pre-patterned surface **C** and a complementary shadow mask for spatially resolved dual polymer surface ligation.

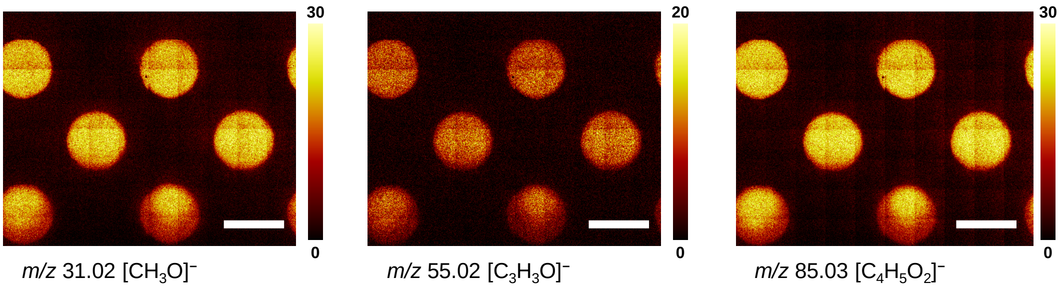

Figure 6.5. ToF-SIMS images of PMMA patterned surface **C**. PMMA-characteristic fragments were exclusively detected in confined areas which had been exposed to UV irradiation. Adapted with permission from reference [339]. Copyright (2018) John Wiley and Sons.

Initial surface photopatterning with PI-PMMA (**12**) was successfully evidenced by ToF-SIMS imaging of surface **C** (**Figure 6.5**). PMMA-characteristic fragments such as $[CH_3O]^-$, $[C_3H_3O]^-$, and $[C_4H_5O_2]^-$ appearing at *m/z* 31.02, 55.02 and 85.03, respectively, were identified exclusively in spatially confined areas which had been exposed to UV irradiation.

Complementary dual surface coding with PI-PTFEMA (**13**) yielding surface **D** was likewise characterised by ToF-SIMS imaging and further supported by XPS mapping (**Figure 6.6**). The ToF-SIMS overlay image of surface **D** (**Figure 6.6b**) clearly shows distinct $[F]^-$ and $[CF_3]^-$ fragments (green) derived from surface attached PTFEMA polymer strands appearing adjacent to the previously conjugated PMMA strands with characteristic $[CH_3O]^-$ fragments (red). F 1s XPS imaging further evidenced successful PTFEMA patterning onto surface **D** (**Figure 6.6c**). Adjacent surface attached PMMA polymer strands, however, could not be visualised by XPS imaging (*e.g.*, *via* the C 1s peak) due to close similarities with the underlying PDA layer.

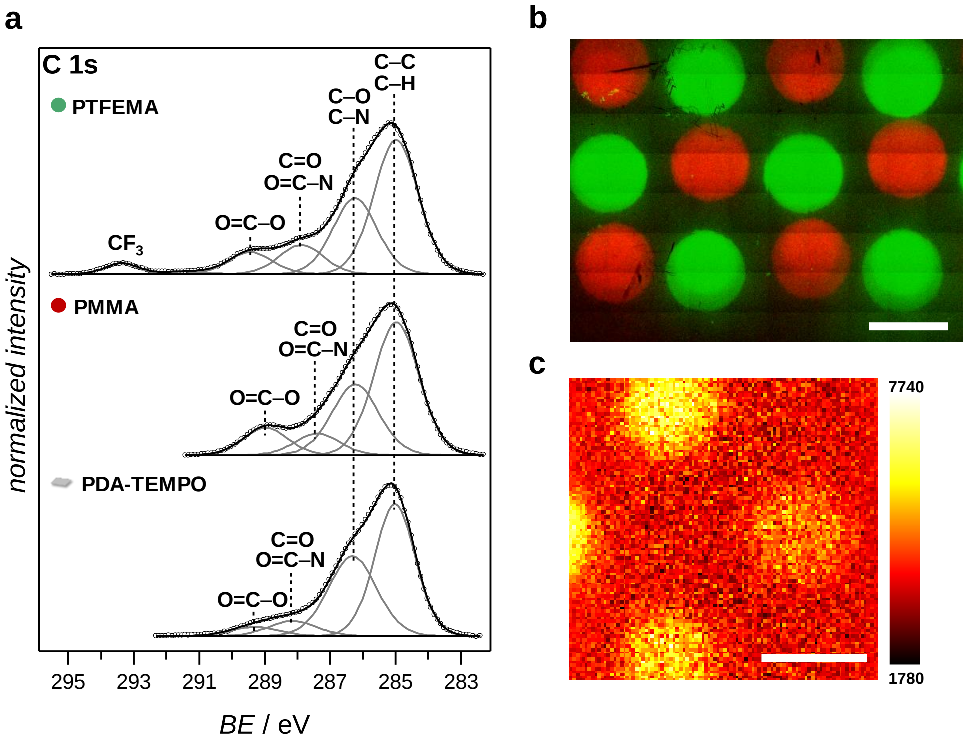

Figure 6.6. XPS and ToF-SIMS characterisation of dual polymer conjugated surface **D**. a) C 1s XP spectra obtained from polymer conjugated and unconjugated areas. PMMA surface ligation in defined areas was evidenced by a pronounced O−C=O peak (at 289.0 eV) in comparison to the underlying PDA-TEMPO matrix derived from methyl methacrylate polymer repeating units. Adjacent PTFEMA polymer strands were unambiguously identified showing a distinct CF_3 signal at 293.4 eV. b) ToF-SIMS overlay image constructed from images of PMMA-characteristic $[CH_3O]^-$ fragments (red), and PTFEMA derived $[F]^-$ and $[CF_3]^-$ fragments (green). c) F 1s XPS mapping (688.6 eV) with distinct pattern derived from PTFEMA polymer strands. Scale bars represent 1 mm. Adapted with permission from reference [339]. Copyright (2018) John Wiley and Sons.

XPS surface mapping and the acquisition of high-resolution C 1s XP spectra at polymer conjugated and non-conjugated areas, however, confirmed the presence of both polymer strands in close spatial proximity (**Figure 6.6a**). PMMA conjugated areas clearly showed an increased O=C−O peak (at 289.0 eV) compared to the underlying PDA layer with a minor peak assigned to O=C−O.[266] Surface attachment of polymer **13** with fluoroalkyl side chains was evidenced by the appearance of a characteristic $-CF_3$ signal (at 293.4 eV) in the C 1s XP spectrum, and was further confirmed by the presence of a fluorine signal in the corresponding F 1s XP spectrum (refer to **Figure D.7** in the Appendix). Critically, and as already discussed for the reversible coding and decoding of nitroxide functional microspheres in Chapter 6.2, control experiments using compound **13** and PDA-coated surface **A** (lacking the nitroxide functional groups) showed significant radical side reactions with the underlying PDA matrix.[343] A precise evaluation of the photo-induced and radical-driven polymer surface immobilisation either implemented *via* NRC or other unidentifiable radical couplings with PDA was not feasible.

6.4 CONCLUSION

In summary, the previously introduced nitroxide functional coating platform based on catecholamine polymerisation was herein exploited for temporally and spatially controlled coding of various material interfaces with small molecules and polymer strands. The coating strategy for the generation of nitroxide functional surfaces was expanded in terms of the type of the underlying material and further, dopamine was introduced as a comonomer to control the coating stability. A thermo-reversible protocol for the post-coating conjugation of nitroxide-decorated polymeric microspheres with small functional units was established and the rewritable coding properties were critically discussed. Thereafter, the light-induced dual polymer surface ligation onto PDA precoated and nitroxide-decorated silicon substrates was presented. Photoinitiator end group terminated synthetic polymer strands were ligated to the surface in rapid photo-click reactions with spatial resolution. Overall, a sophisticated avenue for precise programming of material interfaces was presented using the versatile nitroxide coating strategy. The broad applicability of nitroxide functional surfaces is further expanded in the following chapter investigating their antibiofilm properties.

Chapter 7: Versatile Antibiofilm Coatings

7.1 PREFACE

Bacterial surface colonisation and subsequent biofilm formation is of utmost concern in global public health.[8] The eradication of a biofilm, once it has matured on a surface, often fails using standard antimicrobial agents.[11] Therefore, biofilm preventing countermeasures, *e.g.* antibiofilm surface coatings of medical devices, such as indwelling implants, are urgently needed to reduce biofilm-related infections in hospitals worldwide. Nitroxides have emerged as potential antibiofilm agents owing to their nitric oxide mimetic character, which is an important signalling molecule in the lifecycle of a biofilm.[344] Sublethal doses of nitroxides inhibit initial biofilm formation by Gram-negative bacteria.[4] Furthermore, nitroxides disperse existing biofilms and can potentiate biofilm eradication therapies in combination with standard antibiotics.[5]

The current chapter presents a sophisticated and widely applicable nitroxide-containing coating strategy specifically designed for the prevention of biofilm formation on surfaces. Detailed structural and mechanistic insights, which have been gained on poly(DOPA-TEMPO) coatings in previous chapters, were herein translated into a substrate-independent antibiofilm coating procedure with spatial precision. First, a reference polymer coating system was introduced for the precise biological evaluation of the polymer coating itself: with and without polymer embedded nitroxides. A cyclohexyl (Cy) functional DOPA derivative, denoted as DOPA-Cy, was readily synthesised and subsequently employed as a coating agent for the generation of poly(DOPA-Cy)-coated surfaces. The polymerisation and the surface coatings using DOPA-TEMPO and DOPA-Cy as monomers were carried out under optimised conditions in an alkaline Tris–HCl buffer system using atmospheric oxygen as a mild oxidant. Poly(DOPA-TEMPO) and poly(DOPA-Cy)-coated

---

The biofilm studies presented in the current chapter were conducted during research fieldwork under supervision of Prof. Dr. R.E.W. Hancock at the Department of Microbiology and Immunology at the University of British Columbia (UBC, Vancouver, Canada). Preliminary biofilm studies were performed by S. C. Mansour and M. J. Trimble (UBC). M. J. Trimble supervised the herein presented biofilm experiments. The GFP-labelled PA14 strain was kindly provided by D. Pletzer (UBC). XPS characterisation was conducted by V. Trouillet (KIT), ToF-SIMS measurements were performed by A. Welle (KIT).

hydroxyapatite (HA) and titanium surfaces were exposed to *P. aeruginosa* surface colonisation in a flow cell experimental setup. A GFP-labelled PA14 strain was employed and the biofilm formation on uncoated and polymer-coated substrates was assessed by confocal laser scanning microscopy (CLSM). Synergistic effects between nitroxides and antibiotics were studied using standard antibiotic ciprofloxacin in biofilm eradication assays. Finally, a sophisticated photopatterning protocol was established for the spatially controlled poly(DOPA-TEMPO) surface immobilisation onto titanium implants. Successful polymer surface patterning with submillimeter resolution was evidenced by advanced ToF-SIMS and XPS characterisation techniques and the localised nitroxide-stemming antibiofilm properties were subsequently assessed in static biofilm assays.

7.2 SYNTHESIS OF DOPA-CY AS A REFERENCE COATING AGENT

For the precise biological evaluation of potential antibiofilm properties evolving from nitroxide-expressing poly(DOPA-TEMPO) coatings it was crucial to consider potential side effects stemming from the surrounding poly(DOPA) adhesive matrix. In fact, certain antibacterial properties have been reported for poly(dopamine) coatings (dependent on the PDA surface roughness) against Gram-positive and Gram-negative bacteria.[313] Therefore, it was aimed to examine the biocompatibility of the polymer matrix itself (without nitroxide embedment) in terms potential antibacterial or antifouling properties. The use of DA or L-DOPA was initially considered as suitable reference coating agents. Previously presented and literature-reported observations, however, have clearly shown that both (bare) polymer systems exhibit different intrinsic properties compared to the nitroxide-containing poly(DOPA-TEMPO) coating system.[239, 252] Distinct features encompass the monomer reactivity and the polymerisation behaviour, the intra- and intermolecular structural connectivities (including noncovalent driving forces) as well as the resulting cohesive and adhesive properties. All the above-mentioned factors determine the overall coating morphology and stability, and strongly impact the biocompatibility of these coatings. Thus, poly(dopamine) as well as poly(L-DOPA) coatings were not considered to be suitable negative controls to examine the biocompatibility of the adhesive poly(catecholamine) matrix.[313] Instead, a tailor-made polymer coating system was introduced equipped with (bioinactive) cyclohexyl residues present in the polymer side chains. The cyclohexyl functional group was taken as an ideal TEMPO substitute due to their close structural similarities assuming similar polymerisation behaviour. In analogy to previous coating protocols, a suitable monomer (denoted as DOPA-Cy) was first synthesised composed of a polymerisable DOPA structural motif and a cyclohexyl functional group (**Scheme 7.1**).

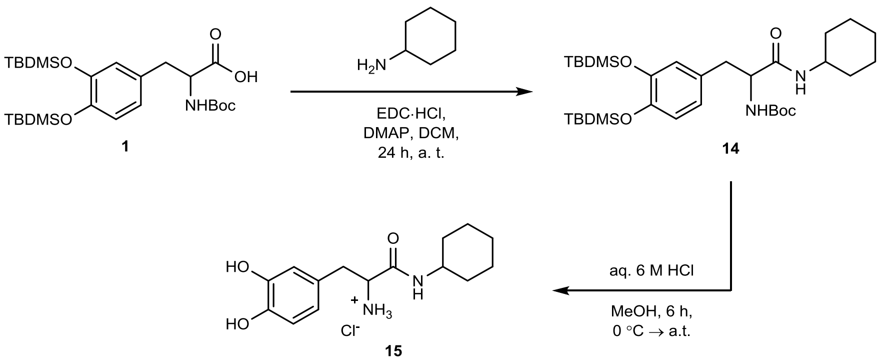

Scheme 7.1. Synthetic pathway for the preparation of DOPA-Cy (**15**), isolated as the corresponding hydrochloride salt.

In brief, DOPA-Cy (**15**) was prepared according to the general synthetic protocol (refer to Chapter 3.2) using $(TBDMS)_2$-*N*-Boc-DOPA (**1**) and commercially available cyclohexylamine as starting materials. TBDMS and Boc protected intermediate **14** was isolated in high yield (82%) after an EDC-mediated amide coupling reaction and purification by column chromatography. The successful synthesis of **14** was confirmed by ^1H and ^{13}C NMR spectroscopy (refer to **Figures E.1** and **E.2** in the Appendix) as well as HR-ESI-MS with $[M+Na]^+$ at *m/z*(exp) 629.3777 (*m/z*(theo) 629.3776). The subsequent cleavage of both protecting groups was carried out under acidic (HCl) conditions and the monomer DOPA-Cy (**15**) was isolated as the corresponding hydrochloride salt in quantitative yield.

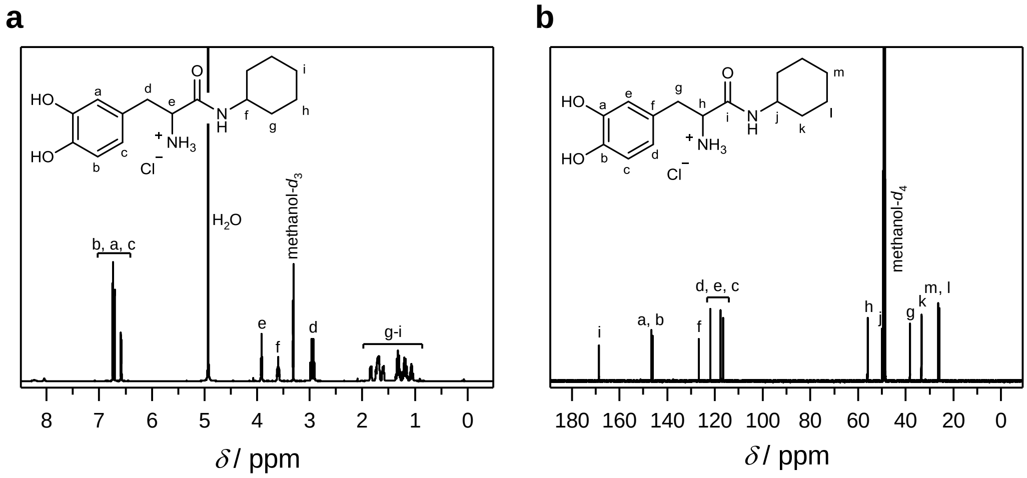

Figure 7.1. NMR spectroscopic characterisation of **15**. (**a**) ^{1}H NMR (600 MHz) and (**b**) ^{13}C NMR spectra (151 MHz) of DOPA-Cy (**15**) were recorded in methanol-d_4 at 298 K.

^{1}H and ^{13}C NMR spectroscopy confirmed the successful synthesis of monomer **15** (**Figure 7.1**). No redox defects of the catechol functional group (*e.g.*, oxidised *o*-quinoic species) were observed in the corresponding NMR spectra. Additional structural evidence for **15** was given by HR-ESI-MS with *m/z*(exp) 279.1702 $[M-Cl]^+$ (*m/z*(theo) 279.1703) assigned to the chloride non-coordinated species of **15**.

7.3 MANUFACTURING OF TEMPO- AND CY-CONTAINING POLYMER COATINGS

Before the preparation of antibiofilm coatings was undertaken, the biocompatibility of the underlying substrate was first critically assessed in preliminary biofilm experiments. Various surfaces (*e.g.*, those which have been employed as underlying materials for poly(DOPA-TEMPO) (**3**) coatings presented in Chapter 5.2) were examined in terms of their biofilm growth promoting properties for later comparative biofilm assays with polymer-coated analogous surfaces. Silicon wafers, which have been employed as model substrates in the previous chapters owing to their excellent surface characterisation properties, were found to not be suitable for *in vitro* biofilm studies. Initial surface attachment of planktonic bacteria, for instance, was strongly hampered due to the ultra-smooth surface properties of the employed Si wafers, and thus adequate biofilm formation was not observed. Other materials, including PTFE, only showed minor biofilm formation with significant amounts of dead cells adherent on the surface indicating unfavourable biofilm growth conditions. However, the versatile and substrate-independent coating approach employing DOPA-TEMPO (**3**) as the coating agent allows the facile surface modification of every type of material, including those with well-known biofilm-promoting surface properties. Hydroxyapatite discs were chosen as model substrates, which have been extensively exploited in biofilm and dental research for their excellent biofilm surface compatibilities.[345-346] In addition, titanium substrates exhibit likewise good inherent surface properties for biofilm studies. Furthermore, titanium is of high biomedical relevance as a composite material for medical devices and implants, which are — as any other type of object and surface in the hospital — vulnerable to biofilm proliferation. Titanium model implants (medical grade) were commercially purchased for the herein presented *in vitro* biofilm experiments and with regard to prospective *in vivo* studies with indwelling Ti implants.[347]

HA and Ti substrates were typically coated for 24 h under optimised conditions (40 mM of coating agent **3** or **15**, 100 mM Tris–HCl buffer, adjusted to pH 9.25) followed by thorough washing with water (**Scheme 7.2**).[257] All coatings were performed under sterile conditions.

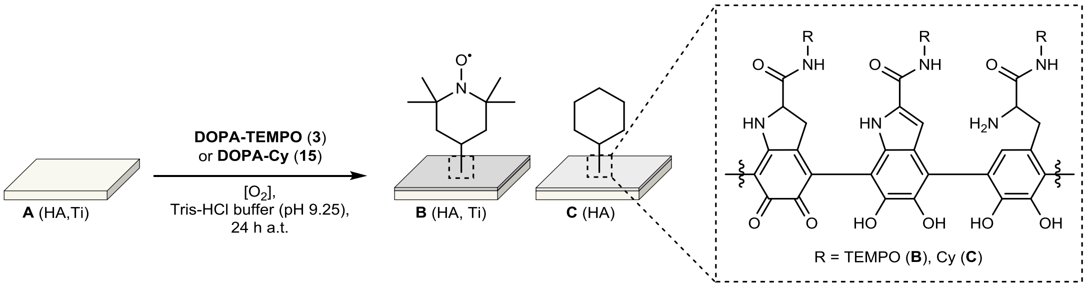

Scheme 7.2. Synthetic route for preparation of nitroxide- and cyclohexyl-containing polymer-coated HA and Ti substrates. The oxidative polymerisation of DOPA-TEMPO (**3**) (40 mM) and DOPA-Cy (**15**) (40 mM) with *in situ* polymer surface deposition was performed in Tris–HCl buffer (100 mM, pH 9.25) in the presence of atmospheric oxygen for 24 h.

The poly(DOPA-TEMPO) (**B**) and poly(DOPA-Cy) (**C**) coated HA surfaces were characterised by XPS and ToF-SIMS (please note that the nitroxide-coated Ti analogous surface has been previously characterised in Chapter 5.2). The corresponding C 1s XP spectra of the polymer-coated surfaces **B** and **C** showed almost identical chemical compositions (**Figure 7.2a**). In fact, both polymer coatings are composed of the same poly(DOPA amide) scaffold with various but similar incorporated building blocks as indicated in **Scheme 7.2**. In addition, the different polymer side chains (TEMPO and Cy) possess likewise close structural similarities. The presence of the *N*-heterocyclic TEMPO residues, however, have resulted in a more pronounced peak at 286.2 eV in the C 1s XP spectrum (**Figure 7.2a**, bottom panel), which is assigned to C–N (and C–O) structural connectivities (in comparison to the homocyclic residues of the poly(DOPA-Cy)-coated surface **C** depicted in **Figure 7.2a**, top panel).

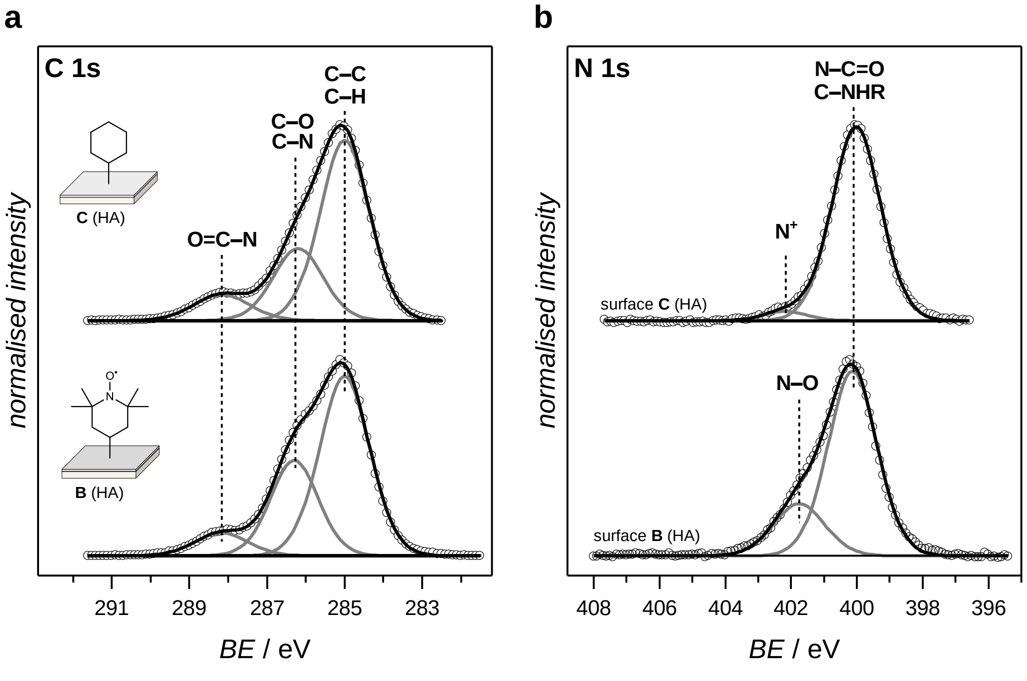

Figure 7.2. XPS characterisation of poly(DOPA-Cy) (**C**, top row) and poly(DOPA-TEMPO) (**B**, bottom row) coated HA substrates: (**a**) C 1s and (**b**) N 1s high-resolution XP spectra.

A more obvious difference between surfaces **B** and **C** was demonstrated in the corresponding N 1s XP spectra (**Figure 7.2b**). The N 1s XP spectrum of the poly(DOPA-TEMPO)-coated surface **B** (**Figure 7.2b**, bottom panel) was deconvoluted into two nitrogen components. According to previous XPS results (refer to Chapter 5.3), the dominant peak (at 400.1 eV, 9.2 atom %) was assigned to various poly(DOPA amide) structures constituting the polymer backbone. The presence of nitroxide side chains, however, was recognised as an additional peak appearing at higher BEs (401.8 eV, 2.7 atom %). Other redox states of the nitroxyl moiety such as higher oxidised species (refer to the N 1s XP spectrum depicted in **Figure 5.1b**) were not evident at higher BEs. The corresponding N 1s XP spectrum of the poly(DOPA-Cy)-coated surface **C** (**Figure 7.2b**, top panel) showed likewise a dominant peak (at 400.1 eV, 9.6 atom %), which corresponds to various *N*-containing DOPA amide building blocks along the polymer backbone. A broad shoulder at higher BEs, however, was not evident in the XP spectrum, which unambiguously confirmed the lack of TEMPO moieties present in poly(DOPA-Cy) analogous system. Instead, a peak of weak intensity present at higher BEs (at 402.1 eV, 0.5 atom %) most likely corresponds to protonated amine species of the polymer backbone.

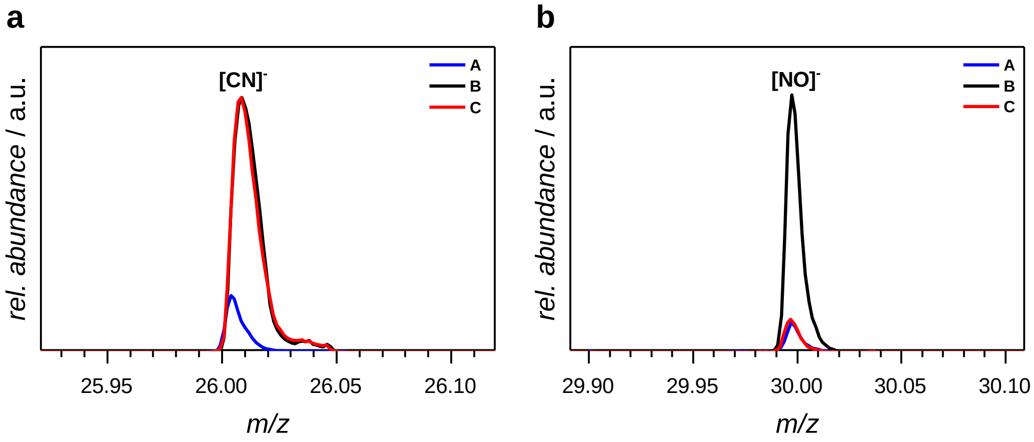

Figure 7.3. (−)ToF-SIMS characterisation of uncoated and polymer-coated HA surfaces. (**a**) The peak at *m/z* 26.01 was assigned to polymer-characteristic $[CN]^-$ fragments (*m/z*(theo) 26.00), detected on polymer-coated surfaces **B** and **C** (black and red solid lines). (**b**) The nitroxide-characteristic $[NO]^-$ fragment at *m/z* 30.00 was exclusively detected on the TEMPO-functionalised surface **B**. Uncoated HA (surface **A**, blue solid line) and cyclohexyl conjugated surface **C** did not show the nitroxyl characteristic peak.

ToF-SIMS measurements were obtained to further investigate the structure of the polymer-coated and uncoated HA surfaces**.** Both modified surfaces **B** and **C,** composed of identical polymer backbone structures, showed dominant peaks at *m/z* 26.01 corresponding to polymer-derived $[CN]^-$ fragments (*m/z*(theo) 26.00) (**Figure 7.3a**).[263] The nitroxide-characteristic $[NO]^-$ fragment at *m/z* 30.00, however, was exclusively detected on surface **B** (**Figure 7.3b**). Overall, both surface characterisation techniques unambiguously confirmed the successful polymer surface modifications of HA substrates. In addition, the key structural differences derived from the TEMPO and Cy residues present in the polymer side chains have been highlighted.

7.4 *P. AERUGINOSA* BIOFILM CULTIVATION AND ERADICATION ASSAYS

Bacterial biofilm assays were performed with *P. aeruginosa* — a Gram-negative opportunistic pathogen with clinical and economic burden in worldwide healthcare systems. Furthermore, *P. aeruginosa* has become a model microorganism in biofilm research, including recent studies using nitroxides and nitric oxide as potent antibiofilm agents.[3-5, 287, 305, 348] A GFP-labelled PA14 strain was employed for the direct visualisation of surface-adherent biomass assessed by confocal laser scanning microscopy (CLSM). Other virulent PA strains, such as PAO1[284] have been tested in preliminary *in vitro* biofilm experiments with similar results compared to PA14. The quantification of biofilm formation by crystal violet staining only showed limited success due to strong (unspecific) polymer–dye interactions.[349] In the herein presented subchapter, coated and uncoated substrates **A**–**C** were exposed to PA14 surface colonisation under flow conditions using basal medium 2 (BM2) as a minimal medium.[4] The substrates were placed adjacently within the same convertible flow cell chamber prior to PA14 inoculation and biofilm cultivation was performed for 72 h.

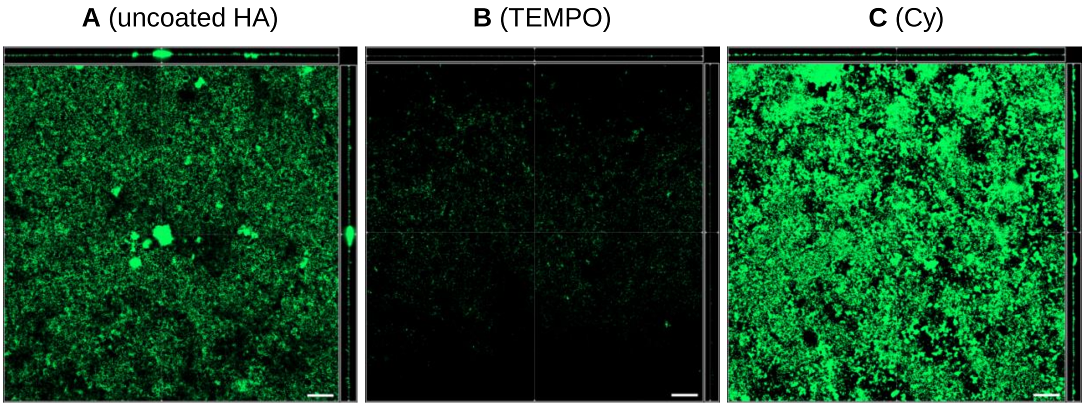

Figure 7.4. *P. aeruginosa* biofilm cultivation on unmodified and polymer-coated HA surfaces. Uncoated (**A**), nitroxide polymer-coated (**B**), and cyclohexyl polymer-coated (**C**) surfaces were exposed to PA14 surface colonisation for 72 h in a flow cell system at 37 °C. Biofilm surface coverage of the employed GFP-tagged PA14 strain was assessed by CLSM. The scale bars represent 50 µm in length. Each panel shows the *xy*, *yz* and *xz* dimensions.

The comparison of the GFP fluorescence on surfaces **A**–**C** unambiguously demonstrated the great antibiofilm properties stemming from surface-immobilised nitroxides with representative confocal images displayed in **Figure 7.4**. Uncoated HA (**Figure 7.4**, left image) showed a widespread PA14 biofilm surface coverage with elaborate biofilm structures spotted on the surface (some of them exceed 15 µm in all three dimensions). In addition, no dead cells were evident on surface **A** as shown in supplementary dead cell staining experiments using propidium iodide (PI) (refer to **Figure E.3** in the Appendix). Thus, optimal biofilm growth was encountered on surface **A**, which served as a control experiment for the direct comparison with polymer-coated analogues. The confocal microscopy image of the nitroxide-functionalised surface **B** only demonstrated a weak fluorescence response. As clearly evident in **Figure 7.4** (centred image), biofilm formation was completely suppressed on surface **B** due to the nitroxide polymer matrix covering the underlying HA surface. Only planktonic bacteria and minor microcolonies were detected on surface **B**. Furthermore, the nonbactericidal properties of surface **B** were confirmed in additional dead cell staining experiments (refer to **Figure E.3** in the Appendix).

The second polymer coating system (surface **C**) bearing cyclohexyl functional polymer side groups was completely covered by a biofilm. Surprisingly, the bacterial biomass, detected on surface **C** by its inherent fluorescence (GFP), was more evident compared to biomass adherent on surface **A.** This indicates certain biofilm promoting properties stemming from the polymer coating. The uniform biofilm coverage on surface **C**, however, was less pronounced in the third dimension (*i.e.*, biofilm thickness). This observation might be attributed to an enhanced bacterial embedment of PA14 into the soft polymer matrix present on surface **C**. The biofilm-promoting effect of the polymer matrix, however, was completely compensated when TEMPO was incorporated into the polymer adhesive system (surface **B**) as previously discussed. The comparison of both polymer coating systems (surfaces **B** and **C**) clearly demonstrated that the antibiofilm coating effect solely derived from the polymer-embedded nitroxide functional groups and not from the surrounding polymer matrix. In addition, no (synergistic) antifouling or antimicrobial effects stemming from the polymer matrix itself were seen.

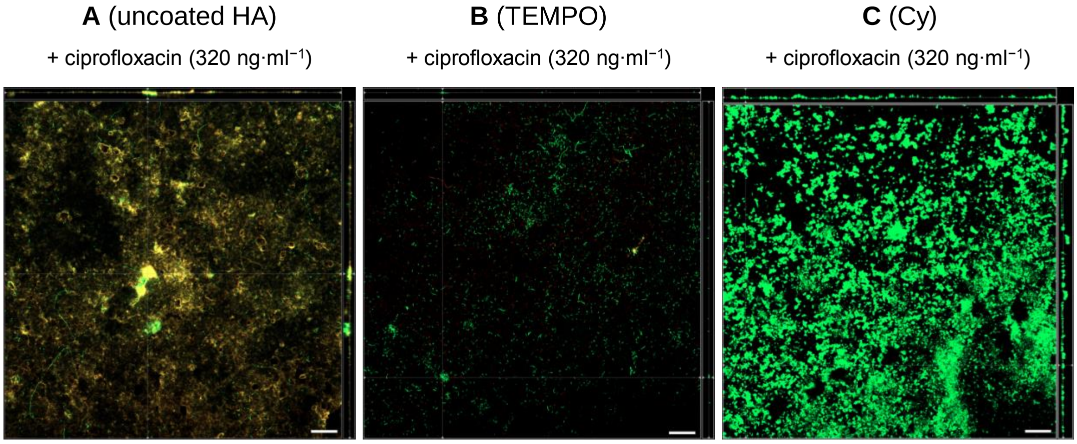
A (uncoated HA)
+ ciprofloxacin (320 ng·ml⁻¹)
B (TEMPO)
+ ciprofloxacin (320 ng·ml⁻¹)
C (Cy)
+ ciprofloxacin (320 ng·ml⁻¹)

Figure 7.5. *P. aeruginosa* biofilm eradication assays with antibiotic ciprofloxacin. PA14 surface colonisation on surfaces **A**–**C** was performed in a flow cell system (37 °C) for 72 h with addition of ciprofloxacin (320 ng·ml^{-1}) after 48 h. Dead cells were stained with propidium iodide (red) prior to confocal microscopy. Merged images composed of PI and GFP channels are displayed and superimposed fluorescence response of live (green) and dead cells (red) appear yellow. The scale bars represent 50 µm in length. Each panel shows the *xy*, *yz* and *xz* dimensions.

Additional antimicrobial eradication experiments were performed in order to investigate the synergistic effects stemming from the nitroxide-induced inhibition of biofilm formation and standard antibiotic therapy.[5] Bacteria within a biofilm are typically hard to treat once a mature biofilm has formed on a surface, and thus biofilm-preventing surface coatings can critically substitute or reduce the use of conventional (biofilm-ineffective) antibiotics. PA14 biofilms were cultivated on surfaces **A**–**C** for 48 h and subsequently exposed to ciprofloxacin at its minimum inhibitory concentration (MIC) (320 ng·ml^{-1})[5] for additional 24 h under flow conditions. Ciprofloxacin is a standard antibiotic for Gram-negative *P. aeruginosa* and the MIC value is the minimal concentration required for inhibition of planktonic cell growth. As shown on the uncoated HA substrate (surface **A**, refer to **Figure 7.5**), the treatment of preformed biofilms with the antibiotic ciprofloxacin clearly failed to eradicate the bacteria within a biofilm due to its recalcitrance to antibiotics at MIC concentrations. Instead, live and dead cells were coexistent on surface **A** (depicted in yellow in **Figure 7.5** by superimposition of green (GFP) and red (PI) fluorescence). The nitroxide-decorated surface **B**, however, remained free from any bacterial proliferation. No dead adherent cells were detected on surface **B** as it is also unlikely to occur under the employed flow conditions. Polymer-coated surface **C** showed a significantly reduced biofilm biomass after treatment with ciprofloxacin. In contrast to the uncoated surface **A**, however, no dead cells were detected on surface **C**.

Similar observations were made when titanium was employed as a substrate (**Figure 7.6**). Extensive biofilm formation on uncoated Ti (surface **A**) was observed (**Figure 7.6**, top left image), which was similar to that detected on uncoated HA (refer to **Figure 7.4**). The nitroxide-coated surface **B,** most strikingly, showed no fluorescence at all when assessed by CLSM. This implies that planktonic surface attachment as well as biofilm formation were completely inhibited after the surface modification with poly(DOPA-TEMPO) (**Figure 7.6**, top right image). Additional antibiotic treatment with ciprofloxacin (320 ng·ml^{-1}) on preformed biofilms (48 h) for 24 h completely failed to eradicate the surface-attached bacteria on uncoated Ti (**Figure 7.6**, bottom left image). The nitroxide polymer-coated surface **B**, however, remained unaffected by the antibiotic treatment.

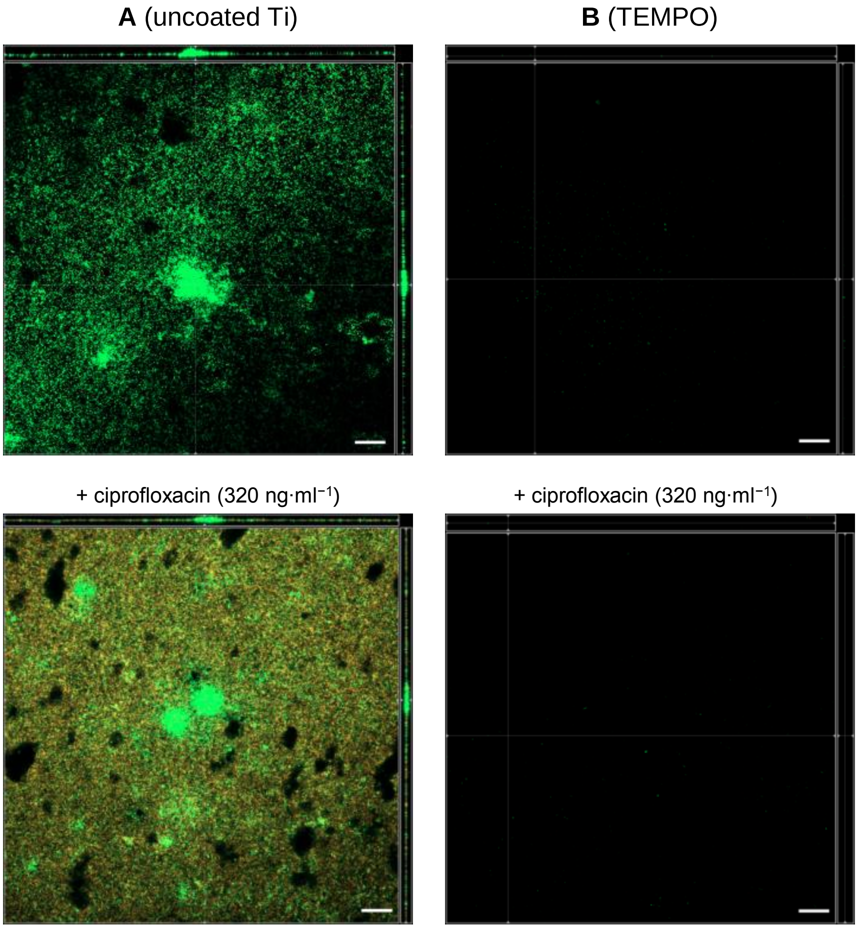
A (uncoated Ti)

B (TEMPO)

+ ciprofloxacin (320 ng·ml^{-1})

+ ciprofloxacin (320 ng·ml^{-1})

Figure 7.6. *P. aeruginosa* biofilm cultivation and biofilm eradication assays with antibiotic ciprofloxacin. Uncoated (**A**) and nitroxide polymer-coated (**B**) titanium surfaces were exposed to PA14 surface colonisation for 72 h (top row) with addition of ciprofloxacin (320 ng·ml^{-1}) after 48 h (bottom row). Biofilm assays were performed in a flow cell system at 37 °C. Dead bacteria were stained with propidium iodide (red) prior to confocal microscopy. Merged images composed of PI and GFP channels are displayed and superimposed fluorescence response of live (green) and dead cells (red) appear yellow. The scale bars represent 50 µm in length. Each panel shows the *xy*, *yz* and *xz* dimensions.

7.5 PHOTOLITHOGRAPHIC NITROXIDE POLYMER IMMOBILISATION ONTO TITANIUM IMPLANTS

The versatile and highly adaptable coating strategy using functional catecholamines as coating agents was further exploited for the spatially controlled polymer surface immobilisation of poly(DOPA-TEMPO) (**4**). The same coating conditions were applied for the surface photopatterning of DOPA-TEMPO (**3**) as previously described for its photopolymerisation without a shadow mask (refer to Chapter 5.4). Titanium flat surfaces (1 × 1 cm^2) were covered by a dotted shadow mask with Ø 1 mm pinholes and subsequently placed into the coating solution containing DOPA-TEMPO (**3**) as the coating agent. The surface photopatterning was performed for 12 h under continuous UV exposure (λ_{max} = 313 nm) (**Scheme 7.3**).

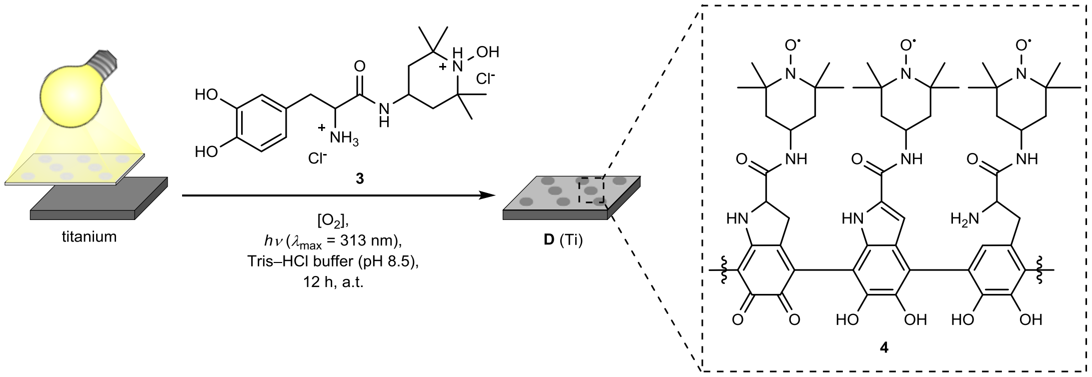

Scheme 7.3. Synthetic route for the spatially controlled surface immobilisation of poly(DOPA-TEMPO (**4**) onto titanium substrates. DOPA-TEMPO (**3**) (5 mM) was dissolved in Tris–HCl buffer (10 mM, pH 8.5) and the Ti substrates were covered by a dotted shadow mask. UV irradiation was performed for 12 h.

The successful surface immobilisation of poly(DOPA-TEMPO) (**4**) thin films in spatially confined areas was characterised by advanced XPS and ToF-SIMS imaging techniques. The XPS mapping of surface **D** (over a 3 × 3 mm^2 area) unambiguously confirmed the precise polymer surface pattern in correspondence to the employed dotted shadow mask. Polymer-derived C 1s and N 1s XPS signals were predominantly detected in circular areas, which have been exposed to UV irradiation (**Figure 7.7a–b**). Simultaneously, no Ti 2p XPS signals (stemming from the underlying Ti substrate) were detected in those areas supporting the successful localised polymer film formation onto surface **D** (**Figure 7.7c**). The surrounding areas, which have been shielded from UV irradiation by the shadow mask showed less pronounced C 1s and N 1s XPS signals, and on the contrary, intense substrate-derived Ti 2p XPS signals. The omnipresent C 1s and N 1s signals indicate polymer film formation over the entire surface, however, with a thickness difference between UV-exposed and UV-shielded areas.

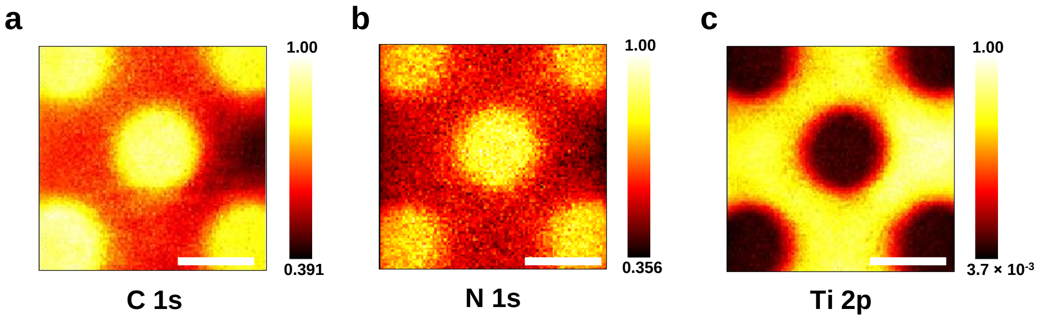

Figure 7.7. C 1s, N 1s and Ti 2p XPS images (**a**–**c**) of poly(DOPA-TEMPO) patterned surface **D**. Scale bars represent 1 mm in length.

The corresponding XPS overlay image constructed from the C 1s (colour-coded in magenta) and the Ti 2p XPS signals (blue) is depicted in **Figure 7.8a**. The acquisition of high-resolution XP spectra at well-defined positions corresponding to polymer-conjugated and non-conjugated areas was performed in a second step (on the base of the obtained XPS image) for the in-depth structural analysis of poly(DOPA-TEMPO) (**4**) immobilised on surface **D**. As described above, strong Ti 2p XPS signals were exclusively detected in areas which have been covered by the shadow mask (**Figure 7.8b**, top spectrum depicted in blue), whereas the polymer conjugated areas did not show any substrate-specific Ti 2p XPS signals (**Figure 7.8b**, bottom spectrum depicted in magenta). This observation indicates a polymer film thickness ≥ 10 nm in the circular areas, which have been exposed to UV light.

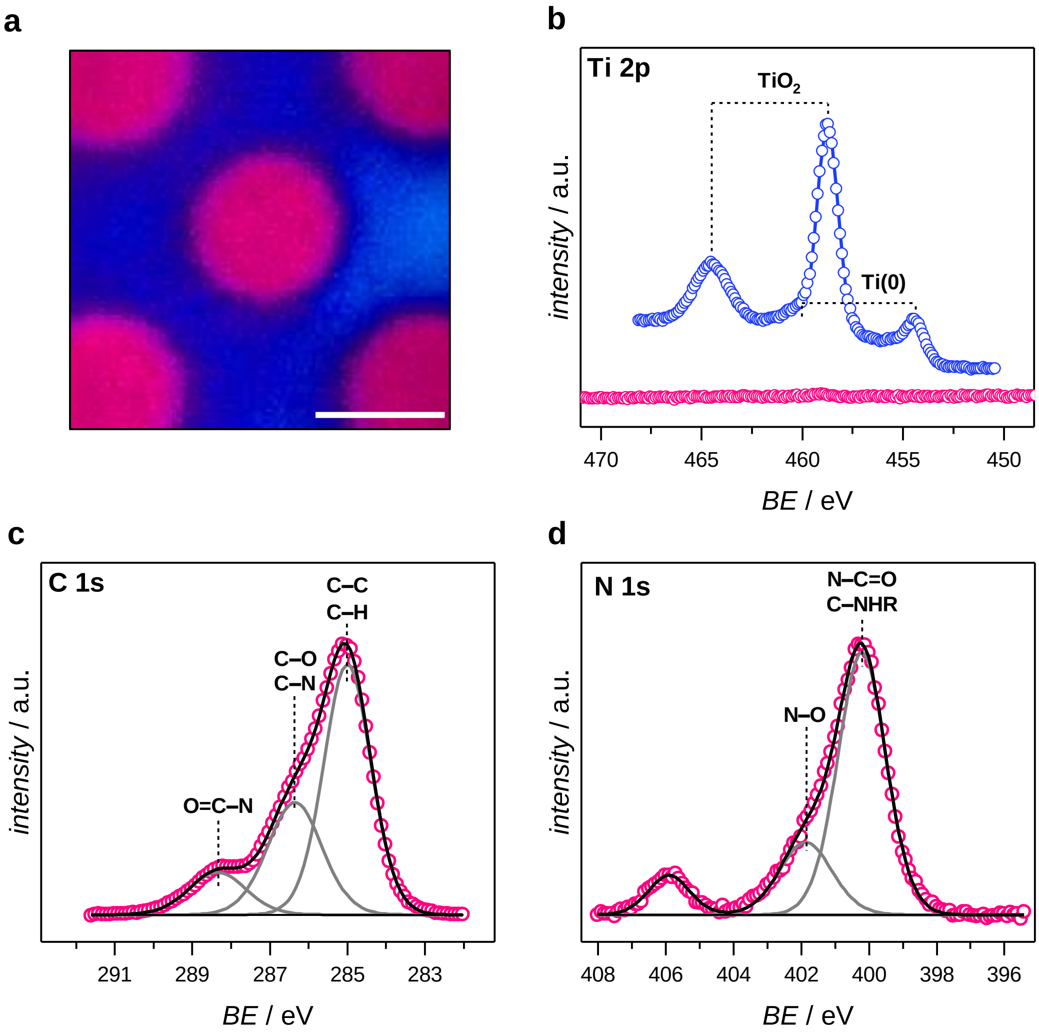

Figure 7.8. In-depth XPS characterisation of poly(DOPA-TEMPO) patterned titanium surface **D**. (**a**) XPS overlay image constructed from of substrate-derived Ti 2p XPS signals (blue) and polymer-derived C 1s XPS signals (magenta). Scale bar represents 1 mm in length. (**b**) Ti 2p XP spectra obtained from polymer conjugated (magenta) and non-conjugated areas (blue). (**c–d**) Corresponding C 1s and N 1s XP spectra of polymer conjugated areas.

The acquisition of C 1s and N 1s XP spectra unambiguously confirmed the existence of poly(DOPA-TEMPO) (**4**) thin films predominantly present in the circular areas (**Figure 7.8c–d**, recorded spectra are depicted in magenta). The C 1s XP spectrum appeared to be identical to previously recorded XP spectra of poly(DOPA-TEMPO) (**4**) analogous systems (refer to **Figure 5.1a** and **Figure 7.2a**). Likewise, the deconvolution of the N 1s XP spectrum showed a similar chemical composition in correspondence to previous results (refer to **Figure 5.1b** and **Figure 7.2b**). The N 1s spectrum was deconvoluted into a dominant peak at 400.2 eV (assigned to N-containing species constituting the polymer backbone) accompanied by a further peak at higher BEs, which is assigned to the nitroxide free radical species (at 401.8 eV). Contrary to previous N 1s XP spectra, the additional peak at higher BEs (405.9 eV) was particularly pronounced, which corresponds to higher oxidised N-containing species, most likely *N*-oxoammonium cations.[142] Similar observations have been made before, however, less abundant (refer to **Figure 5.1b**). The altered reaction conditions (*i.e.*, the use of UV light for the continuous generation of ROS) presumably trigger the overoxidation of the nitroxide moiety initially present as the reduced hydroxylamine hydrochloride salt. The predominant existence of free nitroxide radicals, however, was confirmed in previous EPR spectroscopic measurements (refer to **Figure 5.4d**), which demonstrated an UV-accelerated nitroxide radical formation during the initial stage of the polymerisation. Thus, it is assumed that the overoxidation of the TEMPO moiety is strongly influenced by the time in which the coating solution is exposed to the oxidising agent (*i.e.*, dissolved molecular oxygen and the corresponding ROS).

Additional C 1s and N 1s XPS measurements at spots, which have been covered by the shadow mask, confirmed the omnipresence of poly(DOPA-TEMPO) (**4**) thin films, however clearly less abundant (refer to **Figure E.4** in the Appendix). Those observations clearly indicate that the photopatterning of DOPA-TEMPO (**3**) only controls the localised build-up of reactive and propagating oligomer building blocks (induced by UV-activated ROS) and not the inherent (universal) adhesive properties of the growing poly(catecholamine) chains. Thus, the *in situ* polymer film formation seems to be promoted onto areas which are exposed to UV irradiation. Omnipresent polymer surface deposition onto the entire surface, however, cannot be suppressed in this photolithographic experimental setup due to polymer diffusion and locally unspecific polymer–substrate interactions.

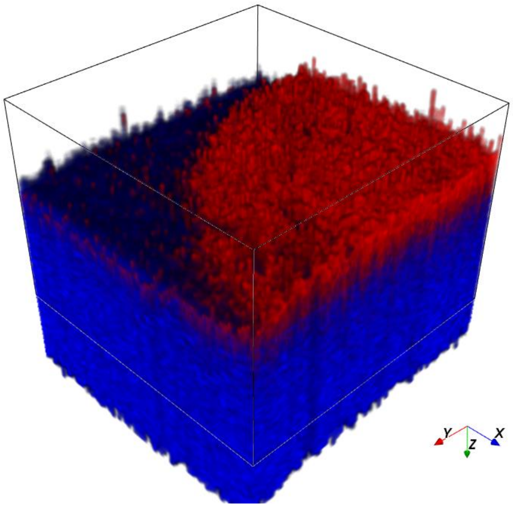

Figure 7.9. 3D ToF-SIMS rendering of poly(DOPA-TEMPO) patterned titanium surface **D**. The Ti substrate is illustrated in blue and a quarter of one nitroxide polymer spot deposited on the surface is depicted in red. Polymer signals (red) are sum of $[C_2H_5]^+$, $[C_3H_5]^+$, $[C_4H_7]^+$, $[C_2H_5N]^+$, and $[NH_4]^+$ fragments. Titanium signals (blue) derived from the sum of all isotopes. The *x* and *y* range is 500 µm (black box), the *z* range is not to scale.

Further evidence of a successful polymer film formation with spatial precision was given by ToF-SIMS (**Figure 7.9**). Initial static SIMS measurements only showed a low contrast between uncoated and polymer conjugated areas due to omnipresent poly(DOPA-TEMPO) (**4**) deposited onto the entire substrate. SIMS has a very low probing depth (in the range of 2–5 nm), and thus the 2D imaging of polymer-characteristic $[CN]^-$ and $[CNO]^-$ fragments showed an almost-uniform distribution of those fragments throughout the entire surface (refer to **Figure E.5** in the Appendix). The imaging of substrate-derived Ti isotopes, however, showed the correct pattern in analogy to the employed dotted shadow mask with Ti signals exclusively detected in areas which have been covered by the shadow mask. Dynamic SIMS experiments (over a 500 × 500 μm^2 area) significantly improved the characterisation of the patterned surface **D** under application of an argon cluster erosion beam. The detailed ToF-SIMS characterisation pathway toward the 3D rendered image depicted in **Figure 7.9** is explained in the Appendix (refer to **Figures E.6–E.8**). A quarter of one poly(DOPA-TEMPO) (**4**) spot was clearly accentuated from the underlying Ti substrate with the visualisation of polymer-characteristic $[C_2H_5]^+$, $[C_3H_5]^+$, $[C_4H_7]^+$, $[C_2H_5N]^+$, and $[NH_4]^+$ fragments (**Figure 7.9**, illustrated in red). The imaging of the Ti substrate (depicted in blue) was achieved *via* the sum of all Ti isotopes.

7.6 SPATIALLY CONTROLLED ANTIBIOFILM SURFACES

The spatially controlled surface immobilisation of poly(DOPA-TEMPO) enabled the direct biological evaluation of the nitroxide-stemming antibiofilm properties in comparison to the surrounding unmodified substrate. The polymer patterned titanium surface **D** was exposed to *P. aeruginosa* surface colonisation for 72 h under static biofilm growth conditions. A GFP-labelled PA14 strain was employed (refer to Chapter 7.4) and the inoculated media (BM2) was replaced with fresh media after 24 h and 48 h, respectively. The localised antibiofilm properties on surface **D** was assessed by CLSM. A clear difference in biofilm surface coverage between polymer-coated and uncoated areas was observed after confocal imaging of individual circular polymer spots (Ø 1 mm) (**Figure 7.10**). The surrounding uncoated areas showed a complete biofilm surface coverage (green fluorescent). The polymer-coated circular area (in the centre of **Figure 7.10**), however, showed great resistance toward *P. aeruginosa* biofilm formation. Only minor biofilm structures have been formed on the polymer-coated area, which might indicate an insufficient surface coverage of poly(DOPA-TEMPO) following the previously introduced photopatterning protocol. The presence of overoxidised nitroxyl species, as detected by XPS (refer to **Figure 7.8**), did not show any significant effects in terms of the overall antibiofilm properties derived from poly(DOPA-TEMPO).

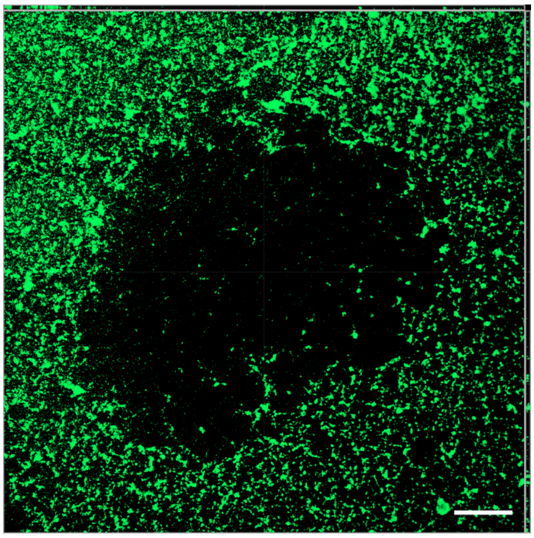

Figure 7.10. *P. aeruginosa* biofilm cultivation on nitroxide patterned titanium surface. Surface **D** was exposed to a GFP-labelled PA14 strain for 72 h under static conditions at 37 °C. Confocal image was obtained through 3 × 3 rastering along the *xy* dimension with approx. 16 µm depths in *yz* and *xz* dimensions (indicated in side panels). The scale bar represents 200 µm in length.

7.7 CONCLUSION

In summary, the antibiofilm properties of nitroxides could be maintained when TEMPO functional groups were covalently incorporated into a polymer matrix and subsequently immobilised onto the surface. The antibiofilm coating system examined on HA and Ti substrates showed great resistance against *P. aeruginosa* biofilm cultivation. Careful consideration of the employed polymer coating system (including the introduction of DOPA-Cy (**15**) as a reference coating agent) enabled the precise biological evaluation of the biofilm preventing properties stemming from the nitroxide functional groups present in the polymer side chains. The polymer coating itself, however, strongly influenced the biofilm formation as shown with poly(DOPA-Cy) as a reference coating system. It is assumed that changes of the surface topography induced by the surface-adherent polymer film might promote bacteria–surface interactions, which consequently result in a more pronounced biofilm formation. Most stinkingly, this effect was not observed when poly(DOPA-TEMPO) coatings were carefully assessed. Instead, the covalent embedment of TEMPO functional groups into the adhesive polymer matrix completely inhibited biofilm formation on the exposed surfaces. In addition, a novel pathway toward the spatially controlled polymer surface deposition of poly(DOPA-TEMPO) was introduced generating localised antibiofilm properties.

Chapter 8: Concluding Remarks

This thesis presented a new methodology for the generation of nitroxide functional polymers, equipped with inherent bioadhesive properties. A widely-applicable coating strategy was introduced for the precise and substrate-independent surface modification of various material interfaces. The characteristic features of this advanced polymer coating platform were carefully assessed, including its structural elucidation, the bioderived adhesive performances as well as the nitroxide-stemming multifunctional properties. Of particular interest was the design of a versatile antibiofilm coating strategy using nitroxide-containing adhesive polymers. The biofilm-preventing properties of these coatings were carefully assessed in *Pseudomonas aeruginosa* biofilm experiments and their potential to reduce device-associated infections in the hospital was clearly shown. In the concluding remarks, the results are shortly summarised and critically discussed under the following aspects: the overall synthetic strategy, the structural elucidation and coating properties as well as the herein presented applications.

Synthetic Strategy

First, the synthesis of a nitroxide functional monomer was presented for the design of adhesive polymer scaffolds with persistent multi-radical character. The amide coupling reaction of L-DOPA with 4-amino-TEMPO was performed under application of standard Boc and TBDMS protecting group chemistries. In fact, a general and straightforward synthetic procedure for the preparation of tailor-made catecholamines was established. The facile introduction of various functional groups (in the current thesis applied to TEMPO, TEMPO-CH_3 and Cy) was achieved following a two-step procedure in high yields (overall 73–83%). The monomer was isolated after a one-step deprotection step employing acidic (HCl) conditions. The obtained hydrochloride-coordinated monomer salts exhibited excellent water solubilities for subsequent aqueous polymerisations. The conversion of the TEMPO free radical moiety to the corresponding hydroxylamine hydrochloride species provided good long-term storage stability (in the solid state) with respect to the air-

and moisture-sensitive catechol and nitroxyl-derived functional groups. The persistent nitroxide radical character was efficiently regenerated (≥ 85%) during the oxidative polymerisation of DOPA-TEMPO. Both concurrent aerobic processes, the catechol polymerisation as well as the hydroxylamine oxidation, showed strong interferences during the initial stage of the polymerisation. However, the covalent assembly of poly(DOPA-TEMPO) and its persistent multi-radical character were unambiguously confirmed by various in-solution characterisation techniques (*e.g.*, HR-ESI-MS and EPR spectroscopy).

The preparation of functional poly(catecholamine)s bearing TEMPO or structurally related functional groups (*i.e.*, TEMPO-CH_3 and Cy) was controlled by various polymerisation and coating parameters. In the current thesis, the monomer concentration (5–40 mM), the supply of atmospheric oxygen as an oxidant, and the employed Tris–HCl buffer system (10–100 mM, pH 8.25–9.25) were carefully adjusted on demand. The use of UV-light for the *in situ* generation of ROS resulted in an accelerated polymerisation of DOPA-TEMPO.

The polymer surface functionalisation of various material interfaces was carried out following a convenient dip-coating procedure in aqueous systems at ambient temperatures. No harmful chemical additives were needed, instead, atmospheric oxygen was employed as a mild oxidising agent. This easy-to-operate experimental setup enabled the facile surface manipulation of various types of materials (*e.g.*, ceramics, metals and polymer composites). Moreover, the coating process proceeded irrespective of the size, shape and purpose of the underlying objects (*e.g.*, flat substrates, spherical polymer microparticles or electrode materials) and was easily scalable (*e.g.*, conducted in 3–100 mL coating solutions). The straightforward poly(DOPA-TEMPO) coating procedure has been proven beneficial for the generation of antibiofilm coatings, which needed to be carefully synchronised with certain requirements for the biofilm assays (*e.g.*, the type of underlying substrate or the introduction of a reference coating system). The copolymerisation of DOPA-TEMPO with (unfunctionalised) dopamine was introduced in order to enhance the coating stability when deposited onto PGMA microspheres. Furthermore, a photolithographic coating protocol for the spatially controlled surface deposition of poly(DOPA-TEMPO) in the submillimeter range was introduced. Overall, a sophisticated and widely-applicable synthetic strategy with high control over the desired properties and functions was demonstrated — from the design of functional monomers to the generation of adhesive polymers and nitroxide functional material interfaces.

Structural Elucidation and Coating Properties

The polymerisation of DOPA-TEMPO and its derivatives was carefully assessed by EPR and UV–vis spectroscopy as well as HR-ESI-MS. NMR spectroscopic characterisation of the radical polymer was strongly hampered by the paramagnetic-induced NMR signal broadening. Subsequent polymer surface coatings were carefully characterised by XPS, AFM, ToF-SIMS, SE and contact angle measurements.

The polymerisation pathway was monitored by UV–vis and EPR spectroscopy under highly diluted conditions in order to suppress polymer precipitation for quantitative analysis. A direct correlation between the oxidative polymerisation mechanism and the concurrent aerobic nitroxide radical formation was elucidated. The catechol oxidation concomitant with the build-up of reactive *o*-quinoic intermediates occurred predominantly in the first stage of the polymerisation. An accelerated nitroxide radical formation was observed after a maximum concentration of oxidised reactive intermediates was reached. Initial oligomer formation (*e.g.,* dimerisation) was indicated by EPR signal broadening. The HR-ESI-MS characterisation platform turned out to be highly suitable for the structural elucidation of polymerised catecholamines. Two structurally related polymer systems, namely poly(DOPA-TEMPO) and poly(DOPA-TEMPO-CH_3), were thoroughly analysed by HR-ESI-MS. Various appearances of the nitroxide functional group (*e.g.*, different redox states as well as the predominant existence of hydrochloride adducts), however, strongly limited the structural elucidation of the radical-containing polymer system. This was not the case when TEMPO was substituted by its methoxyamine derivative (TEMPO-CH_3). Oligomers with up to eight repeating units were detected and each oligomer profile was composed of multiple coexisting species appearing at different *m/z* values. Various building blocks have been proposed to constitute the polymer backbone, including cyclised structures present in different redox states (*e.g.*, the catechol or the *o*-quinone form) and

5,6-dihydroxyindole was designated as the key structural motif. In addition, the covalent incorporation of uncyclised building blocks was clearly evidenced.

The concomitant polymer surface deposition (~1.1 nm·h^{-1} on Si) was monitored by SE, and static water contact angle measurements were carried out in order to demonstrate the successful polymer film formation on selected materials (*e.g.*, silicon, alumina, titanium and PTFE). In addition, XPS quantification of the substrate-specific residual peaks confirmed in more detail the surface-independent coating character of poly(DOPA-TEMPO). The inherent surface roughness of the employed underlying materials, most likely, promoted initial polymer–substrate binding interactions, as evidenced on rough PTFE in comparison to smooth Si wafers (as determined by AFM). In other words, weak binding interactions between poly(DOPA-TEMPO) and the chemically inert PTFE were most likely compensated (to certain extent) by the inherent surface roughness of PTFE. Detailed structural characterisation of the polymer films deposited on the above-mentioned substrates was performed by XPS. The deconvolution of the obtained N 1s high-resolution XP spectra demonstrated the redox-sensitive character of the nitroxide functional group. The use of UV-light during the photopolymerisation of DOPA-TEMPO, for instance, promoted the overoxidation of the nitroxide functional group to the corresponding *N*-oxoammonium species, as detected by XPS. The UV-triggered polymerisation protocol, however, was subsequently exploited for the surface micropatterning of poly(DOPA-TEMPO). Advanced XPS and ToF-SIMS imaging techniques carefully investigated the spatial control of this photolithographic coating setup. Polymer surface deposition predominantly occurred onto areas exposed to UV irradiation. However, thin polymer film formation was observed over the entire surface.

Applications

The facile introduction of nitroxide functional groups to any type of material interface was exploited in multiple ways for the design of tailor-made materials. Of particular interest was to strengthen the nitroxide-characteristic multi-radical, electroactive and antibiofilm properties after incorporation within a polymer system or onto the surface.

The multi-radical coating platform was exploited for the reversible and spatially controlled surface immobilisation of various functional units (*e.g.*, small molecules and polymer strands) applying the concept of thermo-reversible and photo-induced NRC reactions. For instance, nitroxide-coated PGMA microspheres were functionalised with small molecules in a precise and rewritable manner. The reversible coding *via* NRC and decoding *via* thermal alkoxyamine fission was demonstrated by EPR spectroscopy and XPS. In addition, the spatially controlled immobilisation of two photoactive polymer strands onto poly(dopamine) surfaces was introduced. The dual photopatterning of PMMA and PTFEMA, both terminated with an Irgacure 2959 photoinitiator, was visualised by ToF-SIMS and XPS imaging techniques upon rapid NRC photo-click reactions.

The herein presented design of a polymer system with multi-radical character was of further interest in the emerging field of electroactive polymer materials and organic radical batteries. As a proof-of-concept, the electroactive character of poly(DOPA-TEMPO) deposited onto a working electrode was investigated by CV. The reversible oxidation to the *N*-oxoammonium cation followed by the reformation of the free radical species was unambiguously demonstrated in repetitive redox cycles. Thus, poly(DOPA-TEMPO) adhesives are promising candidates for the design of electroactive polymer coatings and materials. Potential (synergistic) side effects deriving from the redox-active catechol moieties need to be investigated in more detail.

The main focus of the current thesis, however, was to deliver nitroxides at the interface of materials, which are typically prone to bacterial proliferation in the hospital (*e.g.*, medical devices and implants). The herein presented versatile coating strategy (particularly its substrate-independent character) has been proven highly suitable for the generation of antibiofilm coatings. The great potential of nitroxide-containing polymer coatings in preventing *Pseudomonas aeruginosa* biofilm formation on surfaces was demonstrated in various *in vitro* biofilm experiments. Most impressively, spatially controlled biofilm formation was demonstrated using nitroxide patterned titanium implants. As clearly shown by detailed investigations using CLSM, this nitroxide-based coating strategy prevented biofilm formation — the predominant mode of bacterial growth. Antifouling or antimicrobial (side) effects stemming from the polymer coating itself could be excluded as shown by reference measurements. Thus, a new prophylactic coating strategy to combat bacterial surface colonisation was introduced, which represents a complementary approach toward existing yet limiting antibacterial or antifouling coatings. In addition, biofilm eradication assays showed great compatibilities of those nitroxide-containing coatings using standard antibiotic ciprofloxacin. Further investigations, *e.g. in vivo* experiments using nitroxide-coated indwelling implants, are desirable in order to promote the mild antibiofilm coating strategy for reducing device-associated infections in the hospital.

The herein employed versatile coating strategy using polymerisable catecholamines as suitable coating agents has rapidly become a standard procedure in modern material design for the precise surface engineering of various material interfaces.[203] Fundamental structural insights into the adhesive polycatecholic system, however, still remain elusive and the substrate-independent character of this type of coating has been overpraised according to a recent critical literature report.[194] Thus, the overall coating stability of the herein employed nitroxide-containing polymer system needs to be carefully assessed in more detail. In addition, the structural elucidation of this polycatecholic system by other characterisation techniques, such as SEC or HPLC, is highly desirable as a complementary access route to the herein employed HR-ESI-MS analysis platform. SEC allows the accurate determination of the overall degree of polymerisation, the dispersity as well as the monomer consumption over the course of time. However, the limited solubility as well as the structural heterogeneity of this class of bioderived polymers typically complicate the precise structural analysis by standard solution state characterisation techniques.

The successful surface immobilisation of nitroxide functional groups has emerged as a promising strategy to control bacterial proliferation and biofilm maturation on surfaces. Clearly, further detailed investigations need to be carried out, including the examination of the long-term stability and biocompatibility of this antibiofilm coating approach — *in vitro* and *in vivo*. The mode of action of surface-immobilised nitroxides should be carefully assessed, whether it is based on a nitroxide release type of system or if contact-active antibiofilm surface properties are predominant. Moreover, combinatorial approaches, such as the fusion of conventional nonfouling polymer coatings with nitroxide-stemming antibiofilm properties can be the ultimate goal to prevent device-associated nosocomial infections. Fortunately, many design strategies are available in polymer chemistry for the precise engineering of functional material interfaces.

Chapter 9: Experimental Section

9.1 MATERIALS

Dry acetonitrile (Sigma-Aldrich, 99.8%; or Acros Organics, 99.9% extra dry), 4-amino-2,2,6,6-tetramethylpiperidine-1-oxyl (abcr or Sigma-Aldrich, 97%), α-bromoisobutyryl bromide (Sigma-Aldrich, 98%), 4-carboxy-2,2,6,6-tetramethylpiperidine-1-oxyl (TCI, 97%), chloroform-d_1 (Sigma-Aldrich, 99.8 atom % D), ciprofloxacin hydrochloride monohydrate (Sigma-Aldrich, LOT #: LRAA8718, 93.4%), copper powder (Sigma-Aldrich, 99%), cyclohexylamine (Sigma-Aldrich, 99%), dry dichloromethane (Acros Organics, 99.8% extra dry), *N*,*N*-diisopropylethylamine (Sigma-Aldrich, 99%), 4-(dimethylamino)pyridine (Acros or Sigma-Aldrich, 99%), dry *N*,*N*-dimethylformamide (Acros Organics, 99.8% extra dry), *N*,*N*-dimethylformamide-d_7 (Sigma-Aldrich, 99.8 atom % D), dimethyl sulfoxide (Carl Roth, 99%), dopamine hydrochloride (Sigma-Aldrich, 98%; or Alfa Aesar 99%), 1-ethyl-3-(3-dimethylaminopropyl) carbodiimide hydrochloride (Carl Roth, 99%; or Sigma-Aldrich, 98%), ethylenediaminetetraacetic acid (EDTA) disodium salt dihydrate (Sigma-Aldrich, 98%), gentamicin sulfate salt (≥ 590 μg gentamicin base per mg, Sigma-Aldrich), hydrogen chloride solution, 2 M in diethyl ether (Alfa Aesar), hydrogen peroxide solution 30% (*w*/*w* in water) (Carl Roth), (2-hydroxy-4′-(2-hydroxyethoxy)-2-methylpropiophenone (Irgacure 2959; TCI, 98%), iron(II) sulfate heptahydrate (VWR, 99%), lysogeny (LB) broth (Lennox, Fischer Bioreagents), 3-mercaptopropionic acid (Acros Organics, 99%), methanol-d_4 (Sigma-Aldrich, 99.8 atom % D), *N*,*N*,*N'*,*N'*,*N''*-pentramethyldiethylenetriamine (Sigma-Aldrich, 99%), silica gel (Merck), *p*-toluenesulfonic acid monohydrate (Sigma-Aldrich, 98%), 2,2,2 trichloroethanol (TCI, 98%), triethylamine (Acros Organics, 99%), 4,4,4-trifluorobutanol (Sigma-Aldrich, 98%), tris-(hydroxymethyl)methylamine (Acros Organics or Sigma-Aldrich, 99%) were used as received.

Methyl methacrylate (Sigma-Aldrich, 99%, stabilised) and 2,2,2-trifluoroethyl methacrylate (Sigma-Aldrich, 99%, stabilised) were passed through a column of activated basic alumina (VWR) to remove the inhibitor. 2,2'-Azoisobutyronitrile

(Fluka, purum, 98.0%) was recrystallised from ethanol prior usage. Thin layer chromatography (TLC) was performed on aluminium plates coated with silica gel 60 F_{254} (Merck). Standard chemicals including solvents (p.a.) and salts (99%) which have been employed for synthesis were purchased from Chem-Supply, Carl Roth, Thermo Fisher Scientific, Sigma-Aldrich or VWR, respectively. Dry solvents were also obtained from solvent purification systems. ESI-MS were performed using acetic acid (Scharlau, AR), acetonitrile (Carl Roth, LC-MS grade $\geq$ 99.95%), methanol (Carl Roth or Fisher Chemical, HPLC grade), tetrahydrofuran (THF; GPC grade, Scharlau, or HPLC grade, Fisher Chemical) and sodium iodate (Sigma-Aldrich, $\geq$ 99%) without further purification. Ultrapure water (*e.g.*, obtained from a Puranity PU 15 water purification system, VWR) was employed for ESI-MS. All solvents employed for the polymerisation and surface coatings were used in HPLC grade or were obtained from solvent purification systems.

Silicon wafers (Si-Mat Silicon Materials, Kaufering, Germany), titanium plates (Trinon Titanium, Karlsruhe, Germany), aluminium oxide plates (high purity alumina; Ceramic Oxide Fabricators, Eaglehawk, Australia), PTFE sheets (Dotmar, Acacia Ridge, Australia), hydroxyapatite discs (Clarkson Chromatography Products Inc., South Williamsport, USA), and PGMA microspheres (10 µm diameter, PSS Polymer Standard Service GmbH, Mainz, Germany) were used as received as substrates and materials for surface coatings and surface functionalisations. Synthesis and characterisation of PGMA microspheres is reported elsewhere.[340, 350] Materials which have been employed for biofilm assays are described in Chapter 9.3.3.

9.2 CHARACTERISATION METHODS AND INSTRUMENTATIONS

Nuclear Magnetic Resonance Spectroscopy

^{1}H NMR, ^{13}C NMR, and ^{19}F NMR spectroscopy was performed on a Bruker Avance III HD spectrometer (^{1}H NMR 600 MHz, ^{13}C NMR 151 MHz) or on a Bruker Ascend 400 spectrometer (^{1}H NMR 400 MHz, ^{13}C NMR 101 MHz, ^{19}F NMR 377 MHz) at 298 K. Chemical shifts are expressed in parts per million (ppm) and coupling constants (J values) are reported in hertz (Hz). The δ scale is referenced to characteristic (residual) signals of the employed deuterated solvents. Appearances of proton signals are described as singlet (s), doublet (d), doublet of doublets (dd), triplet (t), quartet (q), multiplet (m), and broad (br) signal.

High-Resolution Electrospray Ionisation Mass Spectrometry

HR-ESI-MS was performed on a Q Exactive Plus (BioPharma option) Orbitrap mass spectrometer, or on a LTQ Orbitrap XL Q Exactive mass spectrometer (Thermo Fisher Scientific, San Jose, CA, USA), both equipped with a HESI II probe. The capillary was set to 320 °C, and the S-lens radio frequency level was set to 68.0. The instruments were calibrated in the m/z range 74–1822 using standard calibration solutions (Thermo Scientific) and between m/z 1000–6000 with ammonium hexafluorophosphate. All samples were filtered prior to injection. Small molecule characterisation was performed in undoped MeOH, or THF/MeOH 3:2 (*v*/*v*) and DCM/MeOH 3:1 (*v*/*v*) doped with 100 μM sodium trifluoromethanesulfonate. Polymer characterisation presented in Chapter 3.4 was performed on the Q Exactive Plus Orbitrap mass spectrometer with a constant spray voltage in the range of 3.1–3.4 kV. The polymers were dissolved in THF/MeOH 3:2 (*v*/*v*) doped with 100 μM NaI with a concentration of 0.05 mg·mL^{-1}. The dimensionless gas flow rates were set to 10 (sheath gas), 0 (sweep gas), and 0 (aux gas). An in-source collision-induced dissociation (CID) energy of 70 eV for ESI-CID MS and a higher-energy collisional dissociation (HCD) energy of 35 eV for MS/MS, respectively, were employed. Polymer characterisation presented in Chapter 4 was performed on the LTQ Orbitrap XL Q Exactive mass spectrometer. The polymers were dissolved with a concentration of 0.05 mg·mL^{-1} in water/acetonitrile 1:1 (*v*/*v*) doped with 0.1% (*v*/*v*) acetic acid, or in THF/MeOH 3:2 (*v/v*). The gas flow rates were set to 10 (sheath gas), 0 (sweep gas), and 0 (aux gas) employing (−)ESI; and 5 (sheath gas), 1 (sweep gas), and 0 (aux gas) employing (+)ESI. A CID energy of 80 eV was employed and the spectra were recorded with a constant spray voltage of 3.4 ± 0.2 kV for ESI-CID MS. MS/MS experiments were performed using a spray voltage of 4.3 kV and a HCD energy of 15 eV. All recorded and simulated mass spectra were evaluated using the Xcalibur software.

Determination of Melting Points

Melting points were determined on a Gallenkamp variable temperature apparatus using glass capillary tubes.

Electron Paramagnetic Resonance Spectroscopy

EPR spectra were recorded on a Magnettech MiniScope MS400 spectrometer at ambient temperature. Small molecule characterisation was performed in dichloromethane and microspheres were suspended in aqueous solutions prior EPR characterisation.

UV–Visible Spectroscopy

UV–vis spectra were recorded on a Shimadzu UV-2700 UV–vis spectrophotometer in the range of 240–600 nm at ambient temperature. The Tris–HCl-based coating solutions were diluted to 0.1 mM or to 0.05 mM prior to the measurements. A quartz Suprasil cuvette with a 10 mm light path was employed. Spectra were baseline-corrected with respect to pure Tris–HCl buffer.

Cyclic Voltammetry

Electrochemical analysis was conducted on a BioLogic VSP potentiostat using a standard three-electrode setup consisting of a glassy carbon or platinum working electrode (3 mm diameter, BASi, West Lafayette), a Ag/AgCl reference electrode, and a platinum counter electrode. CV measurements were performed in a 0.1 M aqueous NaCl solution (previously purged with N_2 for 15 min) at ambient temperature. Five cycles were recorded in the range of 0–1.0 V employing a scan rate of 100 mV·s^{-1}.

Size-Exclusion Chromatography

SEC measurements were performed on a Polymer Laboratories (Varian) PL-GPC 50 Plus Integrated System, comprising an autosampler, a PLgel 5 mm bead-size guard column (50 × 7.5 mm), one PLgel 5 mm Mixed E column (300 × 7.5 mm), three PLgel 5 mm Mixed C columns (300 × 7.5 mm), and a differential refractive index detector using THF as the eluent at 35 °C with a flow rate of 1 mL·min^{-1}. The SEC system was calibrated using linear poly(styrene) standards ranging from 370 to 2.52×10^6 g·mol^{-1} and linear PMMA standards ranging from 800 to 1.6×10^6 g·mol^{-1}. The samples were prepared with a concentration of 2 mg·mL^{-1}.

X-ray PhotoelectronSspectroscopy

XPS measurements were performed using a K-Alpha+ XPS spectrometer (ThermoFisher Scientific, East Grinstead, United Kingdom) equipped with a microfocused, monochromated Al K_α X-ray source (400 µm spot size). The kinetic energy of the electrons was measured by a 180° hemispherical energy analyser operated in the constant analyser energy mode (CAE) at 50 eV pass energy for elemental spectra. The K-alpha charge compensation system was employed during analysis using electrons of 8 eV energy and low-energy argon ions to prevent any localised charge build-up. The recorded XPS spectra were evaluated using the Thermo Avantage software.[351] The high-resolution spectra were fitted with one or more Voigt profiles (BE uncertainty: ±0.2 eV). The Scofield sensitivity factors were applied for quantification.[352] All spectra were referenced to the C 1s (C–C, C–H) peak at BE 285.0 eV and controlled by means of well-known photoelectron peaks of metallic elements. The K-alpha+ snapmap option permits imaging of an area of 3×3 mm^2 using an X-ray spot of 200 µm. 7–10 iterations were run for better contrasts and the data were collapsed in order to get a better signal-to-noise ratio. Afterwards, a principal component analysis of the data was applied for the generation of the XPS images.

Atomic Force Microscopy

AFM imaging of coated silicon substrates was performed on a Multimode 2 Atomic Force Microscope (Digital Instruments, Santa Barbara). A HQ:NSC18/Al BS (Mikro-Masch, Sofia, Bulgaria) AFM cantilever (typical resonant frequency of 75 kHz and force constant of 2.8 $N\cdot m^{-1}$) was employed in alternating current mode for the determination of the polymer film height profiles. The polymer film was beforehand partially removed, and the underlying Si substrate was set as a zero line. The surface roughness was determined using an NT-MDT Solver Pro atomic force microscope. A ContGD-G (BudgetSensors, Sofia, Bulgaria) AFM cantilever (typical resonant frequency of 13 kHz and force constant of 0.2 $N\cdot m^{-1}$) was employed in contact mode (set point of 2 V deflection). The root-mean-square (RMS) surface roughness was determined over a 20×20 μm^2 area, and the error bars indicate the standard error of five measurements.

Static Water Contact Angle Measurements

Static water contact angle measurements were performed on a Drop Shape Analyser DSA100 (Kruess, Hamburg, Germany). A 5 µL water droplet was placed on the surface according to the sessile-drop method. The reported values indicate the averages of three measurements.

Spectroscopic Ellipsometry

The determination of the polymer film thicknesses deposited on silicon substrates was performed on a J.A. Woollam M-2000UI Ellipsometer in the wavelength range of 245−1690 nm and at angles of incidences of 65, 70, and 75°. Two independent kinetic studies were conducted, both ran in duplicate. Error bars represent 1 standard deviation of uncertainty (refer to Chapter 5.3). Results presented in Chapter 5.4 were obtained from a representative study. The polymer film thickness was determined at least at two different spots on the surface. The data was fitted and evaluated using the CompleteEASE software. A Cauchy model was applied for the polymer surface deposition (with $A = 1.45$, $B = 0.01$, surface roughness excluded) on Si/SiO_x substrates. The SiO_x interlayer was determined prior to surface coatings.

Time-of-Flight Secondary Ion Mass Spectrometry

ToF-SIMS was performed on a TOF.SIMS 5 instrument (ION-TOF GmbH, Münster, Germany) equipped with a Bi cluster primary ion source and a reflectron type time-of-flight analyser. The Bi source was operated in the high current bunched mode providing short Bi_3^+ primary ion pulses at 25 keV and a later resolution of approx. 4 µm. The short pulse length of typically 1.3 ns allowed for high mass resolution. The primary ion beam was rastered in individual patches of 500 × 500 μm^2 and the stage scan mode was employed for larger areas with 10 µm pixel distance. Primary ion doses were kept below 10^{11} $ions \cdot cm^{-2}$ (static SIMS limit). Dynamic SIMS experiments were performed using an argon cluster erosion beam. For these experiments the sample was eroded by a Ar_{1500}^+ beam at 5 keV rastered over 800 × 800 μm^2. A concentric field of view of 500 × 500 μm^2 (the maximum scanning range of the primary ion gun) was imaged continuously. All ToF-SIMS experiments were calibrated on omnipresent (hydro)carbon peaks. Additional information about dynamic ToF-SIMS experiments discussed in Chapter 7.5 can be found in the Appendix E.

Confocal Laser Scanning Microscopy

Microscopy was performed on a Zeiss LSM 800 microscope (Carl Zeiss AG, Oberkochen, Germany). Confocal images were evaluated using the Zeiss ZEN software. Substrates were individually background subtracted with respect to the employed underlying type of material.

9.3 EXPERIMENTAL PROCEDURES

9.3.1 Small Molecule Syntheses

3,4-Bis(*tert*-butyldimethylsilyloxy)-*N*-*tert*-butyloxycarbonyl-L-phenylalanine (**1**) was prepared according to a literature procedure.[217] Synthetic pathways to isoindoline based nitroxides such as TMIO (employed as a radical scavenger in Chapter 6.2) can be found elsewhere.[28, 353]

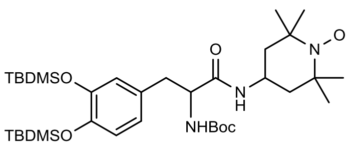

2

(TBDMS)$_2$*-N-Boc-DOPA-TEMPO* (**2**): 4-Amino-2,2,6,6-tetramethylpiperidine-1-oxyl (1.71 g, 10.0 mmol, 1.0 eq.), DMAP (2.44 g, 20.0 mmol, 2.0 eq.) and 4-*bis*(*tert*-butyldimethylsilyloxy)-*N*-*tert*-butyloxycarbonyl-L-phenylalanine (**1**) (5.26 g, 10.0 mmol, 1 eq.) were dissolved in dry DCM (50 mL). Subsequently, EDC·HCl (3.83 g, 20.0 mmol, 2.0 eq) was added, and the reaction solution was stirred at ambient temperature for 24 h, followed by extraction with saturated $NaHCO_3$ solution (50 mL), water (20 mL), and brine (20 mL). The organic phase was dried over Na_2SO_4 and evaporated under reduced pressure. The crude product was purified by silica column chromatography employing ethyl acetate and cyclohexane (1:3) as solvent mixture ($R_f = 0.27$) yielding an orange solid (4.89 g, 7.2 mmol, 72%).

^{1}H NMR (600 MHz, methanol-d_4, 298 K) δ = 6.99–6.54 (br m, 3H, $C_{Ar}H$), 4.34–3.94 (br m, 1H, C_{Ar}–CH_2–C*H*), 3.07–2.62 (br m, 2H, C_{Ar}–CH_2), 1.41 (s, 9H, O–$C(CH_3)_3$), 1.00 (s, 18H, Si–$C(CH_3)_3$), 0.20 (s, 12H, $Si(CH_3)_2$) ppm. ^{13}C NMR (151 MHz, methanol-d_4, 298 K) δ = 173.4 (C), 157.3 (C), 147.6 (C_{Ar}), 146.8 (C_{Ar}), 131.5 (C_{Ar}), 123.6 ($C_{Ar}H$), 123.4 ($C_{Ar}H$), 121.9 ($C_{Ar}H$), 80.5 (C), 60.1 (CH), 38.9 (CH_2), 28.7 (CH_3), 26.7 (CH_3), 26.6 (CH_3), 19.3 (C), 19.2 (C), −3.3 (CH_3), −3.4 (CH_3), −3.6 (CH_3), −3.7 (CH_3) ppm. Not all signals were resolved due to NMR signal broadening induced by the nitroxide radical. HR-ESI-MS (*m/z*) calculated for $C_{35}H_{64}N_3NaO_6Si_2$ $[M+Na]^+$ 701.4226, found 701.4231. M.p. 75 °C. EPR (DCM): $g = 2.0013$, $a_N = 1.575$ mT.

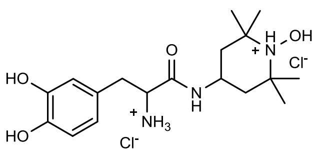

3

DOPA-TEMPO (**3**) (present as the hydroxylamine dihydrochloride species): All solvents were purged with nitrogen for 15 min prior to usage. $(TBDMS)_2$-*N*-Boc-DOPA-TEMPO (**2**) (1.70 g, 2.5 mmol, 1.0 eq.) was dissolved in methanol (10 mL) and the solution was cooled to 0 °C. 6 M aqueous HCl (5 mL, 12 eq.) was added dropwise, and the solution was stirred for 6 h allowed to reach ambient temperature. The solvent and volatiles were carefully removed under reduced pressure. The crude product was redissolved in water (10 mL, acidified with a few drops of 1 M HCl), filtered and lyophilised. The pure product was isolated as a light-brown solid after redissolving in water (10 mL) and subsequent lyophilisation in quantitative yields.

^{1}H NMR (600 MHz, DMF-d_7, 298 K) δ = 12.84 (s, 1H, NH–O), 12.05 (s, 1H, N–OH), 9.25 (br s, 2H, C_{Ar}–OH), 8.92 (d, J = 7.4 Hz, 1H, CONH), 8.80 (–NH_3), 6.84 (d, J = 2.1 Hz, 1H, C_{Ar}H), 6.75 (d, J = 8.0 Hz, 1H, C_{Ar}H), 6.60 (dd, J = 8.0, 2.1 Hz, 1H, C_{Ar}H), 4.33–4.23 (m, 1H, NH–C*H*), 4.22–4.13 (m, 1H, C_{Ar}–CH_2–C*H*), 3.18–3.06 (m, 2H, C_{Ar}–CH_2–CH), 2.30–1.93 (m, 4H, NH–CH–(CH_2)$_2$), 1.60 (s, 3H, $C(CH_3)_2$), 1.59 (s, 3H, $C(CH_3)_2$), 1.47 (s, 3H, $C(CH_3)_2$), 1.46 (s, 3H, $C(CH_3)_2$) ppm. ^{13}C NMR (151 MHz, DMF-d_7, 298 K) δ = 168.3 (C), 146.71(C_{Ar}), 145.5 (C_{Ar}), 126.4 (C_{Ar}), 120.9 (C_{Ar}H), 117.8 (C_{Ar}H), 116.2 (C_{Ar}H), 67.9 (C), 67.8 (C), 55.4 (CH), 41.6 (CH_2), 41.4 (CH_2), 39.9 (CH), 37.0 (CH_2), 27.3 (CH_3), 27.2 (CH_3), 20.22 (CH_3), 20.18 (CH_3) ppm. HR-ESI-MS (*m/z*) calculated for $C_{18}H_{30}N_3O_4$ $[M-HCl-Cl]^+$ 352.2231, found 352.2232. M.p. 185 °C (dec.).

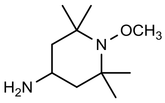

5

1-Methoxy-2,2,6,6-tetramethylpiperidin-4-amine (**5**): Compound **5** was prepared according to a literature procedure.[50] 4-Amino-2,2,6,6-tetramethylpiperidine (1.71 g, 10.0 mmol, 1.0 eq.) was dissolved in DMSO (20 mL) followed by the addition of Fe(II)$SO_4 \cdot 7H_2O$ (6.95 g, 25.0 mmol, 2.5 eq.). The reaction mixture was placed in an ice bath and a H_2O_2 solution (4.30 mL, 30% *w/w*, 5.0 eq.) was added dropwise to the vigorously stirring solution. The reaction mixture was stirred overnight at ambient temperature. The solution was basified using 2 M NaOH (50 mL), the precipitate was filtered off and the filtrate was extracted with diethyl ether (3 × 50 mL). The organic phase was washed with deionised water (15 mL) and dried over Na_2SO_4. The solvent was carefully removed under reduced pressure yielding a yellow liquid (1.38 g, 7.4 mmol, 74%).

^{1}H NMR (400 MHz, $CDCl_3$, 298 K) δ = 3.59 (s, 3H, O–CH_3), 3.04–2.93 (m, 1H, CH), 1.69–1.59 (m, 2H, CH_2), 1.33–1.21 (m, 2H, CH_2), 1.18 (s, 6H, $C(CH_3)_2$), 1.11 (s, 6H, $C(CH_3)_2$) ppm. ^{13}C NMR (101 MHz, $CDCl_3$, 298 K) δ = 65.5 (CH_3), 60.0 (C), 50.0 (CH_2), 42.2 (CH), 33.2 (CH_3), 20.9 (CH_3) ppm. HR-ESI-MS (*m/z*) calculated for $C_{10}H_{23}N_2O$ $[M+H]^+$ 187.1805, found 187.1808.

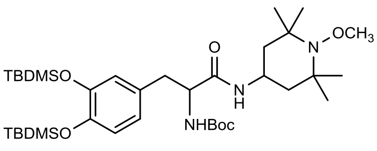

6

(TBDMS)$_2$-N-Boc-DOPA-TEMPO-CH$_3$ (**6**):
Compound **6** was prepared according to the previously reported procedure for compound **2** using 1-methoxy-2,2,6,6-tetramethylpiperidin-4-amine (**5**) (1.12 g, 6.0 mmol, 1.0 eq.) as starting material. The crude product was purified by silica column chromatography employing ethyl acetate and cyclohexane (2:7) as solvent mixture (R_f = 0.44) yielding a yellow solid (3.47 g, 5.0 mmol, 83%).

^{1}H NMR (400 MHz, methanol-*d$_4$*, 298 K) δ = 6.77 (d, J = 8.0 Hz, 1H, $C_{Ar}H$), 6.73 (d, J = 2.1 Hz, 1H, $C_{Ar}H$), 6.70 (dd, J = 8.1, 2.1 Hz, 1H, $C_{Ar}H$), 4.18–4.08 (m, 1H, C_{Ar}–CH_2–C*H*), 4.06–3.94 (m, 1H, NH–C*H*(CH_2)$_2$), 3.59 (s, 3H, O–CH_3), 2.90–2.67 (m, 2H, C_{Ar}–CH_2), 1.71–1.22 (m, 4H, NH–CH(C*H*$_2$)$_2$), 1.40 (s, 9H, O–$C(CH_3)_3$), 1.18 (s, 3H, $C(CH_3)_2$), 1.17(s, 3H, $C(CH_3)_2$), 1.16 (s, 3H, $C(CH_3)_2$), 1.15 (s, 3H, $C(CH_3)_2$), 1.01 (s, 9H, Si–$C(CH_3)_3$), 0.99 (s, 9H, Si–$C(CH_3)_3$), 0.21 (s, 6H, $Si(CH_3)_2$), 0.20 (s, 6H, $Si(CH_3)_2$) ppm. ^{13}C NMR (101 MHz, methanol-*d$_4$*, 298 K) δ = 178.3 (C), 157.4 (C), 147.8 (C_{Ar}), 146.9 (C_{Ar}), 131.7 (C_{Ar}), 123.7 ($C_{Ar}H$), 123.6 ($C_{Ar}H$), 122.0 ($C_{Ar}H$), 80.6 (C), 65.9 (CH_3), 61.0 (C), 57.6 (CH), 46.0 (CH_2), 45.9 (CH_2), 42.1 (CH), 39.0 (CH_2), 33.5 (CH_3), 33.4 (CH_3), 28.7 (CH_3), 26.6 (CH_3), 26.5 (CH_3), 20.9 (CH_3), 20.8 (CH_3), 19.4 (C), −3.7 (CH_3), −3.7 (CH_3) ppm. HR-ESI-MS (*m/z*) calculated for $C_{36}H_{68}N_3O_6Si_2$ $[M+H]^+$ 694.4641, found 694.4648. M.p. 148 °C.

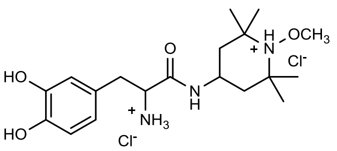

7

DOPA-TEMPO-CH_3 dihydrochloride (**7**): Compound **7** was prepared according to the previously presented procedure for compound **3** using $(TBDMS)_2$-*N*-Boc-DOPA-TEMPO-CH_3 (**6**) (1.20 g, 1.7 mmol, 1.0 eq.) as starting material. The pure product was isolated as a white-orange solid in quantitative yields. A variation of the herein presented synthetic procedure with lower yields is reported elsewhere.[327]

^{1}H NMR (400 MHz, methanol-d_4, 298 K) δ = 6.76 (d, J = 8.0 Hz, 1H, $C_{Ar}H$), 6.67 (d, J = 2.1 Hz, 1H, $C_{Ar}H$), 6.60 (dd, J = 8.0, 2.1 Hz, 1H, $C_{Ar}H$), 4.22–4.15 (m, 1H, NH–C*H*), 4.21 (s, 3H, O–CH_3), 3.94–3.86 (m, 1H, C_{Ar}–CH_2–C*H*), 3.04–2.87 (m, 2H, C_{Ar}–CH_2–CH), 2.10–1.65 (m, 4H, NH–CH–CH_2), 1.62 (s, 3H, $C(CH_3)_2$), 1.61 (s, 3H, $C(CH_3)_2$), 1.51 (s, 3H, $C(CH_3)_2$), 1.50 (s, 3H, $C(CH_3)_2$) ppm. ^{13}C NMR (101 MHz, methanol-d_4, 298 K) δ = 169.2 (C), 146.7 (C_{Ar}), 146.1 (C_{Ar}), 126.8 (C_{Ar}), 121.9 ($C_{Ar}H$), 117.7 ($C_{Ar}H$), 116.8 ($C_{Ar}H$), 71.7 (C), 71.6 (C), 68.5 (CH_3), 56.0 (CH), 42.7 (CH_2), 42.6 (CH_2), 40.5 (CH), 38.2 (CH_2), 28.5 (CH_3), 28.4 (CH_3), 21.0 (CH_3), 21.0 (CH_3) ppm. HR-ESI-MS (*m/z*) calculated for $C_{19}H_{32}ClN_3O_4$ $[M–HCl–Cl]^+$ 366.2387, found 366.2389. M.p. 138 °C (dec.).

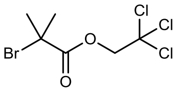

9

2,2,2-Trichloroethyl 2-bromoisobutyrate (**9**): 2,2,2-Trichloroethanol (0.77 mL, 8 mmol, 1 eq.), TEA (1.22 mL, 8.8 mmol, 1.1 eq.) and DMAP (20 mg, 0.16 mmol, 0,02 eq.) were dissolved in dry DCM (15 mL). The reaction solution was placed in an ice bath and α-bromoisobutyryl bromide (1.09 mL, 8.8 mmol, 1.1 eq.) was added dropwise to the vigorously stirring solution. The reaction mixture was stirred overnight allowed to reach ambient temperature. The solvent was removed under reduced pressure and the crude product was extracted with diethyl ether (50 mL) and diluted HCl (20 mL). The organic phase was washed with saturated $NaHCO_3$ solution (20 mL), brine (20 mL) and dried over $MgSO_4$. The solvent was removed under reduced pressure and the crude product was purified by silica column chromatography employing ethyl acetate and cyclohexane (1:3) as solvent mixture (R_f = 0.76) yielding a colourless liquid (2.21 g, 7.4 mmol, 93%).

^{1}H NMR (400 MHz, $CDCl_3$, 298 K) δ = 4.82 (s, 2H, CH_2), 2.01 (s, 6H, $C(CH_3)_2$) ppm. ^{13}C NMR (101 MHz, $CDCl_3$, 298 K) δ = 170.3 (C), 94.7 (C), 74.9 (CH_2), 54.6 (C), 30.8 (CH_3) ppm. HR-ESI-MS (*m/z*) calculated for $C_6H_8BrCl_3NaO_2$ $[M+Na]^+$ 318.8665, found 318.8664.

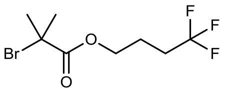

10

4,4,4-Trifluorobutyl 2-bromoisobutyrate (**10**): Compound **10** was synthesised following the previously described procedure for compound **9** using 4,4,4-trifluorobutanol (0.84 mL, 8 mmol, 1 eq.) as starting material. The crude product was purified by silica column chromatography employing ethyl acetate and cyclohexane (1:5) as solvent mixture ($R_f = 0.58$) yielding a colourless liquid (1.98 g, 7.1 mmol, 89%).

^1H NMR (400 MHz, $CDCl_3$, 298 K) $\delta = 4.24$ (t, $J = 6.2$ Hz, 2H, OCH_2), 2.31–2.16 (m, 2H, CH_2CF_3), 2.02–1.95 (m, 2H, OCH_2CH_2), 1.94 (s, 6H, $C(CH_3)_2$) ppm. ^{13}C NMR (101 MHz, $CDCl_3$, 298 K) $\delta = 171.6$ (C), 127.0 (q, $^1J_{CF} = 276$ Hz, CF_3), 64.2 (CH_2), 55.6 (C), 30.8 (CH_3), 30.7 (q, $^2J_{CF} = 29$ Hz, CH_2CF_3), 21.6 (q, $^3J_{CF} = 3$ Hz, $CH_2CH_2CF_3$) ppm. ^{19}F NMR (377 MHz, $CDCl_3$, 298 K) $\delta = -66.4$ (t, $^3J_{FH} = 10.7$ Hz, CF_3) ppm. HR-ESI-MS (*m/z*) calculated for $C_8H_{12}BrF_3NaO_2$ $[M+Na]^+$ 298.9865, found 298.9868.

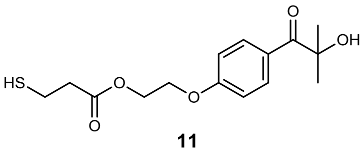

11

Thiol functionalised Irgacure 2959 (**11**)[1]: The synthesis of compound **11** was adapted from the literature.[354] 2-hydroxy-4′-(2-hydroxyethoxy)-2-methylpropiophenone (1.50 g, 6.7 mmol, 1.00 eq.), 3-mercaptopropionic acid (0.71 g, 0.58 mL, 6.7 mmol, 1.00 eq.) and *p*-toluenesulfonic acid monohydrate (127 mg, 0.7 mmol, 0.10 eq.) were dissolved in toluene (10 mL) containing a molecular sieve (1.7 g, 4 Å). The reaction mixture was refluxed overnight under continuous stirring. Subsequently, the cooled reaction solution was filtered through a column of basic alumina. The column was flushed with toluene (3 × 10 mL) and the filtrates were combined. The solvent was removed by distillation under reduced pressure and the crude product was obtained as a viscous liquid. The crude material was dissolved in dichloromethane (40 mL) and the solution was washed with a saturated solution of sodium hydrogen carbonate (4 × 40 mL), followed by washing with deionised water (40 mL) and brine (40 mL). The organic phase was dried over Na_2SO_4 and filtered. The solvent was removed under reduced pressure. Subsequently, the crude product was purified by silica column chromatography employing ethyl acetate and cyclohexane (2:3) as solvent mixture ($R_f = 0.47$) yielding a colourless oil (777 mg, 2.5 mmol, 37%).

---

[1] Compound **11** was synthesised, characterised, and kindly provided by A. Lauer (KIT).

^{1}H NMR (400 MHz, $CDCl_3$, 298 K): $\delta = 8.06$ (d, $J = 9.0$ Hz, 2H, $C_{Ar}H$), 6.95 (d, $J = 9.0$ Hz, 2H, $C_{Ar}H$), 4.50 (t, $J = 4.7$ Hz, 2H, OCH_2), 4.26 (t, $J = 4.7$ Hz, 2H, OCH_2), 4.20 (s, 1H, OH), 2.81–2.68 (m, 4H, $(CH_2)_2$–C=O), 1.63 (s, 6H, $C(CH_3)_2$) ppm. ^{13}C NMR (101 MHz, $CDCl_3$, 298 K) $\delta = 203.1$ (C), 171.9 (C), 162.7 (C_{Ar}), 132.9 ($C_{Ar}H$), 126.9 (C_{Ar}), 114.6 ($C_{Ar}H$), 76.3 (C), 66.4 (CH_2), 63.1 (CH_2), 38.8 (CH_2), 29.1 (CH_3), 20.1 (CH_2) ppm. HR-ESI-MS (*m/z*) calculated for $C_{15}H_{20}NaO_5S$ $[M+Na]^+$ 335.0924, found 335.0921.

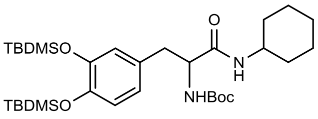

14

(TBDMS)$_2$-N-Boc-DOPA-Cy (**14**): Compound **14** was prepared according to the previously reported procedure for compound **2** using cyclohexylamine (1.72 mL, 15.0 mmol, 1.5 eq.) as starting material. The crude product was purified by silica column chromatography employing ethyl acetate and cyclohexane (3:1) as solvent mixture ($R_f = 0.56$) yielding a yellow solid (5.0 g, 8.2 mmol, 82%).

^{1}H NMR (600 MHz, methanol-d_4) $\delta = 6.76$ (d, $J = 8.1$ Hz, 1H, $C_{Ar}H$), 6.73 (d, $J = 2.1$ Hz, 1H, $C_{Ar}H$), 6.69 (dd, $J = 8.1, 2.1$ Hz, 1H, $C_{Ar}H$), 4.18–4.12 (m, 1H, C_{Ar}–CH_2–CH), 3.62–3.54 (m, 1H, NH–C$H$$(CH_2)_5$), 2.92–2.66 (m, 2H, C_{Ar}–CH_2), 1.86–1.03 (m, 10H, $(CH_2)_5$), 1.40 (s, 9H, O–$C(CH_3)_3$), 1.00 (s, 9H, Si–$C(CH_3)_3$), 0.99 (s, 9H, Si–$C(CH_3)_3$), 0.20 (s, 6H, $Si(CH_3)_2$), 0.19 (s, 6H, $Si(CH_3)_2$) ppm. ^{13}C NMR (151 MHz, methanol-d_4) $\delta = 173.0$ (C), 157.4 (C), 147.7 (C_{Ar}), 146.9 (C_{Ar}), 131.8 (C_{Ar}), 123.7 ($C_{Ar}H$), 123.6 ($C_{Ar}H$), 122.1 ($C_{Ar}H$), 80.6 (C), 57.5 (CH), 49.7 (CH), 39.1 (CH_2), 33.7 (CH_2), 33.6 (CH_2), 28.7 (CH_3), 26.6 (CH_2), 26.54 (CH_3), 26.53 (CH_3), 26.1 (CH_2), 19.34 (C), 19.31 (C), −3.7 (CH_3), −3.8 (CH_3) ppm. HRMS (*m/z*) calculated for $C_{32}H_{58}N_2NaO_5Si_2$ $[M+Na]^+$ 629.3776, found 629.3777. M.p. 114 °C.

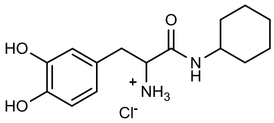
15

DOPA-Cy hydrochloride (**15**): Compound **15** was prepared according to the previously presented procedure for compound **3** using (TBDMS)$_2$-*N*-Boc-DOPA-Cy (**14**) (1.82 g, 3.0 mmol, 1.0 eq.) as starting material. The pure product was isolated as a white solid in quantitative yields.

^{1}H NMR (600 MHz, methanol-d_4) δ = 6.74 (d, J = 8.0 Hz, 1H, C$_{\mathrm{Ar}}H$), 6.70 (d, J = 2.1 Hz, 1H, C$_{\mathrm{Ar}}H$), 6.58 (dd, J = 8.0, 2.1 Hz, 1H, C$_{\mathrm{Ar}}H$),), 3.93–3.88 (m, 1H, C$_{\mathrm{Ar}}$–CH$_2$–CH), 3.64–3.56 (m, 1H, NH–CH(CH$_2$)$_5$), 3.00–2.88 (m, 2H, C$_{\mathrm{Ar}}$–CH_2), 1.89–1.00 (m, 10H, (CH_2)$_5$) ppm. ^{13}C NMR (151 MHz, methanol-d_4) δ = 168.6 (C), 146.7 (C$_{\mathrm{Ar}}$), 146.1 (C$_{\mathrm{Ar}}$), 126.8 (C$_{\mathrm{Ar}}$), 121.9 (C$_{\mathrm{Ar}}$H), 117.6 (C$_{\mathrm{Ar}}$H), 116.6 (C$_{\mathrm{Ar}}$H), 56.0 (CH), 50.0 (CH), 38.3 (CH$_2$), 33.5 (CH$_2$), 33.4 (CH$_2$), 26.5 (CH$_2$), 25.9 (CH$_2$) ppm. HR-ESI-MS (*m/z*) calculated for $C_{15}H_{23}N_2O_3$ [M−Cl]$^+$ 279.1703, found 279.1702. M.p. 84 °C.

9.3.2 Polymerisations and Surface Functionalisations

All polymerisations and surface coatings were conducted using solvents in HPLC grade (or equivalent solvent purities). Tris buffer solutions were typically adjusted using 1 M HCl. Uncoated substrates were cleaned by ultrasonication in methanol (15 min) and water (15 min), followed by drying under nitrogen prior to coating. Electrodes were thoroughly polished prior to coating. Surface coatings for biological studies were conducted under sterile conditions.

Light-triggered catecholamine polymerisations and surface photopatterning reactions presented in Chapter 5.4 and Chapter 7.5 were performed using a Luzchem LZV-4V photoreactor (Luzchem Research Inc., Ottawa, Canada) equipped with 10 UV-B lamps (LZC-UVB, centred at approx. 300 nm, with a peak of 313 nm), irradiating from the top and the sides under continuous rotation or stirring of the samples. Photoreactions presented in Chapter 6.3 were performed in a custom-built photoreactor equipped with an Arimed B6 UV lamp (36 W, λ_{max} = 320 nm, Cosmedico GmbH, Germany). A custom-made sample holder and a dotted shadow mask (Ø 1 mm pinholes) were employed for photolithographic surface patterning. The emission spectrum of the employed lamp, the design of the photoreactor, and the employed shadow masks are described elsewhere.[266, 355]

Catecholamine Polymerisations and Surface Functionalisations

*Mechanistic Polymerisation of **3** (Chapter 3.3)*

DOPA-TEMPO (**3**) (8.49 mg, 0.02 mmol) was dissolved in 10 mM Tris–HCl buffer (20 mL, pH 8.5). The 1 mM solution was vigorously stirred in a closed glass vial. During oxidative polymerisation, aliquots (50 µL) were taken for EPR spectroscopic analysis. UV/vis spectroscopic aliquots (125 µL) were diluted to 0.05 mM prior to spectrophotometric characterisation. EPR spectroscopic radical quantification is referenced to the hydroxylamine oxidation of TEMPOL previously converted to the hydroxylamine hydrochloride species. All experiments were run in duplicate. Error bars representing the 1 standard deviation of uncertainty are smaller than the symbols and are not displayed in **Figure 3.3**.

*Polymerisation of **3** for HR-ESI-MS characterisation (Chapter 3.4)*

Compound **3** (529 mg, 1.25 mmol) was dissolved in 10 mM Tris–HCl buffer (125 mL, pH 8.5). The 10 mM solution of **3** was vigorously stirred in an open glass vial exposed to air. After 72 h, the precipitate was isolated by centrifugation and decantation. The solid was washed with water (3 × 30 mL), followed by centrifugation and decantation. The product was lyophilised and isolated as a yellow-brown solid (78 mg).

*Polymerisation of **7** for HR-ESI-MS characterisation (Chapter 4)*

The polymerisation of **7** (548 mg, 1.25 mmol) was conducted according to the above-mentioned polymerisation procedure for **3**. The pH value was carefully readjusted and maintained within the first 30 min of polymerisation of **7** at pH 8.25 ± 0.05 using Tris. Polymer **8** was isolated as a yellow-brown solid (80 mg). Corresponding ^{1}H and ^{13}C NMR spectra are depicted in **Figures B.3** and **B.4** in the Appendix.

*Poly(DOPA-TEMPO) (**4**) Surface Depositions onto Various Substrates (Chapter 5.2 and Chapter 5.3)*

During polymerisation of monomer **3** (as described above for HR-ESI-MS characterisation), various substrates (silicon, titanium, alumina, PTFE) were typically immersed for 12 h and 24 h, respectively. The polymer deposition kinetic study using silicon substrates was performed within the first 12 h of polymerisation. All substrates were vertically immersed to reduce polymer particle sedimentation. After coating, the substrates were thoroughly rinsed with water and dried under a nitrogen or argon stream. In addition, a glassy carbon and a platinum working electrode were immersed in a 10 mM coating solution of **3** (0.1 mmol, 42 mg) using a Tris–HCl buffer (10 mL, pH 8.5). Electrodes were coated for 1, 4, and 7 days, respectively, with further monomer addition (0.05 mmol) after coating interval. The coated electrodes were thoroughly rinsed with water before electrochemical analysis.

*Light-Dependent Polymerisation of **3** and Polymer Film Formation on Silicon Surfaces (Chapter 5.4)*

Monomer **3** (11 mg, 25 μmol) was dissolved in 10 mM Tris–HCl buffer (5mL, pH 8.5). The 5 mM coating solution was vigorously stirred in a closed glass vial and exposed to UV-B irradiation for 0–12 h using the Luzchem LZV-4V photoreactor. Aliquots (50 μL) were taken for EPR spectroscopic analysis. UV–vis spectroscopic aliquots (50 μL) were diluted to 0.1 mM prior to spectrophotometric characterisation. Silicon substrates were placed in a petri dish and a separate coating solution of **3** was added. The coating solution was exposed to UV irradiation under continuous rotation of the petri dish in the photoreactor. Coated silicon substrates were analysed by SE. Control experiments (in the dark) were conducted likewise.

*Copolymerisation of DA and **3** with Copolymer Surface Deposition onto PGMA microspheres (Chapter 6.2)*

Dopamine hydrochloride (34 mg, 0.18 mmol, 9 eq.) and compound **3** (9 mg, 0.02 mmol, 1 eq.) were dissolved in 10 mM Tris–HCl buffer (20 mL, pH 8.5). PGMA microspheres (0.50 g) were added to the 10 mM coating solution, and the suspension was vigorously shaken for 2 days at ambient temperature. The coated microspheres were thoroughly washed with water, acetonitrile, methanol, toluene, methanol, and water. The nitroxide-functionalised microspheres were dried under vacuum at 40 °C and isolated as brown particles (0.48 g).

Polymerisation of DA concomitant with PDA Surface Deposition onto Silicon Substrates (Chapter 6.3)

Dopamine hydrochloride (250 mg, 1.32 mmol, 2 mg·ml^{-1}) was dissolved in 10 mM Tris–HCl buffer (125 mL, pH 8.5). The oxidative polymerisation of DA with *in situ* polymer deposition onto immersed silicon substrates was performed in an open glass vial under vigorous stirring. After 24 h, the PDA-coated silicon substrates were thoroughly rinsed with water and dried in a stream of nitrogen.

Poly(DOPA-TEMPO) and Poly(DOPA-Cy) Surface Depositions onto HA Discs and Titanium Substrates (Chapter 7.3)

Compound **3** (51 mg) was dissolved in 100 mM Tris–HCl buffer (3 mL, pH 9.25). Uncoated objects (hydroxyapatite discs or titanium substrates) were immersed for 24 h under gentle shaking of the coating solution at ambient temperature. After coating, the substrates were thoroughly rinsed with water and dried under atmospheric conditions. The reference coating system was prepared likewise employing compound **15** (38 mg) as a coating agent.

Photolithographic Surface Patterning of Poly(DOPA-TEMPO) (Chapter 7.5)

Compound **3** (11 mg, 25 μmol) was dissolved in 10 mM Tris–HCl buffer (5 mL, pH 8.5). Titanium substrates (1 × 1 cm^2) covered by a dotted shadow mask were vertically immersed into the coating solution of **3** for 12 h. After coating, patterned surfaces were carefully washed with water.

Post-Coating Surface Functionalisations and Other Polymerisations

*NRC reactions of **MS1** with **9** (Chapter 6.2)*

MS1 (125 mg), copper(0) (4.8 mg, 75 µmol, 0.5 eq.) and compound **9** (45 mg, 0.15 mmol, 1 eq.) were suspended and dissolved in dry acetonitrile (5 mL). The reaction mixture was degassed with argon for 20 min, followed by addition of PMDETA (19 µL, 90 µmol, 0.6 eq.). The suspension was shaken for 18 h at ambient temperature. The conjugated microspheres were thoroughly washed with acetonitrile, 0.05 M aqueous EDTA solution, water, methanol, acetone and dichloromethane. The chlorine-tagged microspheres were dried under air and isolated as brown particles (115 mg).

Thermolysis of alkoxyamine functionalised microspheres (Chapter 6.2)

MS2 (75 mg) was suspended in anisole (5 mL) followed by addition of TMIO (20 mg) as a radical trapping agent. The suspension was purged with argon for 15 min. Alkoxyamine thermolysis was conducted at 110 °C. After 6 h, the solvent was replaced by a fresh solution of anisole (5 mL) containing TMIO (20 mg), and the reaction time was prolonged for additional 6 h. EPR control experiments were performed in the absence of TMIO, yet under the influence of atmospheric oxygen as a radical scavenger. The regenerated nitroxide-functionalised microspheres were thoroughly washed with anisole, methanol, acetone and dichloromethane and dried under air yielding brown particles (70 mg).

*NRC reactions of **MS3** with **10** (Chapter 6.2)*

NRC reactions with **MS3** (30 mg) were performed according to the above-mentioned procedure. Compound **10** (42 mg, 0.15 mmol, 1 eq.) was employed as a coupling agent yielding brown particles (28 mg).

Nitroxide Immobilisation onto PDA-coated Substrates (Chapter 6.3)

4-Carboxy-TEMPO (20 mg, 0.1 mmol, 1.0 eq.) and EDC·HCl (23 mg, 0.12 mmol, 1.2 eq.) were dissolved in dry DFM (6 mL) followed by addition of DIPEA (42 µL, 0.24 mmol, 2.4 eq.). PDA precoated substrates were immersed for 24 h under gentle shaking. Nitroxide-immobilised substrates were carefully washed with DMF, ethanol and water, followed by drying under nitrogen stream.

MMA and TFEMA Chain Transfer Polymerisations (Chapter 6.3)[*]

AIBN (0.04 $mol \cdot L^{-1}$) was dissolved in approximately 0.5 mL of a stock solution of MMA or TFEMA containing 6 eq. of transfer agent **11** (with respect to AIBN). The sample was degassed with nitrogen and polymerised for 20 minutes at 80 °C. The polymers were precipitated twice in *n*-hexane to remove unreacted AIBN and **11**, respectively.

*Surface Polymer Ligations with **12** and **13** (Chapter 6.3)*

The nitroxide-functionalised PDA-coated surface was covered with a shadow mask and placed in Pyrex headspace vial. PI-PMMA (**12**) (10 mg, $M_n = 7000\ g \cdot mol^{-1}$) dissolved in dry acetonitrile (5 mL) was added to the substrate, and the sealed glass vial was purged with nitrogen for 15 min. After 30 min UV irradiation, the substrates were thoroughly washed with acetonitrile, methanol and water, and dried under nitrogen stream. Subsequent polymer surface ligation with PI-PTFEMA (**13**) (15 mg, $M_n = 12000\ g \cdot mol^{-1}$) was performed likewise.

---

[*] Polymer **12** and **13** were synthesised and kindly provided by D. Fast (TU Graz, Austria). SEC characterisation was performed by A. Lauer (KIT).

9.3.3 Biofilm Assays

Biofilm flow cell studies were performed following previously established experimental protocols from the literature.[4-5] All experiments were conducted under sterile conditions. A GPF-labelled PA14 strain was employed carrying a pUCP23.eGFP plasmid, which was constructed from a pBBR1MCS.egfp-t0 and a pUCP23.mCherry plasmid. The pUCP plasmids carry a *Pseudomonas* stabilising fragment that allows replication in *Pseudomonas*.*

Overnight cultures of the GFP-labelled PA14 strain were grown in lysogeny broth (LB) in the presence of gentamicin (50 $\mu g \cdot mL^{-1}$) and were diluted to an OD_{600} of approx. 0.05 prior to biofilm experiments. Biofilm assays were performed in BM2 ((62 mM potassium phosphate buffer (7 mM $(NH_4)_2SO_4$, 40 mM K_2HPO_4, 22 mM KH_2PO_4; pH 7), 0.5 mM MgSO4, and 0.4 wt% glucose) in the presence of gentamicin (50 $\mu g \cdot mL^{-1}$). Coated and uncoated substrates were adjacently placed in flow cell chambers (CFCAS0004, IBI Scientific) and connected to silicon tubing (VWR, 89068-468; 0.062 × 0.125 inch (inner and outer diameter), 0.032 inch wall thickness). The flow cell system was sterilised by pumping a 0.5% hypochlorite solution through the system using a Watson Marlow 205S multichannel peristaltic pump (at 0.5 rpm, 30 min). Afterwards, the experimental setup was rinsed with sterile water (at 0.5 rpm, 1 h) and BM2 medium (1 h). The flow cell chambers were inoculated with aliquots (400 µL) of the overnight culture and left without flow for 3 h. Biofilm experiments were performed under continuous flow (2.4 $mL \cdot h^{-1}$; approx. 0.5 rpm) for 72 h at 37 °C. Biofilm eradication assays were conducted on preformed biofilms (48 h), which were subsequently exposed to ciprofloxacin (320 $ng \cdot ml^{-1}$) for additional 24 h. Staining with propidium iodide (Live/Dead BacLight bacterial viability kit, Thermo Fisher Scientific) was conducted prior to microscopy for visualisation of surface-adherent dead cells.

Static biofilm studies were performed in BM2 (recipe above) supplemented with $FeSO_4$ (10 µM) and gentamicin (50 $\mu g \cdot mL^{-1}$). BM2 was inoculated with aliquots of the overnight culture diluted to an OD_{600} of approx. 0.05. The polymer patterned Ti surfaces were placed in separate wells of a 24-well plate and were covered by the inoculated medium (1 mL). Biofilms were grown for 72 h at 37 °C, and the media

---

[*] The GFP-labelled PA14 strain was kindly provided by Dr. Daniel Pletzer (UBC).

was replaced after 24 and 48 h, respectively. The substrates were gently washed in phosphate buffered saline (PBS) (1×) prior to confocal imaging in order to remove planktonic bacteria.

Bibliography

[1] L. Tebben, A. Studer, *Angew. Chem. Int. Ed.* **2011**, *50*, 5034-5068.

[2] K.-A. Hansen, J. P. Blinco, *Polym. Chem.* **2018**, *9*, 1479-1516.

[3] N. Barraud, M. J. Kelso, S. A. Rice, S. Kjelleberg, *Curr. Pharm. Des.* **2015**, *21*, 31-42.

[4] C. de la Fuente-Núñez, F. Reffuveille, K. E. Fairfull-Smith, R. E. W. Hancock, *Antimicrob. Agents Chemother.* **2013**, *57*, 4877-4881.

[5] F. Reffuveille, C. de la Fuente-Núñez, K. E. Fairfull-Smith, R. E. W. Hancock, *Pathog. Dis.* **2015**, *73*, ftv016.

[6] K. Zhang, M. J. Monteiro, Z. Jia, *Polym. Chem.* **2016**, *7*, 5589-5614.

[7] L. Hall-Stoodley, J. W. Costerton, P. Stoodley, *Nat. Rev. Microbiol.* **2004**, *2*, 95-108.

[8] J. W. Costerton, P. S. Stewart, E. P. Greenberg, *Science* **1999**, *284*, 1318-1322.

[9] H.-C. Flemming, J. Wingender, *Nat. Rev. Microbiol.* **2010**, *8*, 623-633.

[10] P. Watnick, R. Kolter, *J. Bacteriol.* **2000**, *182*, 2675-2679.

[11] D. Davies, *Nat. Rev. Drug Discovery* **2003**, *2*, 114-122.

[12] M. Rosenfeld, R. L. Gibson, S. McNamara, J. Emerson, J. L. Burns, R. Castile, P. Hiatt, K. McCoy, C. B. Wilson, A. Inglis, A. Smith, T. R. Martin, B. W. Ramsey, *Pediatr. Pulmonol.* **2001**, *32*, 356-366.

[13] P. S. Stewart, J. W. Costerton, *Lancet* **2001**, *358*, 135-138.

[14] C. de la Fuente-Núñez, F. Reffuveille, L. Fernández, R. E. W. Hancock, *Curr. Opin. Microbiol.* **2013**, *16*, 580-589.

[15] H. Wolfmeier, D. Pletzer, S. C. Mansour, R. E. W. Hancock, *ACS Infect. Dis.* **2018**, *4*, 93-106.

[16] D. McDougald, S. A. Rice, N. Barraud, P. D. Steinberg, S. Kjelleberg, *Nat. Rev. Microbiol.* **2012**, *10*, 39-50.

[17] Z. K. Zander, M. L. Becker, *ACS Macro Lett.* **2018**, *7*, 16-25.

[18] E. M. Hetrick, M. H. Schoenfisch, *Chem. Soc. Rev.* **2006**, *35*, 780-789.

[19] I. Novak, L. J. Harrison, B. Kovač, L. M. Pratt, *J. Org. Chem.* **2004**, *69*, 7628-7634.

[20] N. Kocherginsky, H. M. Swartz, *Nitroxide Spin Labels: Reactions in Biology and Chemistry*, CRC Press, Boca Raton, **1995**.

[21] E. Fremy, *Ann. Chim. Phys* **1845**, *15*, 408-488.

[22] O. Piloty, B. G. Schwerin, *Ber. Dtsch. Chem. Ges.* **1901**, *34*, 1870-1887.

[23] H. Wieland, M. Offenbächer, *Ber. Dtsch. Chem. Ges.* **1914**, *47*, 2111-2115.

[24] L. B. Volodarsky, V. A. Reznikov, V. I. Ovcharenko, *Synthetic Chemistry of Stable Nitroxides*, CRC Press, Boca Raton, **1994**.

[25] S. Grimaldi, J.-P. Finet, F. Le Moigne, A. Zeghdaoui, P. Tordo, D. Benoit, M. Fontanille, Y. Gnanou, *Macromolecules* **2000**, *33*, 1141-1147.

[26] A. Debuigne, D. Chan-Seng, L. Li, G. K. Hamer, M. K. Georges, *Macromolecules* **2007**, *40*, 6224-6232.

[27] A. C. Greene, R. B. Grubbs, *Macromolecules* **2009**, *42*, 4388-4390.

[28] P. G. Griffiths, G. Moad, E. Rizzardo, *Aust. J. Chem.* **1983**, *36*, 397-401.

[29] S. E. Bottle, U. Chand, A. S. Micallef, *Chem. Lett.* **1997**, *26*, 857-858.

[30] J. P. Blinco, K. E. Fairfull-Smith, B. J. Morrow, S. E. Bottle, *Aust. J. Chem.* **2011**, *64*, 373-389.

[31] S. D. Rychnovsky, T. Beauchamp, R. Vaidyanathan, T. Kwan, *J. Org. Chem.* **1998**, *63*, 6363-6374.

[32] E. G. Rozantsev, V. D. Sholle, *Synthesis* **1971**, *1971*, 190-202.

[33] L. M. Field, P. M. Lahti, F. Palacio, A. Paduan-Filho, *J. Am. Chem. Soc.* **2003**, *125*, 10110-10118.

[34] D. H. Hunter, J. S. Racok, A. W. Rey, Y. Zea-Ponce, *J. Org. Chem.* **1988**, *53*, 1278-1281.

[35] T. Miyazawa, T. Endo, M. Okawara, *J. Org. Chem.* **1985**, *50*, 5389-5391.

[36] D. A. Reid, S. E. Bottle, *Chem. Commun.* **1998**, 1907-1908.

[37] T. D. Lee, J. F. W. Keana, *J. Org. Chem.* **1976**, *41*, 3237-3241.

[38] J. Laun, W. Marchal, V. Trouillet, A. Welle, A. Hardy, M. K. Van Bael, C. Barner-Kowollik, T. Junkers, *Langmuir* **2018**, *34*, 3244-3255.

[39] E. H. H. Wong, T. Junkers, C. Barner-Kowollik, *Polym. Chem.* **2011**, *2*, 1008-1017.

[40] E. H. H. Wong, M. H. Stenzel, T. Junkers, C. Barner-Kowollik, *J. Polym. Sci., Part A: Polym. Chem.* **2011**, *49*, 2118-2126.

[41] E. H. H. Wong, O. Altintas, M. H. Stenzel, C. Barner-Kowollik, T. Junkers, *Chem. Commun.* **2011**, *47*, 5491-5493.

[42] S. A. F. Bon, G. Chambard, A. L. German, *Macromolecules* **1999**, *32*, 8269-8276.

[43] H. Fischer, *Chem. Rev.* **2001**, *101*, 3581-3610.

[44] A. Studer, *Chem. Eur. J.* **2001**, *7*, 1159-1164.

[45] A. Studer, T. Schulte, *Chem. Rec.* **2005**, *5*, 27-35.

[46] C. J. Hawker, A. W. Bosman, E. Harth, *Chem. Rev.* **2001**, *101*, 3661-3688.

[47] D. Yang, C. Feng, J. Hu, *Polym. Chem.* **2013**, *4*, 2384-2394.

[48] T. Maeda, H. Otsuka, A. Takahara, *Prog. Polym. Sci.* **2009**, *34*, 581-604.

[49] T. S. Fischer, S. Spann, Q. An, B. Luy, M. Tsotsalas, J. P. Blinco, H. Mutlu, C. Barner-Kowollik, *Chem. Sci.* **2018**, *9*, 4696-4702.

[50] B. A. Chalmers, J. C. Morris, K. E. Fairfull-Smith, R. S. Grainger, S. E. Bottle, *Chem. Commun.* **2013**, *49*, 10382-10384.

[51] M. K. Eberhardt, R. Colina, *J. Org. Chem.* **1988**, *53*, 1071-1074.

[52] S. Marque, H. Fischer, E. Baier, A. Studer, *J. Org. Chem.* **2001**, *66*, 1146-1156.

[53] J. Sobek, R. Martschke, H. Fischer, *J. Am. Chem. Soc.* **2001**, *123*, 2849-2857.

[54] S. Marque, C. Le Mercier, P. Tordo, H. Fischer, *Macromolecules* **2000**, *33*, 4403-4410.

[55] A. Goto, J. Scaiano, L. Maretti, *Photochem. Photobiol. Sci.* **2007**, *6*, 833-835.

[56] Y. Guillaneuf, D. Bertin, D. Gigmes, D.-L. Versace, J. Lalevee, J.-P. Fouassier, *Macromolecules* **2010**, *43*, 2204-2212.

[57] J. Morris, S. Telitel, K. E. Fairfull-Smith, S. E. Bottle, J. Lalevée, J.-L. Clément, Y. Guillaneuf, D. Gigmes, *Polym. Chem.* **2015**, *6*, 754-763.

[58] M. Baron, J. C. Morris, S. Telitel, J.-L. Clément, J. Lalevée, F. Morlet-Savary, A. Spangenberg, J.-P. Malval, O. Soppera, D. Gigmes, Y. Guillaneuf, *J. Am. Chem. Soc.* **2018**, *140*, 3339-3344.

[59] D.-L. Versace, Y. Guillaneuf, D. Bertin, J. P. Fouassier, J. Lalevée, D. Gigmes, *Org. Biomol. Chem.* **2011**, *9*, 2892-2898.

[60] Y. Guillaneuf, D. L. Versace, D. Bertin, J. Lalevée, D. Gigmes, J. P. Fouassier, *Macromol. Rapid Commun.* **2010**, *31*, 1909-1913.

[61] S. E. Bottle, J.-L. Clement, M. Fleige, E. M. Simpson, Y. Guillaneuf, K. E. Fairfull-Smith, D. Gigmes, J. P. Blinco, *RSC Adv.* **2016**, *6*, 80328-80333.

[62] M. Herder, J.-M. Lehn, *J. Am. Chem. Soc.* **2018**, *140*, 7647-7657.

[63] S. Telitel, S. Telitel, J. Bosson, J. Lalevée, J.-L. Clément, M. Godfroy, J.-L. Fillaut, H. Akdas-Kilig, Y. Guillaneuf, D. Gigmes, O. Soppera, *Langmuir* **2015**, *31*, 10026-10036.

[64] S. Telitel, S. Telitel, J. Bosson, A. Spangenberg, J. Lalevée, F. Morlet-Savary, J.-L. Clément, Y. Guillaneuf, D. Gigmes, O. Soppera, *Adv. Mater. Interfaces* **2014**, *1*, 1400067.

[65] L. Zhang, E. Laborda, N. Darwish, B. B. Noble, J. H. Tyrell, S. Pluczyk, A. P. Le Brun, G. G. Wallace, J. Gonzalez, M. L. Coote, S. Ciampi, *J. Am. Chem. Soc.* **2018**, *140*, 766-774.

[66] B. Goodman, P. Hall, in *Clay Mineralogy: Spectroscopic and Chemical Determinative Methods*, Springer, Dordrecht, **1994**, pp. 173-225.

[67] S. S. Eaton, G. R. Eaton, *Electron Paramagn, Reson.* **2004**, *19*, 318-337.

[68] T. Kurosaki, K. W. Lee, M. Okawara, *J. Polym. Sci., Part A: Polym. Chem.* **1972**, *10*, 3295-3310.

[69] C. Lang, L. Barner, J. P. Blinco, C. Barner-Kowollik, K. E. Fairfull-Smith, *Polym. Chem.* **2018**, *9*, 1348-1355.

[70] J. Zhang, H. Shen, W. Song, G. Wang, *Macromolecules* **2017**, *50*, 2683-2695.

[71] Z. Jia, C. A. Bell, M. J. Monteiro, *Macromolecules* **2011**, *44*, 1747-1751.

[72] V. D. Sen, V. A. Golubev, *J. Phys. Org. Chem.* **2009**, *22*, 138-143.

[73] J. Winsberg, S. Muench, T. Hagemann, S. Morgenstern, T. Janoschka, M. Billing, F. H. Schacher, G. Hauffman, J.-F. Gohy, S. Hoeppener, M. D. Hager, U. S. Schubert, *Polym. Chem.* **2016**, *7*, 1711-1718.

[74] T. Endo, K. Takuma, T. Takata, C. Hirose, *Macromolecules* **1993**, *26*, 3227-3229.

[75] H. Mutlu, C. W. Schmitt, N. Wedler-Jasinski, H. Woehlk, K. E. Fairfull-Smith, J. P. Blinco, C. Barner-Kowollik, *Polym. Chem.* **2017**, *8*, 6199-6203.

[76] S. E. Bottle, D. G. Gillies, D. L. Hughes, A. S. Micallef, A. I. Smirnov, L. H. Sutcliffe, *J. Chem. Soc., Perkin Trans. 2* **2000**, 1285-1291.

[77] J. P. Allen, M. C. Pfrunder, J. C. McMurtrie, S. E. Bottle, J. P. Blinco, K. E. Fairfull-Smith, *Eur. J. Org. Chem.* **2017**, *2017*, 476-483.

[78] J. P. Blinco, J. L. Hodgson, B. J. Morrow, J. R. Walker, G. D. Will, M. L. Coote, S. E. Bottle, *J. Org. Chem.* **2008**, *73*, 6763-6771.

[79] J. E. Baur, S. Wang, M. C. Brandt, *Anal. Chem.* **1996**, *68*, 3815-3821.

[80] J. Winsberg, T. Hagemann, T. Janoschka, M. D. Hager, U. S. Schubert, *Angew. Chem. Int. Ed.* **2017**, *56*, 686-711.

[81] C. D. Smith, J. P. Bartley, S. E. Bottle, A. S. Micallef, D. A. Reid, *J. Mass Spectrom.* **2000**, *35*, 607-611.

[82] D. L. Marshall, M. L. Christian, G. Gryn'ova, M. L. Coote, P. J. Barker, S. J. Blanksby, *Org. Biomol. Chem.* **2011**, *9*, 4936-4947.

[83] D. L. Marshall, G. Gryn'ova, M. L. Coote, P. J. Barker, S. J. Blanksby, *Int. J. Mass spectrom.* **2015**, *378*, 38-47.

[84] T. Gruendling, S. Weidner, J. Falkenhagen, C. Barner-Kowollik, *Polym. Chem.* **2010**, *1*, 599-617.

[85] C. Detrembleur, C. Jérôme, J. De Winter, P. Gerbaux, J.-L. Clément, Y. Guillaneuf, D. Gigmes, *Polym. Chem.* **2014**, *5*, 335-340.

[86] T. S. Fischer, J. Steinkoenig, H. Woehlk, J. P. Blinco, K. E. Fairfull-Smith, C. Barner-Kowollik, *Polym. Chem.* **2017**, *8*, 5269-5274.

[87] V. Sciannamea, R. Jérôme, C. Detrembleur, *Chem. Rev.* **2008**, *108*, 1104-1126.

[88] J. Chiefari, Y. K. Chong, F. Ercole, J. Krstina, J. Jeffery, T. P. T. Le, R. T. A. Mayadunne, G. F. Meijs, C. L. Moad, G. Moad, *Macromolecules* **1998**, *31*, 5559-5562.

[89] C. Barner-Kowollik, T. P. Davis, J. P. Heuts, M. H. Stenzel, P. Vana, M. Whittaker, *J. Polym. Sci., Part A: Polym. Chem.* **2003**, *41*, 365-375.

[90] K. Matyjaszewski, *Macromolecules* **2012**, *45*, 4015-4039.

[91] N. V. Tsarevsky, K. Matyjaszewski, *Chem. Rev.* **2007**, *107*, 2270-2299.

[92] X. Chen, B. Gao, J. Kops, W. Batsberg, *Polymer* **1998**, *39*, 911-915.

[93] Y. Wang, S. Chen, J. Huang, *Macromolecules* **1999**, *32*, 2480-2483.

[94] J. P. Blinco, K. E. Fairfull-Smith, A. S. Micallef, S. E. Bottle, *Polym. Chem.* **2010**, *1*, 1009-1012.

[95] N. J. Turro, G. Lem, I. S. Zavarine, *Macromolecules* **2000**, *33*, 9782-9785.

[96] T. Sato, Y. Amamoto, H. Yamaguchi, T. Ohishi, A. Takahara, H. Otsuka, *Polym. Chem.* **2012**, *3*, 3077-3083.

[97] R. Barbey, L. Lavanant, D. Paripovic, N. Schuwer, C. Sugnaux, S. Tugulu, H.-A. Klok, *Chem. Rev.* **2009**, *109*, 5437-5527.

[98] M. Husseman, E. E. Malmström, M. McNamara, M. Mate, D. Mecerreyes, D. G. Benoit, J. L. Hedrick, P. Mansky, E. Huang, T. P. Russell, C. J. Hawker, *Macromolecules* **1999**, *32*, 1424-1431.

[99] A. Mardyukov, Y. Li, A. Dickschat, A. H. Schäfer, A. Studer, *Langmuir* **2013**, *29*, 6369-6376.

[100] H. C. Kolb, M. Finn, K. B. Sharpless, *Angew. Chem. Int. Ed.* **2001**, *40*, 2004-2021.

[101] C. Barner-Kowollik, F. E. Du Prez, P. Espeel, C. J. Hawker, T. Junkers, H. Schlaad, W. Van Camp, *Angew. Chem. Int. Ed.* **2011**, *50*, 60-62.

[102] K. Matyjaszewski, B. E. Woodworth, X. Zhang, S. G. Gaynor, Z. Metzner, *Macromolecules* **1998**, *31*, 5955-5957.

[103] S. Harrisson, P. Couvreur, J. Nicolas, *Polym. Chem.* **2011**, *2*, 1859-1865.

[104] W. Lin, Q. Fu, Y. Zhang, J. Huang, *Macromolecules* **2008**, *41*, 4127-4135.

[105] N. V. Tsarevsky, W. A. Braunecker, K. Matyjaszewski, *J. Organomet. Chem.* **2007**, *692*, 3212-3222.

[106] V. Percec, T. Guliashvili, J. S. Ladislaw, A. Wistrand, A. Stjerndahl, M. J. Sienkowska, M. J. Monteiro, S. Sahoo, *J. Am. Chem. Soc.* **2006**, *128*, 14156-14165.

[107] B. M. Rosen, V. Percec, *Chem. Rev.* **2009**, *109*, 5069-5119.

[108] Q. Fu, Z. Zhang, W. Lin, J. Huang, *Macromolecules* **2009**, *42*, 4381-4383.

[109] J. Kulis, C. A. Bell, A. S. Micallef, Z. Jia, M. J. Monteiro, *Macromolecules* **2009**, *42*, 8218-8227.

[110] N. Cerit, N. Cakir, A. Dag, O. Sirkecioglu, H. Durmaz, G. Hizal, U. Tunca, *J. Polym. Sci., Part A: Polym. Chem.* **2011**, *49*, 2850-2858.

[111] X. Wang, J. Huang, L. Chen, Y. Liu, G. Wang, *Macromolecules* **2014**, *47*, 7812-7822.

[112] A. Mardyukov, A. Studer, *Macromol. Rapid Commun.* **2013**, *34*, 94-101.

[113] G. Delaittre, M. Dietrich, J. P. Blinco, A. Hirschbiel, M. Bruns, L. Barner, C. Barner-Kowollik, *Biomacromolecules* **2012**, *13*, 1700-1705.

[114] J. Su, H. Huang, Y. Cui, Y. Chen, X. Liu, *Polym. Chem.* **2016**, *7*, 2511-2520.

[115] C. Yuan, M. Z. Rong, M. Q. Zhang, Z. P. Zhang, Y. C. Yuan, *Chem. Mater.* **2011**, *23*, 5076-5081.

[116] H. Otsuka, K. Aotani, Y. Higaki, A. Takahara, *Chem. Commun.* **2002**, 2838-2839.

[117] M. Aiba, T. Higashihara, M. Ashizawa, H. Otsuka, H. Matsumoto, *Macromolecules* **2016**, *49*, 2153-2161.

[118] J. Su, Y. Amamoto, M. Nishihara, A. Takahara, H. Otsuka, *Polym. Chem.* **2011**, *2*, 2021-2026.

[119] H. Otsuka, K. Aotani, Y. Higaki, A. Takahara, *J. Am. Chem. Soc.* **2003**, *125*, 4064-4065.

[120] Z. P. Zhang, M. Z. Rong, M. Q. Zhang, C. Yuan, *Polym. Chem.* **2013**, *4*, 4648-4654.

[121] S. Telitel, Y. Amamoto, J. Poly, F. Morlet-Savary, O. Soppera, J. Lalevée, K. Matyjaszewski, *Polym. Chem.* **2014**, *5*, 921-930.

[122] J. Allgaier, H. Finkelmann, *Makromol. Chem., Rapid Commun,* **1993**, *14*, 267-271.

[123] T. Sukegawa, H. Omata, I. Masuko, K. Oyaizu, H. Nishide, *ACS Macro Lett.* **2014**, *3*, 240-243.

[124] M. Kamachi, M. Tamaki, Y. Morishima, S. Nozakura, W. Mori, M. Kishita, *Polym. J.* **1982**, *14*, 363-369.

[125] S. Nozakura, M. Kamachi, *Makromol. Chem., Suppl.* **1985**, *12*, 255-263.

[126] K. Oyaizu, T. Suga, K. Yoshimura, H. Nishide, *Macromolecules* **2008**, *41*, 6646-6652.

[127] T. Sukegawa, K. Sato, K. Oyaizu, H. Nishide, *RSC Adv.* **2015**, *5*, 15448-15452.

[128] K. Koshika, N. Sano, K. Oyaizu, H. Nishide, *Macromol. Chem. Phys.* **2009**, *210*, 1989-1995.

[129] K. Koshika, N. Sano, K. Oyaizu, H. Nishide, *Chem. Commun.* **2009**, 836-838.

[130] M. Suguro, S. Iwasa, K. Nakahara, *Macromol. Rapid Commun.* **2008**, *29*, 1635-1639.

[131] M. Suguro, S. Iwasa, Y. Kusachi, Y. Morioka, K. Nakahara, *Macromol. Rapid Commun.* **2007**, *28*, 1929-1933.

[132] T. Suga, H. Konishi, H. Nishide, *Chem. Commun.* **2007**, 1730-1732.

[133] T. Katsumata, M. Satoh, J. Wada, M. Shiotsuki, F. Sanda, T. Masuda, *Macromol. Rapid Commun.* **2006**, *27*, 1206-1211.

[134] T. Suga, H. Ohshiro, S. Sugita, K. Oyaizu, H. Nishide, *Adv. Mater.* **2009**, *21*, 1627-1630.

[135] Y. Takahashi, N. Hayashi, K. Oyaizu, K. Honda, H. Nishide, *Polym. J.* **2008**, *40*, 763.

[136] A. Fujii, T. Ishida, N. Koga, H. Iwamura, *Macromolecules* **1991**, *24*, 1077-1082.

[137] K. Oyaizu, T. Sukegawa, H. Nishide, *Chem. Lett.* **2011**, *40*, 184-185.

[138] K. Nakahara, S. Iwasa, M. Satoh, Y. Morioka, J. Iriyama, M. Suguro, E. Hasegawa, *Chem. Phys. Lett.* **2002**, *359*, 351-354.

[139] H. Nishide, S. Iwasa, Y.-J. Pu, T. Suga, K. Nakahara, M. Satoh, *Electrochim. Acta* **2004**, *50*, 827-831.

[140] T. Janoschka, A. Teichler, A. Krieg, M. D. Hager, U. S. Schubert, *J. Polym. Sci., Part A: Polym. Chem.* **2012**, *50*, 1394-1407.

[141] C.-H. Lin, C.-M. Chau, J.-T. Lee, *Polym. Chem.* **2012**, *3*, 1467-1474.

[142] M.-K. Hung, Y.-H. Wang, C.-H. Lin, H.-C. Lin, J.-T. Lee, *J. Mater. Chem.* **2012**, *22*, 1570-1577.

[143] Y.-H. Wang, M.-K. Hung, C.-H. Lin, H.-C. Lin, J.-T. Lee, *Chem. Commun.* **2011**, *47*, 1249-1251.

[144] B. Ernould, M. Devos, J.-P. Bourgeois, J. Rolland, A. Vlad, J.-F. Gohy, *J. Mater. Chem. A* **2015**, *3*, 8832-8839.

[145] J.-J. Yang, C.-C. Li, Y.-F. Yang, C.-Y. Wang, C.-H. Lin, J.-T. Lee, *RSC Adv.* **2016**, *6*, 63472-63476.

[146] H.-C. Lin, C.-C. Li, J.-T. Lee, *J. Power Sources* **2011**, *196*, 8098-8103.

[147] T. Kurosaki, O. Takahashi, M. Okawara, *J. Polym. Sci., Polym. Chem. Ed.* **1974**, *12*, 1407-1420.

[148] M. Tanaka, S. Imai, T. Tanii, Y. Numao, N. Shimamoto, I. Ohdomari, H. Nishide, *J. Polym. Sci., Part A: Polym. Chem.* **2007**, *45*, 521-530.

[149] C. D. Anderson, K. J. Shea, S. D. Rychnovsky, *Org. Lett.* **2005**, *7*, 4879-4882.

[150] J. Luo, C. Pardin, W. D. Lubell, X. Zhu, *Chem. Commun.* **2007**, 2136-2138.

[151] T. K. Kunz, M. O. Wolf, *Polym. Chem.* **2011**, *2*, 640-644.

[152] E. M. Simpson, Z. D. Ristovski, S. E. Bottle, K. E. Fairfull-Smith, J. P. Blinco, *Polym. Chem.* **2015**, *6*, 2962-2969.

[153] T. Yoshitomi, D. Miyamoto, Y. Nagasaki, *Biomacromolecules* **2009**, *10*, 596-601.

[154] H. Fu, D. M. Policarpio, J. D. Batteas, D. E. Bergbreiter, *Polym. Chem.* **2010**, *1*, 631-633.

[155] A. W. Bosman, R. A. J. Janssen, E. W. Meijer, *Macromolecules* **1997**, *30*, 3606-3611.

[156] P. Schattling, F. D. Jochum, P. Theato, *Chem. Commun.* **2011**, *47*, 8859-8861.

[157] Y. Liu, X. Wang, W. Song, G. Wang, *Polym. Chem.* **2015**, *6*, 7514-7523.

[158] F. Busolo, L. Franco, L. Armelao, M. Maggini, *Langmuir* **2010**, *26*, 1889-1893.

[159] Y. I. Avila-Vega, C. C. Leyva-Porras, M. Mireles, M. Quevedo-López, J. Macossay, J. Bonilla-Cruz, *Carbon* **2013**, *63*, 376-389.

[160] J. Choi, H. Lee, K. Kim, B. Kim, S. Kim, *J. Phys. Chem. Lett.* **2010**, *1*, 505-509.

[161] A. E. J. De Nooy, A. C. Besemer, H. van Bekkum, *Synthesis* **1996**, *1996*, 1153-1176.

[162] R. A. Sheldon, I. W. C. E. Arends, G.-J. ten Brink, A. Dijksman, *Acc. Chem. Res.* **2002**, *35*, 774-781.

[163] W. Adam, C. R. Saha-Möller, P. A. Ganeshpure, *Chem. Rev.* **2001**, *101*, 3499-3548.

[164] P. L. Anelli, C. Biffi, F. Montanari, S. Quici, *J. Org. Chem.* **1987**, *52*, 2559-2562.

[165] R. Ciriminna, M. Pagliaro, *Org. Process Res. Dev.* **2010**, *14*, 245-251.

[166] P. T. Anastas, J. C. Warner, *Green Chemistry: Theory and Practice, Vol. 30*, Oxford University Press, Oxford, **2000**.

[167] Z. Zheng, J. Wang, M. Zhang, L. Xu, J. Ji, *ChemCatChem* **2013**, *5*, 307-312.

[168] Y. Shi, Y. Nabae, T. Hayakawa, M. Kakimoto, *RSC Adv.* **2015**, *5*, 1923-1928.

[169] Y. Nabae, M. Mikuni, N. Takusari, T. Hayakawa, M. Kakimoto, *High Perform. Polym.* **2017**, *29*, 646-650.

[170] G. I. Likhtenstein, K. Ishii, S. Nakatsuji, *Photochem. Photobiol.* **2007**, *83*, 871-881.

[171] S. A. Green, D. J. Simpson, G. Zhou, P. S. Ho, N. V. Blough, *J. Am. Chem. Soc.* **1990**, *112*, 7337-7346.

[172] F. S. Abrams, E. London, *Biochemistry* **1993**, *32*, 10826-10831.

[173] R. D. Kaiser, E. London, *Biochemistry* **1998**, *37*, 8180-8190.

[174] N. V. Blough, D. J. Simpson, *J. Am. Chem. Soc.* **1988**, *110*, 1915-1917.

[175] H.-Y. Ahn, K. E. Fairfull-Smith, B. J. Morrow, V. Lussini, B. Kim, M. V. Bondar, S. E. Bottle, K. D. Belfield, *J. Am. Chem. Soc.* **2012**, *134*, 4721-4730.

[176] V. C. Lussini, J. M. Colwell, K. E. Fairfull-Smith, S. E. Bottle, *Sens. Actuators, B* **2017**, *241*, 199-209.

[177] J. P. Blinco, D. J. Keddie, T. Wade, P. J. Barker, G. A. George, S. E. Bottle, *Polym. Degrad. Stab.* **2008**, *93*, 1613-1618.

[178] P. Lederhose, N. L. Haworth, K. Thomas, S. E. Bottle, M. L. Coote, C. Barner-Kowollik, J. P. Blinco, *J. Org. Chem.* **2015**, *80*, 8009-8017.

[179] V. C. Lussini, J. P. Blinco, K. E. Fairfull-Smith, S. E. Bottle, *Chem. Eur. J.* **2015**, *21*, 18258-18268.

[180] K.-A. Hansen, K. E. Fairfull-Smith, S. E. Bottle, J. P. Blinco, *Macromol. Chem. Phys.* **2016**, *217*, 2330-2340.

[181] M. Eing, B. T. Tuten, J. P. Blinco, C. Barner-Kowollik, *Chem. Eur. J.* **2018**, *24*, 12246-12249.

[182] M. Eing, B. Olshausen, K. E. Fairfull-Smith, U. Schepers, C. Barner-Kowollik, J. P. Blinco, *Polym. Chem.* **2018**, *9*, 499-505.

[183] Z. Song, H. Zhou, *Energy Environ. Sci.* **2013**, *6*, 2280-2301.

[184] Y. Liang, Z. Tao, J. Chen, *Adv. Energy Mater.* **2012**, *2*, 742-769.

[185] T. Janoschka, M. D. Hager, U. S. Schubert, *Adv. Mater.* **2012**, *24*, 6397-6409.

[186] S. Muench, A. Wild, C. Friebe, B. Häupler, T. Janoschka, U. S. Schubert, *Chem. Rev.* **2016**, *116*, 9438-9484.

[187] T. Janoschka, N. Martin, U. Martin, C. Friebe, S. Morgenstern, H. Hiller, M. D. Hager, U. S. Schubert, *Nature* **2015**, *527*, 78-81.

[188] H. Prifti, A. Parasuraman, S. Winardi, T. M. Lim, M. Skyllas-Kazacos, *Membranes* **2012**, *2*, 275-306.

[189] K. L. Choy, *Prog. Mater Sci.* **2003**, *48*, 57-170.

[190] Y. Xia, G. M. Whitesides, *Angew. Chem. Int. Ed.* **1998**, *37*, 550-575.

[191] A. Ulman, *Chem. Rev.* **1996**, *96*, 1533-1554.

[192] J. C. Love, L. A. Estroff, J. K. Kriebel, R. G. Nuzzo, G. M. Whitesides, *Chem. Rev.* **2005**, *105*, 1103-1170.

[193] S. Onclin, B. J. Ravoo, D. N. Reinhoudt, *Angew. Chem. Int. Ed.* **2005**, *44*, 6282-6304.

[194] Q. Wei, R. Haag, *Mater. Horiz.* **2015**, *2*, 567-577.

[195] G. Delaittre, A. S. Goldmann, J. O. Mueller, C. Barner-Kowollik, *Angew. Chem. Int. Ed.* **2015**, *54*, 11388-11403.

[196] L. Michalek, L. Barner, C. Barner-Kowollik, *Adv. Mater.* **2018**, 1706321.

[197] M. A. Gauthier, M. I. Gibson, H.-A. Klok, *Angew. Chem. Int. Ed.* **2008**, *48*, 48-58.

[198] H. Lee, B. P. Lee, P. B. Messersmith, *Nature* **2007**, *448*, 338-341.

[199] K. Autumn, Y. A. Liang, S. T. Hsieh, W. Zesch, W. P. Chan, T. W. Kenny, R. Fearing, R. J. Full, *Nature* **2000**, *405*, 681-685.

[200] A. K. Geim, S. V. Dubonos, I. V. Grigorieva, K. S. Novoselov, A. A. Zhukov, S. Y. Shapoval, *Nat. Mater.* **2003**, *2*, 461-463.

[201] H. G. Silverman, F. F. Roberto, *Mar. Biotechnol.* **2007**, *9*, 661-681.

[202] J. H. Waite, M. L. Tanzer, *Science* **1981**, *212*, 1038-1040.

[203] H. Lee, S. M. Dellatore, W. M. Miller, P. B. Messersmith, *Science* **2007**, *318*, 426-430.

[204] B. P. Lee, P. B. Messersmith, J. N. Israelachvili, J. H. Waite, *Annu. Rev. Mater. Res.* **2011**, *41*, 99-132.

[205] J. H. Waite, *Integr. Comp. Biol.* **2002**, *42*, 1172-1180.

[206] J. H. Waite, X. Qin, *Biochemistry* **2001**, *40*, 2887-2893.

[207] G. P. Maier, M. V. Rapp, J. H. Waite, J. N. Israelachvili, A. Butler, *Science* **2015**, *349*, 628-632.

[208] H. Lee, N. F. Scherer, P. B. Messersmith, *Proc. Natl. Acad. Sci. U. S. A.* **2006**, *103*, 12999-13003.

[209] Q. Wei, K. Achazi, H. Liebe, A. Schulz, P.-L. M. Noeske, I. Grunwald, R. Haag, *Angew. Chem. Int. Ed.* **2014**, *53*, 11650-11655.

[210] C. Schlaich, M. Li, C. Cheng, I. S. Donskyi, L. Yu, G. Song, E. Osorio, Q. Wei, R. Haag, *Adv. Mater. Interfaces* **2018**, *5*, 1701254.

[211] C. Schlaich, L. C. Camacho, L. Yu, K. Achazi, Q. Wei, R. Haag, *ACS Appl. Mater. Interfaces* **2016**, *8*, 29117-29127.

[212] C. Schlaich, L. Yu, L. C. Camacho, Q. Wei, R. Haag, *Polym. Chem.* **2016**, *7*, 7446-7454.

[213] J. L. Dalsin, B.-H. Hu, B. P. Lee, P. B. Messersmith, *J. Am. Chem. Soc.* **2003**, *125*, 4253-4258.

[214] J. L. Dalsin, L. Lin, S. Tosatti, J. Vörös, M. Textor, P. B. Messersmith, *Langmuir* **2005**, *21*, 640-646.

[215] E. Faure, C. Falentin-Daudré, C. Jérôme, J. Lyskawa, D. Fournier, P. Woisel, C. Detrembleur, *Prog. Polym. Sci.* **2013**, *38*, 236-270.

[216] E. Faure, P. Lecomte, S. Lenoir, C. Vreuls, C. van De Weerdt, C. Archambeau, J. Martial, C. Jérôme, A.-S. Duwez, C. Detrembleur, *J. Mater. Chem.* **2011**, *21*, 7901-7904.

[217] B. P. Lee, K. Huang, F. N. Nunalee, K. R. Shull, P. B. Messersmith, *J. Biomater. Sci., Polym. Ed.* **2004**, *15*, 449-464.

[218] M. Kharasch, F. Kawahara, W. Nudenberg, *J. Org. Chem.* **1954**, *19*, 1977-1990.

[219] J. D. White, J. J. Wilker, *Macromolecules* **2011**, *44*, 5085-5088.

[220] M. M. Zieger, O. Pop-Georgievski, A. de los Santos Pereira, E. Verveniotis, C. M. Preuss, M. Zorn, B. Reck, A. S. Goldmann, C. Rodriguez-Emmenegger, C. Barner-Kowollik, *Langmuir* **2017**, *33*, 670-679.

[221] G. Westwood, T. N. Horton, J. J. Wilker, *Macromolecules* **2007**, *40*, 3960-3964.

[222] E. Casassa, A. Sarquis, C. Van Dyke, *J. Chem. Educ.* **1986**, *63*, 57-60.

[223] X. Wang, Q. Ye, J. Liu, X. Liu, F. Zhou, *J. Colloid Interface Sci.* **2010**, *351*, 261-266.

[224] H. Han, J. Wu, C. W. Avery, M. Mizutani, X. Jiang, M. Kamigaito, Z. Chen, C. Xi, K. Kuroda, *Langmuir* **2011**, *27*, 4010-4019.

[225] X. Xue, G. Pasparakis, N. Halliday, K. Winzer, S. M. Howdle, C. J. Cramphorn, N. R. Cameron, P. M. Gardner, B. G. Davis, F. Fernández-Trillo, C. Alexander, *Angew. Chem. Int. Ed.* **2011**, *50*, 9852-9856.

[226] H. Shao, K. N. Bachus, R. J. Stewart, *Macromol. Biosci.* **2009**, *9*, 464-471.

[227] H. Shao, R. J. Stewart, *Adv. Mater.* **2010**, *22*, 729-733.

[228] S. Quideau, D. Deffieux, C. Douat-Casassus, L. Pouysegu, *Angew. Chem. Int. Ed.* **2011**, *50*, 586-621.

[229] S. Geißler, A. Barrantes, P. Tengvall, P. B. Messersmith, H. Tiainen, *Langmuir* **2016**, *32*, 8050-8060.

[230] F. Behboodi-Sadabad, H. Zhang, V. Trouillet, A. Welle, N. Plumeré, P. A. Levkin, *Adv. Funct. Mater.* **2017**, *27*, 1700127.

[231] F. Behboodi-Sadabad, H. Zhang, V. Trouillet, A. Welle, N. Plumeré, P. A. Levkin, *Chem. Mater.* **2018**, *30*, 1937-1946.

[232] T. S. Sileika, D. G. Barrett, R. Zhang, K. H. A. Lau, P. B. Messersmith, *Angew. Chem. Int. Ed.* **2013**, *125*, 10966-10970.

[233] D. G. Barrett, T. S. Sileika, P. B. Messersmith, *Chem. Commun.* **2014**, *50*, 7265-7268.

[234] H. Ejima, J. J. Richardson, K. Liang, J. P. Best, M. P. van Koeverden, G. K. Such, J. Cui, F. Caruso, *Science* **2013**, *341*, 154-157.

[235] H. Ejima, J. J. Richardson, F. Caruso, *Nano Today* **2017**, *12*, 136-148.

[236] M. A. Rahim, H. Ejima, K. L. Cho, K. Kempe, M. Müllner, J. P. Best, F. Caruso, *Chem. Mater.* **2014**, *26*, 1645-1653.

[237] J. Guo, Y. Ping, H. Ejima, K. Alt, M. Meissner, J. J. Richardson, Y. Yan, K. Peter, D. von Elverfeldt, C. E. Hagemeyer, F. Caruso, *Angew. Chem.* **2014**, *126*, 5652-5657.

[238] M. A. Rahim, K. Kempe, M. Müllner, H. Ejima, Y. Ju, M. P. van Koeverden, T. Suma, J. A. Braunger, M. G. Leeming, B. F. Abrahams, F. Caruso, *Chem. Mater.* **2015**, *27*, 5825-5832.

[239] R. Mrówczyński, R. Markiewicz, J. Liebscher, *Polym. Int.* **2016**, *65*, 1288-1299.

[240] W. Lee, J. U. Lee, J.-H. Byun, *Compos. Sci. Technol.* **2015**, *110*, 53-61.

[241] S. Hong, J. Kim, Y. S. Na, J. Park, S. Kim, K. Singha, G.-I. Im, D.-K. Han, W. J. Kim, H. Lee, *Angew. Chem. Int. Ed.* **2013**, *52*, 9187-9191.

[242] M. d'Ischia, K. Wakamatsu, F. Cicoira, E. Di Mauro, J. C. Garcia-Borron, S. Commo, I. Galván, G. Ghanem, K. Kenzo, P. Meredith, A. Pezzella, C. Santato, T. Sarna, J. D. Simon, L. Zecca, F. A. Zucca, A. Napolitano, S. Ito, *Pigm. Cell Melanoma Res.* **2015**, *28*, 520-544.

[243] F. Solano, *New J. Sci.* **2014**, *2014*, 498276.

[244] G. Prota, *Melanins and Melanogenesis*, Academic Press, San Diego, **1992**.

[245] H. S. Mason, *J. Biol. Chem.* **1948**, *172*, 83-99.

[246] M. d'Ischia, A. Napolitano, A. Pezzella, *Eur. J. Org. Chem.* **2011**, *2011*, 5501-5516.

[247] M. d'Ischia, A. Napolitano, A. Pezzella, P. Meredith, T. Sarna, *Angew. Chem. Int. Ed.* **2009**, *48*, 3914-3921.

[248] Y. Li, J. Liu, Y. Wang, H. W. Chan, L. Wang, W. Chan, *Anal. Chem.* **2015**, *87*, 7958-7963.

[249] D. R. Dreyer, D. J. Miller, B. D. Freeman, D. R. Paul, C. W. Bielawski, *Chem. Sci.* **2013**, *4*, 3796-3802.

[250] Q. Ye, F. Zhou, W. Liu, *Chem. Soc. Rev.* **2011**, *40*, 4244-4258.

[251] D. R. Dreyer, D. J. Miller, B. D. Freeman, D. R. Paul, C. W. Bielawski, *Langmuir* **2012**, *28*, 6428-6435.

[252] J. Liebscher, R. Mrówczyński, H. A. Scheidt, C. Filip, N. D. Hădade, R. Turcu, A. Bende, S. Beck, *Langmuir* **2013**, *29*, 10539-10548.

[253] Y. Liu, K. Ai, L. Lu, *Chem. Rev.* **2014**, *114*, 5057-5115.

[254] M. E. Lynge, R. van der Westen, A. Postma, B. Städler, *Nanoscale* **2011**, *3*, 4916-4928.

[255] T. G. Barclay, H. M. Hegab, S. R. Clarke, M. Ginic-Markovic, *Adv. Mater. Interfaces* **2017**, *4*, 1601192.

[256] B. K. Ahn, *J. Am. Chem. Soc.* **2017**, *139*, 10166-10171.

[257] S. H. Hong, S. Hong, M.-H. Ryou, J. W. Choi, S. M. Kang, H. Lee, *Adv. Mater. Interfaces* **2016**, *3*, 1500857.

[258] C.-T. Chen, F. J. Martin-Martinez, G. S. Jung, M. J. Buehler, *Chem. Sci.* **2017**, *8*, 1631-1641.

[259] V. Proks, J. Brus, O. Pop-Georgievski, E. Večerníková, W. Wisniewski, J. Kotek, M. Urbanová, F. Rypáček, *Macromol. Chem. Phys.* **2013**, *214*, 499-507.

[260] M. Lee, S.-H. Lee, I.-K. Oh, H. Lee, *Small* **2017**, *13*, 1600443.

[261] W. Zheng, H. Fan, L. Wang, Z. Jin, *Langmuir* **2015**, *31*, 11671-11677.

[262] D. Perrot, C. Croutxé-Barghorn, X. Allonas, *Polym. Chem.* **2016**, *7*, 2635-2638.

[263] X. Du, L. Li, J. Li, C. Yang, N. Frenkel, A. Welle, S. Heissler, A. Nefedov, M. Grunze, P. A. Levkin, *Adv. Mater.* **2014**, *26*, 8029-8033.

[264] T. S. Sileika, H.-D. Kim, P. Maniak, P. B. Messersmith, *ACS Appl. Mater. Interfaces* **2011**, *3*, 4602-4610.

[265] H. Lee, J. Rho, P. B. Messersmith, *Adv. Mater.* **2009**, *21*, 431-434.

[266] C. Rodriguez-Emmenegger, C. M. Preuss, B. Yameen, O. Pop-Georgievski, M. Bachmann, J. O. Mueller, M. Bruns, A. S. Goldmann, M. Bastmeyer, C. Barner-Kowollik, *Adv. Mater.* **2013**, *25*, 6123-6127.

[267] L. A. Burzio, J. H. Waite, *Biochemistry* **2000**, *39*, 11147-11153.

[268] M. J. LaVoie, B. L. Ostaszewski, A. Weihofen, M. G. Schlossmacher, D. J. Selkoe, *Nature medicine* **2005**, *11*, 1214-1221.

[269] B. Yameen, C. Rodriguez-Emmenegger, C. M. Preuss, O. Pop-Georgievski, E. Verveniotis, V. Trouillet, B. Rezek, C. Barner-Kowollik, *Chem. Commun.* **2013**, *49*, 8623-8625.

[270] O. Pop-Georgievski, C. Rodriguez-Emmenegger, A. de los Santos Pereira, V. Proks, E. Brynda, F. Rypáček, *J. Mater. Chem. B* **2013**, *1*, 2859-2867.

[271] O. Pop-Georgievski, D. Verreault, M.-O. Diesner, V. Proks, S. Heissler, F. Rypáček, P. Koelsch, *Langmuir* **2012**, *28*, 14273-14283.

[272] D. Hong, K. Bae, S.-P. Hong, J. H. Park, I. S. Choi, W. K. Cho, *Chem. Commun.* **2014**, *50*, 11649-11652.

[273] D. Hong, H. Lee, B. J. Kim, T. Park, J. Y. Choi, M. Park, J. Lee, H. Cho, S.-P. Hong, S. H. Yang, S. H. Jung, S.-B. Ko, I. S. Choi, *Nanoscale* **2015**, *7*, 20149-20154.

[274] Z. Shafiq, J. Cui, L. Pastor-Pérez, V. San Miguel, R. A. Gropeanu, C. Serrano, A. del Campo, *Angew. Chem. Int. Ed.* **2012**, *124*, 4408-4411.

[275] B. Geiseler, L. Fruk, *J. Mater. Chem.* **2012**, *22*, 735-741.

[276] A. S. Goldmann, C. Schödel, A. Walther, J. Yuan, K. Loos, A. H. E. Müller, *Macromol. Rapid Commun.* **2010**, *31*, 1608-1615.

[277] A. Petran, R. Mrówczyński, C. Filip, R. Turcu, J. Liebscher, *Polym. Chem.* **2015**, *6*, 2139-2149.

[278] C. M. Preuss, A. S. Goldmann, V. Trouillet, A. Walther, C. Barner-Kowollik, *Macromol. Rapid Commun.* **2013**, *34*, 640-644.

[279] C. M. Preuss, M. M. Zieger, C. Rodriguez-Emmenegger, N. Zydziak, V. Trouillet, A. S. Goldmann, C. Barner-Kowollik, *ACS Macro Lett.* **2014**, *3*, 1169-1173.

[280] C. M. Preuss, T. Tischer, C. Rodriguez-Emmenegger, M. M. Zieger, M. Bruns, A. S. Goldmann, C. Barner-Kowollik, *J. Mater. Chem. B* **2014**, *2*, 36-40.

[281] M. Kohri, H. Kohma, Y. Shinoda, M. Yamauchi, S. Yagai, T. Kojima, T. Taniguchi, K. Kishikawa, *Polym. Chem.* **2013**, *4*, 2696-2702.

[282] J. N. Wilking, V. Zaburdaev, M. De Volder, R. Losick, M. P. Brenner, D. A. Weitz, *Proc. Natl. Acad. Sci. U. S. A.* **2013**, *110*, 848-852.

[283] V. Sperandio, A. G. Torres, B. Jarvis, J. P. Nataro, J. B. Kaper, *Proc. Natl. Acad. Sci. U. S. A.* **2003**, *100*, 8951-8956.

[284] C. K. Stover, X. Q. Pham, A. L. Erwin, S. D. Mizoguchi, P. Warrener, M. J. Hickey, F. S. L. Brinkman, W. O. Hufnagle, D. J. Kowalik, M. Lagrou, R. L. Garber, L. Goltry, E. Tolentino, S. Westbrock-Wadman, Y. Yuan, L. L. Brody, S. N. Coulter, K. R. Folger, A. Kas, K. Larbig, R. Lim, K. Smith, D. Spencer, G. K.-S. Wong, Z. Wu, I. T. Paulsen, J. Reizer, M. H. Saier, R. E. W. Hancock, S. Lory, M. V. Olson, *Nature* **2000**, *406*, 959-964.

[285] R. S. Smith, B. H. Iglewski, *J. Clin. Invest.* **2003**, *112*, 1460-1465.

[286] K. P. Rumbaugh, *Anal. Bioanal. Chem.* **2007**, *387*, 425-435.

[287] S.-K. Kim, J.-H. Lee, *J. Microbiol.* **2016**, *54*, 71-85.

[288] J. B. Kaplan, *J. Dent. Res.* **2010**, *89*, 205-218.

[289] R. Van Houdt, C. W. Michiels, *J. Appl. Microbiol.* **2010**, *109*, 1117-1131.

[290] P. S. Stewart, *Int. J. Med. Microbiol.* **2002**, *292*, 107.

[291] J. Musk, J. Dinty, P. J. Hergenrother, *Curr. Med. Chem.* **2006**, *13*, 2163-2177.

[292] P. Wu, D. W. Grainger, *Biomaterials* **2006**, *27*, 2450-2467.

[293] F. Siedenbiedel, J. C. Tiller, *Polymers* **2012**, *4*, 46-71.

[294] L. Timofeeva, N. Kleshcheva, *Appl. Microbiol. Biotechnol.* **2011**, *89*, 475-492.

[295] R. E. W. Hancock, H.-G. Sahl, *Nat. Biotechnol.* **2006**, *24*, 1551-1557.

[296] S. I. Jeon, J. H. Lee, J. D. Andrade, P. G. De Gennes, *J. Colloid Interface Sci.* **1991**, *142*, 149-158.

[297] S. Chen, L. Li, C. Zhao, J. Zheng, *Polymer* **2010**, *51*, 5283-5293.

[298] E. Ostuni, R. G. Chapman, R. E. Holmlin, S. Takayama, G. M. Whitesides, *Langmuir* **2001**, *17*, 5605-5620.

[299] T. J. Kinnari, J. Jero, *Otolaryngol. Head and Neck Surgery* **2005**, *133*, 596-600.

[300] T. J. Kinnari, E.-M. Salonen, J. Jero, *Int. J. Pediatr. Otorhinolaryngol.* **2003**, *67*, 157-164.

[301] M. E. Callow, R. L. Fletcher, *Int. Biodeterior. Biodegrad.* **1994**, *34*, 333-348.

[302] A. Colas, J. Curtis, in *Biomaterials Science: An Introduction to Materials in Medicine, Vol. 2,* San Diego, **2004**, pp. 80-85, 697-707.

[303] C. S. Gudipati, J. A. Finlay, J. A. Callow, M. E. Callow, K. L. Wooley, *Langmuir* **2005**, *21*, 3044-3053.

[304] L. D. Renner, D. B. Weibel, *MRS Bull.* **2011**, *36*, 347-355.

[305] N. Barraud, D. J. Hassett, S.-H. Hwang, S. A. Rice, S. Kjelleberg, J. S. Webb, *J. Bacteriol.* **2006**, *188*, 7344-7353.

[306] D. Park, J. Kim, Y. M. Lee, J. Park, W. J. Kim, *Adv. Healthcare Mater.* **2016**, *5*, 2019-2024.

[307] H. T. T. Duong, N. N. M. Adnan, N. Barraud, J. S. Basuki, S. K. Kutty, K. Jung, N. Kumar, T. P. Davis, C. Boyer, *J. Mater. Chem. B* **2014**, *2*, 5003-5011.

[308] S.-A. Alexander, C. Kyi, C. H. Schiesser, *Org. Biomol. Chem.* **2015**, *13*, 4751-4759.

[309] S.-A. Alexander, E. M. Rouse, J. M. White, N. Tse, C. Kyi, C. H. Schiesser, *Chem. Commun.* **2015**, *51*, 3355-3358.

[310] A. D. Verderosa, C. de la Fuente-Núñez, S. C. Mansour, J. Cao, T. K. Lu, R. E. W. Hancock, K. E. Fairfull-Smith, *Eur. J. Med. Chem.* **2017**, *138*, 590-601.

[311] A. D. Verderosa, S. C. Mansour, C. de la Fuente-Núñez, R. E. W. Hancock, K. E. Fairfull-Smith, *Molecules* **2016**, *21*, 841.

[312] N. R. B. Boase, M. D. T. Torres, N. Fletcher, C. de la Fuente-Núñez, K. E. Fairfull-Smith, *Polym. Chem.* **2018**, *9*, 5308-5318.

[313] L. Su, Y. Yu, Y. Zhao, F. Liang, X. Zhang, *Sci. Rep.* **2016**, *6*, 24420.

[314] H. Woehlk, J. Steinkoenig, C. Lang, L. Michalek, V. Trouillet, P. Krolla, A. S. Goldmann, L. Barner, J. P. Blinco, C. Barner-Kowollik, K. E. Fairfull-Smith, *Langmuir* **2018**, *34*, 3264-3274.

[315] E. Blasco, M. B. Sims, A. S. Goldmann, B. S. Sumerlin, C. Barner-Kowollik, *Macromolecules* **2017**, *50*, 5215-5252.

[316] V. D. Sen’, I. V. Tikhonov, L. I. Borodin, E. M. Pliss, V. A. Golubev, M. A. Syroeshkin, A. I. Rusakov, *J. Phys. Org. Chem.* **2015**, *28*, 17-24.

[317] S. L. Y. Tang, R. L. Smith, M. Poliakoff, *Green Chem.* **2005**, *7*, 761-762.

[318] S. Hong, Y. S. Na, S. Choi, I. T. Song, W. Y. Kim, H. Lee, *Adv. Funct. Mater.* **2012**, *22*, 4711-4717.

[319] N. F. Della Vecchia, A. Luchini, A. Napolitano, G. D’Errico, G. Vitiello, N. Szekely, M. d’Ischia, L. Paduano, *Langmuir* **2014**, *30*, 9811-9818.

[320] W. Barreto, S. Ponzoni, P. Sassi, *Spectrochim. Acta, Part A* **1998**, *55*, 65-72.

[321] J. Yang, V. Saggiomo, A. H. Velders, M. A. Cohen Stuart, M. Kamperman, *PloS one* **2016**, *11*, e0166490.

[322] Q. Wei, F. Zhang, J. Li, B. Li, C. Zhao, *Polym. Chem.* **2010**, *1*, 1430-1433.

[323] M. Bisaglia, S. Mammi, L. Bubacco, *J. Biol. Chem.* **2007**, *282*, 15597-15605.

[324] B. P. Murphy, T. M. Schultz, *J. Org. Chem.* **1985**, *50*, 2790-2791.

[325] D. C. Bobela, B. K. Hughes, W. A. Braunecker, T. W. Kemper, R. E. Larsen, T. Gennett, *J. Phys. Chem. Lett.* **2015**, *6*, 1414-1419.

[326] M. M. Cecchini, S. Reale, P. Manini, M. d'Ischia, F. De Angelis, *Chem. Eur. J.* **2017**, *23*, 8092-8098.

[327] H. Woehlk, J. Steinkoenig, C. Lang, A. S. Goldmann, L. Barner, J. P. Blinco, K. E. Fairfull-Smith, C. Barner-Kowollik, *Polym. Chem.* **2017**, *8*, 3050-3055.

[328] M. M. Cecchini, J. Steinkoenig, S. Reale, L. Barner, J. Yuan, A. S. Goldmann, F. De Angelis, C. Barner-Kowollik, *Chem. Sci.* **2016**, *7*, 4912-4921.

[329] N. F. Della Vecchia, R. Avolio, M. Alfè, M. E. Errico, A. Napolitano, M. d'Ischia, *Adv. Funct. Mater.* **2013**, *23*, 1331-1340.

[330] L. Panzella, A. Pezzella, A. Napolitano, M. d'Ischia, *Org. Lett.* **2007**, *9*, 1411-1414.

[331] M. d'Ischia, A. Napolitano, K. Tsiakas, G. Prota, *Tetrahedron* **1990**, *46*, 5789-5796.

[332] F. Binns, J. A. G. King, S. N. Mishra, A. Percival, N. C. Robson, G. A. Swan, A. Waggott, *J. Chem. Soc. C* **1970**, 2063-2070.

[333] F. K. Yang, B. Zhao, *Open Surf. Sci. J* **2011**, *3*, 115-122.

[334] T. Tischer, R. Gralla-Koser, V. Trouillet, L. Barner, C. Barner-Kowollik, C. Lee-Thedieck, *ACS Macro Lett.* **2016**, *5*, 498-503.

[335] F. Bernsmann, A. Ponche, C. Ringwald, J. Hemmerlé, J. Raya, B. Bechinger, J.-C. Voegel, P. Schaaf, V. Ball, *J. Phys. Chem. C* **2009**, *113*, 8234-8242.

[336] Y. Ding, L.-T. Weng, M. Yang, Z. Yang, X. Lu, N. Huang, Y. Leng, *Langmuir* **2014**, *30*, 12258-12269.

[337] V. Ball, D. Del Frari, V. Toniazzo, D. Ruch, *J. Colloid Interface Sci.* **2012**, *386*, 366-372.

[338] H. A. Houck, F. E. Du Prez, C. Barner-Kowollik, *Nat. Commun.* **2017**, *8*, 1869.

[339] H. Woehlk, A. Lauer, V. Trouillet, A. Welle, L. Barner, J. P. Blinco, K. E. Fairfull-Smith, C. Barner-Kowollik, *Chem. Eur. J.* **2018**, *24*, 18873-18879.

[340] B. Ketterer, H. W. Ooi, D. Brekel, V. Trouillet, L. Barner, M. Franzreb, C. Barner-Kowollik, *ACS Appl. Mater. Interfaces* **2018**, *10*, 1450-1462.

[341] R. Wang, Y. Zhang, G. Ma, Z. Su, *Colloids Surf., B* **2006**, *51*, 93-99.

[342] A. Nordborg, F. Limé, A. Shchukarev, K. Irgum, *J. Sep. Sci.* **2008**, *31*, 2143-2150.

[343] W. Sheng, B. Li, X. Wang, B. Dai, B. Yu, X. Jia, F. Zhou, *Chem. Sci.* **2015**, *6*, 2068-2073.

[344] D. P. Arora, S. Hossain, Y. Xu, E. M. Boon, *Biochemistry* **2015**, *54*, 3717-3728.

[345] D. Wang, M. Haapasalo, Y. Gao, J. Ma, Y. Shen, *Bioact. Mater.* **2018**, *3*, 418-425.

[346] B. Guggenheim, E. Giertsen, P. Schüpbach, S. Shapiro, *J. Dent. Res.* **2001**, *80*, 363-370.

[347] G. Gao, D. Lange, K. Hilpert, J. Kindrachuk, Y. Zou, J. T. J. Cheng, M. Kazemzadeh-Narbat, K. Yu, R. Wang, S. K. Straus, D. E. Brooks, B. H. Chew, R. E. W. Hancock, J. N. Kizhakkedathu, *Biomaterials* **2011**, *32*, 3899-3909.

[348] F. Cutruzzolà, N. Frankenberg-Dinkel, *J. Bacteriol.* **2015**, *198*, 55-65.

[349] E. F. Haney, M. J. Trimble, J. T. Cheng, Q. Vallé, R. E. W. Hancock, *Biomolecules* **2018**, *8*, 29.

[350] M. Kaupp, A. P. Vogt, J. C. Natterodt, V. Trouillet, T. Gruendling, T. Hofe, L. Barner, C. Barner-Kowollik, *Polym. Chem.* **2012**, *3*, 2605-2614.

[351] K. L. Parry, A. G. Shard, R. D. Short, R. G. White, J. D. Whittle, A. Wright, *Surf. Interface Anal.* **2006**, *38*, 1497-1504.

[352] J. H. Scofield, *J. Electron. Spectrosc. Relat. Phenom.* **1976**, *8*, 129-137.

[353] K. Thomas, B. A. Chalmers, K. E. Fairfull-Smith, S. E. Bottle, *Eur. J. Org. Chem.* **2013**, *2013*, 853-857.

[354] J. G. Woods, R. Coffey, A. F. Jacobine, *WO/2011/119272* **2011**.

[355] C. Lang, S. Bestgen, A. Welle, R. Müller, P. W. Roesky, C. Barner-Kowollik, *Chem. Eur. J.* **2015**, *21*, 14728-14731.

Appendices

Appendix A

Supporting Information for Chapter 3

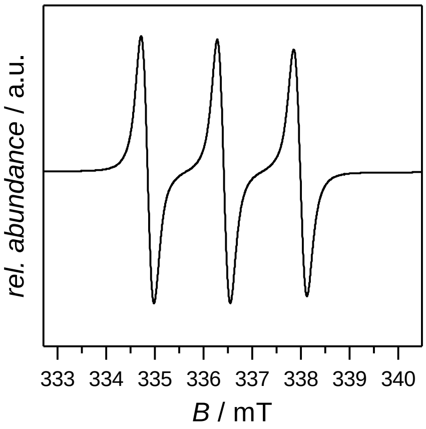

Figure A.1. EPR spectrum of **2** recorded in DCM. Adapted with permission from reference [314]. Copyright (2018) American Chemical Society.

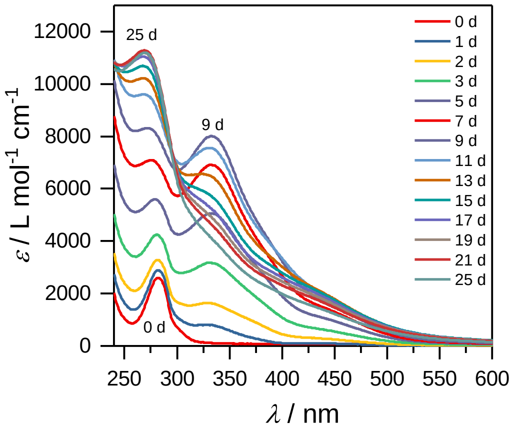

Figure A.2. Complementary UV–vis spectra recorded during polymerisation of **3.** Adapted with permission from reference [314]. Copyright (2018) American Society.

Table A.1. (−)ESI-CID MS peak assignments of most abundant tetramer species (refer to **Figure 3.4c**). Adapted with permission from reference [314]. Copyright (2018) American Chemical Society.

label	formula	m/z(exp)	m/z(theo)	$\Delta m/z$	resolution
○	$C_{72}H_{90}N_{12}O_{16}$	1378.6597	1378.6592	0.0005	60800
□	$C_{72}H_{89}N_{12}O_{16}\cdot HCl$	1413.6278	1413.6281	0.0002	51600
△	$C_{72}H_{87}N_{12}O_{16}\cdot 2HCl$	1447.5866	1447.5891	0.0025	54300

Table A.2. (−)ESI-HCD MS/MS peak assignments of most abundant trimer fragments (refer to **Figure 3.5b**). Adapted with permission from reference [314]. Copyright (2018) American Chemical Society.

label	formula	m/z(exp)	m/z(theo)	$\Delta m/z$	resolution
■	$C_{53}H_{63}N_9O_{12}\cdot HCl$	1053.4371	1053.4357	0.0013	67300
▣	$C_{52}H_{60}N_9O_{12}\cdot HCl$	1038.4129	1038.4123	0.0006	68900
●	$C_{53}H_{65}N_9O_{12}$	1019.4753	1019.4747	0.0006	68800
◉	$C_{52}H_{62}N_9O_{12}$	1004.4521	1004.4512	0.0009	71000

Appendix B

Supporting Information for Chapter 4

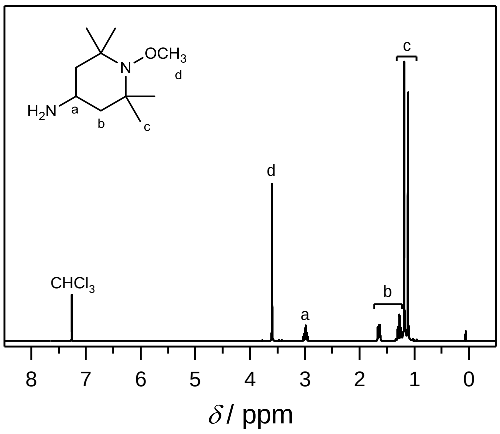

Figure B.1. ^1H NMR spectrum (400 MHz, methanol-d_4, 298 K) of compound **5**. Adapted with permission from reference [327]. Copyright (2017) The Royal Chemical Society.

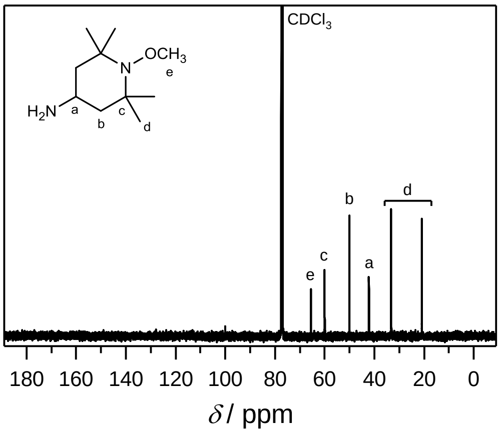

Figure B.2. ^{13}C NMR spectrum (101 MHz, methanol-d_4, 298 K) of compound **5**. Adapted with permission from reference [327]. Copyright (2017) The Royal Chemical Society.

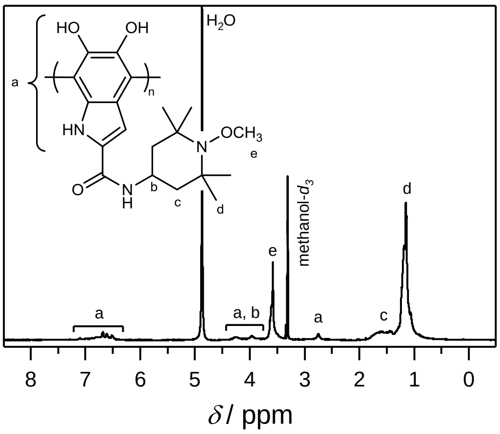

Figure B.3. ^{1}H NMR spectrum (400 MHz, methanol-d_4, 298 K) of polymer **8**. Adapted with permission from reference [327]. Copyright (2017) The Royal Chemical Society.

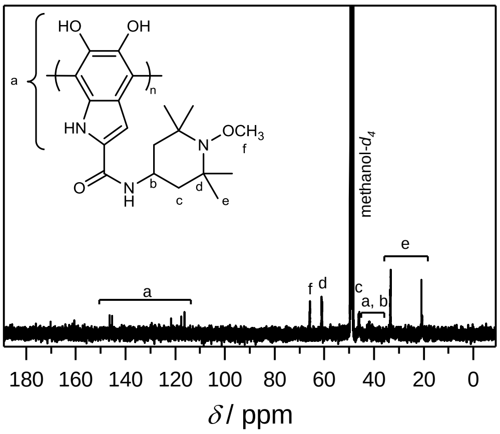

Figure B.4. ^{13}C NMR spectrum (101 MHz, methanol-d_4, 298 K) of polymer **8**. Adapted with permission from reference [327]. Copyright (2017) The Royal Chemical Society.

Table B.1. (−)ESI-CID MS peak assignments of $[M_n{-}H]^-$ oligomers (with n = 2–6) of poly(DOPA-TEMPO-CH_3) (**8**). The displayed *m/z*(theo) values were obtained from isotopic pattern simulations of each individual profile pattern. Adapted with permission from reference [327]. Copyright (2017) The Royal Chemical Society.

$[M_2{-}H]^-$, DIMER ●● ± 2*x*H

label	formula of M_2	*m/z*(exp)	*m/z*(theo)	Δ*m/z*	resolution	relative ratio
-4H	$C_{38}H_{48}N_6O_8$	715.3471	715.3450	0.0021	77000	0.01
-2H	$C_{38}H_{50}N_6O_8$	717.3631	717.3603	0.0028	76000	0.03
●●	$C_{38}H_{52}N_6O_8$	719.3788	719.3763	0.0025	77000	1.00
+2H	$C_{38}H_{54}N_6O_8$	721.3959	721.3885	0.0074	73300	0.21
+4H	$C_{38}H_{56}N_6O_8$	723.4102	723.4071	0.0031	77600	0.57

$[M_3{-}H]^-$, TRIMER ●●● ± 2*x*H

label	formula of M_3	*m/z*(exp)	*m/z*(theo)	Δ*m/z*	resolution	relative ratio
-2H	$C_{57}H_{75}N_9O_{12}$	1076.5486	1076.5451	0.0034	62100	0.02
●●●	$C_{57}H_{77}N_9O_{12}$	1078.5637	1078.5607	0.0030	63500	0.46
+2H	$C_{57}H_{79}N_9O_{12}$	1080.5788	1080.5738	0.0050	60300	0.29
+4H	$C_{57}H_{81}N_9O_{12}$	1082.5949	1082.5914	0.0035	62200	1.00
+6H	$C_{57}H_{83}N_9O_{12}$	1084.6078	1084.6032	0.0046	57700	0.29
+8H	$C_{57}H_{85}N_9O_{12}$	1086.6257	1086.6192	0.0065	60400	0.14

$[M_4{-}H]^-$, TETRAMER ●●●● ± 2*x*H

label	formula of M_4	*m/z*(exp)	*m/z*(theo)	Δ*m/z*	resolution	relative ratio
●●●●	$C_{76}H_{102}N_{12}O_{16}$	1437.7479	1437.7453	0.0026	55900	0.31
+2H	$C_{76}H_{104}N_{12}O_{16}$	1439.7605	1439.7563	0.0042	54700	0.14
+4H	$C_{76}H_{106}N_{12}O_{16}$	1441.7791	1441.7758	0.0034	56100	0.89
+6H	$C_{76}H_{108}N_{12}O_{16}$	1443.7913	1443.7874	0.0039	54100	0.38
+8H	$C_{76}H_{110}N_{12}O_{16}$	1445.8102	1445.8055	0.0047	56000	0.72
+10H	$C_{76}H_{112}N_{12}O_{16}$	1447.8255	1447.8211	0.0044	55100	1.00

Table B.1. continued.

$[M_5{-}H]^-$, PENTAMER ●●●●● ± 2xH

label	formula of M_5	m/z(exp)	m/z(theo)	$\Delta m/z$	resolution	relative ratio
+2H	$C_{95}H_{129}N_{15}O_{20}$	1798.9469	1798.9455	0.0014	54600	0.35
+4H	$C_{95}H_{131}N_{15}O_{20}$	1800.9596	1800.9592	0.0004	50300	0.90
+6H	$C_{95}H_{133}N_{15}O_{20}$	1802.9748	1802.9727	0.0021	47300	0.90
+8H	$C_{95}H_{135}N_{15}O_{20}$	1804.9910	1804.9881	0.0029	47300	1.00
+10H	$C_{95}H_{137}N_{15}O_{20}$	1807.0075	1807.0031	0.0044	48800	0.85

$[M_6{-}H]^-$, HEXAMER ●●●●●● ± 2xH

label	formula of M_6	m/z(exp)	m/z(theo)	$\Delta m/z$	resolution	relative ratio
+2H	$C_{114}H_{154}N_{18}O_{24}$	2158.1271	2158.1300	0.0028	44600	0.08
+4H	$C_{114}H_{156}N_{18}O_{24}$	2160.1414	2160.1434	0.0020	46400	0.25
+6H	$C_{114}H_{158}N_{18}O_{24}$	2162.1562	2162.1591	0.0029	46500	0.88
+8H	$C_{114}H_{160}N_{18}O_{24}$	2164.1701	2164.1716	0.0015	45100	0.76
+10H	$C_{114}H_{162}N_{18}O_{24}$	2166.1858	2166.1873	0.0015	43000	1.00
+12H	$C_{114}H_{164}N_{18}O_{24}$	2168.1994	2168.2012	0.0018	45000	0.60
+14H	$C_{114}H_{166}N_{18}O_{24}$	2170.2128	2170.2156	0.0029	47200	0.35

Table B.2. (+)ESI-CID MS peak assignments of $[M_7+H]^+$ species and $[M_8+H+NaCl]^+$ species of poly(DOPA-TEMPO-CH_3) (**8**). The displayed *m/z*(theo) values were obtained from isotopic pattern simulations of each individual profile pattern. Adapted with permission from reference [327]. Copyright (2017) The Royal Chemical Society.

<table>
<tr><td colspan="7">$[M_7+H]^+$, HEPTAMER ●●●●●●● ± 2xH</td></tr>
<tr><td>label</td><td>formula of M_7</td><td><i>m/z</i>(exp)</td><td><i>m/z</i>(theo)</td><td>Δ<i>m/z</i></td><td>resolution</td><td>relative ratio</td></tr>
<tr><td>+4H</td><td>$C_{133}H_{181}N_{21}O_{28}$</td><td>2521.3790</td><td>2521.3458</td><td>0.0332</td><td>42500</td><td>0.20</td></tr>
<tr><td>+6H</td><td>$C_{133}H_{183}N_{21}O_{28}$</td><td>2523.3941</td><td>2523.3586</td><td>0.0355</td><td>36300</td><td>0.60</td></tr>
<tr><td>+8H</td><td>$C_{133}H_{185}N_{21}O_{28}$</td><td>2525.4050</td><td>2525.3715</td><td>0.0334</td><td>38500</td><td>0.70</td></tr>
<tr><td>+10H</td><td>$C_{133}H_{187}N_{21}O_{28}$</td><td>2527.4202</td><td>2527.3869</td><td>0.0333</td><td>37800</td><td>1.00</td></tr>
<tr><td>+12H</td><td>$C_{133}H_{189}N_{21}O_{28}$</td><td>2529.4338</td><td>2529.4007</td><td>0.0330</td><td>38100</td><td>0.70</td></tr>
<tr><td>+14H</td><td>$C_{133}H_{191}N_{21}O_{28}$</td><td>2531.4493</td><td>2531.4152</td><td>0.0341</td><td>39200</td><td>0.50</td></tr>
<tr><td>+16H</td><td>$C_{133}H_{193}N_{21}O_{28}$</td><td>2533.4655</td><td>2533.4309</td><td>0.0345</td><td>38600</td><td>0.40</td></tr>
<tr><td colspan="7">$[M_8+H+NaCl]^+$, OCTAMER ●●●●●●●● ± 2xH</td></tr>
<tr><td>label</td><td>formula of M_8</td><td><i>m/z</i>(exp)</td><td><i>m/z</i>(theo)</td><td>Δ<i>m/z</i></td><td>resolution</td><td>relative ratio</td></tr>
<tr><td>+4H</td><td>$C_{152}H_{206}N_{24}O_{32}$</td><td>2938.5251</td><td>2938.4889</td><td>0.0362</td><td>38500</td><td>0.40</td></tr>
<tr><td>+6H</td><td>$C_{152}H_{208}N_{24}O_{32}$</td><td>2940.5264</td><td>2940.4997</td><td>0.0266</td><td>35300</td><td>1.00</td></tr>
<tr><td>+8H</td><td>$C_{152}H_{210}N_{24}O_{32}$</td><td>2942.5366</td><td>2942.5096</td><td>0.0270</td><td>34800</td><td>0.60</td></tr>
<tr><td>+10H</td><td>$C_{152}H_{212}N_{24}O_{32}$</td><td>2944.5502</td><td>2944.5227</td><td>0.0275</td><td>34500</td><td>0.80</td></tr>
<tr><td>+12H</td><td>$C_{152}H_{214}N_{24}O_{32}$</td><td>2946.5641</td><td>2946.5371</td><td>0.0270</td><td>34600</td><td>0.40</td></tr>
</table>

Table B.3. (−)ESI-HCD MS/MS peak assignments of fragments $[F_n\text{-}H]^-$ with n = 3−5 of poly(DOPA-TEMPO-CH_3) (**8**) performed on hexameric species $[M_6{-}H]^-$ apparent at *m/z* 2166 ± 5. Only most abundant peaks of oligomeric fragments were selected and listed in this table. The *m/z*(theo) values of most abundant peaks were calculated without simulation of the overlapping isotopic patterns of the remaining species. Adapted with permission from reference [327]. Copyright (2017) The Royal Chemical Society.

<table>
<tr><td colspan="7">$[F_5{-}H]^-$, PENTAMER FRAGMENTS ●●●●● + 6H</td></tr>
<tr><td>label</td><td>formula of F_5</td><td><i>m/z</i>(exp)</td><td><i>m/z</i>(theo)</td><td>Δ<i>m/z</i></td><td>resolution</td><td>relative ratio</td></tr>
<tr><td>+6H</td><td>$C_{95}H_{131}N_{15}O_{20}$</td><td>1800.9606</td><td>1800.9611</td><td>0.0005</td><td>49000</td><td>1.00</td></tr>
<tr><td colspan="7">$[F_4{-}H]^-$, TETRAMER FRAGMENTS ●●●● +6H</td></tr>
<tr><td>label</td><td>formula of F_4</td><td><i>m/z</i>(exp)</td><td><i>m/z</i>(theo)</td><td>Δ<i>m/z</i></td><td>resolution</td><td>relative ratio</td></tr>
<tr><td>+6H</td><td>$C_{76}H_{106}N_{12}O_{16}$</td><td>1441.7780</td><td>1441.7766</td><td>0.0014</td><td>56100</td><td>1.00</td></tr>
<tr><td colspan="7">$[F_3{-}H]^-$, TRIMER FRAGMENTS ●●● +6H</td></tr>
<tr><td>label</td><td>formula of F_3</td><td><i>m/z</i>(exp)</td><td><i>m/z</i>(theo)</td><td>Δ<i>m/z</i></td><td>resolution</td><td>relative ratio</td></tr>
<tr><td>+6H</td><td>$C_{57}H_{81}N_9O_{12}$</td><td>1082.5941</td><td>1082.5921</td><td>0.0020</td><td>65100</td><td>1.00</td></tr>
</table>

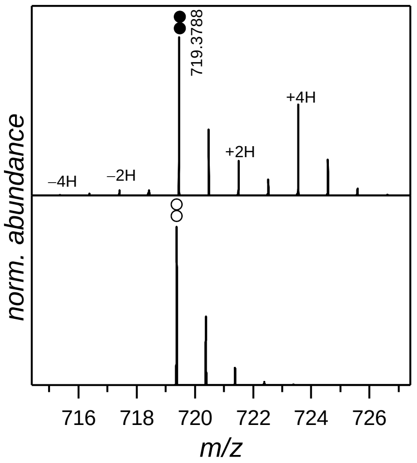

Figure B.5. Comparison of experimentally obtained spectrum of the $[M_2{-}H]^-$ dimer region (top panel) and simulated isotopic pattern of the DHI homodimer apparent as the most abundant peak (bottom panel) indicating the presence of higher molecular weight species such as +2H and +4H dimers. Adapted with permission from reference [327]. Copyright (2017) The Royal Chemical Society.

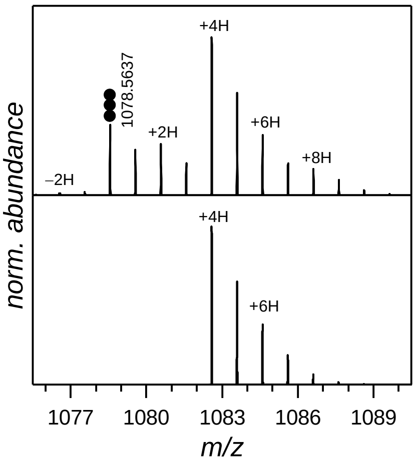

Figure B.6. Comparison of experimentally obtained spectrum of the $[M_3{-}H]^-$ trimer region (top panel) and simulated isotopic pattern of the +4H and the +6H species (bottom panel) clearly indicating the presence of a +8H trimer with incorporated open-chain dopamine units. Adapted with permission from reference [327]. Copyright (2017) The Royal Chemical Society.

Appendix C

Supporting Information for Chapter 5

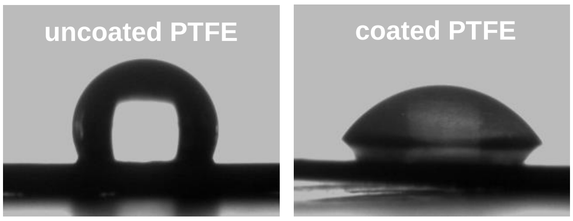

Figure C.1. Images taken during static water contact angle measurements showing deposited water droplet on uncoated (left) and polymer **4** coated PTFE (right). Adapted with permission from reference [314]. Copyright (2018) American Chemical Society.

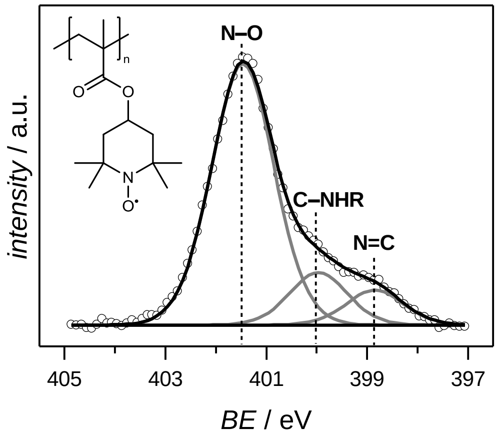

Figure C.2. N 1s XP spectrum of PTMA for identification of the TEMPO-characteristic N–O peak. The dominant peak (at 401.5 eV) of PTMA (drop-casted on silicon) was assigned to the N–O functional group. Peaks a lower BEs correspond to residual non-oxidised 2,2,6,6-tetramethylpiperidine moieties of the polymer precursor. PTMA was kindly provided by K.-A. Hansen (QUT). Adapted with permission from reference [314]. Copyright (2018) American Chemical Society.

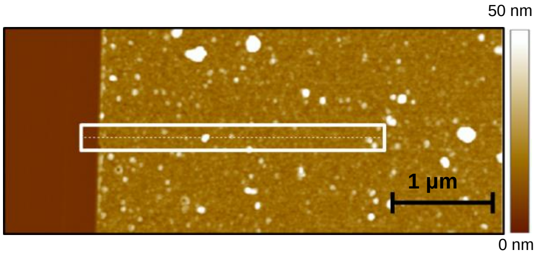

Figure C.3. AFM image obtained for determination of average polymer film thickness (refer to **Figure 5.2b**, top panel). Adapted with permission from reference [314]. Copyright (2018) American Chemical Society.

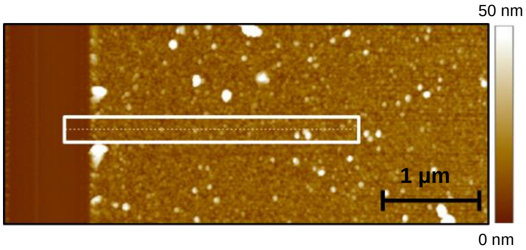

Figure C.4. AFM image obtained for determination of average polymer film thickness (refer to **Figure 5.2b**, bottom panel). Adapted with permission from reference [314]. Copyright (2018) American Chemical Society.

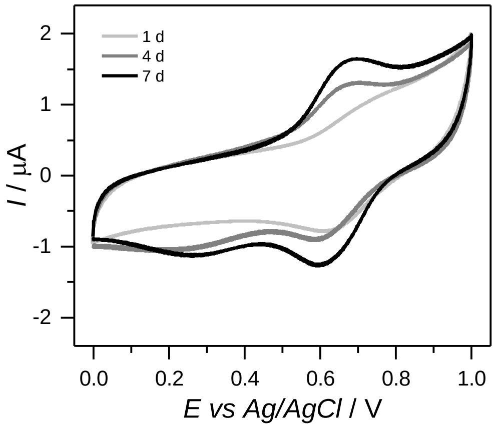

Figure C.5. Cyclic voltammograms of poly(DOPA-TEMPO) (**4**) thin films deposited on a platinum working electrode. Polymerisation of **3** was performed for 1, 4 and 7 days, respectively, and cyclic voltammograms were recorded after five cycles with a scan rate of 100 mV·s^{-1} in a 0.1 M aqueous NaCl solution. Adapted with permission from reference [314]. Copyright (2018) American Chemical Society.

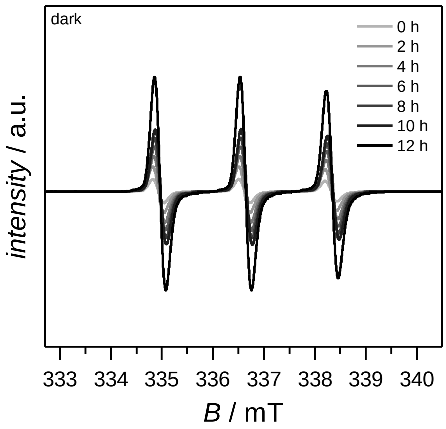

Figure C.6. First-derivative EPR spectra during polymerisation of **3** performed in the dark concomitant with nitroxide radical formation.

Appendix D

Supporting Information for Chapter 6

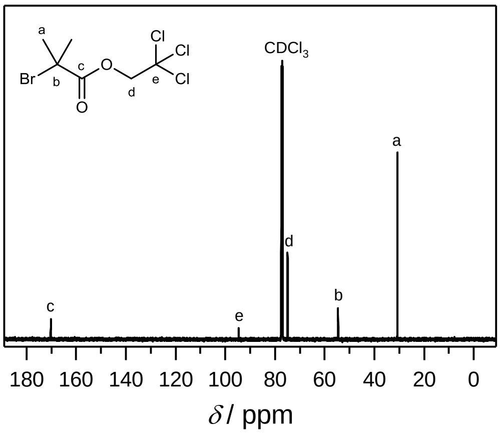

Figure D.1. ^{13}C NMR spectrum (101 MHz, $CDCl_3$, 298 K) of compound **9**. Adapted with permission from reference [339]. Copyright (2018) John Wiley and Sons.

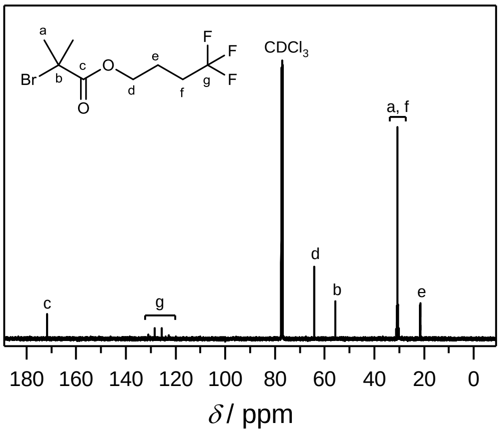

Figure D.2. ^{13}C NMR spectrum (101 MHz, $CDCl_3$, 298 K) of compound **10**. Adapted with permission from reference [339]. Copyright (2018) John Wiley and Sons.

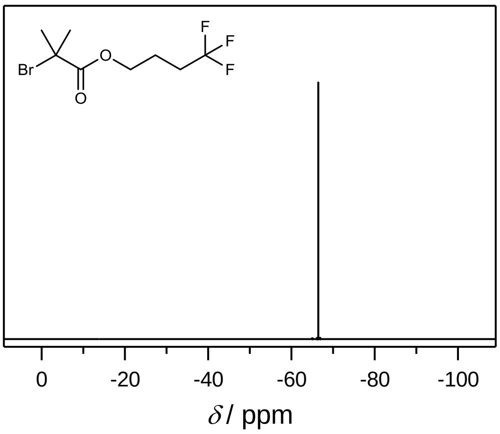

Figure D.3. ^{19}F NMR spectrum (377 MHz, $CDCl_3$, 298 K) of compound **10**. Adapted with permission from reference [339]. Copyright (2018) John Wiley and Sons.

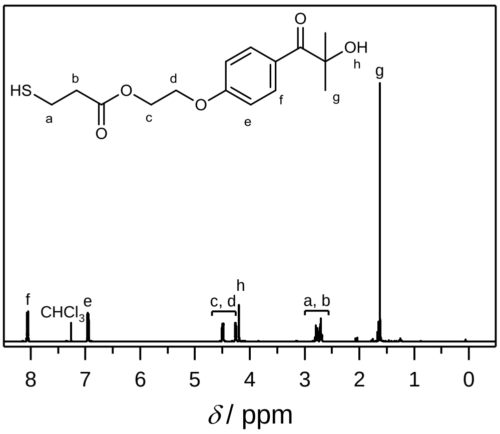

Figure D.4. ^{1}H NMR spectrum (400 MHz, $CDCl_3$, 298 K) of compound **11**. Adapted with permission from reference [339]. Copyright (2018) John Wiley and Sons.

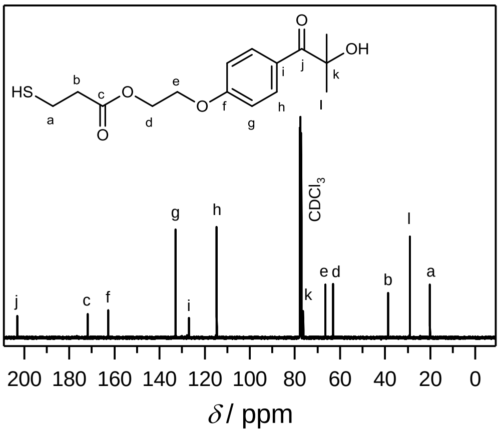

Figure D.5. ^{13}C NMR spectrum (101 MHz, $CDCl_3$, 298 K) of compound **11**. Adapted with permission from reference [339]. Copyright (2018) John Wiley and Sons.

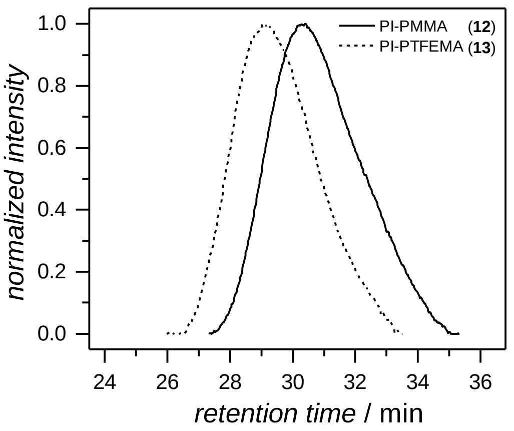

Figure D.6. Size-exclusion chromatograms of PI-PMMA (**12**) (solid line, M_n = 7000 g·mol^{-1}), and PI-PTFEMA (**13**) (dashed line, M_n = 12000 g·mol^{-1}). Adapted with permission from reference [339]. Copyright (2018) John Wiley and Sons.

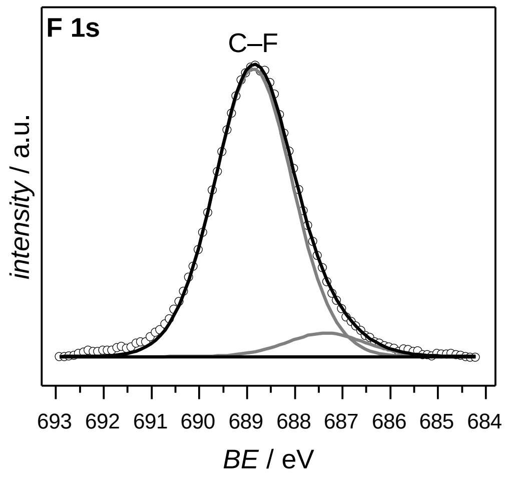

Figure D.7. F 1s XP spectrum of PTFEMA functionalised surface **D** with main characteristic C−F peak (at 688.8 eV) derived from PTFEMA fluorinated alkyl side chains. Minor peak at lower binding energies indicates anionic fluoride species. Adapted with permission from reference [339]. Copyright (2018) John Wiley and Sons.

Appendix E

Supporting Information for Chapter 7

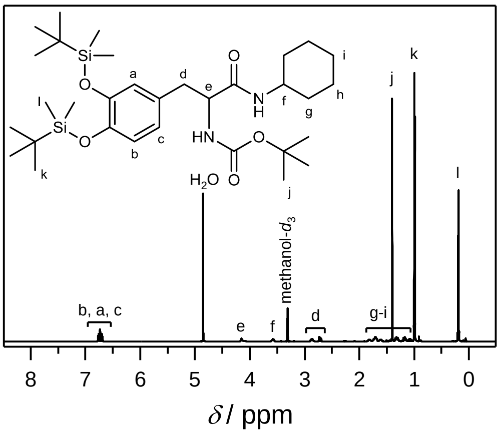

Figure E.1. ^{1}H NMR spectrum (600 MHz, methanol-d_4, 298 K) of compound **14**.

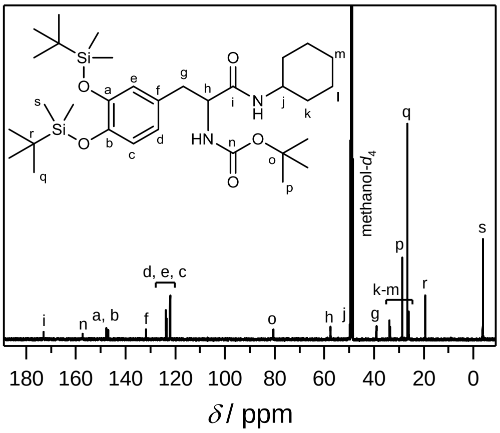

Figure E.2. ^{13}C NMR spectrum (151 MHz, methanol-d_4, 298 K) of compound **14**.

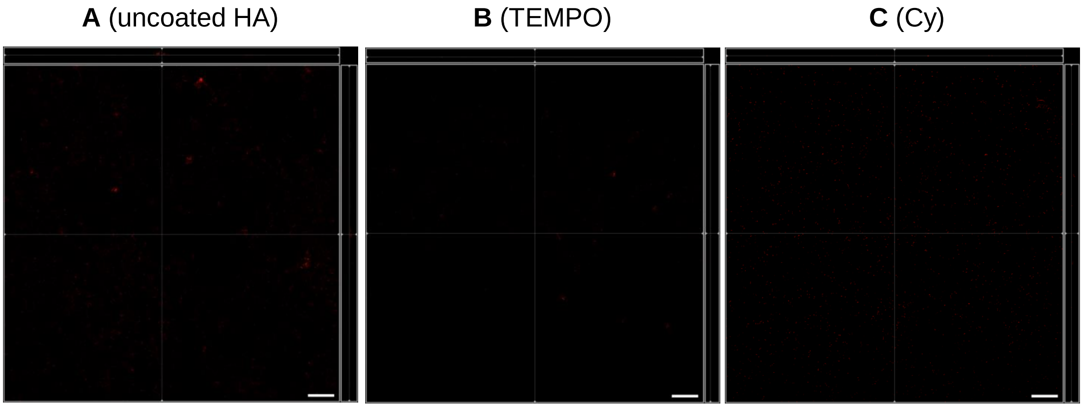

Figure E.3. *P. aeruginosa* biofilm cultivation on hydroxyapatite discs with additional propidium iodide (PI) staining for visualisation of dead cells. GFP-tagged PA14 biofilms were grown for 72 h at 37° C in flow cell chambers in the presence of uncoated (**A**), nitroxide-coated (**B**) and polymer-coated (**C**) HA substrates. Biofilm growth was assessed by CLSM. The scale bars represent 50 µm in length. Each panel shows the *xy*, *yz* and *xz* dimensions.

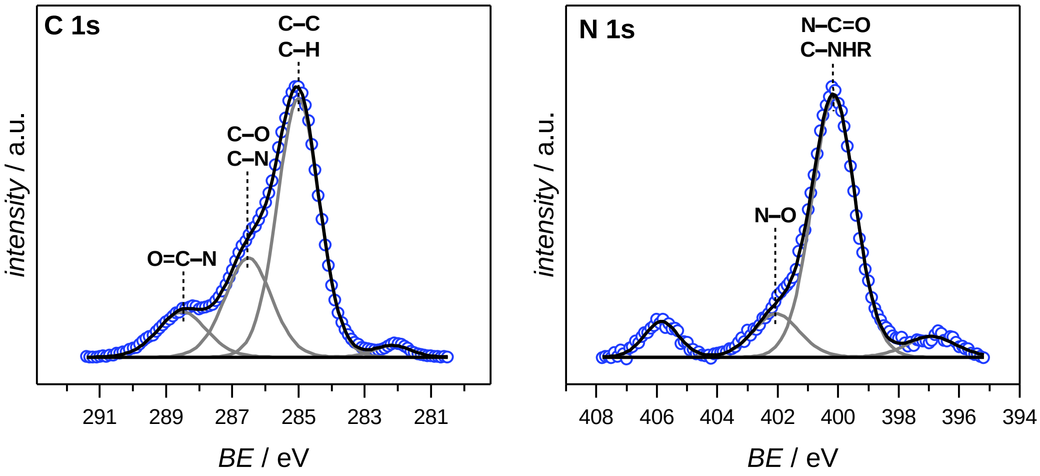

Figure E.4. XPS characterisation of poly(DOPA-TEMPO) patterned titanium surface **D** which have been covered by a shadow mask during UV irradiation.

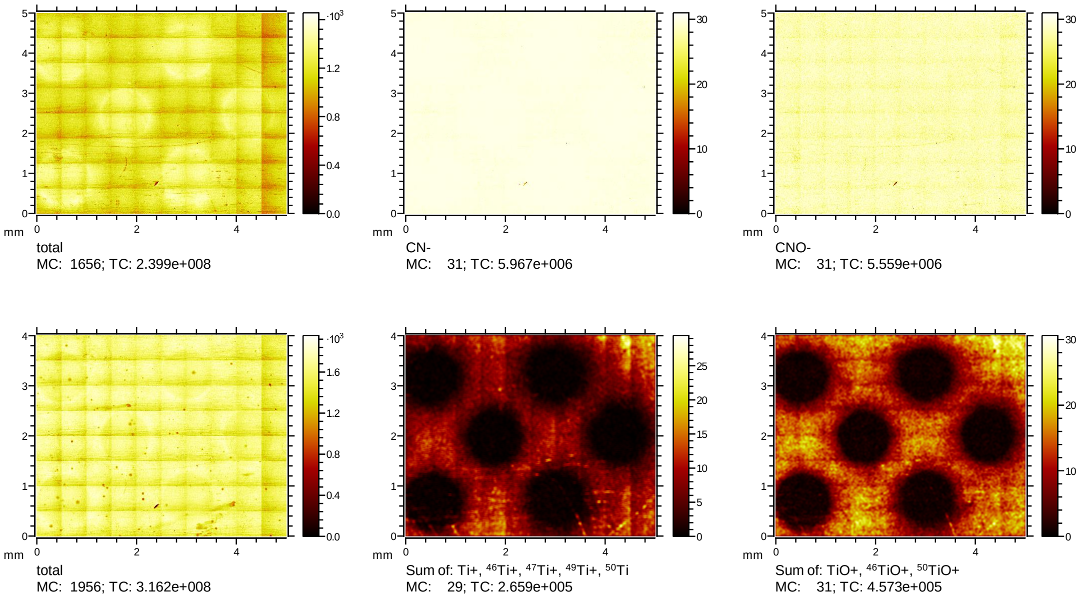

Figure E.5. Static ToF-SIMS characterisation of poly(DOPA-TEMPO) (**4**) patterned surface **D**. Imaging of polymer-characteristic $[CN]^-$ and $[CNO]^-$ fragments (top row) and several Ti isotopes derived from the underlying substrate (bottom row). As clearly shown, a direct imaging of the polymer pattern by static SIMS is hampered by the very low probing depth (in the range of 2–5 nm) and by the onset of signal saturation for the strong $[CN]^-$ and $[CNO]^-$ signals. Therefore, the image contrast of the polymer peaks is quite low. Weak substrate peaks are detectable (please note that the count rates are about one order of magnitude lower as compared to $[CN]^-$ and $[CNO]^-$), leading to the conclusion that a very thin adsorbate layer has also formed in between the irradiated spots. Ti and TiO images were 4 pixel binned to increase the dynamic range on the expense of reduced lateral resolution.

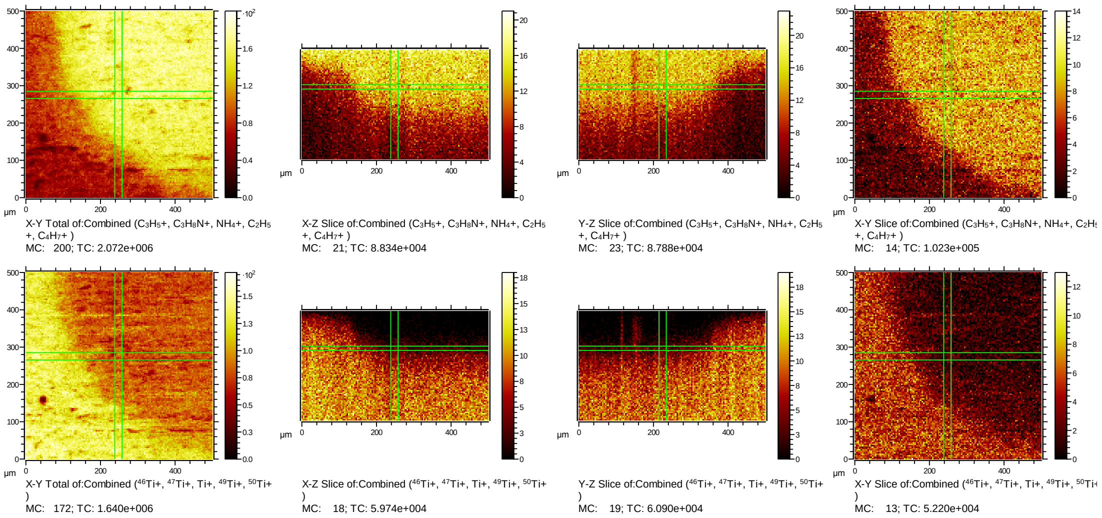

Figure E.6. Dynamic ToF-SIMS characterisation of polymer patterned surface **D**. Both leftmost images show the lateral distribution of the depth integrated signals of some fragments characteristic for the polymer layer, hydrocarbons and NH_4^+ (top row), and for the underlying Ti substrate (bottom row), respectively. The *xz* and *yz* cross sections are depicted in the central images, and the *xy* slices along the green lines are depicted in the rightmost images.

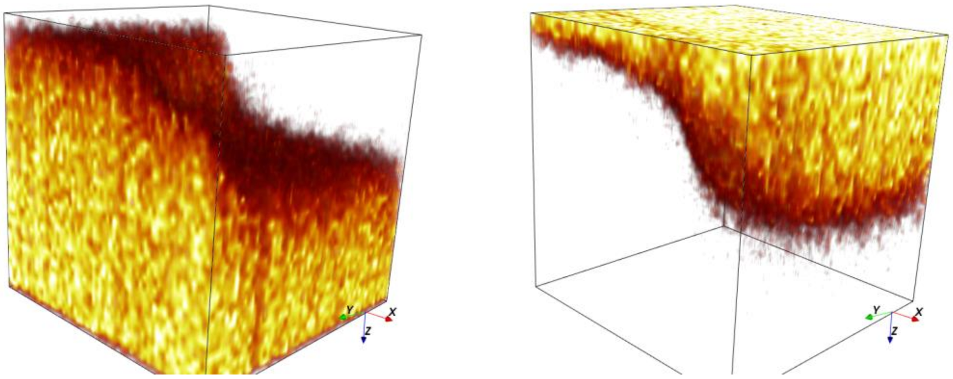

Figure E.7. ToF-SIMS 3D rendering of Ti signals (left image, sum of all isotopes) and polymer fragments (right image, sum of $[C_2H_5]^+$, $[C_3H_5]^+$, $[C_4H_7]^+$, $[C_2H_5N]^+$, and $[NH_4]^+$ fragments). The intensities are indicated by a heat scale. The *x* and *y* range is 500 µm (black box), the *z* range is not to scale.

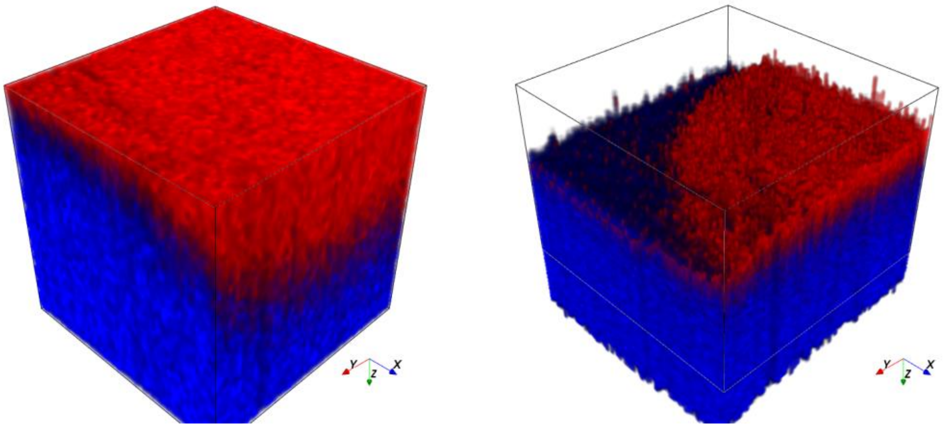

Figure E.8. ToF-SIMS colour coded 3D rendering and overlay of Ti signals (blue) and polymer signals (red). The data representation (left image) is based directly on obtained raw data, hence showing a flat topmost surface of the sample, which does not hold true for this specimen. Rather, the underlying titanium substrate can be regarded as being flat on the 500 × 500 µm^2 area (with only random surface roughness features). Therefore, the dataset can be rearranged in a way that for voxels representing the Ti signals reaching a predefined threshold intensity level is set to equal *z* values, and all other voxels are referenced to that *z* level. In practice, a certain voxel binning was required to increase the dynamic range and to reduce noise. A *xy* binning of 4 pixel and a *z* binning of 2 was applied and setting the threshold intensity for Ti as high as possible but still reached by all (binned) voxel. The height compensation to level out the Ti surface is shown at the bottom of the right image. The *x* and *y* range is 500 µm (black box), the *z* range is not to scale.

List of Figures

Figure 1.1. Schematic illustration of the projects presented in the current thesis. 3

Figure 2.1. Commonly employed classes of nitroxides with different core structures. 8

Figure 2.2. Schematic representation of a redox flow battery based on a nitroxide polymer catholyte and a viologen polymer anolyte. Adapted and reproduced with permission from reference [187]. Copyright (2015) Springer Nature. 24

Figure 2.3. The adhesion system of the mussel byssus based on mfps. (**a**) Schematic illustration of the adhesive plaque composed of various types of mfps, which are found at the end of the mussel's byssal thread. (**b**) Peptide sequence of mfp-5. (**c**) Simplified molecular structure of a mfp with DOPA-derived catechol surface anchors and lysine-derived amino side chains. Adapted and reproduced with permission from references [204] and [203]. Copyright (2011) Annual Reviews and (2007) American Association for the Advancement of Science. 27

Figure 2.4. Overview of bioinspired approaches for the generation of functional polymer coatings: (**a**) mfp-like dendritic polymers, (**b**) catechol-containing (linear) polymers, (**c**) tannic acid and other plant polyphenolic coating agents, (**d**) metal-phenolic hybrid networks, and (**e**) catecholamines as polymerisable coating agents. 28

Figure 2.5. Proposed structural key elements for PDA and its derivatives (*e.g.*, eumelanins). Adapted and reproduced with permission from reference [252]. Copyright (2013) The American Chemical Society. 33

Figure 2.6. Polymer surface patterning of PDA. (**a**) Schematic representation of the UV-assisted DA photopolymerisation concomitant with PDA surface deposition in spatially confined areas. (**b**) ToF-SIMS characterisation of polymer patterned surface *via* imaging of PDA-characteristic $[CN]^-$ fragments. Adapted and reproduced with permission from reference [263]. Copyright (2014) John Wiley and Sons. 34

Figure 2.7. Surface photopatterning of poly(MeOEGMA) polymer brushes onto PDA precoated surfaces. (**a**) Schematic representation for the generation of photo-active PDA surfaces, followed by the SI-ATRP of MeOEGMA in spatially defined areas. (**b**) ToF-SIMS overlay image of poly(MeOEGMA)-characteristic fragments (green) exclusively detected in areas which have been exposed to UV irradiation. Fragments derived from the underlying PDA layer are illustrated in blue. (**c**) Corresponding cell pattern with meander shaped antifouling domains. Adapted and reproduced with permission from reference [266]. Copyright (2013) John Wiley and Sons. 36

Figure 2.8. The lifecycle of a bacterial biofilm including the reversible bacterial surface attachment and microcolonisation followed by biofilm maturation and biofilm dispersal. Reproduced with permission from reference [11]. Copyright (2003) Springer Nature. 42

Figure 2.9. Common antibacterial and antifouling coating strategies for the reduction of device-associated infections. Reproduced with permission from reference [17]. Copyright American Chemical Society. 45

Figure 2.10. Common examples of small NO donor molecules. 46

Figure 2.11. Images of swarming motility experiments with PA14 wild-type and a *nirS* mutant in the presence of nitroxides. Adapted and redrawn with permission from reference [4]. Copyright (2013) American Society for Microbiology. 47

Figure 2.12. *P. aeruginosa* biofilm experiments with the PA14 wild-type and a *nirS* mutant in the presence of nitroxides (20 μM). Adapted and redrawn with permission from reference [4]. Copyright (2013) American Society for Microbiology 48

Figure 2.13. *P. aeruginosa* biofilm inhibition and biofilm dispersal assays using 4-carboxy-TEMPO (20 μM). Adapted and redrawn with permission from reference [4]. Copyright (2013) American Society for Microbiology. 49

Figure 2.14. Biofilm eradication experiments with 4-carboxy-TEMPO and antibiotic ciprofloxacin using Gram-negative *P. aeruginosa* and *E. coli*. Reproduced with permission from reference [5]. Copyright (2015) Oxford University Press. 50

Figure 3.1. NMR spectroscopic characterisation of **2**. (**a**) ^{1}H NMR (600 MHz) and (**b**) ^{13}C NMR spectra (151 MHz) of (TBDMS)$_2$-*N*-Boc-DOPA-TEMPO (**2**) were recorded in methanol-d_4 at 298 K. Adapted with permission from reference [314]. Copyright (2018) American Chemical Society. 56

Figure 3.2. NMR spectroscopic characterisation of **3**. (**a**) ^{1}H NMR (600 MHz) and (**b**) ^{13}C NMR spectra (151 MHz) of DOPA-TEMPO (**3**), present as the hydroxylamine dihydrochloride salt, were recorded in DMF-d_7 at 298 K. Adapted with permission from reference [314]. Copyright (2018) American Chemical Society. 57

Figure 3.3. UV–vis and EPR spectroscopic monitoring of the oxidative polymerisation of DOPA-TEMPO (**3**) in Tris–HCl buffer (1mM, pH 8.5). (**a**) Selected UV–vis spectra showing the aerobic polymerisation of **3** (solid lines), complemented by reference measurements (dashed lines) with TEMPOL (initially present as the hydroxylamine hydrochloride salt). Aliquots were diluted by factor 20 prior to spectrophotometric analysis. (**b**) Time-dependent absorbances of **3** at λ_{max} = 282 → 269 nm (●) indicating the polymerisation progress and at λ = 333 nm (■) implying *o*-quinoic reactive intermediates. (**c**) Selected first-derivative EPR spectra monitoring the nitroxide radical formation during aerobic polymerisation of **3**, initially present as a hydroxylamine dihydrochloride species. (**d**) Corresponding time-resolved radical quantification of **3** (■) in comparison to the nitroxide radical formation of the hydroxylamine hydrochloride salt of TEMPOL serving as a reference (☐). EPR quantification was performed by double integration of the EPR signals depicted in (**c**). Adapted with permission from reference [314]. Copyright (2018) American Chemical Society. 63

Figure 3.4. (−)ESI-CID (70 eV) mass spectra of poly(DOPA-TEMPO) (**4**). (**a**–**b**) Overview spectra recorded in THF/MeOH 3:2 (*v*/*v*) doped with 100 µM NaI. Single-charged oligomer structures composed of n = 2–6 repeating units were detected as molecular ions or deprotonated hydroxylamine species (labelled as ○), monohydrochloride adducts (☐), or dihydrochloride adducts (△). (**c**) Expanded region exemplarily showing the trimer and tetramer profiles of **4**. (**d**) Proposed structure of homotrimer (*m/z*(theo) 1034.4982) and homotetramer (*m/z*(theo) 1378.6592) with n = 3–4 composed of covalently linked DHI units along the polymer backbone and free radical TEMPO moieties in the polymer side chains. Adapted with permission from reference [314]. Copyright (2018) American Chemical Society. 68

Figure 3.5. (−)ESI-CID (70 eV) HCD (35 eV) MS/MS characterisation of a pentamer hydrochloride adduct of **4** apparent at *m/z* 1757. (**a**) Overview spectrum recorded in THF/MeOH 3:2 (*v*/*v*) doped with 100 µM NaI and (**b**) expanded trimer fragmentation region. Uncoordinated fragments are labelled as ● and ⭘, hydrochloride adducts are labelled as ■ and ◘. Filled and unfilled symbols present typical (−)ESI-induced fragmentation pattern with multiple ejections of TEMPO-derived methyl radicals. Further fragmentations are summarised as ⬢ and correspond to repetitive losses of CH_x and/or OH fragments. (**c**) Proposed DHI-timer of **4** with suggested nitrone formation during (−)ESI. Adapted with permission from reference [314]. Copyright (2018) American Chemical Society. 70

Figure 4.1. NMR spectroscopic characterisation of **6** and **7**. (**a**) ^{1}H NMR (400 MHz) and (**b**) ^{13}C NMR spectra (101 MHz) of $(TBDMS)_2$-*N*-Boc-DOPA-TEMPO-CH_3 (**6**). (**c**) ^{1}H NMR (400 MHz) and (**d**) ^{13}C NMR spectra (101 MHz) of DOPA-TEMPO-CH_3 (7), present as the dihydrochloride salt. All spectra were recorded in methanol-d_4 at 298 K. Adapted with permission from reference [327]. Copyright (2017) The Royal Chemical Society. 75

Figure 4.2. (−)ESI-CID (80 eV) mass spectra of poly(DOPA-TEMPO-CH_3) (**8**). Overview spectra depicted in (**a**) and (**b**) were recorded in H_2O/acetonitrile 1:1 (*v*/*v*) doped with 0.1% (*v*/*v*) acetic acid. A selected expanded oligomer region is depicted in (**c**) showing the single-charged tetramer profile. Characteristic patterns at lower *m/z* derived from $[M_4{-}H]^-$ tetramer fragmentations suggesting liberations of –OH, –CH_3, –OCH_3 and portions of the phenyl ring. Adapted with permission from reference [327]. Copyright (2017) The Royal Chemical Society. 79

Figure 4.3. (+)ESI-CID (80 eV) mass spectra of poly(DOPA-TEMPO-CH_3) (**8**). Overview spectrum depicted in (**a**) was recorded in H_2O/acetonitrile 1:1 (*v*/*v*) doped with 0.1% (*v*/*v*) acetic acid. (**b**−**c**) Zoomed spectra showing the $[M_7+H]^+$ heptamer profile and the $[M_8+H+NaCl]^+$ octamer profile. Peak assignments in (**b**) and (**c**) labelled with (± *x*H) refer to the corresponding DHI homooligomers. Adapted with permission from reference [327]. Copyright (2017) The Royal Chemical Society. 79

Figure 4.4. Proposed structures of poly(DOPA-TEMPO-CH_3) (**8**) incorporated building blocks. The building block composed of a DHI element constituting the polymer backbone was designated as a key structural unit (labelled with ●). Other structures refer to the DHI building block and are labelled with ± *x*H (*x* = even number of additional hydrogen atoms). Adapted with permission from reference [327]. Copyright (2017) The Royal Chemical Society. 80

Figure 4.5. (−)ESI-CID expanded mass spectra of poly(DOPA-TEMPO-CH_3) (**8**) dimers and trimers. Comparison of experimentally obtained spectra (top) with simulated isotopic patterns (bottom) of (**a**) $[M_2-H]^-$ dimer region and (**b**) $[M_3-H]^-$ trimer region. (**c**) Proposed structures with DHI as the polymer backbone repeating unit (labelled as ●) identified as the corresponding homodimer in (**a**) and homotrimer in (**b**). Unfilled circles (○) represent simulated molecular ion peaks of the DHI homooligomers. Other peak assignments labelled with ± *x*H refer to the DHI homooligomers. Adapted with permission from reference [327]. Copyright (2017) The Royal Chemical Society. 82

Figure 4.6. Proposed structures of +8H trimeric isomers with *m/z*(theo) 1086.6192 (*m/z*(exp) 1086.6257) and different numbers of incorporated open-chain units. Adapted with permission from reference [327]. Copyright (2017) The Royal Chemical Society. 84

Figure 4.7. (−)ESI-CID expanded mass spectra of poly(DOPA-TEMPO-CH_3) (**8**) tetramers and pentamers. Comparison of experimentally obtained spectra (top) with simulated isotopic patterns (bottom) of (**a**) $[M_4-H]^-$ tetramer region and (**b**) $[M_5-H]^-$ pentamer region. (**c**) Proposed structure of DHI homooligomers with n = 4–5. Adapted with permission from reference [327]. Copyright (2017) The Royal Chemical Society. 85

Figure 4.8. (−)ESI-CID MS and (−)ESI-HCD (15 eV) MS/MS characterisation of poly(DOPA-TEMPO-CH_3) (**8**) hexamers. (**a**) MS/MS analysis of most abundant hexamer species of **8** apparent at *m/z* 2166 ± 5. The spectrum was recorded in THF/MeOH 3:2 (*v*/*v*). Insets show complementary zoomed spectra of fragmentation regions with n = 3–5. The fragmentation pattern can be assigned to multiple losses of monomer units and filled circles (●) refer to DHI fragments ($C_{19}H_{25}N_3O_4$) with Δ*m/z*(theo) 358.1840. (**b**) Expanded mass spectrum of **8** showing the $[M_6-H]^-$ hexamer profile. The spectrum was recorded in H_2O/acetonitrile 1:1 (*v*/*v*) doped with 0.1% (*v*/*v*) acetic acid. Other peak assignments labelled with (± *x*H) refer to the DHI homooligomers. Adapted with permission from reference [327]. Copyright (2017) The Royal Chemical Society. 87

Figure 5.1. XPS characterisation poly(DOPA-TEMPO) (**4**) thin films. (**a**) C 1s and (**b**) N 1s high-resolution XP spectra of **4** deposited on Si for 24 h. Adapted with permission from reference [314]. Copyright (2018) American Chemical Society. 96

Figure 5.2. Time-resolved determination of coating thicknesses of polymer **4** deposited on silicon substrates. (**a**) Monitoring of growing polymer film formation during the initial stage of polymerisation (between 1 and 12 h) accessed through SE. (**b**) Selected AFM height profiles of polymer-coated silicon substrates after 12 h of polymerisation. Dashed lines indicate averaged polymer film thickness with 14.3 nm (top panel, excluding peaks ≥ 18 nm derived from polymer particle sedimentation) and 10.1 nm (bottom panel, excluding peaks ≥ 15 nm). Adapted with permission from reference [314]. Copyright (2018) American Chemical Society. 98

Figure 5.3. Electrochemical characterisation of poly(DOPA-TEMPO) (**4**) thin films deposited on a glassy carbon working electrode for 1, 4 and 7 days, respectively. (**a**) Cyclic voltammograms (five cycles) recorded with a scan rate of 100 $mV \cdot s^{-1}$ in 0.1 M aqueous NaCl solution. (**b**) Schematic illustration of polymer **4** showing the reversible nitroxide oxidation to corresponding *N*-oxoammonium cationic species and subsequent reduction back to the nitroxide free radicals. Adapted with permission from reference [314]. Copyright (2018) American Chemical Society. 99

Figure 5.4. In-depth and time-resolved characterisation of light-dependent polymerisation of **3** with *in situ* polymer surface deposition onto immersed silicon substrates. (**a**) Determination of coating thickness of polymer **4** by SE. (**b**) UV–vis spectroscopic monitoring of oxidative polymerisation of **3** under UV-B irradiation (left panel) and in the dark (right panel). (**c**) First derivative EPR spectra during polymerisation of **3** concomitant with nitroxide radical formation. (**d**) EPR quantification of nitroxide-derived unpaired electron spins *via* double integration of the recorded EPR signals. 102

Figure 6.1. EPR and XPS characterisation of **MS1**. (**a**) EPR spectrum showing the persistent radical character of the nitroxide encased PGMA microspheres (suspended in aqueous solutions for solution state EPR analysis). (**b**) C 1s XP spectrum deconvoluted into three components: C−C and C−H (at 285.0 eV), C−O and C−N (286.6 eV), and O−C=O and N−C=O (288.9 eV) assigned to PGMA core structures and thin nitroxide functional polymer film. (**c**) N 1s XP spectrum with dominant peak at 399.8 eV assigned to poly(catecholamine) backbone structures. Minor peak at 402.0 eV corresponds to the nitroxide functional group and most likely other oxidised N-containing species. Adapted with permission from reference [339]. Copyright (2018) John Wiley and Sons. 108

Figure 6.2. ^{1}H NMR spectra (400 MHz, $CDCl_3$, 298 K) of (**a**) chlorine-tagged NRC agent **9** and (**b**) fluorine-tagged NRC agent **10**. Adapted with permission from reference [339]. Copyright (2018) John Wiley and Sons. 109

Figure 6.3. EPR and XPS characterisation of **MS2**–**MS4**. (**a**) Qualitative EPR analysis with EPR silent alkoxyamine derivatives **MS2** and **MS4** as well as EPR active **MS3**. (**b**) and (**c**) Cl 2p and F 1s XP spectra quantifying the rewritable properties of nitroxide functional microspheres based on NRC reactions and alkoxyamine fission exemplified in a small molecule conjugation study with chlorine- and fluorine-tagged NRC agents **9** and **10**. Adapted with permission from reference [339]. Copyright (2018) John Wiley and Sons. 111

Figure 6.4. ToF-SIMS and XPS characterisation of precursor surfaces **A** and **B**. (**a**) (−)ToF-SIMS spectra of non-functionalised (**A**) and nitroxide conjugated (**B**) surfaces. The nitroxide immobilisation (**B**, black solid line) onto PDA precoated Si substrates (**A**, blue solid line) was evidenced by the appearance of the $[NO]^-$ fragment at *m/z* 30.00. 4-carboxy-TEMPO (black dashed line) served as a reference. (**b**) C 1s XP spectrum of surface **B** deconvoluted into four components: C−C and C−H (at 285.0 eV), C−O and C−N (286.3 eV), C=O and N−C=O (288.1 eV), and O−C=O (289.3 eV) assigned to PDA with only minor contribution of the surface-immobilised nitroxide functional groups. Adapted with permission from reference [339]. Copyright (2018) John Wiley and Sons. 115

Figure 6.5. ToF-SIMS images of PMMA patterned surface **C**. PMMA-characteristic fragments were exclusively detected in confined areas which had been exposed to UV irradiation. Adapted with permission from reference [339]. Copyright (2018) John Wiley and Sons. 116

Figure 6.6. XPS and ToF-SIMS characterisation of dual polymer conjugated surface **D**. a) C 1s XP spectra obtained from polymer conjugated and unconjugated areas. PMMA surface ligation in defined areas was evidenced by a pronounced O−C=O peak (at 289.0 eV) in comparison to the underlying PDA-TEMPO matrix derived from methyl methacrylate polymer repeating units. Adjacent PTFEMA polymer strands were unambiguously identified showing a distinct CF_3 signal at 293.4 eV. b) ToF-SIMS overlay image constructed from images of PMMA-characteristic $[CH_3O]^-$ fragments (red), and PTFEMA derived $[F]^-$ and $[CF_3]^-$ fragments (green). c) F 1s XPS mapping (688.6 eV) with distinct pattern derived from PTFEMA polymer strands. Scale bars represent 1 mm. Adapted with permission from reference [339]. Copyright (2018) John Wiley and Sons. 117

Figure 7.1. NMR spectroscopic characterisation of **15**. (**a**) ^1H NMR (600 MHz) and (**b**) ^{13}C NMR spectra (151 MHz) of DOPA-Cy (**15**) were recorded in methanol-d_4 at 298 K. 122

Figure 7.2. XPS characterisation of poly(DOPA-Cy) (**C**, top row) and poly(DOPA-TEMPO) (**B**, bottom row) coated HA substrates: (**a**) C 1s and (**b**) N 1s high-resolution XP spectra.. 124

Figure 7.3. (−)ToF-SIMS characterisation of uncoated and polymer-coated HA surfaces. (**a**) The peak at *m/z* 26.01 was assigned to polymer-characteristic $[CN]^-$ fragments (*m/z*(theo) 26.00), detected on polymer-coated surfaces **B** and **C** (black and red solid lines). (**b**) The nitroxide-characteristic $[NO]^-$ fragment at *m/z* 30.00 was exclusively detected on the TEMPO-functionalised surface **B**. Uncoated HA (surface **A**, blue solid line) and cyclohexyl conjugated surface **C** did not show the nitroxyl characteristic peak. ... 125

Figure 7.4. *P. aeruginosa* biofilm cultivation on unmodified and polymer-coated HA surfaces. Uncoated (**A**), nitroxide polymer-coated (**B**), and cyclohexyl polymer-coated (**C**) surfaces were exposed to PA14 surface colonisation for 72 h in a flow cell system at 37 °C. Biofilm surface coverage of the employed GFP-tagged PA14 strain was assessed by CLSM. The scale bars represent 50 µm in length. Each panel shows the *xy*, *yz* and *xz* dimensions. ... 127

Figure 7.5. *P. aeruginosa* biofilm eradication assays with antibiotic ciprofloxacin. PA14 surface colonisation on surfaces **A**–**C** was performed in a flow cell system (37 °C) for 72 h with addition of ciprofloxacin (320 $ng \cdot ml^{-1}$) after 48 h. Dead cells were stained with propidium iodide (red) prior to confocal microscopy. Merged images composed of PI and GFP channels are displayed and superimposed fluorescence response of live (green) and dead cells (red) appear yellow. The scale bars represent 50 µm in length. Each panel shows the *xy*, *yz* and *xz* dimensions ... 128

Figure 7.6. *P. aeruginosa* biofilm cultivation and biofilm eradication assays with antibiotic ciprofloxacin. Uncoated (**A**) and nitroxide polymer-coated (**B**) titanium surfaces were exposed to PA14 surface colonisation for 72 h (top row) with addition of ciprofloxacin (320 $ng \cdot ml^{-1}$) after 48 h (bottom row). Biofilm assays were performed in a flow cell system at 37 °C. Dead bacteria were stained with propidium iodide (red) prior to confocal microscopy. Merged images composed of PI and GFP channels are displayed and superimposed fluorescence response of live (green) and dead cells (red) appear yellow. The scale bars represent 50 µm in length. Each panel shows the *xy*, *yz* and *xz* dimensions ... 130

Figure 7.7. C 1s, N 1s and Ti 2p XPS images (**a**–**c**) of poly(DOPA-TEMPO) patterned surface **D**. Scale bars represent 1 mm in length. ... 132

Figure 7.8. In-depth XPS characterisation of poly(DOPA-TEMPO) patterned titanium surface **D.** (**a**) XPS overlay image constructed from of substrate-derived Ti 2p XPS signals (blue) and polymer-derived C 1s XPS signals (magenta). Scale bar represents 1 mm in length. (**b**) Ti 2p XP spectra obtained from polymer conjugated (magenta) and non-conjugated areas (blue). (**c**–**d**) Corresponding C 1s and N 1s XP spectra of polymer conjugated areas. ... 133

Figure 7.9. 3D ToF-SIMS rendering of poly(DOPA-TEMPO) patterned titanium surface **D**. The Ti substrate is illustrated in blue and a quarter of one nitroxide polymer spot deposited on the surface is depicted in red. Polymer signals (red) are sum of $[C_2H_5]^+$, $[C_3H_5]^+$, $[C_4H_7]^+$, $[C_2H_5N]^+$, and $[NH_4]^+$ fragments. Titanium signals (blue) derived from the sum of all isotopes. The *x* and *y* range is 500 µm (black box), the *z* range is not to scale. 135

Figure 7.10. *P. aeruginosa* biofilm cultivation on nitroxide patterned titanium surface. Surface **D** was exposed to a GFP-labelled PA14 strains for 72 h under static conditions at 37 °C. Confocal image was obtained through 3 × 3 rastering along the *xy* dimension with approx. 16 µm depths in *yz* and *xz* dimensions (indicated in side panels). The scale bar represents 200 µm in length. 136

Figure A.1. EPR spectrum of **2** recorded in DCM. Adapted with permission from reference [314]. Copyright (2018) American Chemical Society. 185

Figure A.2. Complementary UV–vis spectra recorded during polymerisation of **3.** Adapted with permission from reference [314]. Copyright (2018) American Chemical Society. 185

Figure B.1. ^{1}H NMR spectrum (400 MHz, methanol-d_4, 298 K) of compound **5**. Adapted with permission from reference [327]. Copyright (2017) The Royal Chemical Society. 187

Figure B.2. ^{13}C NMR spectrum (101 MHz, methanol-d_4, 298 K) of compound **5**. Adapted with permission from reference [327]. Copyright (2017) The Royal Chemical Society. 187

Figure B.3. ^{1}H NMR spectrum (400 MHz, methanol-d_4, 298 K) of polymer **8**. Adapted with permission from reference [327]. Copyright (2017) The Royal Chemical Society. 188

Figure B.4. ^{13}C NMR spectrum (101 MHz, methanol-d_4, 298 K) of polymer **8**. Adapted with permission from reference [327]. Copyright (2017) The Royal Chemical Society. 188

Figure B.5. Comparison of experimentally obtained spectrum of the $[M_2{-}H]^-$ dimer region (top panel) and simulated isotopic pattern of the DHI homodimer apparent as the most abundant peak (bottom panel) indicating the presence of higher molecular weight species such as +2H and +4H dimers. Adapted with permission from reference [327]. Copyright (2017) The Royal Chemical Society. 193

Figure B.6. Comparison of experimentally obtained spectrum of the $[M_3{-}H]^-$ trimer region (top panel) and simulated isotopic pattern of the +4H and the +6H species (bottom panel) clearly indicating the presence of a +8H trimer with incorporated open-chain dopamine units. Adapted with permission from reference [327]. Copyright (2017) The Royal Chemical Society. 193

Figure C.1. Images taken during static water contact angle measurements showing deposited water droplet on uncoated (left) and polymer **4** coated PTFE (right). Adapted with permission from reference [314]. Copyright (2018) American Chemical Society. 194

Figure C.2. N 1s XP spectrum of PTMA for identification of the TEMPO-characteristic N–O peak. The dominant peak (at 401.5 eV) of PTMA (drop-casted on silicon) was assigned to the N–O functional group. Peaks a lower BEs correspond to residual non-oxidised 2,2,6,6-

tetramethylpiperidine moieties of the polymer precursor. PTMA was kindly provided by K.-A. Hansen (QUT). Adapted with permission from reference [314]. Copyright (2018) American Chemical Society. 194

Figure C.3. AFM image obtained for determination of average polymer film thickness (refer to **Figure 5.2b**, top panel). Adapted with permission from reference [314]. Copyright (2018) American Chemical Society. 195

Figure C.4. AFM image obtained for determination of average polymer film thickness (refer to **Figure 5.2b**, bottom panel). Adapted with permission from reference [314]. Copyright (2018) American Chemical Society. 195

Figure C.5. Cyclic voltammograms of poly(DOPA-TEMPO) (**4**) thin films deposited on a platinum working electrode. Polymerisation of **3** was performed for 1, 4 and 7 days, respectively, and cyclic voltammograms were recorded after five cycles with a scan rate of 100 $mV \cdot s^{-1}$ in a 0.1 M aqueous NaCl solution. Adapted with permission from reference [314]. Copyright (2018) American Chemical Society. 195

Figure C.6. First-derivative EPR spectra during polymerisation of **3** performed in the dark concomitant with nitroxide radical formation. 196

Figure D.1. ^{13}C NMR spectrum (101 MHz, $CDCl_3$, 298 K) of compound **9**. Adapted with permission from reference [339]. Copyright (2018) John Wiley and Sons. 197

Figure D.2. ^{13}C NMR spectrum (101 MHz, $CDCl_3$, 298 K) of compound **10**. Adapted with permission from reference [339]. Copyright (2018) John Wiley and Sons. 197

Figure D.3. ^{19}F NMR spectrum (377 MHz, $CDCl_3$, 298 K) of compound **10**. Adapted with permission from reference [339]. Copyright (2018) John Wiley and Sons. 198

Figure D.4. ^{1}H NMR spectrum (400 MHz, $CDCl_3$, 298 K) of compound **11**. Adapted with permission from reference [339]. Copyright (2018) John Wiley and Sons. 198

Figure D.5. ^{13}C NMR spectrum (101 MHz, $CDCl_3$, 298 K) of compound **11**. Adapted with permission from reference [339]. Copyright (2018) John Wiley and Sons. 198

Figure D.6. Size-exclusion chromatograms of PI-PMMA (**12**) (solid line, M_n = 7000 $g \cdot mol^{-1}$), and PI-PTFEMA (**13**) (dashed line, M_n = 12000 $g \cdot mol^{-1}$). Adapted with permission from reference [339]. Copyright (2018) John Wiley and Sons. 199

Figure D.7. F 1s XP spectrum of PTFEMA functionalised surface **D** with main characteristic C−F peak (at 688.8 eV) derived from PTFEMA fluorinated alkyl side chains. Minor peak at lower binding energies indicates anionic fluoride species. Adapted with permission from reference [339]. Copyright (2018) John Wiley and Sons. 199

Figure E.1. ^{1}H NMR spectrum (600 MHz, methanol-d_4, 298 K) of compound **14**. 200

Figure E.2. ^{13}C NMR spectrum (151 MHz, methanol-d_4, 298 K) of compound **14**. 200

Figure E.3. *P. aeruginosa* biofilm cultivation on hydroxyapatite discs with additional propidium iodide (PI) staining for visualisation of dead cells. GFP-tagged PA14 biofilms were grown for 72 h at 37° C in flow cell chambers in the presence of uncoated (**A**), nitroxide-coated (**B**) and polymer-coated (**C**) HA substrates. Biofilm growth was assessed by CLSM. The scale bars represent 50 µm in length. Each panel shows the *xy*, *yz* and *xz* dimensions. 201

Figure E.4. XPS characterisation of poly(DOPA-TEMPO) patterned titanium surface **D** which have been covered by a shadow mask during UV irradiation. 201

Figure E.5. Static ToF-SIMS characterisation of poly(DOPA-TEMPO) (**4**) patterned surface **D**. Imaging of polymer-characteristic $[CN]^-$ and $[CNO]^-$ fragments (top row) and several Ti isotopes derived from the underlying substrate (bottom row). As clearly shown, a direct imaging of the polymer pattern by static SIMS is hampered by the very low probing depth (in the range of 2–5 nm) and by the onset of signal saturation for the strong $[CN]^-$ and $[CNO]^-$ signals. Therefore, the image contrast of the polymer peaks is quite low. Weak substrate peaks are detectable (please note that the count rates are about one order of magnitude lower as compared to $[CN]^-$ and $[CNO]^-$), leading to the conclusion that a very thin adsorbate layer has also formed in between the irradiated spots. Ti and TiO images were 4 pixel binned to increase the dynamic range on the expense of reduced lateral resolution. 202

Figure E.6. Dynamic ToF-SIMS characterisation of polymer patterned surface **D**. Both leftmost images show the lateral distribution of the depth integrated signals of some fragments characteristic for the polymer layer, hydrocarbons and NH_4^+ (top row), and for the underlying Ti substrate (bottom row), respectively. The *xz* and *yz* cross sections are depicted in the central images, and the *xy* slices along the green lines are depicted in the rightmost images. 202

Figure E.7. ToF-SIMS 3D rendering of Ti signals (left image, sum of all isotopes) and polymer fragments (right image, sum of $[C_2H_5]^+$, $[C_3H_5]^+$, $[C_4H_7]^+$, $[C_2H_5N]^+$, and $[NH_4]^+$ fragments). The intensities are indicated by a heat scale. The *x* and *y* range is 500 µm (black box), the *z* range is not to scale. 203

Figure E.8. ToF-SIMS colour coded 3D rendering and overlay of Ti signals (blue) and polymer signals (red). The data representation (left image) is based directly on obtained raw data, hence showing a flat topmost surface of the sample, which does not hold true for this specimen. Rather, the underlying titanium substrate can be regarded as being flat on the 500 × 500 µm^2 area (with only random surface roughness features). Therefore, the dataset can be rearranged in a way that for voxels representing the Ti signals reaching a predefined threshold intensity level is set to equal *z* values, and all other voxels are referenced to that *z* level. In practice, a certain voxel binning was required to increase the dynamic range and to reduce noise. A *xy* binning of 4 pixel and a *z* binning of 2 was applied and setting the threshold intensity for Ti as high as possible but still reached by all (binned) voxel. The height compensation to level out the Ti surface is shown at the bottom of the right image. The *x* and *y* range is 500 μm (black box), the *z* range is not to scale. 203

List of Schemes

Scheme 2.1. The nitroxyl key structural element of nitroxides with an unpaired electron delocalised over the *N*,*N*-disubstituted nitrogen atom and the oxygen atom. 7

Scheme 2.2. Overview of synthetic pathways for the preparation of nitroxides. 9

Scheme 2.3. The principle of the nitroxide-mediated polymerisation technique. 14

Scheme 2.4. Schematic presentation of (**a**) copper-mediated or (**b**) photo-induced nitroxide radical coupling reactions for polymer end group functionalisations. 15

Scheme 2.5. Synthetic pathways with direct access to nitroxide-containing polymers. Common examples include (**a**) the anionic ring-opening polymerisation of TEMPO-glycidyl ether, (**b**) cationic polymerisation of TEMPO-vinyl ether, (**c**) ROMP of a norbornene derivative, and (**d**) the generation of nitroxide substituted poly(phenylacetylene)s. 18

Scheme 2.6. General procedure for the preparation of PTMA using TMPM as a monomer, followed by the post-polymerisation oxidation to the corresponding nitroxide-containing polymer. 20

Scheme 2.7. Nitroxide-mediated oxidation of an alcohol in the presence of cooxidant NaOCl and KBr. 22

Scheme 2.8. Schematic illustration of the preparation of profluorescent nitroxides and the regeneration of the fluorescence upon radical trapping reaction or redox processes. Adapted with permission from reference [30]. Copyright (2011) CSIRO Publishing. 23

Scheme 2.9. Biosynthesis of eumelanins explained by the Raper–Manson mechanism. Adapted and reproduced with permission from reference [239]. Copyright (2016) John Wiley and Sons. 31

Scheme 2.10. Proposed intramolecular reaction pathway of DA (under oxidative conditions) prior to its polymerisation. 32

Scheme 2.11. Schematic depiction of PDA post- modification pathways: (**a**) nucleophilic conjugation with primary amino or mercapto groups (*e.g.*, *via* Schiff base or Michael-type addition reactions) and (**b**) acylation reactions. 35

Scheme 2.12. Direct access to highly defined surfaces using prefunctionalised catecholamines as coating agents.[213, 272-274] 37

Scheme 2.13. Examples of bioinspired surface immobilisations of various functional groups for subsequent (orthogonal) post-coating modification reactions.[276-281] 39

Scheme 3.1. Synthetic pathway for the preparation of DOPA-TEMPO (**3**), isolated as the corresponding hydroxylamine dihydrochloride salt.

Adapted with permission from reference [314]. Copyright (2018) American Chemical Society. 55

Scheme 3.2. Oxidative polymerisation of DOPA-TEMPO (**3**). The reaction was performed under aerobic alkaline conditions using Tris–HCl buffer (pH 8.5) at ambient temperature. Several catecholamine-derived structures (**3a–c**) have been proposed as key intermediate states throughout polymerisation. Adapted with permission from references [314] and [327]. Copyright (2018) American Chemical Society and (2017) The Royal Chemical Society. 60

Scheme 4.1. Synthetic pathway for the generation of DOPA-TEMPO-CH_3 (**7**), isolated as the corresponding dihydrochloride salt. Adapted with permission from reference [327]. Copyright (2017) The Royal Chemical Society. 74

Scheme 4.2. Oxidative polymerisation of DOPA-TEMPO-CH_3 (**7**). The reaction was performed under aerobic alkaline conditions using Tris–HCl buffer (pH 8.5) at ambient temperature. Adapted with permission from reference [327]. Copyright (2017) The Royal Chemical Society. 76

Scheme 5.1. Synthetic route for the oxidative polymerisation of **3** (10 mM) with *in situ* polymer surface deposition onto various immersed substrates. The dip-coating procedure was performed in Tris–HCl buffer (10 mM, pH 8.5) under aerobic conditions. Substrates were typically coated for 12 or 24 h, respectively. Uncoated objects encompass silicon, titanium, alumina and PTFE flat substrates. Adapted with permission from reference [314]. Copyright (2018) American Chemical Society. 93

Scheme 5.2. Light-dependent oxidative polymerisation of DOPA-TEMPO (**3**) (5 mM) with *in situ* polymer surface deposition onto immersed silicon substrates. The reaction was performed in Tris–HCl buffer (10 mM, pH 8.5) for 0–12 h under UV-B irradiation (λ_{max} = 313 nm) and in the dark, respectively. 101

Scheme 6.1. Synthetic pathway for the preparation of nitroxide-coated PGMA microspheres. The oxidative copolymerisation of DA hydrochloride and DOPA-TEMPO (**3**) (molar ratio 9:1) concomitant with copolymer film deposition onto suspended PGMA microspheres was performed under aerobic conditions in Tris–HCl buffer (10 mM, pH 8.5) for 2 d. Adapted with permission from reference [339]. Copyright (2018) John Wiley and Sons. 106

Scheme 6.2. Synthesis of 2,2,2-trichloroethyl 2-bromoisobutyrate (**9**) and 4,4,4-trifluorobutyl 2-bromoisobutyrate (**10**) for targeted NRC reactions. 109

Scheme 6.3. Thermo-reversible small molecule conjugations onto nitroxide-decorated microspheres. Coding of **MS1** was performed in a copper-mediated NRC reaction with compound **9**. Subsequent thermal alkoxyamine dissociation of **MS2** was conducted in the presence of a radical scavenger (*e.g.*, TMIO or atmospheric oxygen). Re-coding of **MS3** was carried out using compound **10** as a NRC agent. Adapted with permission from reference [339]. Copyright (2018) John Wiley and Sons. 110

Scheme 6.4. Synthetic overview for the preparation of nitroxide-decorated PDA surfaces employed for photopatterning with PI-terminated polymer strands. (**a**) Oxidative DA polymerisation concomitant with PDA surface deposition onto silicon substrates and subsequent nitroxide ad-layer surface functionalisation in an EDC-mediated amide coupling reaction of PDA incorporated free amino side chains and 4-carboxy-TEMPO. (**b**) Chain transfer polymerisations of MMA and TFEMA in the presence of thiol-functionalised Irgacure 2959 (**11**) yielding end group photoreactive PI-PMMA (**12**, M_n = 7000 g·mol^{-1}) and PI-PTFEMA (**13**, M_n = 12000 g·mol^{-1}) polymer strands. (**c**) Consecutive surface photopatterning with **12** and **13** onto nitroxide-functionalised PDA surface **B**. Adapted with permission from reference [339]. Copyright (2018) John Wiley and Sons. 113

Scheme 7.1. Synthetic pathway for the preparation of DOPA-Cy (**15**), isolated as the corresponding hydrochloride salt. 121

Scheme 7.2. Synthetic route for preparation of nitroxide- and cyclohexyl-containing polymer-coated HA and Ti substrates. The oxidative polymerisation of DOPA-TEMPO (**3**) (40 mM) and DOPA-Cy (**15**) (40 mM) with *in situ* polymer surface deposition was performed in Tris–HCl buffer (100 mM, pH 9.25) in the presence of atmospheric oxygen for 24 h. 123

Scheme 7.3. Synthetic route for the spatially controlled surface immobilisation of poly(DOPA-TEMPO (**4**) onto titanium substrates. DOPA-TEMPO (**3**) (5 mM) was dissolved in Tris–HCl buffer (10 mM, pH 8.5) and the Ti substrates were covered by a dotted shadow mask. UV irradiation was performed for 12 h. 131

List of Tables

Table 4.1. (−)ESI-CID MS peak assignments of $[M_2{-}H]^-$ dimers of poly(DOPA-TEMPO-CH_3) (**8**). The *m/z*(theo) values were obtained from isotopic pattern simulations of each individual profile pattern. The displayed relative ratios were employed for constructing the simulated spectra. Adapted with permission from reference [327]. Copyright (2017) The Royal Chemical Society. 83

Table 4.2. (−)ESI-CID MS peak assignments of $[M_3{-}H]^-$ trimers of poly(DOPA-TEMPO-CH_3) (**8**). Adapted with permission from reference [327]. Copyright (2017) The Royal Chemical Society. 83

Table 4.3. (−)ESI-CID MS peak assignments of $[M_4{-}H]^-$ tetramers of poly(DOPA-TEMPO-CH_3) (**8**). Adapted with permission from reference [327]. Copyright (2017) The Royal Chemical Society. 86

Table 4.4. (−)ESI-CID MS peak assignments of $[M_5{-}H]^-$ pentamers of poly(DOPA-TEMPO-CH_3) (**8**). Adapted with permission from reference [327]. Copyright (2017) The Royal Chemical Society. 86

Table 5.1. Surface characterisation of uncoated and poly(DOPA-TEMPO) (**4**) coated substrates by XPS, AFM and static water contact angle measurements. Adapted with permission from reference [314]. Copyright (2018) American Chemical Society. 94

Table A.1. (−)ESI-CID MS peak assignments of most abundant tetramer species (refer to **Figure 3.4c**). Adapted with permission from reference [314]. Copyright (2018) American Chemical Society. 186

Table A.2. (−)ESI-HCD MS/MS peak assignments of most abundant trimer fragments (refer to **Figure 3.5b**). Adapted with permission from reference [314]. Copyright (2018) American Chemical Society. 186

Table B.1. (−)ESI-CID MS peak assignments of $[M_n{-}H]^-$ oligomers (with n = 2–6) of poly(DOPA-TEMPO-CH_3) (**8**). The displayed *m/z*(theo) values were obtained from isotopic pattern simulations of each individual profile pattern. Adapted with permission from reference [327]. Copyright (2017) The Royal Chemical Society. 189

Table B.2. (+)ESI-CID MS peak assignments of $[M_7+H]^+$ species and $[M_8+H+NaCl]^+$ species of poly(DOPA-TEMPO-CH_3) (**8**). The displayed *m/z*(theo) values were obtained from isotopic pattern simulations of each individual profile pattern. Adapted with permission from reference [327]. Copyright (2017) The Royal Chemical Society. 191

Table B.3. (−)ESI-HCD MS/MS peak assignments of fragments $[F_n\text{-}H]^-$ with n = 3−5 of poly(DOPA-TEMPO-CH_3) (**8**) performed on hexameric species $[M_6{-}H]^-$ apparent at *m/z* 2166 ± 5. Only most abundant peaks of oligomeric fragments were selected and listed in this table. The *m/z*(theo) values of most abundant peaks were calculated without simulation of the overlapping isotopic patterns of the remaining species. Adapted with permission from reference [327]. Copyright (2017) The Royal Chemical Society. 192

List of Abbreviations

ACN	acetonitrile
AIBN	2,2’-azoisobutyronitrile
AFM	atomic force microscopy
a.t.	ambient temperature
AT	atom transfer
ATNRC	atom transfer nitroxide radical coupling
ATRP	atom transfer radical polymerisation
a.u.	arbitrary units
BE	binding energy
BM	basal medium
Boc	*tert*-butyloxycarbonyl
CID	collision-induced dissociation
CF	cystic fibrosis
CLSM	confocal laser scanning microscopy
***m*CPBA**	*meta*-chloroperoxybenzoic acid
CuAAC	copper catalysed azide alkine cycloaddition
CV	cyclic voltammetry
d	day(s)
DA	dopamine (3,4-dihydroxyphenethylamine)
DCM	dichloromethane
DIPEA	*N*,*N*-diisopropylethylamine
DHI	5,6-dihydroxyindole
L-DOPA	L-3,4-dihydroxyphenylalanine
DMAP	4-dimethylaminopyridine
DMSO	dimethyl sulfoxide
DMF	*N*,*N*-dimethylformamide
DOPA	3,4,-dihydroxyphenylalanine
ε	molar attenuation coefficient
EDC	1-ethyl-3-3(3-dimethylaminopropyl)carbodiimide

EPR	electron paramagnetic resonance
ESI	electrospray ionisation
HA	hydroxyapatite
HCD	higher-energy collisional dissociation
HPLC	high-performance liquid chromatography
HR	high-resolution
integr.	integrated
IR	infrared
Irgacure 2959	(2-hydroxy-4′-(2-hydroxyethoxy)-2-methylpropiophenone
LRP	living radical polymerisation
m	molar ($\text{mol}\cdot\text{L}^{-1}$)
MeOEGMA	oligo(ethylene glycol) methyl ether methacrylate
mfp	mussel foot protein
MIC	minimum inhibitory concentration
MMA	methyl methacrylate
MPN	metal-phenolic network
MS	mass spectrometry or microsphere(s)
MS/MS	tandem mass spectrometry
NMP	nitroxide-mediated polymerisation
NMR	nuclear magnetic resonance
norm.	normalised
NRC	nitroxide radical coupling
ORB	organic radical battery
PA	*Pseudomonas aeruginosa*
PDA	poly(dopamine)
PEG	poly(ethylene glycol)
PI	photoinitiator or propidium iodide
PFN	profluorescent nitroxide
PGMA	poly(glycidyl methacrylate)
PMDETA	*N*,*N*,*N’*,*N’’*,*N’’*-pentamethyldiethylenetriamine
PMMA	poly(methyl methacrylate)
ppm	parts per million

PRE	persistent radical effect
PS	poly(styrene)
PTFE	poly(tetrafluoroethylene)
PTFEMA	poly(2,2,2-trifluoroethyl methacrylate)
PTMA	poly(TEMPO methacrylate)
PTMPM	poly(2,2,6,6-tetramethylpiperidyl-4-methacrylate)
RAFT	reversible addition fragmentation chain transfer
RDRP	reversible deactivation radical polymerisation
rel.	relative
RMS	root mean square
ROMP	ring-opening metathesis polymerisation
ROS	reactive oxygen species
SE	spectroscopic ellipsometry
SEC	size-exclusion chromatography
SET	single electron transfer
SETNRC	single electron transfer nitroxide radical coupling
SI	surface-initiated
TBDMS	*tert*-butyldimethylsilyl
TEA	triethylamine
TEMPO	2,2,6,6-tetramethylpiperidine-1-oxyl
TEMPOL	4-hydroxy-TEMPO
TFEMA	2,2,2-trifluoroethyl methacrylate
THF	tetrahydrofuran
TMA	TEMPO methacrylate
TMPM	2,2,6,6-tetramethylpiperidyl-4-methacrylate
ToF-SIMS	time-of-flight secondary ion mass spectrometry
Tris	tris(hydroxyl)methylaminomethane
UV	ultraviolet
vis	visible
XPS	X-ray photoelectron spectroscopy

List of Publications and Conference Contributions

Publications Arising during PhD Studies

1. **Dynamic Nitroxide Functional Materials**

   H. Woehlk, A. Lauer, V. Trouillet, A. Welle, L. Barner, J. P. Blinco, K. E. Fairfull-Smith and C. Barner-Kowollik, *Chem. Eur. J.*, **2018**, *24*, 18873-18879.

2. **Engineering Nitroxide Functional Surfaces Using Bioinspired Adhesion**

   H. Woehlk, J. Steinkoenig, C. Lang, L. Michalek, V. Trouillet, P. Krolla, A. S. Goldmann, L. Barner, J. P. Blinco, C. Barner-Kowollik and K. E. Fairfull-Smith, *Langmuir*, **2018**, *34*, 3264-3274.

3. **Spin Fluorescence Silencing Enables an Efficient Thermally Driven Self-Reporting Polymer Release System**

   H. Mutlu, C. W. Schmitt, N. Wedler-Jasinski, **H. Woehlk**, K. E. Fairfull-Smith, J. P. Blinco, C. Barner-Kowollik, *Polym. Chem.*, **2017**, *8*, 6199-6203.

4. **High Resolution Mass Spectrometric Access to Nitroxide Containing Polymers**

   T. S. Fischer, J. Steinkoenig, **H. Woehlk**, J. P. Blinco, K. E. Fairfull-Smith, C. Barner-Kowollik, *Polym. Chem.*, **2017**, *8*, 5269-5274

5. **Oxidative Polymerization of Catecholamines: Structural Access by High-Resolution Mass Spectrometry**

   H. Woehlk, J. Steinkoenig, C. Lang, A. S. Goldmann, L. Barner, J. P. Blinco, K. E. Fairfull-Smith and C. Barner-Kowollik, *Polym. Chem.*, **2017**, *8*, 3050-3055.

Additional Publication

6. **End group functionalization of poly(ethylene glycol) with phenolphthalein: towards star-shaped polymers based on supramolecular interactions**

   C. Fleischmann, **H. Wöhlk**, H. Ritter, *Beilstein J. Org. Chem.*, **2014**, *10*, 2263-2269.

Conference Contribution

Oxidative Polymerization of Catecholamines: Structural Access by High-Resolution Mass Spectrometry

H. Woehlk, J. Steinkoenig, C. Lang, A. S. Goldmann, L. Barner, J. P. Blinco, K. E. Fairfull-Smith and C. Barner-Kowollik, *RACI Centenary Congress*, Melbourne, Australia, **July 2017**, oral presentation.

Acknowledgements

I would like to express my gratitude to my supervisors Professor Christopher Barner-Kowollik and Associate Professor Kathryn E. Fairfull-Smith for their dedication and mentorship throughout my doctoral studies at the Karlsruhe Institute of Technology and at the Queensland University of Technology (QUT) in Brisbane, Australia. Their continuous support, encouragement and professionalism are highly appreciated. This joint PhD programme has been a unique opportunity for me and I am very grateful for being part of this international research team. In this context, both institutions are thanked for supporting this fruitful German–Australian collaboration and for providing excellent research environments. The Australian Research Council is acknowledged for funding my PhD studies.

Dr. James P. Blinco is thanked for his co-supervision. Furthermore, I would like to thank Associate Professor Leonie Barner and Dr. Anja S. Goldmann for their scientific input throughout my entire PhD candidature.

I gratefully acknowledge Professor R.E.W. (Bob) Hancock and his group for hosting my research stay at the Department of Microbiology and Immunology at the University of British Columbia in Vancouver, Canada. I experienced a truly remarkable hospitality and a great working atmosphere. Special thanks go to my excellent collaboration partners Dr. Sarah C. Mansour and Dr. Mike J. Trimble for introducing me to the fascinating world of biofilms.

I would like to thank Vanessa Trouillet and Dr. Alexander Welle for their countless XPS and ToF-SIMS measurements. Your expertise, dedication and continuous support are highly appreciated and have resulted in great scientific outcomes. In addition, I would like to thank Peter Krolla and Lukas Michalek for AFM measurements and their excellent scientific collaboration. Dr. Jan Steinkönig is gratefully acknowledged for HR-ESI-MS measurements. Our continuous scientific discussions have significantly contributed to the quality of this PhD thesis. Andrea Lauer is thanked for our successful collaborative project. Furthermore, I would like to thank all staff members, senior postdocs and research technicians for running the KIT laboratories. I experienced a great macroarc team spirit in the KIT labs and a big thanks goes to my colleagues and postdocs for carefully proofreading this thesis. I would like to thank soon-to-be PhDs Federica Cavalli, Hannah Rothfuß and David Marschner for their great friendship during our PhD studies and of course Matthias Eing and Hannes Houck for being in the same German–Australian (via Belgium) (commuting) boat.

Dr. Christiane Lang is thanked for her great support, particularly during the early days of my PhD candidature at QUT. Furthermore, I would like to thank Dr. Josh Lipton-Duffin and Dr. Peter Hines for their dedicated time in training me on various instruments available at CARF and for our fruitful scientific discussions. A big thanks goes to all members of the QUT M6 and M4 laboratories, including the free radical chemistry group, all staff members and lab technicians, for their great support providing an excellent working environment. In particular, I would like to thank Dr. Kai-Anders Hansen and Anthony Verderosa from the M6 team. Kristina Jovic is thanked for our friendship and our joint adventures — what an amazing time we have spent together in Australia.

My deepest gratitude goes to my family for their support, patience and motivation during my PhD studies. For very good reasons this doctoral thesis is dedicated to you. Furthermore, I want to thank my friends from Kiel and Düsseldorf— your friendship means a lot to me. In addition, I have met many new and inspiring people from all around the world during my time in Germany, Canada and Australia. Thank you all for so many unforgettable moments we have shared together.